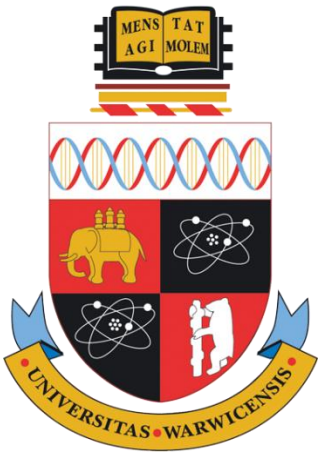

Electrochemical Imaging of Energy Conversion and Storage Materials

by

Binglin Tao

Thesis submitted to the University of Warwick for the degree of

Doctor of Philosophy

Department of Chemistry

September 2020

For

Patrick R. Unwin

Who gave me a chance to start my PhD

Contents

List of Figures

List of Tables

Abbreviations

2D Two-Dimensional

AC Alternating Current

AFM Atomic Force Microscopy

c-AFM Conductive Atomic Force Microscopy

CV Cyclic Voltammetry

CVD Chemical Vapour Deposition

DAQ Data Acquisition

DC Direct Current

DI Deionized Water

DFT Density functional theory

EBSD Electron Backscatter Diffraction

ECSA Electrochemical Surface Area

ESM Electrochemical Strain Microscopy

FESEM Field Emission Scanning Electron Microscopy

FEM Finite Element Method (Modelling)

FPGA Field-Programmable Gate Array

GC Glassy Carbon

h-BN Hexagonal Boron Nitride

HER Hydrogen Evolution Reaction

HOPG High Oriented Pyrolytic Graphite

KPFM Kelvin probe force microscopy

LSV Linear-sweep Voltammetry (Voltammograms)

MOF Metal Organic Frameworks

OER Oxygen Evolution Reaction

ORR Oxygen Reduction Reaction

pBDD Polycrystalline Boron Doped Diamond

PMMA Polymethyl-methacrylate

PZC Potential of Zero Charge

QRCE Quasi-Reference Counter Electrode

RHE Reversible Hydrogen Electrode

SCCM Standard Cubic Centimeters

SCE Saturated Calomel Electrode

SECCM Scanning Electrochemical Cell Microscopy

SECM Scanning Electrochemical Microscopy

SEI Solid Electrolyte Interphase

SEM Scanning Electron Microscopy

SEPM Scanning Electrochemical Probe Microscopy

SICM Scanning Ion Conductance Microscopy

SMCM Scanning Micropipette Contact Method

SPM Scanning Probe Microscopy

STEM Scanning Transmission Electron Microscopy

STM Scanning Tunnelling Microscopy

TMDs Transition Metal Dichalcogenides

TEM Transmission Electron Microscopy

UME Ultra-microelectrode

XRD X-ray diffraction

Acknowledgements

First and foremost, I would like to thank my supervisor Prof. Patrick R. Unwin for his kindness of recognizing my capability and accepted me as one of his students. His support, encouragement and enthusiasm about research provided me a constant driving force over the past three years. I also would like to thank Dr. Cameron L. Bentley for his help with training the Electrochemical Scanning Probe Microscopy system and assistance in the latter stage of all my research projects.

I would like to acknowledge the Warwick Chancellor's International Scholarship for the financial support. It is my great honour to be supported by this funding for 3.5 years to finish my PhD degree. Thanks to all the postdoctoral researchers working in our groups who teach me quite a lot both in research and life, such as David Perry, Gabriel Meloni, Minkyung Kang, Slava Shkirskiy, Ian McPherson and Daniel Martin Yerga. Thanks to everyone in the Warwick Electrochemistry and Interfaces Group who helped to establish and improve the Warwick Electrochemical Platform, and to the department of physics for making and helping with all the electronics and hardware. Based on all these people's hard work, I could learn the state-of-the art Scanning Electrochemical Cell Microscopy (SECCM) technique.

Finally, a huge thank to my wife, Yuehong Qi, who gave up her PhD career in China and accompanied with me in UK for the last 3 years. Our new born baby in June 2020, Guanying (Emily) Tao, becomes the best gift from God in the last year of my PhD.

Declaration

The work presented in this thesis is entirely original and my own work, except where acknowledged in the text. I confirm that this thesis has not been submitted for a degree at another university. This work is being submitted to University of Warwick for thesis by publication.

Chapter 3 was published as:

Metal support effects in electrocatalysis at hexagonal boron nitride

Dan-Qing Liu, **Binglin Tao**, Hong-Cheng Ruan, Cameron L. Bentley, and Patrick R. Unwin, *Chem. Commun.* **2019**, 55, 628-631.

This section also provided the basis of a chapter in Dan-Qing Liu's thesis who design the experiment and jointly performed the experiments.

Chapter 4 was published as:

Nanoscale Variations in the Electrocatalytic Activity of Layered Transition-Metal Dichalcogenides

Binglin Tao, Patrick R. Unwin, and Cameron L. Bentley, *J. Phys. Chem. C.* **2020**, 124, 1, 789-798.

Chapter 5 was published as:

Correlative Electrochemical Microscopy of Li-Ion (De)intercalation at a Series of Individual $LiMn_2O_4$ Particles

Binglin Tao, Lewis C. Yule, Enrico Daviddi, Cameron L. Bentley, and Patrick R. Unwin, *Angew. Chem. Int. Ed.* **2019**, 131, 4654-4659.

Chapter 6 was prepared as:

Rate Controlling Factors in $LiMn_2O_4$ Cathode: Multiscale Analysis of Contact Resistance and Ensemble Effect

Additionally, I have also contributed to the following papers, as co-author in the **Main Text** (paper 1) or acknowledged for helping with the figures drawing in the **Acknowledgements** (paper 2 and 3):

1. Correlating the Local Electrocatalytic Activity of Amorphous Molybdenum Sulfide Thin Films with Microscopic Composition, Structure and Porosity

Cameron L. Bentley, Roland Agoston, **Binglin Tao**, Marc Walker, Xiangdong Xu, Anthony P O'Mullane, and Patrick R. Unwin *ACS Appl. Mater. Interfaces*, **2020**

2. Flexo-photovoltaic effect

Ming-Min Yang, Dong Jik Kim, Marin Alexe, *Science*, **2018**, 360, 904-907.

3. Facile Preparation of Haggite by Reducing V_2O_5 in Guaiacol/Methanol Solution

Fei Yan, Yunfei Bai, Yushuai Sang, Linhao Yu, Kai Wu, Kai Cui, Zhe Wen, Fuhang Mai, Zewei Ma, Hong Chen and Yondan Li, *Inorg. Chem.* **2018**, 57, 15, 8705-8708

Abstract

This thesis presents various functionalities of scanning electrochemical cell microscopy (SECCM) in the field of energy conversion and storage materials, via focusing on hydrogen evolution reaction (HER) catalysis at two-dimensional materials and Li-ion (de)intercalation at battery cathode materials ($LiMn_2O_4$). In the context of HER catalysis, through the use of local (spatially resolved) linear sweep voltammetry, the activity of hexagonal boron nitride (h-BN) nanosheets supported on different metal substrates (Cu and Au) are compared. Au-supported h-BN exhibited significantly enhanced HER charge-transfer kinetics (*i.e.*, higher exchange current density) and a smaller Tafel slope compared to Cu-supported h-BN. These results demonstrate that the electronic interaction with the underlying metal substrate plays a significant role in modulating the electrocatalytic activity of h-BN. The same methodology has also been used to measure the intrinsic electrochemical properties of pristine MoS_2/WS_2 crystals. Catalytic activity for the HER is greatly enhanced at the macroscopic surface defects of these electrodes, measured directly where the active edge plane (*e.g.*, crevices, holes, cracks, *etc.*), with single-layer sensitivity. Besides, nanometer-resolved measurements reveal previously unseen electrochemical phenomena at these electrodes, *i.e.*, spatial activity variations on basal surface, attributed to localized minor structural deformities (*e.g.* mechanical strain and defect density) throughout the crystal. In the context of Li-ion (de)intercalation, using a correlative electrochemistry-microscopy method, the redox activity (reveals through cyclic voltammetry) of a series of individual $LiMn_2O_4$ particles is linked to their corresponding particle size, morphology, crystallinity, and other factors. It has been observed that subtle changes in particle form can greatly influence electrochemical properties of these nominally similar particles. Further spatially-resolved galvanostatic measurements prove that individual $LiMn_2O_4$ particles can be charge/discharged at superfast rate (more than 200 C, where 1C mean fully charge/discharge battery in one hour, 200 C means fully charge/discharge in 18 s). Finally, a series of SECCM probes with graded diameters was exploited to study the electrochemical behavior evolution from single $LiMn_2O_4$ particles to the $LiMn_2O_4$ agglomerates level. Precisely controlling the position of the micropipette in 3D space allowed the influence of ensemble effects and particle-support contact resistance on Li^+ (de)intercalation kinetics to be studied separately, proving that the charge-transfer barrier

in $LiMn_2O_4$ ensembles is largely dictated by interparticle interactions, while the nature of the particle-support contact (*i.e.*, wet vs dry contact) also play an important role.

Chapter 1. Introduction

Novel electrocatalysts and electrode nanomaterials have attracted much attention in the past few years, as they play important role in the energy conversion and storage process. To better understand how subtle structure variations influence the electrochemistry properties, it is important to develop robust and versatile techniques for electrochemical measurements/characterization at the nanoscale, especially scanning probe-based techniques. This Chapter gives an overview of scanning probe microscopy techniques and how they can be implemented for the understanding of structure-function relationships in materials science, which is the major focus of the work herein. This chapter also introduces the basic concept of hydrogen evolution reaction, which is the most popular technique to produce clean energy (H_2). In addition, the basic working principle of Li-ion battery is described, together with the research development on single particle electrodes. Finally, a brief summary of the work undertaken in this thesis is provided.

1.1 Scanning Probe Microscopy

Scanning probe microscopy (SPM) is a large family of probe-based analytical tools, which has attracted great attention ever since its inception. Some of the primary examples of SPM techniques include scanning tunnelling microscopy (STM),[1-2] atomic force microscopy (AFM),[3-5] conductive atomic force microscopy (c-AFM),[6] Kelvin probe force microscopy (KPFM),[7-8] electrochemical strain microscopy (ESM),[9-10] scanning ion conductance microscopy (SICM)[11-12], scanning electrochemical microscopy (SECM),[13-14] scanning electrochemical cell microscopy (SECCM)[15-16] and their hybrids[17-22]. A schematic describes the development of scanning probe techniques is shown in **Figure 1.1**.

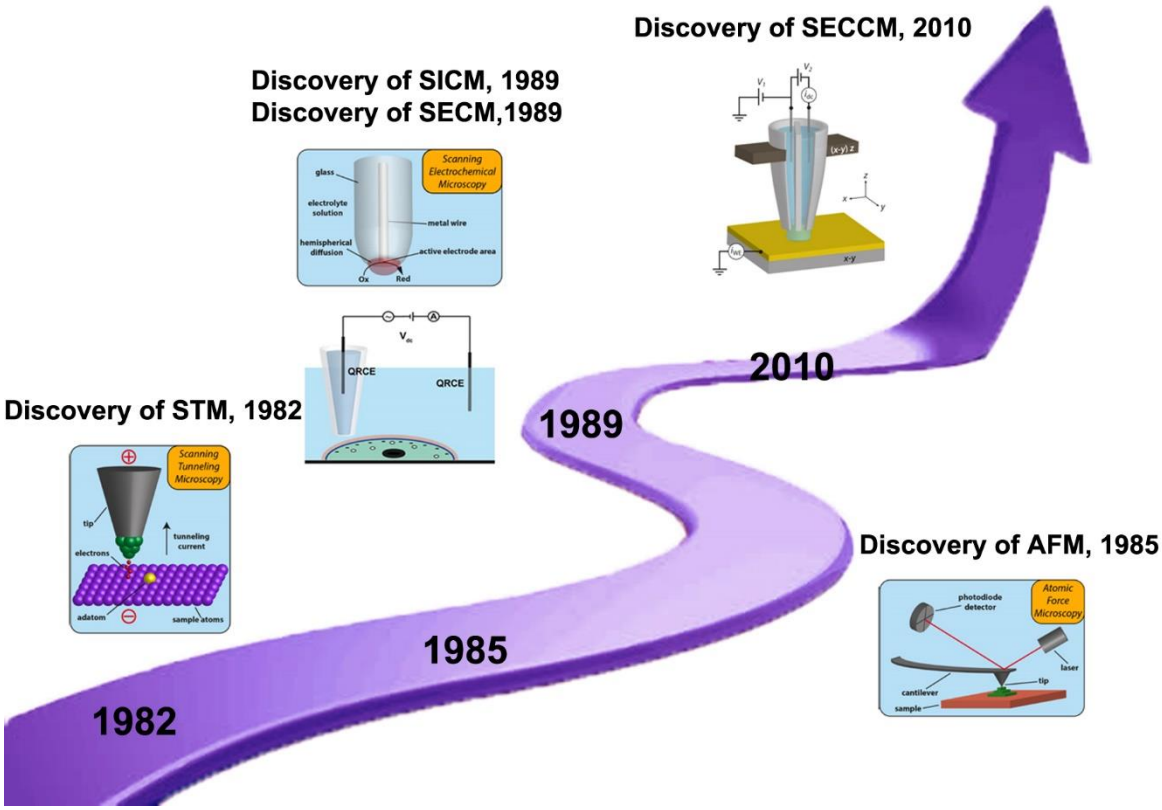

Figure 1.1 Historical development of probe based scanning techniques. Figure 1.1 is adapted from Reference [23].

Scanning tunnelling microscopy (STM) was the first scanning probe-based technique, invented by Binning and Rohrer in 1982 at IBM, Zurich, Switzerland.[1] During the STM operation process, the sample is positively or negatively biased with respect to the metallic tip, such that a small current can tunnel through the space between the tip and sample surface at length scales on the order of ~ 10 Å. A small change in this sample-tip distance can result in large changes in the tunnelling current. The major requirement for this technique relates to the sample surfaces, which should be either an electrical conductor or semiconductor. Initial studies of STM were performed in ultra-high vacuum (UHV), but later on it was also found suitable as an analytical tool in both air and solutions.[24-26]

Scanning ion conductance microscopy (SICM) is another kind of SPM technique, which was first described in 1989 by Hansma *et al*.[12] Generally, SICM utilises the ionic current between two Ag/AgCl quasi reference counter electrodes (QRCE), one immersed in bulk solution and the other inside a glass or quartz nanopipette. As the nanopipette approaches

the samples (either conductive or non-conductive), the ionic current would decrease owing to the steric hindrance between the nanopipette wall and the samples, especially when the distance is comparable with the tip diameter. A schematic of SICM and the corresponding working principles are described in **Figure 1.2**. Historically, SICM was operated in two different modes according to the tip-surface distance: constant height and constant distance.[11-12, 27-28] Later the constant distance mode with scan-hoping regime became dominant,[29] which carried out self-calibration at every pixel to avoid the artefacts from the drift of QRCE and/or environment variations, and then developed into three different modes according to feedback types (*i.e.*, origin of the feedback current): direct current, distance modulation, and bias modulation mode.[30-31]

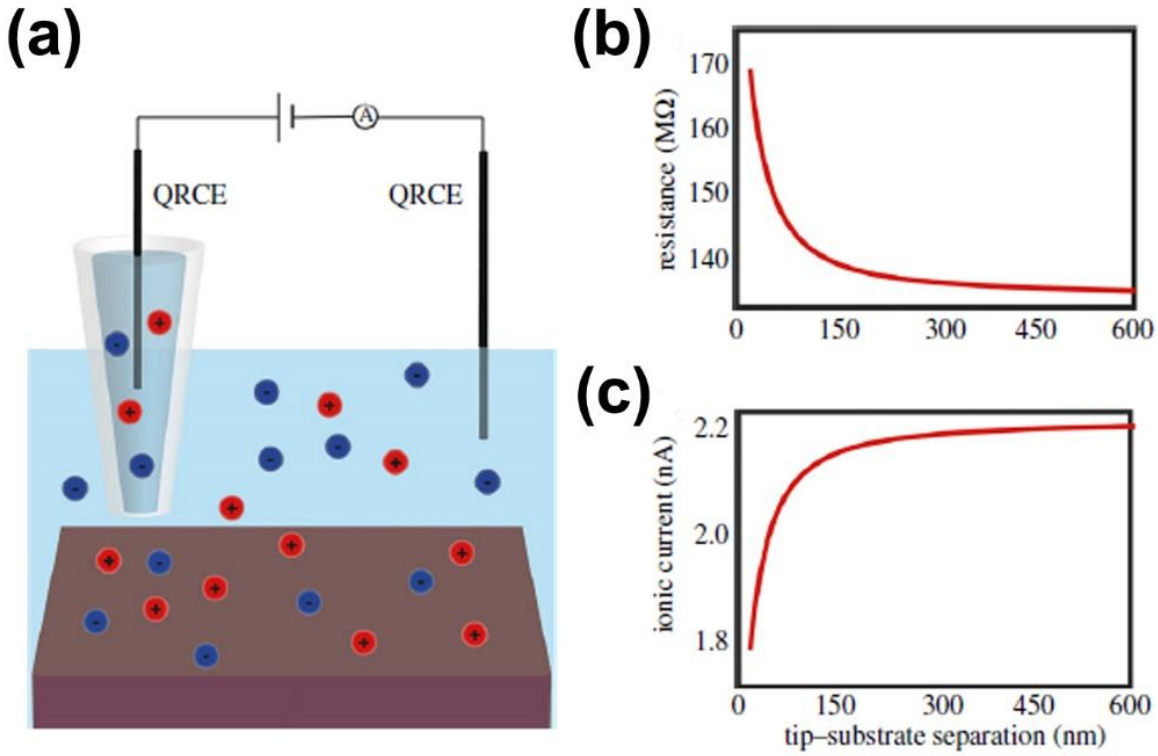

Figure 1.2 (a) Schematic of the SICM set-up with a nanopipette filled and bathed in electrolyte solution above a sample of interest. A bias is applied between a QRCE in the nanopipette and one in bulk solution in order to generate an ionic current that can be used as a means of the nanopipette sensing the surface. **(b)** Simulated resistance approach curve of a nanopipette, with 100 nm diameter, approaching an uncharged surface at 300 mV tip bias in 10 mM KCl.

(c) Corresponding ionic current as a function of tip-sample distance from the simulation in **(b)**. Figure 1.2 is adapted from Reference [30].

As a non-contact scanning probe technique, SICM can provide both an ionic conductivity (related to surface activity) and the topography map simultaneously. To date, SICM has been predominantly used as a tool for topographical mapping of biological samples with very limited functional applications,[32-33] as the deconvolution of topography and surface activity from the ionic current map need very delicate experimental design and post explanation with finite elemental modelling (FEM).[34-36]

Around the same time as the invention of SICM, Bard established scanning electrochemical microscopy (SECM), which has been widely used as an effective tool to interrogate local electrochemistry via ultra-microelectrode (UME) probes.[14, 37] Distinct from SICM measuring the ion flux at and around the samples, SECM surveys reactive flux of redox active species at liquid/liquid, liquid/gas and liquid/solid sample interfaces.[38-40] Typically, the probe in this technique incorporates a thin Pt/carbon wire (usually several micrometres) sealed inside glass shealth to compose a disk electrode. Unlike SICM, a general SECM system has four electrodes: reference, counter and two working electrodes (UME and the sample served as independent working electrodes I and II, respectively) dipped into an electrolyte solution a containing mediator species, as schematically shown in **Figure 1.3**. The mediators work as redox species between the SECM probe (usually termed as working electrode-I) and the sample (working electrode-II) to indicate on the surface activity or topography.[41] The redox mediators and recent advances in the SECM technique were summarized in a comprehensive review.[42] Since these initial reports in the early 1990s, a wide variety of new SECM modes have been developed in order to accommodate different applications. The common SECM operation principle includes feedback mode, generation/collection mode, competition mode, direct mode, and potentiometric mode.

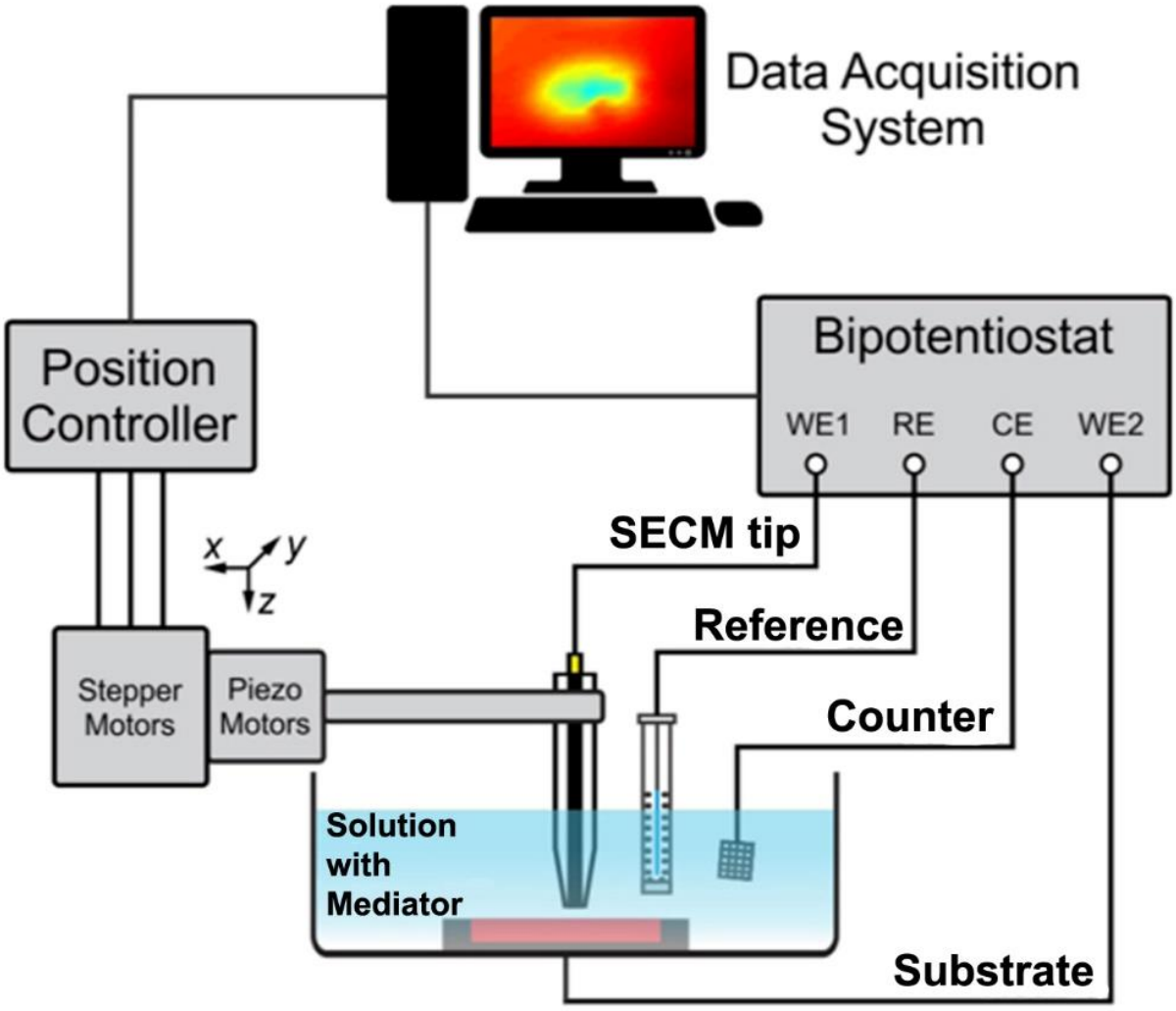

Figure 1.3 Schematic of the SECM instrument. Figure 1.3 is adapted from Reference [42].

Overall, SECM is a powerful tool for studying interfacial physicochemical phenomena, but non-constancy in maintaining the tip-to-substrate separation is a big issue, as the convolution between topography and activity may cause artefacts. The resolution of SECM is restricted by the concentric configuration of UME, which is also not very straightforward for fabrication. Another concern is that SECM (and SICM, see above) requires the whole sample to be immersed in the electrolyte during the scanning process, which may change the surface properties over time, such as the interrogation of metal corrosion or screening of electrocatalytic nanomaterials.

1.2 Scanning Electrochemical Cell Microscopy

Scanning electrochemical cell microscopy (SECCM) is a new generation of scanning probe technique that addresses a number of the limitations of SECM and SICM, as highlighted above.[15-16, 43] In SECCM, the electrode surface is not immersed into the electrolyte solution, but rather the electrochemical reaction cell is confined in a small meniscus formed at the end of a nanopipette. The benefit of this technique is that it can operate in air, as well as immiscible liquids, with versatile electrolytes inside of the tip (not only aqueous solutions[44-46], but also organic solvents[47] and ionic liquids[48-49]). This system is also designed to provide a highly sensitive feedback signal for the control of probe-to-substrate separation, as well as good versatility in terms of applicability with different substrate materials (*i.e.*, with both conductors and semiconductors). Thus, one of the main employments of SECCM is in material science, to elucidate a myriad of structure-function relationships, which is important for both fundamental research and practical applications.[50-52]

1.2.1 Operational Principles

In SECCM, electrochemistry is probed directly and locally at the sample electrode, with a spatial resolution defined by the area of meniscus contact, whose dimension is similar to the the orifice of capillary (*i.e.*, nanopipette). A schematic describing the SECCM setup is shown in **Figure 1.4**. Typically, the nanopipette is pulled from glass/quartz capillary and then filled with solution of interest (*e.g*, organic or aqueous). A QRCE is inserted from the back of the nanopipette, and electrochemical measurement is performed by bias the potential between QRCE and sample electrode. Ag/AgCl wires are the most widely used QRCE in aqueous solution, while Pd-H_2 electrodes are also available, especially in acid solutions. The nanopipette and sample are mounted on z and xy piezoelectric positioners respectively, allowing local measurements to be performed in an automated fashion, which are typically controlled by LabVIEW interfaces with FPGA data collection card (details are in the **Experimental Chapter**). In particular, topographical (through the recorded *z*-positions) and electrochemical activity maps of the sample can be built synchronously, through a series of spatially resolved electrochemical measurements (*e.g*, cyclic voltammetry, galvanostatic charge-discharge, linear sweep voltammetry and chronoamperometry.

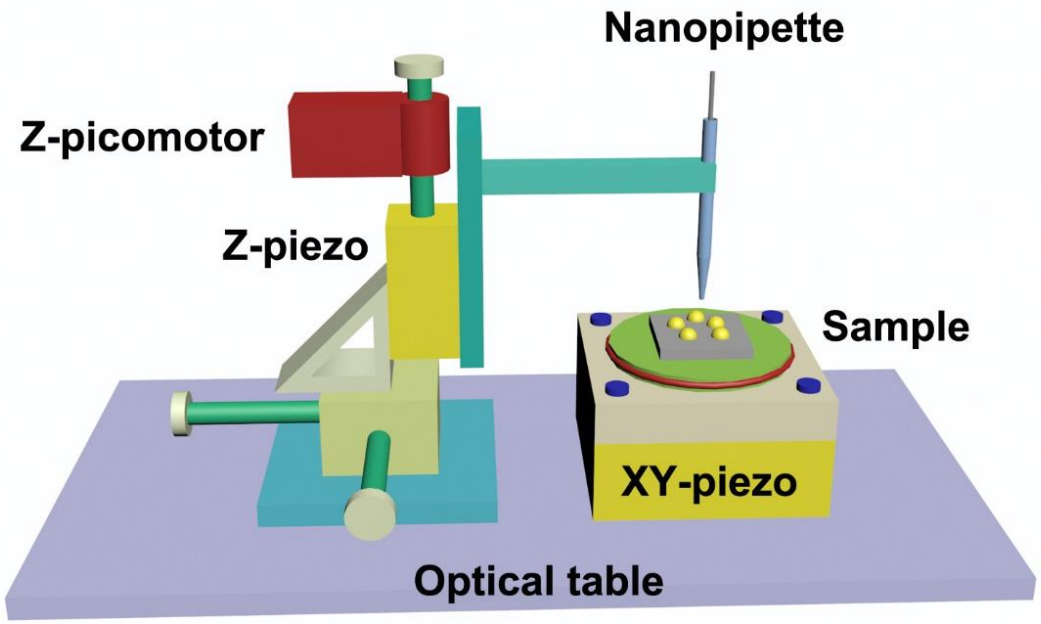

Figure 1.4 Schematic showing the typical electrochemical measurements performed on targeted sample electrode using SECCM setup, which is controlled by the Warwick Electrochemical Scanning Probe Microscopy (WEC-SPM) user interfaces.

1.2.2 Development and State-of-the-art

Before the introduction of SECCM in 2010, microcapillary based techniques were widely used to probe the local corrosion-related properties of macroscopic electrode (*e.g.*, polycrystalline metal) surfaces over two decades ago.[53-54] Inspired by this technique, scanning micropipette contact method (SMCM) was first developed for high-resolution imaging (*ca.* 1.5 µm) in 2009.[15] This configuration employs hopping mode with a single barrelled probe approaching the substrate (working) surface at a series of predefined locations (shown in **Figure 1.5a**). To be more specific, the substrate is connected to a current amplifier and a specific bias voltage (E_{app}) is applied before approach, and the QRCE is connected to the common ground. The tip is brought to contact with the sample surface via the meniscus at the end. When the meniscus just makes contact with the surface, the electric circuit is closed and a small threshold value (usually a little bigger than the equipment noise level, a fixed threshold is applied during whole scan) is triggered to stop the tip from further approaching. After that, electrochemical reaction is performed at this fixed position, and the tip height is recorded, enabling both the electrochemical activity and topography map to be tracked at the same time.

Based on the SMCM, dual barrelled theta-pipette probes that are able to provide positional feedback independent of the current flowing at the substrate (working electrode) surface were introduced in 2010, and the term "SECCM" was coined.[16, 43] During operation, each barrel of the theta pipette is filled with an electrolyte of interest, and equipped with an Ag/AgCl QRCE in each barrel, as shown in **Figure 1.5b**. A constant potential (E_1) is applied between two QRCEs to induce an ionic conductance current, i_{dc}, through the electrolyte meniscus formed at the tip end. A small harmonic oscillation of probe in the z-direction (*e.g.*, at a frequency of 300 Hz and an amplitude of *ca.* 10 % of the tip diameter, distance modulation) is added through an external lock-in amplifier. Upon meniscus-surface contact, a periodic deformation of the meniscus cell occurs (*i.e.*, at the same frequency of harmonic oscillation of the probe), which induces an AC current (i_{ac}) component in the ionic conductance current flowing between the QRCEs. Herein, the amplitude of this AC current is used as a feedback signal to control the distance between the end of the probe and the surface. Electrochemistry is performed within the area of the surface confined by the meniscus cell, by controlling E_2 while maintaining E_1 fixed. The effective potential felt at the substrate with respect to the QRCE is equal to $-(E_2+E_1/2)$, and the surface current at the substrate can be measured as i_{surf}. According to the above-mentioned working principle, this configuration can be used to investigate any surfaces (*i.e.*, conductors, semiconductors and insulators), as the i_{ac} feedback is independent of substrate conductivity (*i.e.*, electrochemical current). Again, it should be reiterated that the effective working electrode area is defined by the size of meniscus at the end of the theta pipette.

Ion conductance current feedback control afforded by the dual barrel configuration of SECCM allows this technique to be operated in a constant distance scanning mode. With the capability of precisely controlling of the pipette oscillation, the tip-to-substrate separation was maintained constantly by monitoring the amplitude of the AC current in between two barrels, whilst moving the electrode substrate laterally in the x or y directions. A high-speed, high-resolution Archimedes spiral scan pattern based on the constant tip−substrate scanning mode has also been developed to obtain potential-resolved image sequences comprising thousands of pixels at rates as fast as *ca.* 4 s per frame.[55] Besides, as the positional feedback signal comes from the ion current in between two barrels and is independent of the working

current flowing the sample surface, this configuration allows SECCM to probe a variety of materials including conductors[56-57], semiconductors[58-59] and insulators[60-61].

In 2014, Takahashi *et al.* readopted the single nanopipette SECCM method (SMCM, shown in **Figure 1.5a**) to perform spatially resolved voltammetric analysis on $LiFePO_4$ battery composite electrode and a series of individual particles.[62] Reintroduction of the hopping mode has re-enabled the use of single-channelled probes and simplified experimental setups, mainly featured by the removal of lock-in amplifier.[63] Besides, this configuration allows great advances in terms of spatial-resolution and image acquisition rates being reported in the field of nanoscale electrochemical imaging. Owing to these advantages, most of the SECCM experiments were performed using this configuration very recently.[64-68] It should be noted that in this configuration, the sample needs to be (semi)conductive, and biased at a voltage where electrochemical reaction could happen, as redox current flowing the sample serves as the feedback signal (*vide supra,* SMCM). For brevity, all meniscus cell-based techniques, regardless of whether single- or double-barrelled probes were used are collectively referred to as SECCM hereafter.

In order to investigate the electrochemical activities of polymer electrodes (with well-defined conductive and nonconductive domains on the same substrate) at faster image acquisition rates, Daviddi *et al.* proposed a new dual barrel SECCM configuration with self-referencing DC ion current feedback in 2019.[69] Compared to distance modulated SECCM mentioned above (an absolute threshold value of current amplitude is set throuhgout the whole scan), this configuration employs the changes of ion conductance current in between two channels as the threshold at each and every pixel to aviod any drift of this current (*e.g.*, drift of QRCE). The scheme of the voltammetric SECCM setup employed herein is shown in **Figure 1.5c**. During operation, a potential bias (E_1) was applied between identical Ag/AgCl QRCEs located in the two barrels of the nanopipet probe to induce a ion conductance current (i_{dc}). Due to the deformation of the meniscus when landing on the surface, a large spike current of i_{dc} (several hundreds of pA) can be detected, which serves as the feedback signal to halt the approach. As the same with dual barrel distance modulted SECCM (shown above), the voltage applied on the substrate surface with respect to the QRCE is - (V_2+V_1/2).

Inspired by the bias modulated scanning ion conductance microscopy, a recent application of SECCM in mapping of the potential of zero charge (PZC) on metal−electrolyte interface introduced a single barrel based bias modulated SECCM technique (configuration is shown in **Figure 1.5d**).[70] The aim of this work was to measure the distribution of PZC on a polycrystalline Pt electrode, thus AC current is preferred as the net charge is zero without perturbing the surface charge itself. In brief, an AC signal is added to the applied working electrode potential through the lock-in amplifier, and the amplitude of this current is used as the feedback to halt the tip moving once the droplet is in contact with the sample surface. After that, electrochemical measurents are performed in the confined meniscus, as is the same with single barrelled SECCM (*vide supra*).

Overall, the advantage of SECCM over other scanning probe microscopy is that electrochemical measurements are performed locally and directly. The small current measured in SECCM renders this technique relatively immune to bulk resistance which is a major problem for macroscopic measurements on resistive materials. Finally, in SECCM experiments, there is no need to fully immerse the substrate electrode in solution during scanning, thus avoiding the contamination/degradation of the whole sample. Compared to the macroscopic experiments, where the “average” properties of the electrode are under investigation (*e.g.*, ensembles of nanomaterials and binders, conductive additives, explored below), SECCM in tandem with other characterization techniques enables particular surface features (even on the nanoscale size) to be targeted, revealing structure-function relationships unambiguously.

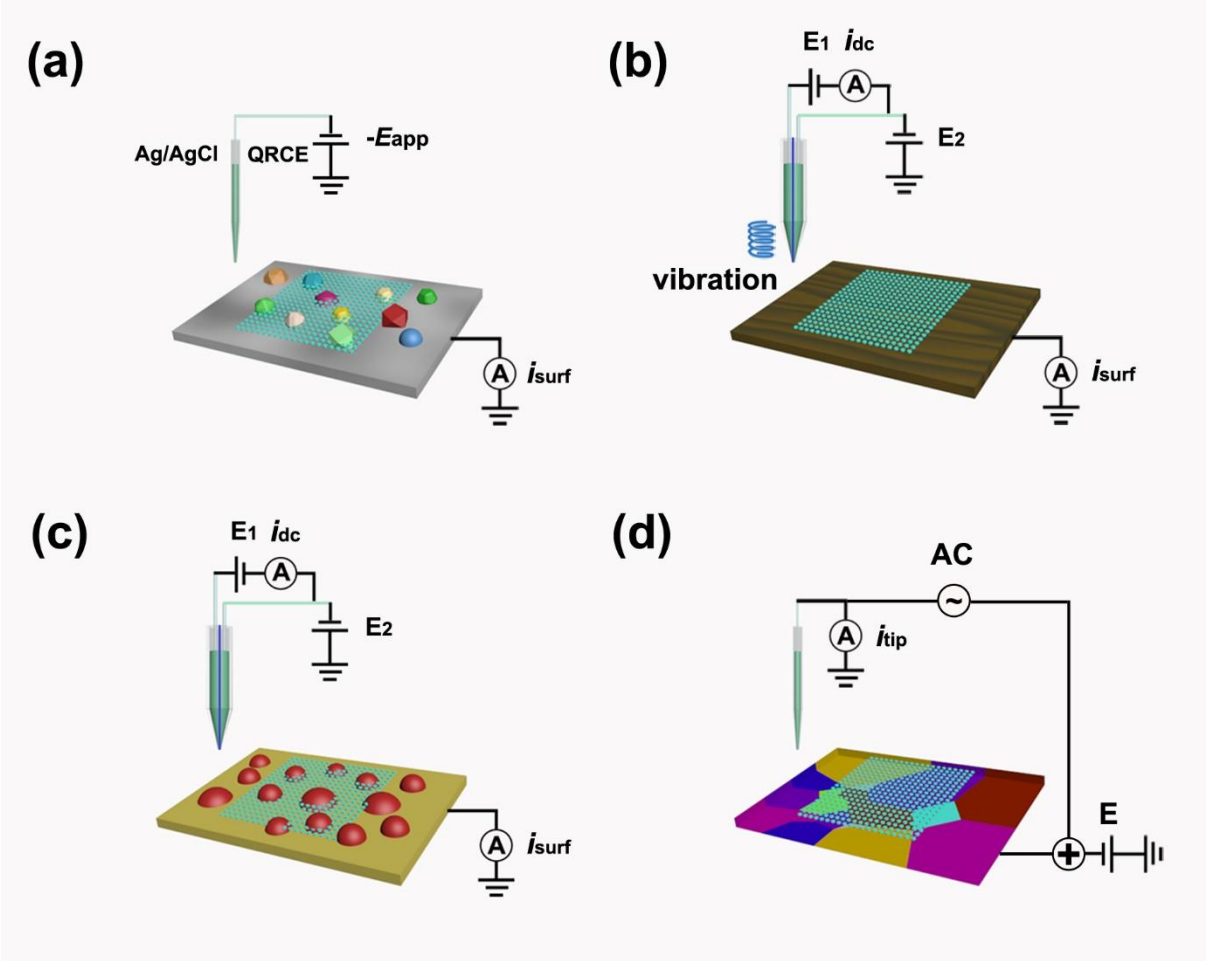

Figure 1.5 Schematic showing the development of SECCM with different configurations at different times. **(a)** Single barrelled SECCM (originally scanning micropipette contact method) with surface current (flowing working electrode) feedback. The substrate is electrocatalytic particles supported on glassy carbon. **(b)** Distance modulated dual barrelled SECCM with ion conductance current feedback. The substrate is HOPG. **(c)** Dual barrelled SECCM with self-referencing ion conductance current feedback. The substrate is P3HT (local domain) and PMMA (matrix) blend electrode. **(d)** Bias modulated SECCM with surface current (flowing working electrode) feedback. The substrate is polycrystalline metal, *e.g.*, Pt.

1.2.3 Applications and Prospects for SECCM

As a powerful characterization method, a major focus of most SECCM studies has been to establish the electrochemical properties of a range of materials (especially carbon-based electrodes[44, 71-73], metal particles[57, 74-76], polymers[69, 77-78], polycrystalline metals[79] and 2D materials[50, 64, 80-81]) ever since its inception. One advantage of SECCM is its capability in

measuring the local electrochemistry (activity) with high spatial-resolution, as the confined mobile electrochemical cell can effectively isolate each different component of a heterogeneous material. Thus, a comprehensive view of structure- activity relationship can be provided by correlating SECCM images with many other complementary analytical and microscopy techniques, such as SEM, TEM and AFM.[69, 82-83] Besides, SECCM could bridge the gap between nanoscale and microscale electrochemistry via employing a series of probes with graded sizes.

The capability of SECCM is demonstrated powerfully in visualizing and quantifying heterogeneous electron transfer kinetics at different metal electrode surfaces. For example, Aaronson *et al.* investigated the electrochemical activity of the $Fe^{2+/3+}$ redox couple on polycrystalline platinum with different crystallographic orientations via coupling SECCM with electron backscatter diffraction (EBSD).[79] In perchloric acid solution (weakly adsorbing anion), each grain exhibits different electrochemical activity, while uniform activity can be observed within a given grain (shown in **Figure 1.6a**). In contrast, with strongly adsorbing media (sulphuric acid), small variations in activity between different grain facets was seen, while significant enhanced activity was evident at grain boundaries (shown in **Figure 1.6b**). Overall, this 'pseudo-single-crystal' approach avoids the tedious processes involved in preparing single crystals or exposing specific grains (such as lithographic processing), offering a means of screening multiple crystallographic orientations and grain boundaries (GBs) on a polycrystalline metal surface directly.

Similarly, by combination of bulk electrochemical measurements and SECCM with submicrometer resolution, Mariano *et al.* showed that grain boundaries in gold electrodes are more active than grain surfaces for CO_2 reduction, but this conclusion is not applicable to the competing hydrogen evolution reaction (shown in **Figure 1.6c** and **d**).[84] Very recently, SECCM has also found wide applications in corrosion science, especially the study of corrosion of low carbon steel under neutral[65] or acid conditions.[56, 85] In neutral solutiona of 10 mM KNO_3, the more densely packed (101) was most susceptible to anodic oxidation compared to (100) and (111) planes, while in acid conditions of 5 mM H_2SO_4, the grain-dependent anodic iron dissolution rates that increase in the order (100) > (111) > (101). It should be noted that in all of these experiments, complementary structural information from electron backscatter

diffraction (EBSD) in a correlative multi-microscopy approach is necessary to bridge the structure-activity relationship at the (sub)microscale.

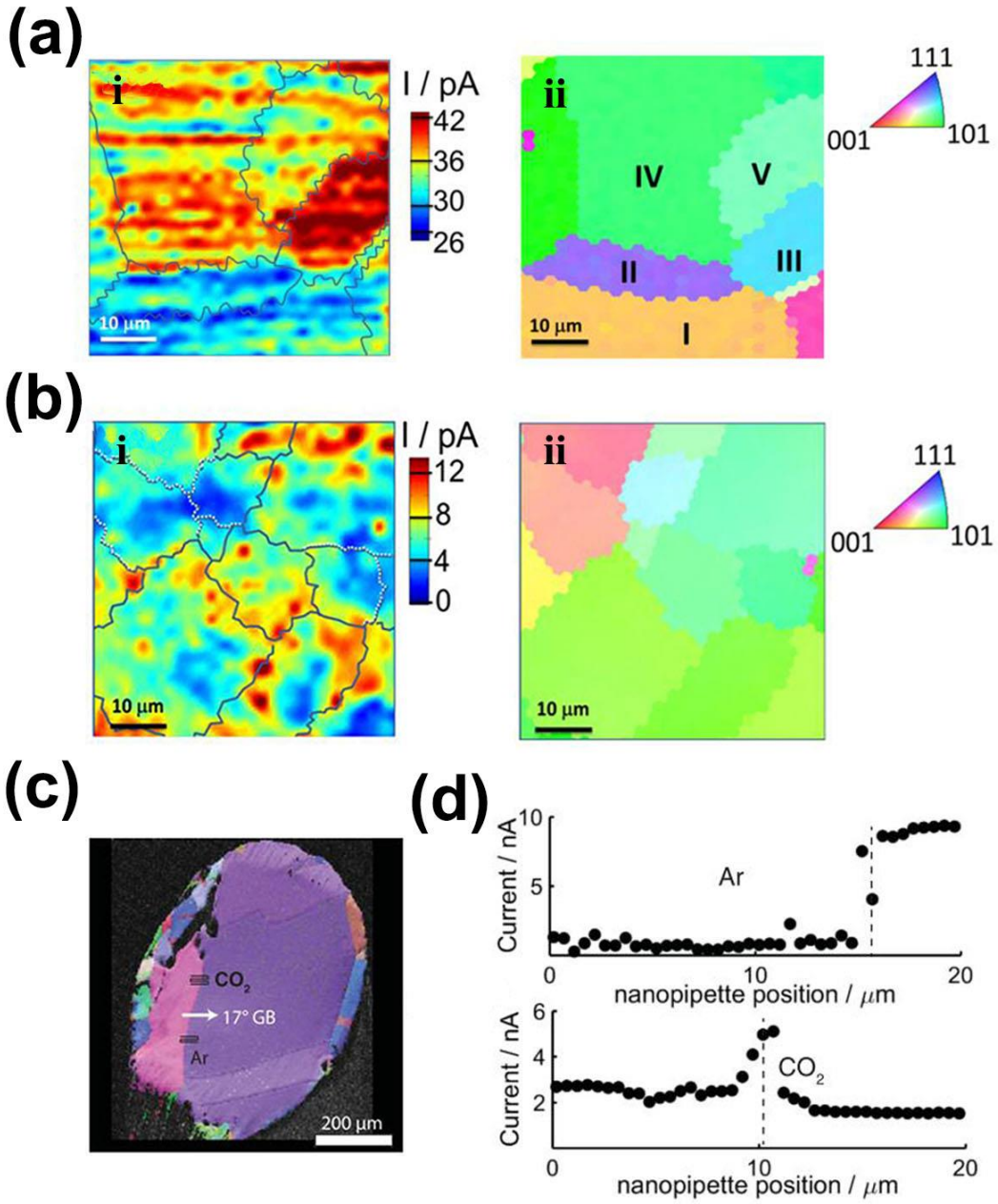

Figure 1.6 (a) Representative SECCM images of the oxidation of 2 mM Fe^{2+} to Fe^{3+} in 10 mM $HClO_4$ at 1.0 V relative to Pd−H_2 **(i)** with corresponding EBSD images **(ii)**. The five grains in the scanned regions are labelled "I", "II", "III", "IV", and "V". The boundaries between the grains deduced from EBSD are marked with blue lines to guide the eye. **(b)** Representative SECCM images of the oxidation of 1 mM Fe^{2+} to Fe^{3+} in 10 mM H_2SO_4 at 1.0 V relative to Pd−H_2 **(i)** and corresponding EBSD image **(ii)**. Grain boundaries (from EBSD) are marked with either black

lines (boundaries at which an enhanced current was observed) or white dotted lines (with no enhanced current) to guide the eye. **(c)** EBSD map of Au wire showing the path of two sets of SECCM line scans across a GB in Ar and CO_2. **(d)** SECCM line scan for HER in Ar (top) and CO_2 reduction (bottom). Dashed lines indicate the position of GBs. Figure 1.6 is adapted from Reference [79, 84].

As noted above, SECCM has also found many applications in mapping the electrochemical activity of numerous carbon materials,[86] such as polycrystalline boron doped diamond (pBDD),[87-88] graphene,[59, 89] highly oriented pyrolytic graphite (HOPG)[45, 90] and carbon nanotubes.[72, 91] As SECCM allows access to study key features on these materials within confined working areas, the heterogeneities of these materials in relation to electrochemical activity could be observed directly via high-throughput scanning process. For example, Patten *et al.* investigated three important classes of electrode reaction processes [oxidation of ferrocenylmethyl trimethylammonium ($FcTMA^+$), oxidation of Fe^{2+}, and oxidation of serotonin] on pBDD, which possesses heterogeneous surfaces due to variations in dopant density across different facets.[88] In all cases, the entire pBDD surface is electroactive, but there are variations in activity between different crystal facets, which correlate with differences in the local dopant level (**shown in Figure 1.7**). Strikingly, there is no evidence for the enhancement of activity at grain boundaries for any of these reactions. In 2012, Lai *et al.* demonstrated fast electron transfer at the basal planes of HOPG under conditions of high mass transport rate, which overturned the views of more than two decades of past research.[71] By traditional consensus, the basal surfaces of HOPG were thought to be completely or largely inert, while the step edges are electrochemically active, and thus dominate the electron transfer. Similarly, Miller *et al.* showed that single walled carbon nanotubes with closed ends, as well as their sidewalls, could promote fast electron transfer for outer sphere redox process.[72]

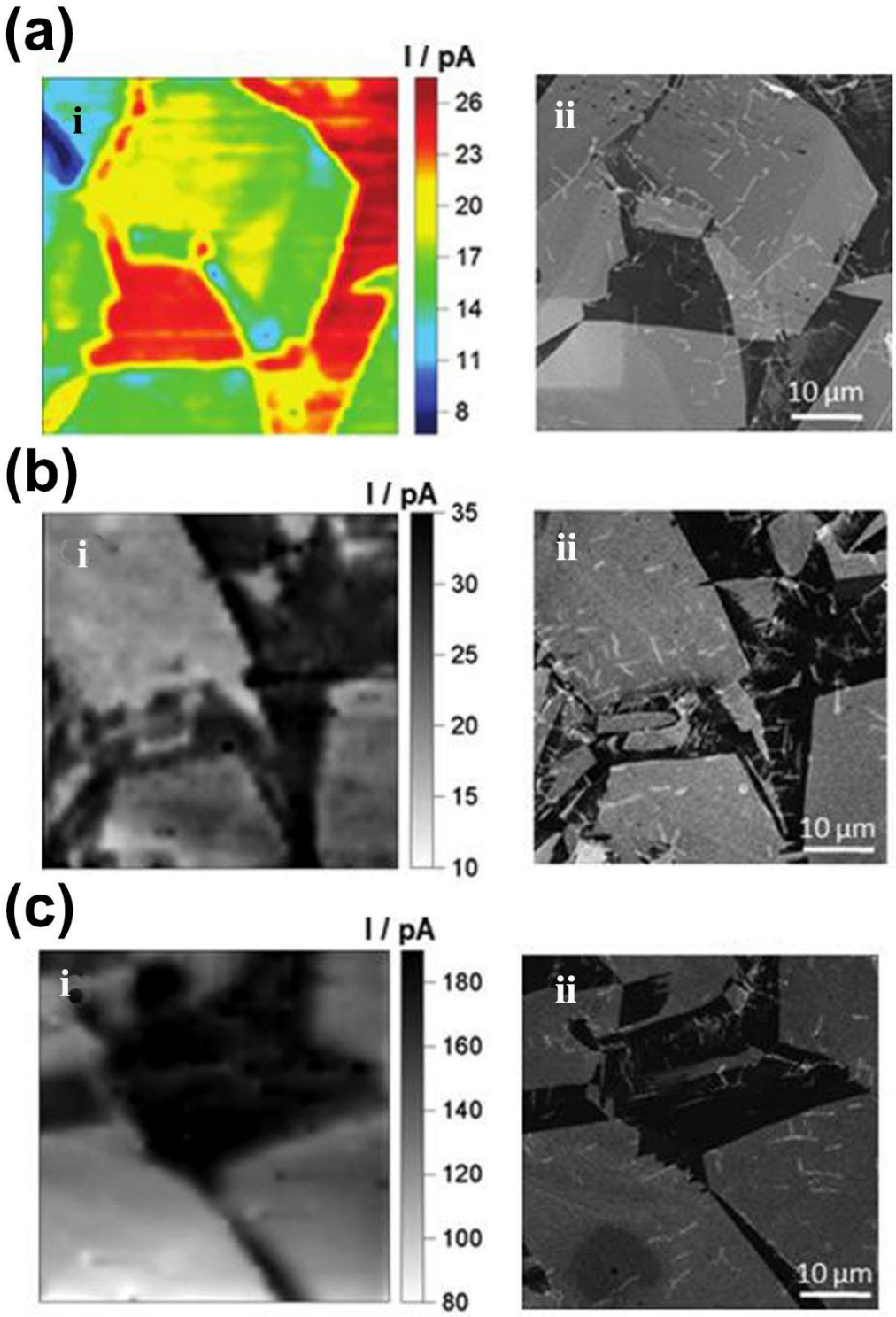

Figure 1.7 SECCM image (**i**) and corresponding FE-SEM image (**ii**) showing the oxidation of 2 mM $FcTMA^+$ in 50 mM KCl at 300 mV vs Ag/AgCl **(a)**, the oxidation of 2 mM Fe^{2+} in 0.5 M H_2SO_4 at 1.2 V vs Pd−H_2, η = 470 mV **(b)** and the oxidation of 2 mM serotonin at 650 mV vs Ag/AgCl **(c)**. A clear effect of facet structure can be observed in each and every case. Figure 1.7 is adapted from Reference [88].

Utilization of SECCM to study the local electrochemistry of battery materials exhibits its potential capability in understanding phenomena at the single particle/agglomerate level. In 2014, Takahashi *et al.* used SECCM to perform cyclic voltammetry and charge-discharge on primary and secondary $LiFePO_4$ particles in aqueous solution (3M LiCl), and observed local heterogeneities in both topography and activity on a pasted composite electrode ($LiFePO_4$, PVDF, and conductive agent).[62] By correlating with complementary scanning electron microscopic (SEM), the structure-activity relationship of single $LiFePO_4$ particle are revealed (**Figure 1.8a**). Later, Mauzeroll *et al.* analysed the electrochemical behaviour of $LiFePO_4$ and $LiNi_{0.33}Co_{0.33}Mn_{0.33}O_2$ clusters in non-aqueous [propylene carbonate and 1-Ethyl-3-methylimidazolium bis(trifluoromethylsulfonyl)imide] with the scanning micropipette contact method, which paved the way for their applications in diagnosing the electrochemical reactions in real lithium-ion batteries (some important data is shown **Figure 1.8b**). [92-93] Unwin *et al.* exploited a unique gel polymer electrolyte to electrochemically interrogate the redox activity of insulating Li_2O_2, and revealed considerable local heterogeneities with significantly enhanced electrochemical activity at toroidal structures when compared to the conformal layers that is usually formed on the cathode of $Li–O_2$ batteries.[47] Very recently, Takahashi *et al.* measured the diffusion coefficient of thin-film electrodes via SECCM, and observed the facet-dependent character of Li^+ diffusivity on an anode electrode ($Li_4Ti_5O_{12}$).[94]

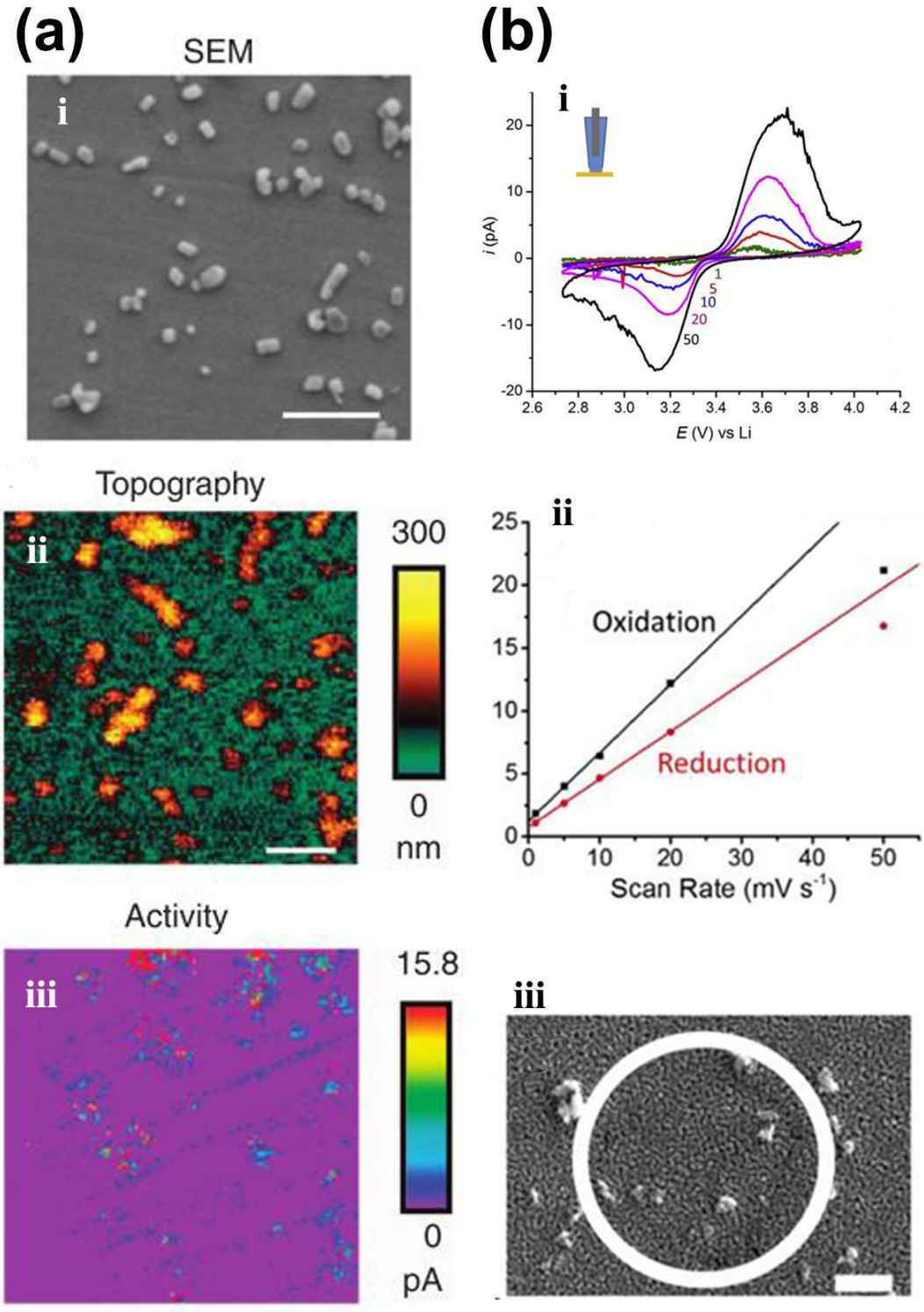

Figure 1.8 (a) Characterization of the activity and topography of individual $LiFePO_4$ nanoparticles in 3M LiCl aqueous solution. **(i)** SEM image of $LiFePO_4$ nanoparticles on a Pt collector electrode (scale bar, 1 mm). **(ii, iii)** Simultaneous SECCM topography (left) and current (right) images. Scan range is 5×5 mm (scale bar, 1mm). The substrate potential was 0.65V versus Ag/AgCl QRCE. **(b)** Localized measurement of isolated lithium iron phosphate

particles (LFP) in 0.1 M $LiClO_4$ in propylene carbonate solution. **(i)** CVs performed at different scan rates using the micropipette method on a LFP dispersion. **(ii)** Plot of peak heights vs. scan rate, for the oxidation and reduction of LFP. **(iii)** SEM image of the area of the LFP dispersion probed in (i). The scale bar is 2 mm. Figure 1.8 is adapted from Reference [62, 92].

In addition to investigation of surface reactions, SECCM is also an ideal platform for nanofabrication. McKelvey *et al.* fabricated continuous polyaniline (PANI) structure across a conducting Au and non-conducting SiO_2 wafer via distance modulated SECCM (shown in **Figure 1.9a**).[77] Different from previous meniscus-based fabrication techniques, which usually employs single channel probes to created structures point by point, this configuration allows the controlling of meniscus-surface contact and the deposition rate respectively, as two different electrical loops are working separately (*vide supra*, dual barrelled SECCM). Another nanofabrication example is the nanoscale nucleation of Ag particles on HOPG (see **Figure 1.9b**).[95] In this process, step edge sites of HOPG do not play a dominant role in nucleation events compared to the HOPG basal plane, and a nucleation, aggregative growth and detachment mechanism was proposed to explain the disparity between the number of calculated nucleation sites and particles observed by scanning electron microscopy. The application of SECCM for studying the metal deposition on electrode surfaces gives hope for future applications to study the dendrite/solid electrolyte interphases formation in lithium-ion battery electrodes.[96-97] Another interesting nanofabrication example is the development of a nano-precision 3D printing method for the preparation of organic–inorganic metal halide perovskites (shown in **Figure 1.9c**).[98] By precisely controlling the working parameters (*e.g.*, pulling speed and humidity), the outer and inner diameter can be modulated. Besides, lots of freeform 3D perovskite architectures can be made by omnidirectional meniscus guiding. It is expected that this technique could create freeform perovskite nanostructures for customized optoelectronics.

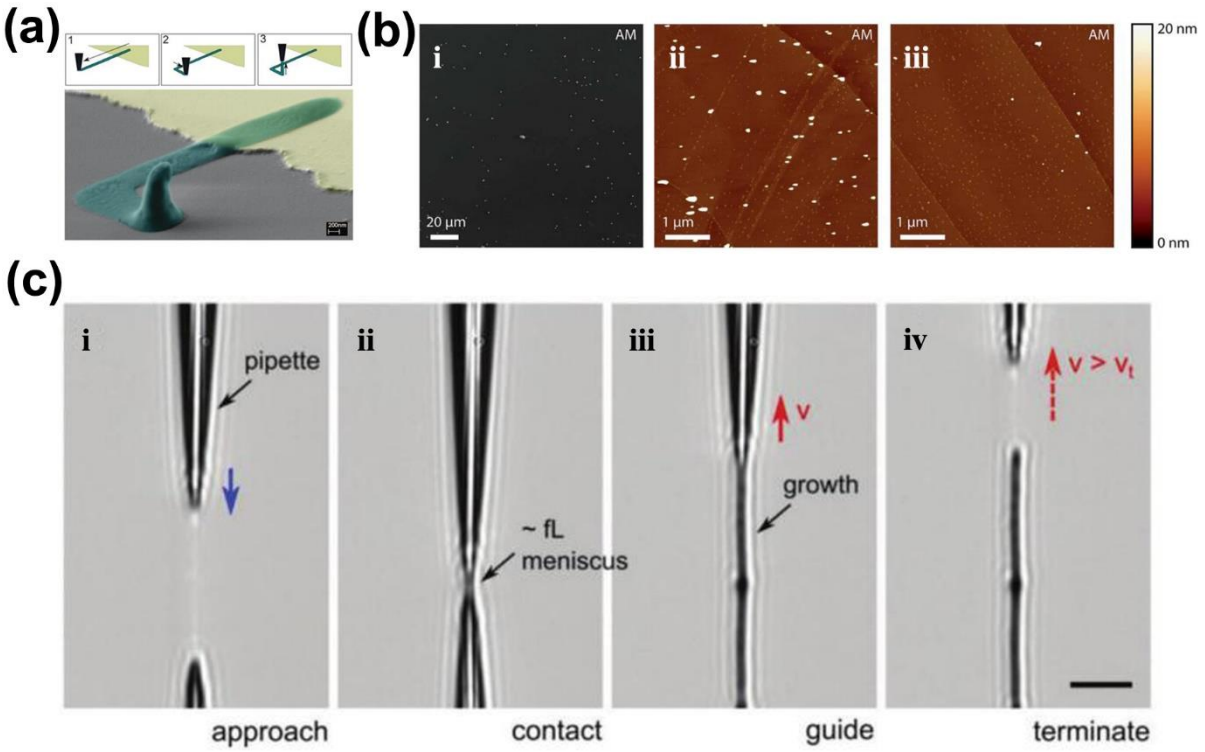

Figure 1.9 (a) SEM (false colour) of a three-dimensional PANI structure (green) created on a conducting (gold) and non-conducting (grey) surface. The probe movement steps are shown as: 1 the lateral movement from a conducting substrate and over an insulating substrate; 2 the change in lateral movement direction on an insulating substrate; and 3 moving the probe away from the surface. **(b)** FE-SEM image **(i)** and AFM images (**ii, iii** are two different areas) of macroscale electrodeposition of silver (from 1mM $AgNO_3$) on AM grade HOPG. **(c)** A series of optical microscopy images showing the 3D printing process (scale bar: 10 µm): **(i)** An ink-filled glass nanopipette approaches to a Si substrate. **(ii)** When the pipette contacts the substrate, an ink meniscus is formed. **(iii)** Meniscus-confined perovskite crystallization is vertically guided by pulling the pipette under solvent evaporation. **(iv)** The crystal growth is terminated at will by abruptly increasing the pulling speed above the threshold speed, v_t. Figure 1.9 is adapted from Reference [77, 95, 98].

1.3 Hydrogen Evolution Reaction

Nowadays, utilization of clean and sustainable energy as the alternative to fossil fuels has attracted growing attention, due to the exacerbation of greenhouse effect and air pollution year by year. H_2 is a clean energy to substitute hydrocarbons, with high energy density and zero carbon footprint discharge to the environment. In industry, gas reforming is the main

way to produce H_2, which is an energy-consuming process that takes place at high temperatures. In contrast, electrochemical water splitting can operate under mild conditions, which is an ideal process to obtain H_2 on large scale. As the same with many traditional catalysis processes, the realization of the "hydrogen economy" requires efficient, stable and low-cost new catalysts. Despite extensive research from the rational materials synthesis and characterization perspective to screening of composite electrodes (including the catalyst, binder and conducting additive), a general literature search reveals a comparative lack of basic understanding on the intrinsic electrochemical properties of the catalysts themselves. SECCM provides the capability to reveal the structure-function relationship unambiguously, which helps to understand electrocatalyst and optimize the electrode from a nanoscale perspective.

1.3.1 HER Mechanism and Tafel Slope

Hydrogen evolution reaction (HER) is a multi-step electrochemical process, which takes place on the surface of an electrode.[99] Generally, the HER mechanism is postulated to proceed via the Volmer reaction, followed by either the Heyrovsk or Tafel reaction in aqueous solutions, as shown in Table 1.[100] Herein, only the reaction in acid solution is considered. The first step of HER in acid solution is the adsorption process (Volmer reaction, as shown in Table 1.1, where H^+ is hydrogen proton, and H* is the adsorption sate of hydrogen atom), by transferring a proton from the acid electrolyte that combines with an electron transferred through electrode surface to form adsorbed hydrogen atoms (H*). In the second step, H_2 molecule is formed through either Heyrovsky reaction (the adsorbed hydrogen atom combines with an electron transferred from the electrode surface and a proton from the electrolyte, desorption process) or Tafel reaction (recombination of two adjacent adsorbed hydrogen atoms H*).

Table 1.1 Overall reaction pathways for HER in acidic solutions.

Overall reaction	Reation Step	Reaction pathway
$2H^+ + 2e^- \rightarrow H_2$	1	Volmer reaction: $H^+ + e^- + * \rightarrow H^*$ (H^+ adsorption)
	2 either A or B	A: Heyrovsky reaction: $H^+ + e^- + H^* \rightarrow H_2$ (H^* desorption)
		B: Tafel reaction: $2H^* \rightarrow H_2$ (2 of H^* recombination)

The preferred reaction pathway depends on the nature of the electrode material. Through calculating the Tafel slope value from polarization curves, the rate-controlling step can be determined.[101-102] Tafel plot is the curve of overpotential (η) versus logarithm current (mA/cm^2), and the linear portions of the Tafel plots can be fit to the Tafel equation ($\eta = b \log j + a$, where b is the Tafel slope, j is the current density and a is empirical constant). Typically, Tafel slope can be obtained by replotting the corresponding LSV curve. For the primary adsorption step (Volmer reaction, equation 1),

$$b = \frac{2.3\ \mathrm{RT}}{\alpha \mathrm{F}} \approx 120\ mV/decade \qquad \text{Eq. 1}$$

where R is the ideal gas constant, T is the absolute temperature, $\alpha \approx 0.5$ is the symmetry coefficient, and F is the Faraday constant. This step is followed by either a desorption step (Heyrovsky reaction, equation 2)

$$b = \frac{2.3\ \mathrm{RT}}{(1+\alpha)\mathrm{F}} \approx 40\ mV/decade \qquad \text{Eq. 2}$$

or a recombination step (Tafel reaction, equation 3)

$$b = \frac{2.3\ \mathrm{RT}}{(1+\alpha)\mathrm{F}} \approx 30\ mV/decade \qquad \text{Eq. 3}$$

Besides, empirical constant a can be calculated according to the following equation (equation 4)

$$a = \frac{2.3\ \mathrm{RT} lg(\mathrm{j_0})}{(1+\alpha)\mathrm{F}} \qquad \text{Eq. 4}$$

Where j_0 is defined as exchange current density (the current density of the electrode when η = 0). An advanced catalyst for the electrochemical HER should possess a low overpotential (η) and Tafel slop (b), together with high exchange current density (j_0). Although the most effective electrocatalysts are Pt-group metals with low overpotential and high stability, the scarcity and high cost hinder their wide application. It remains very challenging to develop highly active HER catalysts based on abundant materials (such as carbon based material[103-104], non-precious metals[105-107] and some 2D semiconductors[108-111]).

1.3.2 Hexagonal Boron Nitride

Hexagonal boron nitride (h-BN) is a kind of sp^2-bonded layered compound. As is similar with the layed physical structure of graphene, h-BN is also referred to as 'white graphene'.[112-113] In the monolayer of h-BN, the boron and nitrogen atoms are alternatively arranged, resulting in a honeycomb structure similar with graphene (shown in **Figure 1.10**).[114] Boron and nitrogen atoms within each layer are bound by strong covalent bonds, whereas between different layers are held together by weak van-der-Waals forces. The B-N bond length in the plane is 1.45 Å and the interlayer spacing of h-BN is 0.333 nm. Besides, h-BN has a wide band gap of 5.97 eV, which is in contrast to the semimetallic nature of graphite.[115-116] Besides, h-BN is a compound possessing exceptional chemical stability and anti-oxidation/ corrosion capability in harsh conditions.

Due to its wide band gap (low conductivity) and electrochemical inertness itself, h-BN has not drawn intense attention in the electrocatalysis field. However, as the bandgap of hexagonal boron nitride can be considerably reduced when introduced onto a metal substrate[117-118], it has been reported as an electrocatalyst both for the oxygen reduction reaction (ORR)[117, 119-120] and hydrogen evolution reaction (HER)[121-122]. For example, Uosaki *et al.* showed that the overpotential for the ORR reaction performed on a BN nanosheet modified Au electrode was 0.27 V lower than that of a bare gold electrode.[119] Density functional theory (DFT) calculations revealed a slight protrusion of the unoccupied BN states toward the Fermi level of the h-BN nanosheet was supported on Au (111), which was caused by the strong interaction between BN and Au. Electrocatalytic performance towards HER of insulating h-BN nanosheets supported on inert Au substrate showed that the size-controlled h-BN nanosheets (<1 um) possessed the higher efficiency for the electrochemical HER.[121]

Combined experimental results with theoretical calculation, the higher activity was linked to edge atom sites provided by the h-BN nanosheets, which is more energetically favoured for the hydrogen adsorption (H*) process. From the fundamental study prospect, verifying the electronic coupling effect between h-BN and metal substrate in modulating the catalytic activity of h-BN, together with detecting the active edge atom sites mentioned above is important to understand and optimise these electrocatalysts. To achieve this, HER activity of two different metal substrate (Cu and Au) supported h-BN is compared in **Chapter 3**.

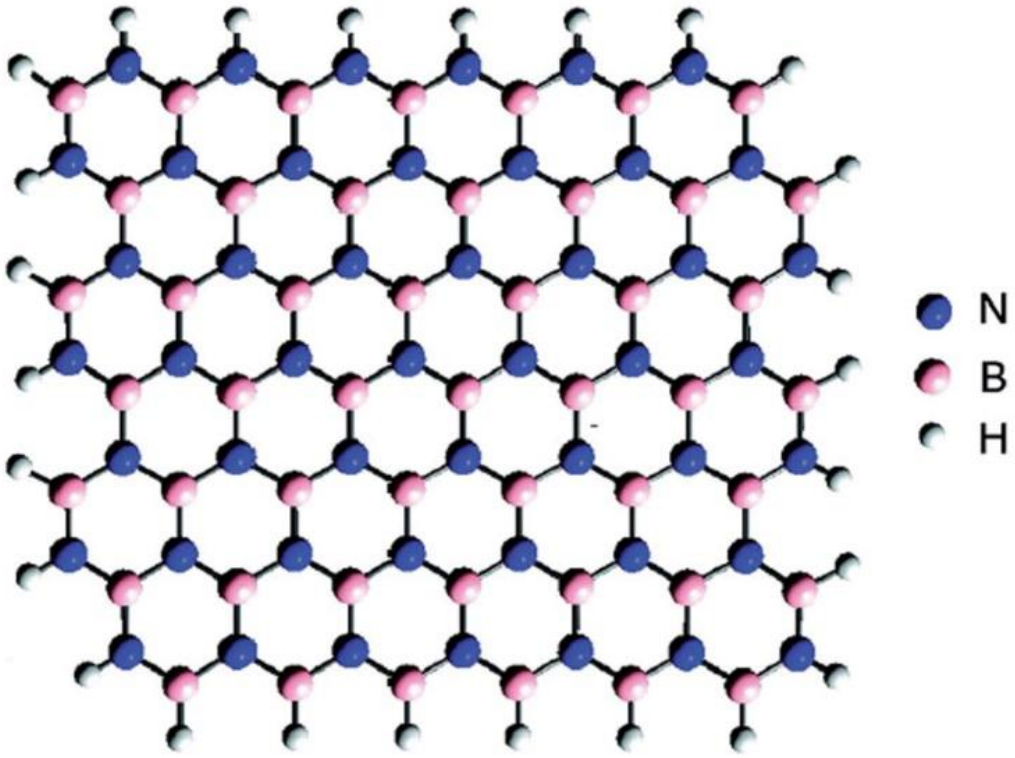

Figure 1.10 Flat structure diagram of hexagonal boron nitride. Blue balls are nitrogen atoms, pink balls are boron atoms and green balls are hydrogen atoms, respectively. This figure is adapted from Reference [114].

1.3.3 Transition Metal Dichalcogenides

As kind of layered-structure material similar with graphite, transition metal dichalcogenides (TMDs) bulk crystals are formed of monolayers bound to each other by relatively weak Van-der-Waals forces between each layer. In each monolayer, TMDs are atomically thin semiconductors of the type MX_2, with M a transition metal atom (M = Mo, W, *etc.*) and X a

chalcogenide atom (X = S, Se, or Te).[123-124] Depending on the arrangement of the atoms, the structures of 2D TMDs can be categorized as trigonal prismatic (hexagonal, H), octahedral (tetragonal, T) and their distorted phase (T') as shown in **Figure 1.11**.[124]

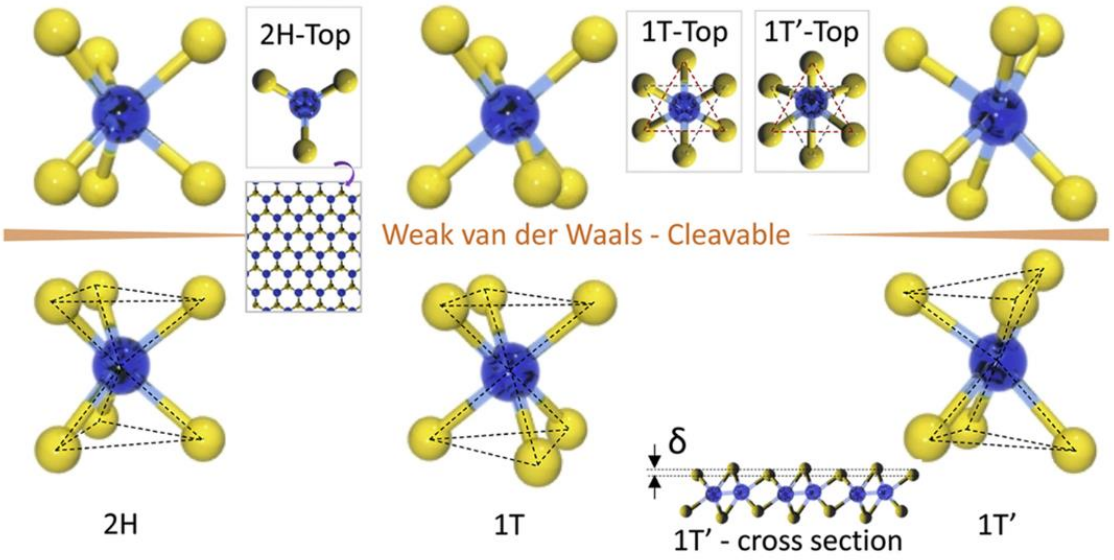

Figure 1.11 Typical structures of layered transition metal dichalcogenides. Cleavable 2H, 1T and 1T' structures in layered TMD are shown. This figure is adapted from Reference [124].

TMDs have been widely used as hydrodesulphurization catalysts in petroleum refining process over several decades[125-126]. Recent work showed that these materials, especially MoS_2, WS_2, $MoSe_2$, and WSe_2 are finding new applications as the next generation of electrochemical HER catalysts.[127-128] Based on both computational and experimental results, the HER catalytic activity aroused from active sites located along the edge of 2D TMDs plates, while the basal surfaces were claimed to be catalytically inert.[129-130] Thus, most of the research work focused on the nanostructure growth and surface engineering to maximize the density of active edge sites[111, 127], or hybrid with carbon based materials[101] to enhance the electrical conductivity, which facilitate the electron transfer in this porous electrode. Although TMDs have been widely accepted as a next generation HER electrocatalysts to substitute Pt, these conclusions were obtained from bulk measurement conditions with composite electrodes, which reflected the total electrochemical behaviour of all components.

Besides, in traditional electrodes, the porous structure character made the actual active surface area hard to be determined, thus all the results based on areas are not accurate, such as exchange current density and turnover frequency. Different from these previous work, **Chapter 4** focused on the intrinsic electrochemical properties (*e.g.*, electrocatalytic activity) of TMDs.

1.4 Lithium-ion Battery

1.4.1 Battery Configuration and Working Principles

The Nobel Prize in Chemistry (2019) was awarded to Prof. Stanley Whittingham, Dr. Akira Yoshino, and Prof. John B. Goodenough for their pioneering work on lithium-ion batteries. Batteries enable humankind to store, transport, and use electricity on demand, which helped the development of portable electronic products (*e.g.*, video cameras, notebook computers, and cell phones) and electric vehicles (*e.g.*, hybrid and/or pure). Dating back to 1990, Sony company realized first lithium-ion battery via using the transition metal oxide, $LiCoO_2$ as cathode and carbonaceous materials as anode.[131] In general, a lithium-ion battery cell is composed of four main parts, *i.e.*, cathode, anode, electrolyte and separator (shown in **Figure 1.12**), although they can be assembled as cylindrical, prismatic, pouch, or button cells.[132-135] The main component of cathode material is lithium metal oxide powder (*e.g.*, $LiCoO_2$, $LiMn_2O_4$, $LiFePO_4$ and $LiNi_{0.33}Co_{0.33}Mn_{0.33}O_2$), which is also the most important and expensive constitution for the whole battery.[136-137] Typically, the metal oxide powder is mixed with carbon black and binder to form a viscous paste, and then coated onto aluminium foil. Similarly, the main constitution of anode is graphite powder, which is supported on copper foil with the help of binding agent. The electrolyte contains inorganic salts dissolved in organic solvents, completing the circuit by transporting the lithium-ion between the cathode and anode.[138-139] The separator is usually made of polymer based micro-porous membranes, which prevents short circuit between the cathode and anode due to physical contact.[140]

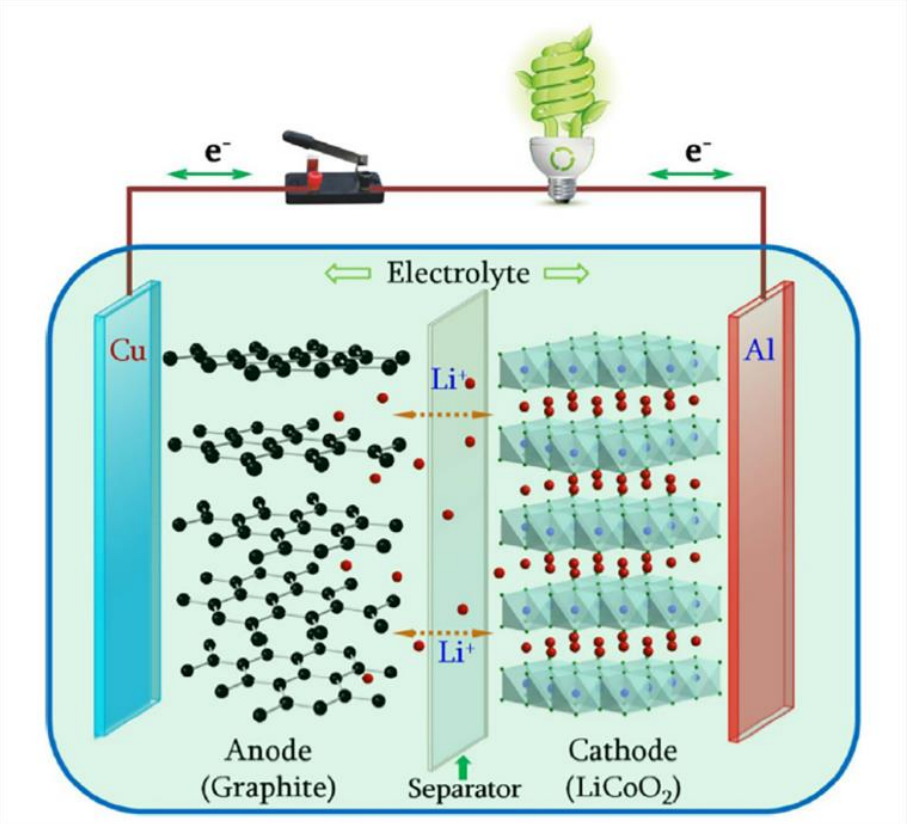

Figure 1.12 Schematic of rechargeable Li-ion batteries. For a Li-ion battery, the anode material is usually graphite, while the cathode material can be $LiCoO_2$, $LiFePO_4$, $LiMn_2O_4$, *etc*. This figure is adapted from Reference [132].

During the battery discharge process, the lithium ions move from the negative electrode (anode) to the positive electrode (cathode) through the electrolyte, and the electrons flow through the external circuit in the same direction (so the current is from positive to negative electrode, which is the reverse direction of electron flow). The half reactions on different electrodes are

$$\text{Cathode: } Li_{1-x}CoO_2 + xLi^+ + xe^- \rightarrow LiCoO_2 \qquad \text{Eq. 5}$$

$$\text{Anode: } xLiC_6 \rightarrow xC_6 + xLi^+ + xe^- \qquad \text{Eq. 6}$$

Thus, the full reaction in discharge process is

$$Li_{1-x}CoO_2 + xLiC_6 \rightarrow LiCoO_2 + xC_6 \qquad \text{Eq. 7}$$

When the cell is charging, the reverse process occurs with the lithium ions move back from cathode to anode. The half reactions on different electrodes are

$$\text{Cathode: } LiCoO_2 \rightarrow Li_{1-x}CoO_2 + xLi^+ + xe^- \qquad \text{Eq. 8}$$

$$\text{Anode: } xC_6 + xLi^+ + x\,e^- \rightarrow xLiC_6 \qquad \text{Eq. 9}$$

The full reaction charge process is

$$LiCoO_2 + xC_6 \rightarrow Li_{1-x}CoO_2 + xLiC_6 \quad \text{Eq. 10}$$

where x < 0.5 (x in mole unit), as overcharging would not be reversible for the layered structure of $LiCoO_2$. As the freshly assembled battery is at discharged state, charge and discharge for several cycles to form a dense solid electrolyte interphase (SEI) on the anode is critical before use (formation process), which plays important role in enhancing the cycling stability and shelf life of a lithium-ion battery. [141-143]

1.4.2 Electrochemistry Methods in Battery Research

Cyclic voltammetry (CV) is a powerful and popular electrochemical technique commonly employed to investigate the reduction and oxidation processes.[144] Before the cyclic voltammetry measurement, the terminal voltage (E_1 and E_2) and scan rate (v) should be determined according to the properties of active materials. Then a triangular voltage-time waveform is applied on the electrochemical system (from E_1 to E_2 then back to E_1). The trace in **Figure 1.13a** are typical cyclic voltammograms in battery experiment. The x-axis represents the applied potential (E) imposed on the system and the y-axis is the response of the resulting current (i) detected. From the corresponding CV curve, the peak voltage (E_p) and peak current (i_p) in both anodic and cathodic scan can be easily identified, and the difference of peak voltage could be used to judge/compare the electrochemical reversibility of reactions. **Figure 1.13b** depicts the galvanostatic charge-discharge curve of a typical battery electrode. Different from cyclic voltammetry process (chronoamperometry), galvanostatic charge-discharge is chronopotentiometry process. The charge/discharge plateaus correspond to the anodic/cathodic peak voltages (shown in **Figure 1.13a**, E_{pa} and E_{pc}). Columbic efficiency is defined as the quotient of charge/discharge capacity, from which the reversibility is indicated. For example, the capacity loss in the charge/discharge profiles can be attribute the loss of active materials, solid electrolyte interphase (SEI) formation process and/or other side reactions.

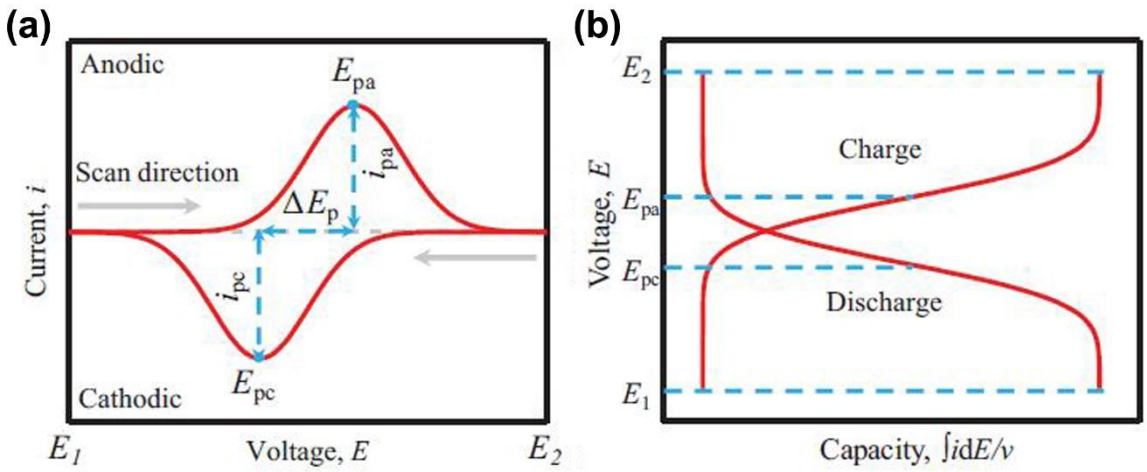

Figure 1.13 (a) Cyclic voltammetry curves and **(b)** galvanostatic charge-discharge curves in a typical battery test.

1.4.3 Structure of $LiMn_2O_4$

Electrochemical extraction of lithium from spinel lithium manganese oxide ($LiMn_2O_4$) was first reported in 1984. As a promising Li-ion battery cathode material in both aqueous and organic electrolytes, $LiMn_2O_4$ has attracted much attention in recent years due to its large theoretical capacity, high abundance and nontoxicity. $LiMn_2O_4$ is a cation ordered member of the spinel structural family (space group Fd3m), as shown in **Figure 1.14**.[145] In each cell unit, there are 56 atoms in total, including 8 lithium atoms, 16 manganese atoms (the amount of Mn^{3+} and Mn^{4+} atoms are equal) and 32 oxygen atoms. In addition to containing inexpensive materials, the three-dimensional structure of $LiMn_2O_4$ endows a high-rate capability (compared to layer-structured cathode materials, such as $LiCoO_2$) by providing a well-connected framework for the insertion and de-insertion of Li^+ ions during fast charge and discharge.

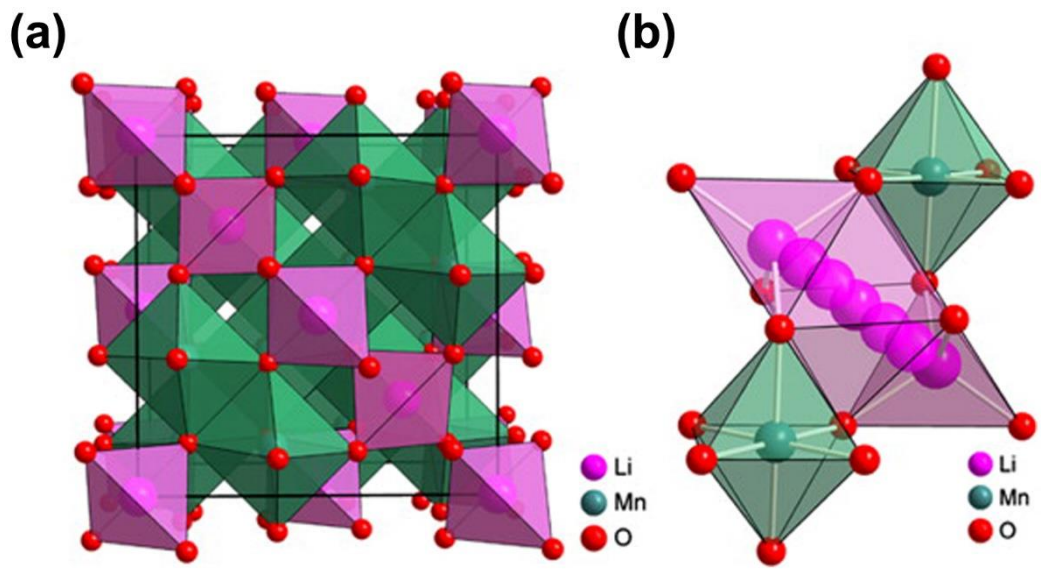

Figure 1.14 (a) Crystalline structure of spinel $LiMn_2O_4$ and **(b)** its corresponding lithium diffusion pathways. This figure was adapted from reference [145].

1.4.4 Research Development of Single Battery Particle

The conventional way to evaluate the battery active materials is to mix them with organic binder and conductive additive, then test the composite powder (porous electrode) under constant current charge-discharge, cyclic voltammetry, and/or alternate current impedance method.[146-147] Parameters such as diffusion coefficients or exchange current determined via this kind of electrode configuration need to be treated carefully in these bulk measurement, as the straightforward current/potential relationship is "diluted" by the binder and conductive additive. Thus, there is a great need for new techniques to study the intrinsic properties of active materials in complex composite electrodes in a systematic way, *e.g.*, by removing all of the auxiliary elements and only focusing on the electrochemistry of single $LiMn_2O_4$ particles or small ensembles of active particles.

Ultra-microelectrode techniques are very versatile in kinetics study because of their high diffusion flux rates and low capacitive background current. Thus, ultra-microelectrodes have been exploited as an effective method to investigate the electrochemical properties of single particle electrodes.[148-150] **Figure 1.15a** depicts the schematic of the first electrochemical setup to study a single battery particle.[148] Basically, the microelectrode was introduced to single particle by handling the positioner and an electric *X-Y-Z* stage, which were all placed in

a small dry box filled with Ar atmosphere. The target single particle was immersed in organic electrolyte (such as 1.0 M $LiClO_4$ in propylene carbonate) and the size of the single particle was determined with the help of optical microscope. Once the contact was made between Pt-Rh microelectrode and single particle (shown in **Figure 1.15 b**), electrochemical measurements were carried out, with Li foil serving as the counter/reference electrode. It should be noted that the single particle used herein can be primary particle or secondary particle, which possesses a wide diameter range from 10 to 200 micrometres.[151-153] Based on the microelectrode technique, Uchida *et al.* investigated the Li^+ insertion kinetics and Li^+ diffusivity in $LiCoO_2$.[152] The diffusion coefficient was measured to vary within 10^{-9} to 10^{-7} cm^2 s^{-1} (state of charge dependent),[54] being multiple orders of magnitude higher than the values determined using composite electrodes.[154-155] With the same method, the diffusion coefficient of $LiMn_2O_4$ measured via single particle measurement is 2-5 orders of magnitude higher compared to its counterpart measured via polycrystalline electrode (10^{-9} - 10^{-6} vs 10^{-11} cm^2 s^{-1}), indicating significant impact of grain boundary on Li^+ diffusivity.[153]

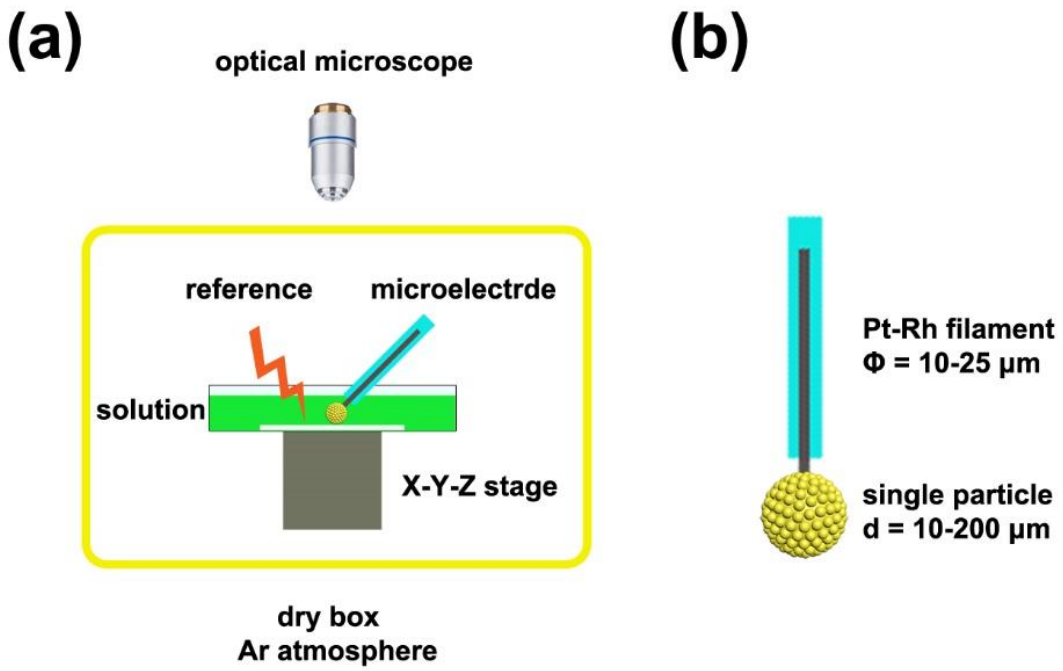

Figure 1.15 Schematic illustration of the measurement system **(a)** and illustration of a single particle electrode **(b)**.

As mentioned above, the configuration of battery electrode (*i.e.*, the way particles interact in an ensemble) may have substantial influence on Li^+ diffusion behaviour. Ultra-microelectrode techniques effectively strip away the matrix effect, circumventing the influence from the binders and conductive additives necessary for the fabrication of porous composite electrodes. The disadvantage of the ultra-microelectrode approach is the fast evaporation of the electrolyte inside the glove box and the range the particles (size and shape) to be investigated is limited.

As explored in **Chapters 5** and **6**, the fluidic micropipette/nanopipette probe of SECCM can be used to perform electrochemistry on isolated battery particles and ensembles. Compared to the particle-by-particle approach outlined above (microelectrode technique), in SECCM the electrochemistry of a series of individual particles/clusters is probed in a single high-throughput scanning experiment, which can be further correlated to co-located structural information (*e.g.*, revealed by correlating SEM) to assign single-particle structure−function relationship unambiguously. **Chapter 5** focuses on the variations of electrochemical properties in each individual particle via correlative electrochemistry-microscopy method. **Chapter 6** follows **Chapter 5,** investigating the rate controlling steps of Li^+ (de)intercalation on $LiMn_2O_4$ agglomerates level.

1.5 Aims of the Thesis

This thesis is concerned with the advancement of scanning electrochemical cell microscopy (SECCM), a scanning probe microscope (SPM) technique first introduced by Unwin *et al.* in 2010. While SECCM has typically been widely used for the fundamental study of carbon-based materials and polycrystalline metal electrodes, this thesis focuses on the extension of its capabilities as a powerful tool for the investigation of electrochemical phenomena related with energy conversion and storage process, especially for the hydrogen evolution reaction on two-dimensional (2D) materials and lithium-ion (de)intercalation at individual/agglomerates $LiMn_2O_4$ particles (battery cathode material).

In the work presented in **Chapters 3 and 4**, SECCM has been deployed to observe the HER on Cu/Au supported h-BN and pristine MoS_2/WS_2, respectively. In **Chapter 3,** the substrate effect on HER catalytic activity of h-BN was studed. The interaction with the

underlying metal support tunes the molecular processes (including electrode kinetics and mechanisms) during HER, through the perturbation of the electronic states of h-BN. Spatially-resolved voltammetry and Tafel analysis reveals that Au-supported h-BN exhibiting significantly enhanced HER charge-transfer kinetics compared to Cu-supported h-BN, owing to its strong bonding than the latter. **Chapter 4** provides an in-depth observation of HER on pristine transition metal chalcogenides. Stripping of the influence of matrix effect in macroscopic measurements allows previously unseen electrochemical phenomena at TMD electrodes, such as the influence of localized folding or variations in electronic structure on HER activity to be observed. The presence of surface defects, including crevices, holes, cracks, *etc.*, where the active edge plane is exposed show enhanced electrocatalytic activity compared to the defect-free basal plane. In addition, it also addresses the importance of aging effect (deactivation) on the HER activity, which is largely overlooked in bulk measurement. It also should be noted that in this work, few layers (≤ 2) of TMDs can be discerned from the activity map, demonstrating the high resolution of SECCM.

Chapter 5 and 6 introduce new applications of SECCM in battery electrode materials, using $LiMn_2O_4$ as an example. In **Chapter 5**, correlative electrochemistry-microscopy method was applied to scrutinize the Li-ion (de)intercalation at a series of individual $LiMn_2O_4$ particles in the absence of matrix effect (without the interference of binders and conducting agents). These nominally similar particles exhibit heterogeneous electrochemical responses from the cyclic voltammetric measurement, while galvanostatic charge-discharge later proves fast Li^+ and charge transfer capability inside of the $LiMn_2O_4$ particle, indicating the sluggish kinetics of the whole battery come from other components of the battery electrode. **Chapter 6** answers the origin of sluggish kinetics issue head on, by analyzing electrochemical behaviour evolution from individual $LiMn_2O_4$ particles to small clusters (*ca.* 5-10 particles) then to the ensemble level (*ca.* 100 particles) using a series of micropipette probes with graded diameters. Besides, with the precisely controlling the position of the micropipette in 3D space, the wetting properties of $LiMn_2O_4$ particles and supporting substrate can be modulated, allowing the particle ensemble effects and particle-support contact resistance to be studied separately. Experimental results prove that the charge-transfer kinetics in $LiMn_2O_4$ ensembles is largely dictated by interparticle interactions, and the nature of the particle-support contact (*i.e.*, *wet* vs *dry* contact) also plays an important role.

1.6 References

1. Binnig, G.; Rohrer, H., Scanning Tunneling Microscopy. *Surface Science* **1983**, *126*, 236-244.

2. Hansma, P. K.; Tersoff, J., Scanning Tunneling Microscopy. *Journal of Applied Physics* **1987**, *61*, R1-R24.

3. Binnig, G.; Quate, C. F.; Gerber, C., Atomic Force Microscope. *Physical Review Letters* **1986**, *56*, 930-933.

4. Rugar, D.; Hansma, P., Atomic Force Microscopy. *Physics Today* **1990**, *43*, 23-30.

5. Zhong, J.; Yan, J., Seeing Is Believing: Atomic Force Microscopy Imaging for Nanomaterial Research. *RSC Advances* **2016**, *6*, 1103-1121.

6. Xu, D.; Watt, G. D.; Harb, J. N.; Davis, R. C., Electrical Conductivity of Ferritin Proteins by Conductive Afm. *Nano Letters* **2005**, *5*, 571-577.

7. Nonnenmacher, M.; O'Boyle, M. P.; Wickramasinghe, H. K., Kelvin Probe Force Microscopy. *Applied Physics Letters* **1991**, *58*, 2921-2923.

8. Melitz, W.; Shen, J.; Kummel, A. C.; Lee, S., Kelvin Probe Force Microscopy and Its Application. *Surface Science Reports* **2011**, *66*, 1-27.

9. Morozovska, A. N.; Eliseev, E. A.; Balke, N.; Kalinin, S. V., Local Probing of Ionic Diffusion by Electrochemical Strain Microscopy: Spatial Resolution and Signal Formation Mechanisms. *Journal of Applied Physics* **2010**, *108*, 053712.

10. Luchkin, S. Y.; Romanyuk, K.; Ivanov, M.; Kholkin, A. L., Li Transport in Fresh and Aged $LiMn_2O_4$ Cathodes Via Electrochemical Strain Microscopy. *Journal of Applied Physics* **2015**, *118*, 072016.

11. Chen, C.C.; Zhou, Y.; Baker, L. A., Scanning Ion Conductance Microscopy. *Annual Review of Analytical Chemistry* **2012**, *5*, 207-228.

12. Hansma, P. K.; Drake, B.; Marti, O.; Gould, S. A.; Prater, C. B., The Scanning Ion-Conductance Microscope. *Science* **1989**, *243*, 641.

13. Kwak, J.; Bard, A. J., Scanning Electrochemical Microscopy. Apparatus and Two-Dimensional Scans of Conductive and Insulating Substrates. *Analytical Chemistry* **1989**, *61*, 1794-1799.

14. Bard, A. J.; Fan, F. R. F.; Kwak, J.; Lev, O., Scanning Electrochemical Microscopy. Introduction and Principles. *Analytical Chemistry* **1989**, *61*, 132-138.

15. Williams, C. G.; Edwards, M. A.; Colley, A. L.; Macpherson, J. V.; Unwin, P. R., Scanning Micropipet Contact Method for High-Resolution Imaging of Electrode Surface Redox Activity. *Analytical Chemistry* **2009**, *81*, 2486-2495.

16. Ebejer, N.; Schnippering, M.; Colburn, A. W.; Edwards, M. A.; Unwin, P. R., Localized High Resolution Electrochemistry and Multifunctional Imaging: Scanning Electrochemical Cell Microscopy. *Analytical Chemistry* **2010**, *82*, 9141-9145.

17. Takahashi, Y.; Shevchuk, A. I.; Novak, P.; Murakami, Y.; Shiku, H.; Korchev, Y. E.; Matsue, T., Simultaneous Noncontact Topography and Electrochemical Imaging by SECM/SICM Featuring Ion Current Feedback Regulation. *Journal of the American Chemical Society* **2010**, *132*, 10118-10126.

18. Morris, C. A.; Chen, C.C.; Baker, L. A., Transport of Redox Probes through Single Pores Measured by Scanning Electrochemical-Scanning Ion Conductance Microscopy (SECM-SICM). *Analyst* **2012**, *137*, 2933-2938.

19. Comstock, D. J.; Elam, J. W.; Pellin, M. J.; Hersam, M. C., Integrated Ultramicroelectrode-Nanopipet Probe for Concurrent Scanning Electrochemical Microscopy and Scanning Ion Conductance Microscopy. *Analytical Chemistry* **2010**, *82*, 1270-1276.

20. O'Connell, M. A.; Wain, A. J., Mapping Electroactivity at Individual Catalytic Nanostructures Using High-Resolution Scanning Electrochemical-Scanning Ion Conductance Microcopy. *Analytical Chemistry* **2014**, *86*, 12100-12107.

21. Kranz, C.; Friedbacher, G.; Mizaikoff, B.; Lugstein, A.; Smoliner, J.; Bertagnolli, E., Integrating an Ultramicroelectrode in an Afm Cantilever: Combined Technology for Enhanced Information. *Analytical Chemistry* **2001**, *73*, 2491-2500.

22. Macpherson, J. V.; Unwin, P. R., Combined Scanning Electrochemical−Atomic Force Microscopy. *Analytical Chemistry* **2000**, *72*, 276-285.

23. Tripathi, A. M.; Su, W. N.; Hwang, B. J., In Situ Analytical Techniques for Battery Interface Analysis. *Chemical Society Review* **2018**, *47*, 736-851.

24. Heben, M. J.; Dovek, M. M.; Lewis, N. S.; Penner, R. M.; Quate, C. F., Preparation of STM Tips for in-Situ Characterization of Electrode Surfaces. *Journal of Microscopy* **1988**, *152*, 651-661.

25. Li, J.; Wang, E., Scanning Tunneling Microscopy Characterization of Electrode Materials in Electrochemistry. *Electroanalysis* **1996**, *8*, 107-112.

26. Hansma, P. K.; Elings, V. B.; Marti, O.; Bracker, C. E., Scanning Tunneling Microscopy and Atomic Force Microscopy: Application to Biology and Technology. *Science* **1988**, *242*, 209.

27. Korchev, Y. E.; Bashford, C. L.; Milovanovic, M.; Vodyanoy, I.; Lab, M. J., Scanning Ion Conductance Microscopy of Living Cells. *Biophysical Journal* **1997**, *73*, 653-658.

28. Korchev, Y. E.; Gorelik, J.; Lab, M. J.; Sviderskaya, E. V.; Johnston, C. L.; Coombes, C. R.; Vodyanoy, I.; Edwards, C. R. W., Cell Volume Measurement Using Scanning Ion Conductance Microscopy. *Biophysical Journal* **2000**, *78*, 451-457.

29. Novak, P.; Li, C.; Shevchuk, A. I.; Stepanyan, R.; Caldwell, M.; Hughes, S.; Smart, T. G.; Gorelik, J.; Ostanin, V. P.; Lab, M. J.; Moss, G. W. J.; Frolenkov, G. I.; Korchev, Y. E. Nanoscale Live-Cell Imaging Using Hopping Probe Ion Conductance Microscopy. *Nature Methods* **2009**, *6*, 279-281.

30. Page, A.; Perry, D.; Unwin, P. R., Multifunctional Scanning Ion Conductance Microscopy. *Proceedings of the Royal Society A: Mathematical, Physical and Engineering Sciences* **2017**, *473*, 20160889.

31. Kang, M.; Momotenko, D.; Page, A.; Perry, D.; Unwin, P. R., Frontiers in Nanoscale Electrochemical Imaging: Faster, Multifunctional, and Ultrasensitive. *Langmuir* **2016**, *32*, 7993-8008.

32. Perry, D.; Al Botros, R.; Momotenko, D.; Kinnear, S. L.; Unwin, P. R., Simultaneous Nanoscale Surface Charge and Topographical Mapping. *ACS Nano* **2015**, *9*, 7266-7276.

33. Perry, D.; Paulose Nadappuram, B.; Momotenko, D.; Voyias, P. D.; Page, A.; Tripathi, G.; Frenguelli, B. G.; Unwin, P. R., Surface Charge Visualization at Viable Living Cells. *Journal of the American Chemical Society* **2016**, *138*, 3152-3160.

34. McKelvey, K.; Kinnear, S. L.; Perry, D.; Momotenko, D.; Unwin, P. R., Surface Charge Mapping with a Nanopipette. *Journal of the American Chemical Society* **2014**, *136*, 13735-13744.

35. Sa, N.; Lan, W.J.; Shi, W.; Baker, L. A., Rectification of Ion Current in Nanopipettes by External Substrates. *ACS Nano* **2013**, *7*, 11272-11282.

36. Kang, M.; Perry, D.; Bentley, C. L.; West, G.; Page, A.; Unwin, P. R., Simultaneous Topography and Reaction Flux Mapping at and around Electrocatalytic Nanoparticles. *ACS Nano* **2017**, *11*, 9525-9535.

37. Bard, A. J.; Fan, F.R. F.; Pierce, D. T.; Unwin, P. R.; Wipf, D. O.; Zhou, F., Chemical Imaging of Surfaces with the Scanning Electrochemical Microscope. *Science* **1991**, *254*, 68.

38. Amemiya, S.; Bard, A. J.; Fan, F.-R. F.; Mirkin, M. V.; Unwin, P. R., Scanning Electrochemical Microscopy. *Annual Review of Analytical Chemistry* **2008**, *1*, 95-131.

39. Bülter, H.; Peters, F.; Schwenzel, J.; Wittstock, G., Spatiotemporal Changes of the Solid Electrolyte Interphase in Lithium-Ion Batteries Detected by Scanning Electrochemical Microscopy. *Angewandte Chemie International Edition* **2014**, *53*, 10531-10535.

40. Barker, A. L.; Gonsalves, M.; Macpherson, J. V.; Slevin, C. J.; Unwin, P. R., Scanning Electrochemical Microscopy: Beyond the Solid/Liquid Interface. *Analytica Chimica Acta* **1999**, *385*, 223-240.

41. Zampardi, G.; Ventosa, E.; La Mantia, F.; Schuhmann, W., In Situ Visualization of Li-Ion Intercalation and Formation of the Solid Electrolyte Interphase on TiO_2 Based Paste Electrodes Using Scanning Electrochemical Microscopy. *Chemical Communications* **2013**, *49*, 9347-9349.

42. Polcari, D.; Dauphin-Ducharme, P.; Mauzeroll, J., Scanning Electrochemical Microscopy: A Comprehensive Review of Experimental Parameters from 1989 to 2015. *Chemical Reviews* **2016**, *116*, 13234-13278.

43. Ebejer, N.; Güell, A. G.; Lai, S. C. S.; McKelvey, K.; Snowden, M. E.; Unwin, P. R., Scanning Electrochemical Cell Microscopy: A Versatile Technique for Nanoscale Electrochemistry and Functional Imaging. *Annual Review of Analytical Chemistry* **2013**, *6*, 329-351.

44. Byers, J. C.; Güell, A. G.; Unwin, P. R., Nanoscale Electrocatalysis: Visualizing Oxygen Reduction at Pristine, Kinked, and Oxidized Sites on Individual Carbon Nanotubes. *Journal of the American Chemical Society* **2014**, *136*, 11252-11255.

45. Zhang, G.; Kirkman, P. M.; Patel, A. N.; Cuharuc, A. S.; McKelvey, K.; Unwin, P. R., Molecular Functionalization of Graphite Surfaces: Basal Plane Versus Step Edge Electrochemical Activity. *Journal of the American Chemical Society* **2014**, *136*, 11444-11451.

46. Patel, A. N.; McKelvey, K.; Unwin, P. R., Nanoscale Electrochemical Patterning Reveals the Active Sites for Catechol Oxidation at Graphite Surfaces. *Journal of the American Chemical Society* **2012**, *134*, 20246-20249.

47. E, S. P.; Kang, M.; Wilson, P.; Meng, L.; Perry, D.; Basile, A.; Unwin, P. R., High Resolution Visualization of the Redox Activity of Li_2O_2 in Non-Aqueous Media: Conformal Layer vs. Toroid Structure. *Chemical Communications* **2018**, *54*, 3053-3056.

48. Aaronson, B. D. B.; Byers, J. C.; Colburn, A. W.; McKelvey, K.; Unwin, P. R., Scanning Electrochemical Cell Microscopy Platform for Ultrasensitive Photoelectrochemical Imaging. *Analytical Chemistry* **2015**, *87*, 4129-4133.

49. Aaronson, B. D. B.; Lai, S. C. S.; Unwin, P. R., Spatially Resolved Electrochemistry in Ionic Liquids: Surface Structure Effects on Triiodide Reduction at Platinum Electrodes. *Langmuir* **2014**, *30*, 1915-1919.

50. Bentley, C. L.; Kang, M.; Maddar, F. M.; Li, F.; Walker, M.; Zhang, J.; Unwin, P. R., Electrochemical Maps and Movies of the Hydrogen Evolution Reaction on Natural Crystals of Molybdenite (MoS_2): Basal Vs. Edge Plane Activity. *Chemical Science* **2017**, *8*, 6583-6593.

51. Bentley, C. L.; Andronescu, C.; Smialkowski, M.; Kang, M.; Tarnev, T.; Marler, B.; Unwin, P. R.; Apfel, U.P.; Schuhmann, W., Local Surface Structure and Composition Control the Hydrogen Evolution Reaction on Iron Nickel Sulfides. *Angewandte Chemie International Edition* **2018**, *57*, 4093-4097.

52. Bentley, C. L.; Kang, M.; Unwin, P. R., Nanoscale Surface Structure-Activity in Electrochemistry and Electrocatalysis. *Journal of the American Chemical Society* **2019**, *141*, 2179-2193.

53. Suter, T.; Böhni, H., A New Microelectrochemical Method to Study Pit Initiation on Stainless Steels. *Electrochimica Acta* **1997**, *42*, 3275-3280.

54. Andreatta, F.; Fedrizzi, L., The Use of the Electrochemical Micro-Cell for the Investigation of Corrosion Phenomena. *Electrochimica Acta* **2016**, *203*, 337-349.

55. Momotenko, D.; Byers, J. C.; McKelvey, K.; Kang, M.; Unwin, P. R., High-Speed Electrochemical Imaging. *ACS Nano* **2015**, *9*, 8942-8952.

56. Yule, L. C.; Shkirskiy, V.; Aarons, J.; West, G.; Bentley, C. L.; Shollock, B. A.; Unwin, P. R., Nanoscale Active Sites for the Hydrogen Evolution Reaction on Low Carbon Steel. *The Journal of Physical Chemistry C* **2019**, *123*, 24146-24155.

57. Kleijn, S. E. F.; Lai, S. C. S.; Miller, T. S.; Yanson, A. I.; Koper, M. T. M.; Unwin, P. R., Landing and Catalytic Characterization of Individual Nanoparticles on Electrode Surfaces. *Journal of the American Chemical Society* **2012**, *134*, 18558-18561.

58. Güell, A. G.; Meadows, K. E.; Dudin, P. V.; Ebejer, N.; Macpherson, J. V.; Unwin, P. R., Mapping Nanoscale Electrochemistry of Individual Single-Walled Carbon Nanotubes. *Nano Letters* **2014**, *14*, 220-224.

59. Güell, A. G.; Cuharuc, A. S.; Kim, Y.-R.; Zhang, G.; Tan, S.y.; Ebejer, N.; Unwin, P. R., Redox-Dependent Spatially Resolved Electrochemistry at Graphene and Graphite Step Edges. *ACS Nano* **2015**, *9*, 3558-3571.

60. Kinnear, S. L.; McKelvey, K.; Snowden, M. E.; Peruffo, M.; Colburn, A. W.; Unwin, P. R., Dual-Barrel Conductance Micropipet as a New Approach to the Study of Ionic Crystal Dissolution Kinetics. *Langmuir* **2013**, *29*, 15565-15572.

61. Parker, A. S., et al., Combinatorial Localized Dissolution Analysis: Application to Acid-Induced Dissolution of Dental Enamel and the Effect of Surface Treatments. *Journal of Colloid and Interface Science* **2016**, *476*, 94-102.

62. Takahashi, Y., et al., Nanoscale Visualization of Redox Activity at Lithium-Ion Battery Cathodes. *Nature Communications* **2014**, *5*, 5450.

63. Bentley, C. L.; Kang, M.; Unwin, P. R., Nanoscale Structure Dynamics within Electrocatalytic Materials. *Journal of the American Chemical Society* **2017**, *139*, 16813-16821.

64. Liu, D. Q.; Tao, B.; Ruan, H.C.; Bentley, C. L.; Unwin, P. R., Metal Support Effects in Electrocatalysis at Hexagonal Boron Nitride. *Chemical Communications* **2019**, *55*, 628-631.

65. Yule, L. C.; Bentley, C. L.; West, G.; Shollock, B. A.; Unwin, P. R., Scanning Electrochemical Cell Microscopy: A Versatile Method for Highly Localised Corrosion Related Measurements on Metal Surfaces. *Electrochimica Acta* **2019**, *298*, 80-88.

66. Shkirskiy, V.; Yule, L. C.; Daviddi, E.; Bentley, C. L.; Aarons, J.; West, G.; Unwin, P. R., Nanoscale Scanning Electrochemical Cell Microscopy and Correlative Surface Structural Analysis to Map Anodic and Cathodic Reactions on Polycrystalline Zn in Acid Media. *Journal of The Electrochemical Society* **2020**, *167*, 041507.

67. Yule, L. C.; Daviddi, E.; West, G.; Bentley, C. L.; Unwin, P. R., Surface Microstructural Controls on Electrochemical Hydrogen Absorption at Polycrystalline Palladium. *Journal of Electroanalytical Chemistry* **2020**, 114047.

68. Daviddi, E.; Gonos, K. L.; Colburn, A. W.; Bentley, C. L.; Unwin, P. R., Scanning Electrochemical Cell Microscopy (SECCM) Chronopotentiometry: Development and Applications in Electroanalysis and Electrocatalysis. *Analytical Chemistry* **2019**, *91*, 9229-9237.

69. Daviddi, E.; Chen, Z.; Beam Massani, B.; Lee, J.; Bentley, C. L.; Unwin, P. R.; Ratcliff, E. L., Nanoscale Visualization and Multiscale Electrochemical Analysis of Conductive Polymer Electrodes. *ACS Nano* **2019**, *13*, 13271-13284.

70. Wang, Y.; Gordon, E.; Ren, H., Mapping the Potential of Zero Charge and Electrocatalytic Activity of Metal–Electrolyte Interface Via a Grain-by-Grain Approach. *Analytical Chemistry* **2020**, *92*, 2859-2865.

71. Lai, S. C. S.; Patel, A. N.; McKelvey, K.; Unwin, P. R., Definitive Evidence for Fast Electron Transfer at Pristine Basal Plane Graphite from High-Resolution Electrochemical Imaging. *Angewandte Chemie International Edition* **2012**, *51*, 5405-5408.

72. Miller, T. S.; Ebejer, N.; Güell, A. G.; Macpherson, J. V.; Unwin, P. R., Electrochemistry at Carbon Nanotube Forests: Sidewalls and Closed Ends Allow Fast Electron Transfer. *Chemical Communications* **2012**, *48*, 7435-7437.

73. Patel, A. N.; Collignon, M. G.; O'Connell, M. A.; Hung, W. O. Y.; McKelvey, K.; Macpherson, J. V.; Unwin, P. R., A New View of Electrochemistry at Highly Oriented Pyrolytic Graphite. *Journal of the American Chemical Society* **2012**, *134*, 20117-20130.

74. Lai, S. C. S.; Dudin, P. V.; Macpherson, J. V.; Unwin, P. R., Visualizing Zeptomole (Electro)Catalysis at Single Nanoparticles within an Ensemble. *Journal of the American Chemical Society* **2011**, *133*, 10744-10747.

75. Choi, M.; Siepser, N. P.; Jeong, S.; Wang, Y.; Jagdale, G.; Ye, X.; Baker, L. A., Probing Single-Particle Electrocatalytic Activity at Facet-Controlled Gold Nanocrystals. *Nano Letters* **2020**, *20*, 1233-1239.

76. Tarnev, T.; Aiyappa, H. B.; Botz, A.; Erichsen, T.; Ernst, A.; Andronescu, C.; Schuhmann, W., Scanning Electrochemical Cell Microscopy Investigation of Single ZIF-Derived Nanocomposite Particles as Electrocatalysts for Oxygen Evolution in Alkaline Media. *Angewandte Chemie International Edition* **2019**, *58*, 14265-14269.

77. McKelvey, K.; O'Connell, M. A.; Unwin, P. R., Meniscus Confined Fabrication of Multidimensional Conducting Polymer Nanostructures with Scanning Electrochemical Cell Microscopy (SECCM). *Chemical Communications* **2013**, *49*, 2986-2988.

78. Aaronson, B. D. B.; Garoz-Ruiz, J.; Byers, J. C.; Colina, A.; Unwin, P. R., Electrodeposition and Screening of Photoelectrochemical Activity in Conjugated Polymers Using Scanning Electrochemical Cell Microscopy. *Langmuir* **2015**, *31*, 12814-12822.

79. Aaronson, B. D. B.; Chen, C.H.; Li, H.; Koper, M. T. M.; Lai, S. C. S.; Unwin, P. R., Pseudo-Single-Crystal Electrochemistry on Polycrystalline Electrodes: Visualizing Activity at Grains and Grain Boundaries on Platinum for the Fe^{2+}/Fe^{3+} Redox Reaction. *Journal of the American Chemical Society* **2013**, *135*, 3873-3880.

80. Tao, B.; Unwin, P. R.; Bentley, C. L., Nanoscale Variations in the Electrocatalytic Activity of Layered Transition-Metal Dichalcogenides. *The Journal of Physical Chemistry C* **2020**, *124*, 789-798.

81. Takahashi, Y., et al., High-Resolution Electrochemical Mapping of the Hydrogen Evolution Reaction on Transition-Metal Dichalcogenide Nanosheets. *Angewandte Chemie International Edition* **2020**, *59*, 3601-3608.

82. Tao, B.; Yule, L. C.; Daviddi, E.; Bentley, C. L.; Unwin, P. R., Correlative Electrochemical Microscopy of Li-Ion (De)Intercalation at a Series of Individual $LiMn_2O_4$ Particles. *Angewandte Chemie International Edition* **2019**, *58*, 4606-4611.

83. Ustarroz, J.; Ornelas, I. M.; Zhang, G.; Perry, D.; Kang, M.; Bentley, C. L.; Walker, M.; Unwin, P. R., Mobility and Poisoning of Mass-Selected Platinum Nanoclusters During the Oxygen Reduction Reaction. *ACS Catalysis* **2018**, *8*, 6775-6790.

84. Mariano, R. G.; McKelvey, K.; White, H. S.; Kanan, M. W., Selective Increase in CO_2 Electroreduction Activity at Grain-Boundary Surface Terminations. *Science* **2017**, *358*, 1187.

85. Yule, L. C.; Shkirskiy, V.; Aarons, J.; West, G.; Shollock, B. A.; Bentley, C. L.; Unwin, P. R., Nanoscale Electrochemical Visualization of Grain-Dependent Anodic Iron Dissolution from Low Carbon Steel. *Electrochimica Acta* **2020**, *332*, 135267.

86. Unwin, P. R.; Güell, A. G.; Zhang, G., Nanoscale Electrochemistry of sp^2 Carbon Materials: From Graphite and Graphene to Carbon Nanotubes. *Accounts of Chemical Research* **2016**, *49*, 2041-2048.

87. Maddar, F. M.; Lazenby, R. A.; Patel, A. N.; Unwin, P. R., Electrochemical Oxidation of Dihydronicotinamide Adenine Dinucleotide (NADH): Comparison of Highly Oriented Pyrolytic Graphite (HOPG) and Polycrystalline Boron-Doped Diamond (PBDD) Electrodes. *Physical Chemistry Chemical Physics* **2016**, *18*, 26404-26411.

88. Patten, H. V.; Lai, S. C. S.; Macpherson, J. V.; Unwin, P. R., Active Sites for Outer-Sphere, Inner-Sphere, and Complex Multistage Electrochemical Reactions at Polycrystalline Boron-Doped Diamond Electrodes (PBDD) Revealed with Scanning Electrochemical Cell Microscopy (SECCM). *Analytical Chemistry* **2012**, *84*, 5427-5432.

89. Kumatani, A., et al., Chemical Dopants on Edge of Holey Graphene Accelerate Electrochemical Hydrogen Evolution Reaction. *Advanced Science* **2019**, *6*, 1900119.

90. Zhang, G.; Tan, S. Y.; Patel, A. N.; Unwin, P. R., Electrochemistry of $Fe^{3+}/^{2+}$ at Highly Oriented Pyrolytic Graphite (HOPG) Electrodes: Kinetics, Identification of Major Electroactive Sites and Time Effects on the Response. *Physical Chemistry Chemical Physics* **2016**, *18*, 32387-32395.

91. Güell, A. G.; Ebejer, N.; Snowden, M. E.; McKelvey, K.; Macpherson, J. V.; Unwin, P. R., Quantitative Nanoscale Visualization of Heterogeneous Electron Transfer Rates in 2d Carbon Nanotube Networks. *Proceedings of the National Academy of Sciences* **2012**, *109*, 11487.

92. Snowden, M. E.; Dayeh, M.; Payne, N. A.; Gervais, S.; Mauzeroll, J.; Schougaard, S. B., Measurement on Isolated Lithium Iron Phosphate Particles Reveals Heterogeneity in Material Properties Distribution. *Journal of Power Sources* **2016**, *325*, 682-689.

93. Dayeh, M.; Ghavidel, M. R. Z.; Mauzeroll, J.; Schougaard, S. B., Micropipette Contact Method to Investigate High-Energy Cathode Materials by Using an Ionic Liquid. *ChemElectroChem* **2019**, *6*, 195-201.

94. Takahashi, Y.; Yamashita, T.; Takamatsu, D.; Kumatani, A.; Fukuma, T., Nanoscale Kinetic Imaging of Lithium Ion Secondary Battery Materials Using Scanning Electrochemical Cell Microscopy. *Chemical Communications* **2020**.

95. Lai, S. C. S.; Lazenby, R. A.; Kirkman, P. M.; Unwin, P. R., Nucleation, Aggregative Growth and Detachment of Metal Nanoparticles During Electrodeposition at Electrode Surfaces. *Chemical Science* **2015**, *6*, 1126-1138.

96. Inomata, H.; Takahashi, Y.; Takamatsu, D.; Kumatani, A.; Ida, H.; Shiku, H.; Matsue, T., Visualization of Inhomogeneous Current Distribution on ZrO_2-Coated $LiCoO_2$ Thin-Film Electrodes Using Scanning Electrochemical Cell Microscopy. *Chemical Communications* **2019**, *55*, 545-548.

97. Danis, L.; Gateman, S. M.; Kuss, C.; Schougaard, S. B.; Mauzeroll, J., Nanoscale Measurements of Lithium-Ion-Battery Materials Using Scanning Probe Techniques. *ChemElectroChem* **2017**, *4*, 6-19.

98. Chen, M., et al., 3D Nanoprinting of Perovskites. *Advanced Materials* **2019**, *31*, 1904073.

99. Kibler, L. A., Hydrogen Electrocatalysis. *ChemPhysChem* **2006**, *7*, 985-991.

100. Jiao, Y.; Zheng, Y.; Jaroniec, M.; Qiao, S. Z., Design of Electrocatalysts for Oxygen-and Hydrogen-Involving Energy Conversion Reactions. *Chemical Society Reviews* **2015**, *44*, 2060-2086.

101. Li, Y.; Wang, H.; Xie, L.; Liang, Y.; Hong, G.; Dai, H., MoS_2 Nanoparticles Grown on Graphene: An Advanced Catalyst for the Hydrogen Evolution Reaction. *Journal of the American Chemical Society* **2011**, *133*, 7296-7299.

102. Conway, B. E.; Tilak, B. V., Interfacial Processes Involving Electrocatalytic Evolution and Oxidation of H_2, and the Role of Chemisorbed H. *Electrochimica Acta* **2002**, *47*, 3571-3594.

103. Wang, J.; Xu, F.; Jin, H.; Chen, Y.; Wang, Y., Non-Noble Metal-Based Carbon Composites in Hydrogen Evolution Reaction: Fundamentals to Applications. *Advanced Materials* **2017**, *29*, 1605838.

104. Zhou, W.; Jia, J.; Lu, J.; Yang, L.; Hou, D.; Li, G.; Chen, S., Recent Developments of Carbon-Based Electrocatalysts for Hydrogen Evolution Reaction. *Nano Energy* **2016**, *28*, 29-43.

105. Kong, D.; Wang, H.; Lu, Z.; Cui, Y., $CoSe_2$ Nanoparticles Grown on Carbon Fiber Paper: An Efficient and Stable Electrocatalyst for Hydrogen Evolution Reaction. *Journal of the American Chemical Society* **2014**, *136*, 4897-4900.

106. Deng, J.; Ren, P.; Deng, D.; Yu, L.; Yang, F.; Bao, X., Highly Active and Durable Non-Precious-Metal Catalysts Encapsulated in Carbon Nanotubes for Hydrogen Evolution Reaction. *Energy & Environmental Science* **2014**, *7*, 1919-1923.

107. Wang, D.Y., et al., Highly Active and Stable Hybrid Catalyst of Cobalt-Doped FeS_2 Nanosheets-Carbon Nanotubes for Hydrogen Evolution Reaction. *Journal of the American Chemical Society* **2015**, *137*, 1587-1592.

108. Wang, X.; Maeda, K.; Chen, X.; Takanabe, K.; Domen, K.; Hou, Y.; Fu, X.; Antonietti, M., Polymer Semiconductors for Artificial Photosynthesis: Hydrogen Evolution by Mesoporous Graphitic Carbon Nitride with Visible Light. *Journal of the American Chemical Society* **2009**, *131*, 1680-1681.

109. Liao, G.; Gong, Y.; Zhang, L.; Gao, H.; Yang, G.J.; Fang, B., Semiconductor Polymeric Graphitic Carbon Nitride Photocatalysts: The "Holy Grail" for the Photocatalytic Hydrogen Evolution Reaction under Visible Light. *Energy & Environmental Science* **2019**, *12*, 2080-2147.

110. Cheng, L.; Huang, W.; Gong, Q.; Liu, C.; Liu, Z.; Li, Y.; Dai, H., Ultrathin WS_2 Nanoflakes as a High-Performance Electrocatalyst for the Hydrogen Evolution Reaction. *Angewandte Chemie International Edition* **2014**, *53*, 7860-7863.

111. Lukowski, M. A.; Daniel, A. S.; Meng, F.; Forticaux, A.; Li, L.; Jin, S., Enhanced Hydrogen Evolution Catalysis from Chemically Exfoliated Metallic MoS_2 Nanosheets. *Journal of the American Chemical Society* **2013**, *135*, 10274-10277.

112. Zeng, H.; Zhi, C.; Zhang, Z.; Wei, X.; Wang, X.; Guo, W.; Bando, Y.; Golberg, D., "White Graphenes": Boron Nitride Nanoribbons Via Boron Nitride Nanotube Unwrapping. *Nano Letters* **2010**, *10*, 5049-5055.

113. Zhi, C.; Bando, Y.; Tang, C.; Kuwahara, H.; Golberg, D., Large-Scale Fabrication of Boron Nitride Nanosheets and Their Utilization in Polymeric Composites with Improved Thermal and Mechanical Properties. *Advanced Materials* **2009**, *21*, 2889-2893.

114. Wang, J.; Ma, F.; Sun, M., Graphene, Hexagonal Boron Nitride, and Their Heterostructures: Properties and Applications. *RSC Advances* **2017**, *7*, 16801-16822.

115. Watanabe, K.; Taniguchi, T.; Kanda, H., Direct-Bandgap Properties and Evidence for Ultraviolet Lasing of Hexagonal Boron Nitride Single Crystal. *Nature Materials* **2004**, *3*, 404-409.

116. Blase, X.; Rubio, A.; Louie, S. G.; Cohen, M. L., Stability and Band Gap Constancy of Boron Nitride Nanotubes. *Europhysics Letters (EPL)* **1994**, *28*, 335-340.

117. Lyalin, A.; Nakayama, A.; Uosaki, K.; Taketsugu, T., Functionalization of Monolayer h-BN by a Metal Support for the Oxygen Reduction Reaction. *The Journal of Physical Chemistry C* **2013**, *117*, 21359-21370.

118. Koitz, R.; Nørskov, J. K.; Studt, F., A Systematic Study of Metal-Supported Boron Nitride Materials for the Oxygen Reduction Reaction. *Physical Chemistry Chemical Physics* **2015**, *17*, 12722-12727.

119. Uosaki, K.; Elumalai, G.; Noguchi, H.; Masuda, T.; Lyalin, A.; Nakayama, A.; Taketsugu, T., Boron Nitride Nanosheet on Gold as an Electrocatalyst for Oxygen Reduction Reaction: Theoretical Suggestion and Experimental Proof. *Journal of the American Chemical Society* **2014**, *136*, 6542-6545.

120. Elumalai, G.; Noguchi, H.; Uosaki, K., Electrocatalytic Activity of Various Types of h-BN for the Oxygen Reduction Reaction. *Physical Chemistry Chemical Physics* **2014**, *16*, 13755-13761.

121. Uosaki, K.; Elumalai, G.; Dinh, H. C.; Lyalin, A.; Taketsugu, T.; Noguchi, H., Highly Efficient Electrochemical Hydrogen Evolution Reaction at Insulating Boron Nitride Nanosheet on Inert Gold Substrate. *Scientific Reports* **2016**, *6*, 32217.

122. Guha, A.; Veettil Vineesh, T.; Sekar, A.; Narayanaru, S.; Sahoo, M.; Nayak, S.; Chakraborty, S.; Narayanan, T. N., Mechanistic Insight into Enhanced Hydrogen Evolution Reaction Activity of Ultrathin Hexagonal Boron Nitride-Modified Pt Electrodes. *ACS Catalysis* **2018**, *8*, 6636-6644.

123. Manzeli, S.; Ovchinnikov, D.; Pasquier, D.; Yazyev, O. V.; Kis, A., 2D Transition Metal Dichalcogenides. *Nature Reviews Materials* **2017**, *2*, 17033.

124. Choi, W.; Choudhary, N.; Han, G. H.; Park, J.; Akinwande, D.; Lee, Y. H., Recent Development of Two-Dimensional Transition Metal Dichalcogenides and Their Applications. *Materials Today* **2017**, *20*, 116-130.

125. Miller, J. T.; Reagan, W. J.; Kaduk, J. A.; Marshall, C. L.; Kropf, A. J., Selective Hydrodesulfurization of Fcc Naphtha with Supported MoS_2 Catalysts: The Role of Cobalt. *Journal of Catalysis* **2000**, *193*, 123-131.

126. Lauritsen, J. V.; Nyberg, M.; Nørskov, J. K.; Clausen, B. S.; Topsøe, H.; Lægsgaard, E.; Besenbacher, F., Hydrodesulfurization Reaction Pathways on MoS_2 Nanoclusters Revealed by Scanning Tunneling Microscopy. *Journal of Catalysis* **2004**, *224*, 94-106.

127. Yu, Y.; Huang, S.Y.; Li, Y.; Steinmann, S. N.; Yang, W.; Cao, L., Layer-Dependent Electrocatalysis of MoS_2 for Hydrogen Evolution. *Nano Letters* **2014**, *14*, 553-558.

128. Wu, Z.; Fang, B.; Wang, Z.; Wang, C.; Liu, Z.; Liu, F.; Wang, W.; Alfantazi, A.; Wang, D.; Wilkinson, D. P., MoS_2 Nanosheets: A Designed Structure with High Active Site Density for the Hydrogen Evolution Reaction. *ACS Catalysis* **2013**, *3*, 2101-2107.

129. Jaramillo, T. F.; Jørgensen, K. P.; Bonde, J.; Nielsen, J. H.; Horch, S.; Chorkendorff, I., Identification of Active Edge Sites for Electrochemical H_2 Evolution from MoS_2 Nanocatalysts. *Science* **2007**, *317*, 100.

130. Bonde, J.; Moses, P. G.; Jaramillo, T. F.; Nørskov, J. K.; Chorkendorff, I., Hydrogen Evolution on Nano-Particulate Transition Metal Sulfides. *Faraday Discussions* **2009**, *140*, 219-231.

131. Xu, K., A Long Journey of Lithium: From the Big Bang to Our Smartphones. *Energy & Environmental Materials* **2019**, *2*, 229-233.

132. Liu, C.; Neale, Z. G.; Cao, G., Understanding Electrochemical Potentials of Cathode Materials in Rechargeable Batteries. *Materials Today* **2016**, *19*, 109-123.

133. Harper, G., et al., Recycling Lithium-Ion Batteries from Electric Vehicles. *Nature* **2019**, *575*, 75-86.

134. Li, H., Practical Evaluation of Li-Ion Batteries. *Joule* **2019**, *3*, 911-914.

135. Chen, S., et al., Critical Parameters for Evaluating Coin Cells and Pouch Cells of Rechargeable Li-Metal Batteries. *Joule* **2019**, *3*, 1094-1105.

136. Li, M.; Lu, J.; Chen, Z.; Amine, K., 30 Years of Lithium-Ion Batteries. *Advanced Materials* **2018**, *30*, 1800561.

137. Park, M.; Zhang, X.; Chung, M.; Less, G. B.; Sastry, A. M., A Review of Conduction Phenomena in Li-Ion Batteries. *Journal of Power Sources* **2010**, *195*, 7904-7929.

138. Sloop, S. E.; Kerr, J. B.; Kinoshita, K., The Role of Li-Ion Battery Electrolyte Reactivity in Performance Decline and Self-Discharge. *Journal of Power Sources* **2003**, *119-121*, 330-337.

139. Jie, Y.; Ren, X.; Cao, R.; Cai, W.; Jiao, S., Advanced Liquid Electrolytes for Rechargeable Li Metal Batteries. *Advanced Functional Materials* **2020**, *30*, 1910777.

140. Huang, X.; Hitt, J., Lithium Ion Battery Separators: Development and Performance Characterization of a Composite Membrane. *Journal of Membrane Science* **2013**, *425-426*, 163-168.

141. Heiskanen, S. K.; Kim, J.; Lucht, B. L., Generation and Evolution of the Solid Electrolyte Interphase of Lithium-Ion Batteries. *Joule* **2019**, *3*, 2322-2333.

142. Peled, E., Advanced Model for Solid Electrolyte Interphase Electrodes in Liquid and Polymer Electrolytes. *Journal of The Electrochemical Society* **1997**, *144*, L208.

143. Aurbach, D.; Moshkovich, M.; Cohen, Y.; Schechter, A., The Study of Surface Film Formation on Noble-Metal Electrodes in Alkyl Carbonates/Li Salt Solutions, Using Simultaneous in Situ AFM, EQCM, FTIR, and EIS. *Langmuir* **1999**, *15*, 2947-2960.

144. Elgrishi, N.; Rountree, K. J.; McCarthy, B. D.; Rountree, E. S.; Eisenhart, T. T.; Dempsey, J. L., A Practical Beginner's Guide to Cyclic Voltammetry. *Journal of Chemical Education* **2018**, *95*, 197-206.

145. Zhang, T.; Li, D.; Tao, Z.; Chen, J., Understanding Electrode Materials of Rechargeable Lithium Batteries Via Dft Calculations. *Progress in Natural Science: Materials International* **2013**, *23*, 256-272.

146. Chan, C. K.; Peng, H.; Liu, G.; McIlwrath, K.; Zhang, X. F.; Huggins, R. A.; Cui, Y., High-Performance Lithium Battery Anodes Using Silicon Nanowires. *Nature Nanotechnology* **2008**, *3*, 31-35.

147. Liu, N.; Lu, Z.; Zhao, J.; McDowell, M. T.; Lee, H.W.; Zhao, W.; Cui, Y., A Pomegranate-Inspired Nanoscale Design for Large-Volume-Change Lithium Battery Anodes. *Nature Nanotechnology* **2014**, *9*, 187-192.

148. Uchida, I.; Fujiyoshi, H.; Waki, S., Microvoltammetric Studies on Single Particles of Battery Active Materials. *Journal of Power Sources* **1997**, *68*, 139-144.

149. Heubner, C.; Langklotz, U.; Lämmel, C.; Schneider, M.; Michaelis, A., Electrochemical Single-Particle Measurements of Electrode Materials for Li-Ion Batteries: Possibilities, Insights and Implications for Future Development. *Electrochimica Acta* **2020**, *330*, 135160.

150. Dokko, K.; Nakata, N.; Kanamura, K., High Rate Discharge Capability of Single Particle Electrode of $LiCoO_2$. *Journal of Power Sources* **2009**, *189*, 783-785.

151. Uchida, I.; Mohamedi, M.; Dokko, K.; Nishizawa, M.; Itoh, T.; Umeda, M., Recent Investigations on Thin Films and Single Particles of Transition Metal Oxides for Lithium Batteries. *Journal of Power Sources* **2001**, *97-98*, 518-524.

152. Dokko, K.; Mohamedi, M.; Fujita, Y.; Itoh, T.; Nishizawa, M.; Umeda, M.; Uchida, I., Kinetic Characterization of Single Particles of $LiCoO_2$ by AC Impedance and Potential Step Methods. *Journal of The Electrochemical Society* **2001**, *148*, A422.

153. Dokko, K.; Mohamedi, M.; Umeda, M.; Uchida, I., Kinetic Study of Li-Ion Extraction and Insertion at $LiMn_2O_4$ Single Particle Electrodes Using Potential Step and Impedance Methods. *Journal of The Electrochemical Society* **2003**, *150*, A425.

154. Hess, A.; Roode-Gutzmer, Q.; Heubner, C.; Schneider, M.; Michaelis, A.; Bobeth, M.; Cuniberti, G., Determination of State of Charge-Dependent Asymmetric Butler-Volmer Kinetics for Li_xCoO_2 Electrode Using Gitt Measurements. *Journal of Power Sources* **2015**, *299*, 156-161.

155. Levi, M. D.; Salitra, G.; Markovsky, B.; Teller, H.; Aurbach, D.; Heider, U.; Heider, L., Solid-State Electrochemical Kinetics of Li-Ion Intercalation into $Li_{1-x}CoO_2$: Simultaneous Application of Electroanalytical Techniques SSCV, PITT, and EIS. *Journal of The Electrochemical Society* **1999**, *146*, 1279-1289.

Chapter 2. Experimental

This chapter provides a brief summary of the materials and chemicals, experimental setup and instrumentation used in this thesis. Detailed information can be found in each chapter, which is specific to each experiment design.

2.1 Chemicals

All chemicals were used as received and all solutions were prepared with high purity water (Purite, Select HP) with a resistivity of *ca.* 18.2 MΩ cm at 25°C. **Table 2.1** lists all the chemicals used in this thesis.

Table 2.1 List of chemicals used in this thesis.

Chemicals	Product Source
Potassium chloride (> 99.99%)	Sigma- Aldrich
Perchloric acid (70 %)	Sigma- Aldrich
Lithium chloride (≥ 99 %)	Sigma- Aldrich
Lithium manganese oxide (electrochemical grade)	Sigma- Aldrich
Molybdenum disulfide (MoS_2)	Manchester Nanomaterials Ltd (U. K.)
Tungsten disulfide (WS_2)	Sigma- Aldrich
Alumina slurry (0.005-micron suspension)	Buehler
Glassy carbon substrate (25 mm x25mm)	Alfa Aesar
Highly oriented pyrolytic graphite (12×12×2 mm)	SPI Materials

2.2 Electrode Preparation

2.2.1 Preparation of Cu/Au Supported h-BN Electrode

The h-BN samples were prepared by Dr. Hong-Cheng Ruan, in Prof. Tianyou Zhai's lab at Huazhong University of Science and Technology, China. The h-BN/Cu sample was directly grown on polycrystalline Cu foils by the atmospheric pressure chemical vapour deposition

(CVD) method, while the h-BN/Au sample was derived from the h-BN/Cu sample via the polymethyl-methacrylate (PMMA) transfer process.[1] The scanning electron microscopy (SEM) images of these samples are shown in **Figure 2.1**. It should be noted that both the h-BN/Cu and h-BN/Au samples were stored under vacuum and then shipped to UK for further characterization and electrochemical measurements.

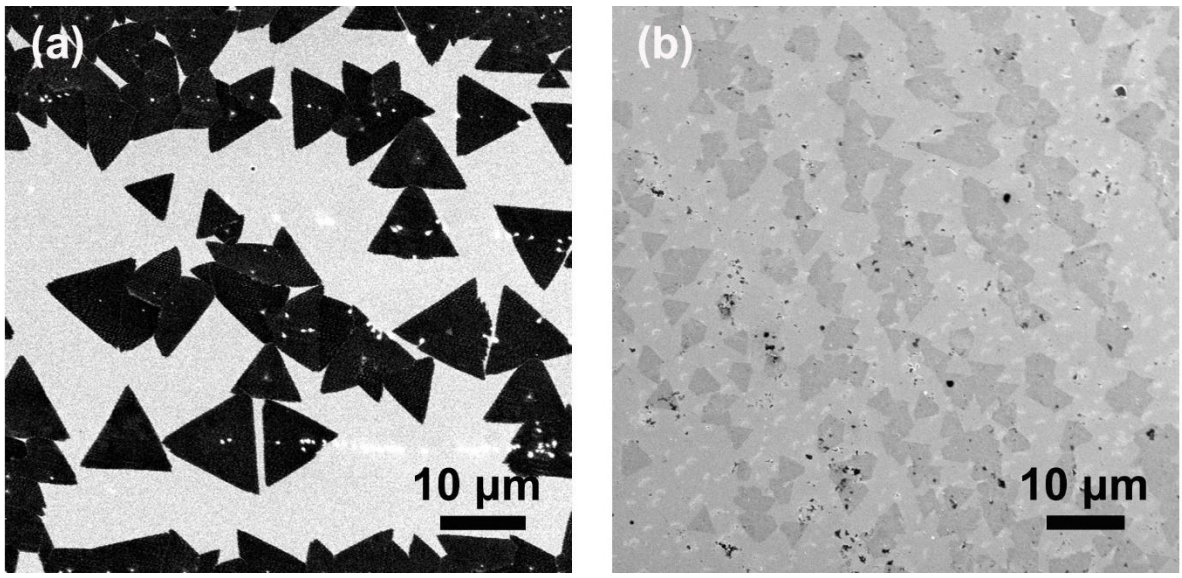

Figure 2. 1 SEM image of the as-grown h-BN/Cu sample **(a)** and transferred h-BN/Au sample **(b)**, respectively.

2.2.2 Preparation of MoS_2/WS_2 Electrode

Both the MoS_2 and WS_2 samples were cleaved using Scotch tape to achieve a freshly clean surface.[2] The cleavage direction was carefully maintained to avoid distortion of the surface. In order to ensure electrical connection, the freshly cleaved MS_2 flakes were electrically connected through top contact with single side adhesive copper tape.[3] As shown in **Figure 2.2**, on the copper tape, a small punch hole (*ca.* 0.2 mm) is made by a puncher in order to expose a small area of MS_2. From the optical microscopy image, it can be observed that on each sample surface, both basal planes and features (macroscopic cracks/defects) have been exposed.

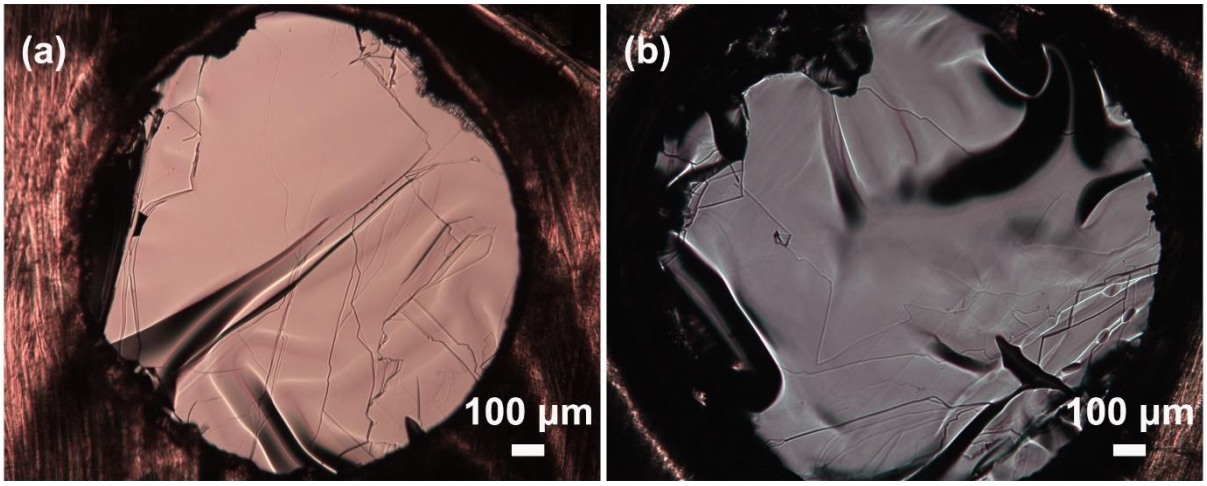

Figure 2.2 Optical micrograph of the surface of bulk MoS_2 **(a)** and WS_2 **(b)**, respectively, fresh after mechanical exfoliation.

2.2.3 Preparation of Drop-casted $LiMn_2O_4$ Electrode

Typically, approximate 0.1 g of $LiMn_2O_4$ powder was sonicated in 10 mL of deionized water for about 10 min until a stable slurry formed. After that, this slurry was rested for about 30 min, then 0.6-1.0 µL of the supernatant was drop cast onto a polished glassy carbon substrate. Before used as the working electrode, this freshly made substrate was left at room conditions for about 30 min until all the solvent evaporated. The as prepared drop-casted $LiMn_2O_4$ nanoparticles sample is depicted in **Figure 2.3**. It should be noted that $LiMn_2O_4$ particles would degrade at ambient conditions after several months, probably originating from their high surface energy, as all the particles are less than 500 nm.

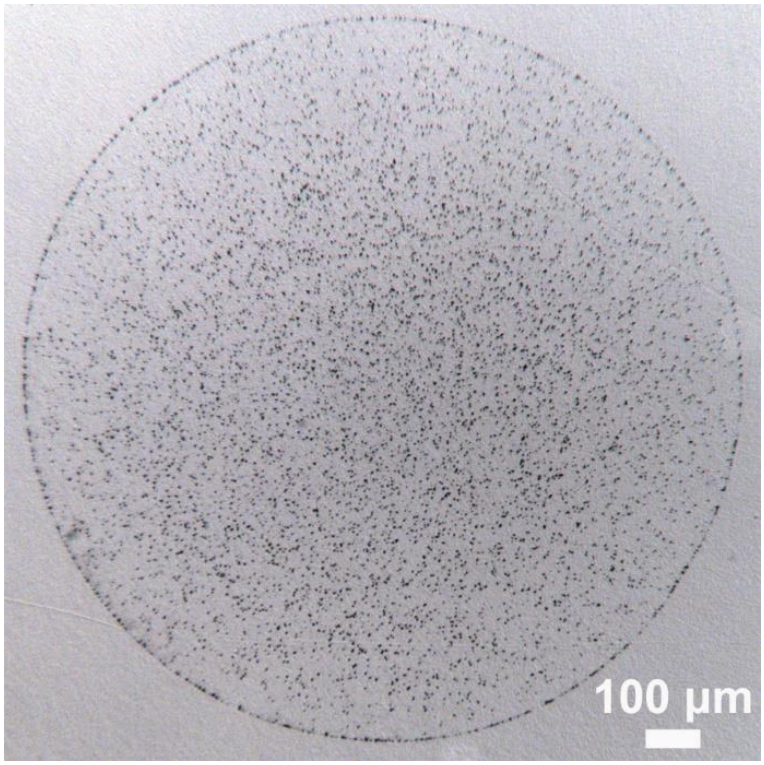

Figure 2.3 Optical micrograph of a $LiMn_2O_4$/GC electrode, which was prepared by drop-casting method.

2.3 Pipette Fabrication and Characterization

The size of the pipette defines the spatial resolution of SECCM, as the meniscus (contact area) is comparable with the size of the orifice. Usually, nanopipettes are made from borosilicate glass or quartz capillary, pulled to a sharp end via a laser based nanopipette puller (P-2000 from *Sutter Instruments*, shown in **Figure 2.4a**). For the tips with diameter on micrometre scale (especially above 5 µm), a PC-100 puller from *Narishige* (shown in **Figure 2.4b**) with heating coil is preferred.

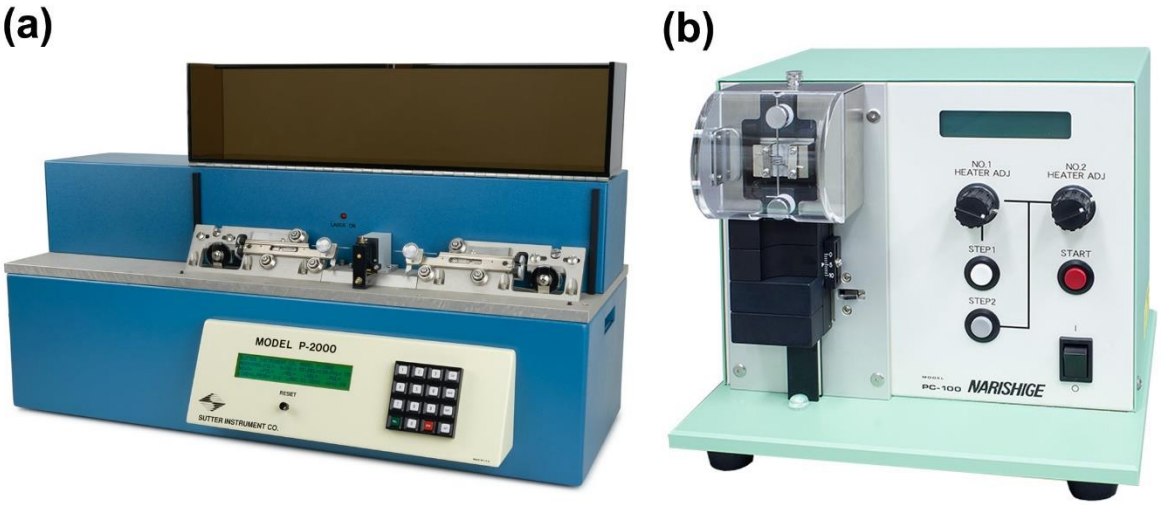

Figure 2.4 (a) P-2000 laser puller from Sutter Instruments and **(b)** PC-100 heating puller from Narishige.

In both cases, the size of the probe can be controlled by adjusting the pulling parameters, *e.g.*, heating, filament, velocity, dwell time, pull force, *etc.* Once the parameters have been determined, each pull would produce two probes at a time with a mirror image relationship. The puller is very reproducible to allow the user to make the same pipette as the last pull consistently. The capillary parameters, pulling conditions and the obtained diameters of pipettes are listed on **Table 2.2**.

The dimensions of the pipette orifice were measured using scanning electron microscopy (SEM) on a Zeiss Supra 55VP system, which was operated at an accelerating voltage of 2 kV (tips with diameter larger than 500 nm), or with scanning transmission electron microscopy (STEM) mode on a Zeiss Gemini 500 system, which was operated at an accelerating voltage of 20 kV (tips with diameter less than 500 nm). In addition, scanning transmission electron microscopy (STEM) is able to provide information on the internal geometry of the pipette probes.

Table 2.2 Nanopipette dimensions, capillary parameters and the pulling conditions of the pipettes utilised in this thesis.

Diameter	Capillary Parameters	Pulling Conditions
30 nm	Quartz capillaries (QTF120-90-100, Friedrich & Dimmock Inc., U.S.A.)	Line 1: 750, 4, 30, 150, 80 Line 2: 650, 3, 40, 135, 120
150 nm	Borosilicate glass capillaries (GC120F-10, 1.2OD×0.69×100 Harvard Apparatus, U. S. A.)	Line 1: 350, 3, 30, 220, - Line 2: 350, 3, 40, 180, 120
500 nm	Borosilicate glass capillaries (GC120F-10, 1.2OD×0.69×100 Harvard Apparatus, U.S.A.)	Line 1: 350, 3, 40, 220, - Line 2: 350, 3, 40, 180, 100
2 µm	Borosilicate glass capillaries (GC120F-10, 1.2OD×0.69×100 Harvard Apparatus, U.S.A.)	Line 1: 350, 4, 40, 200, -
5 µm	Quartz capillaries (QTF120-90-100, Friedrich & Dimmock Inc., U.S.A.)	Line 1: 680, 4, 45, 130, 35
8 µm	Borosilicate glass capillaries (GC120F-10 1.0OD×0.58×100 mm, Harvard Apparatus, U.S.A.)	Line 1: 350, 3, 40, 220, -
50 µm	Borosilicate glass capillaries (GC120F-10 1.0OD×0.58×100 mm, Harvard Apparatus, U.S.A.)	Step 1: heater 70, weight 3, and slider 8 Step 2: heater 55, weight 3, and slider 4

2.4 Preparation of Ag/AgCl Quasi Reference Electrodes

Silver-silver chloride (Ag/AgCl), comprising AgCl coated Ag wire, which was prepared by anodizing 0.125 mm diameter polished silver wire (Goodfellow, U.K., 99.99 %) in a saturated KCl solution at + 5 V (versus a Pt counter electrode), was used as quasi-reference counter electrode (QRCE).[4] The QRCE potential was calibrated against a commercial saturated calomel electrode (SCE) before and after each experiment. In 0.1 M $HClO_4$ solution, the QRCE possess a reference potential of 0.2 ± 0.05 V *vs.* SCE, while in 1 M LiCl solution, the potential is ± 0.005 V *vs.* SCE.

2.5 SECCM Operating System

The SECCM probes need to be moved vertically towards and away from the substrate surface of interest, which is typically achieved using a very precise z-direction piezoelectric positioner (*e.g.*, P-753.3CD, Physik Instrumente, Germany). The sample is mounted on a two-axis piezoelectric positioner with relatively large ranges (*e.g.*, P-622.2CD, 100×100 μm^2 Physik Instrumente), which allow horizontal (both x and y direction) movement. The selection of piezoelectric positioner with different working ranges is according to the experimental design, such as probe diameter, feature morphology, and size of scan area. The movement of the piezoelectric positioners are controlled by their corresponding amplifier modules (E-665 and E-500, respectively), which are set and calibrated by the manufacturer. Typically, a closed loop mode is chosen in order to make a precise control, although higher translation speed can be employed if the open loop mode is adapted. As alluded to before, the xy and z piezoelectric positioners are mounted on different panels, which are suitable for high-resolution images, as the cross talk between different positioners is minimised.

The amplifier modules are connected to a breakout box, which is adapted from the output side of a SHC68-NT-S cable (National Instruments, USA). The other side of this cable linked to a field programmable gate array (FPGA) card, which is mount on the PCIe express 3.0 x16 slot of a computer motherboard. Usually, a data acquisition (DAQ) card is exploited in most of the SPM technique. As the data acquisition speed is ultrafast (on the scale of μs) in SECCM, a reasonable FPGA card (PCIe-7852R) is needed to substitute the DAQ card. The comparisions in data acquisition speed and system response time of the two types of cards

(configuration) are illustrated in **Figure 2.5**. A lock-in amplifier is utlized to generate and extract oscillating signals (SR830, Stanford Research Systems), when carrying out optional alternating current (AC) variants of SECCM. All the other auxiliary electronics, such as the electrometers, filters, signal adders and Faraday cages, are all custom made by Dr. Alex Colburn in Department of Physics, University of Warwick. These electronics are utilized to perform cyclic voltammetry and galvanostatic charge-discharge measurements in the following chapters (maximum range from -10 to 10 V). At the user interfaces, a custom software written in Labview graphical language (WEC-SPM, www.warwick.ac.uk/electrochemistry) is used to control the whole system, in the sequence level of user interfaces-host-FPGA card-electronics.

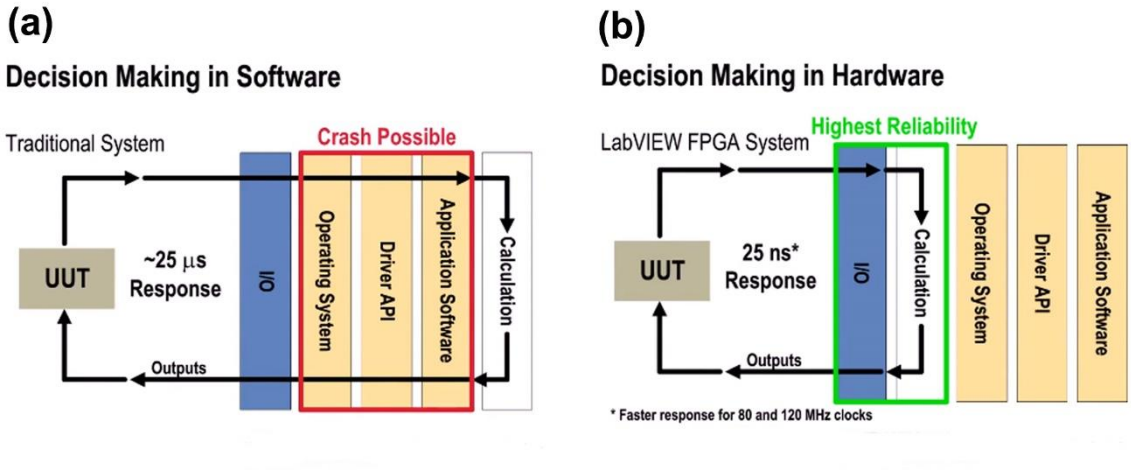

Figure 2.5 Comaparision between traditional system **(a)** and Labview PFGA system **(b)**. With the fast response capability of FPGA card, data collection speed could be performed at megahertz. Besides, most of the data collection and calculation process can be finished on the FPGA card, which is highly reliable compare to the traditional system where the same process finishing on the software level. In both figures, UUT stands for unit under test.

In this thesis, all the experiments were performed under single channel pipette SECCM configuration with DC current as the feedback. To be more specific, the sample is biased at electroactive state before approach, then the tip moves toward the surface of interest. Upon contact, the tip stops moving as the closed electric circuit triggers a current higher than the noise level (when tip in the air). At this fixed position, electrochemical reaction (linear sweep voltammetry or cyclic voltammetry) is performed and both the tip height and the reaction

current are recorded. After that, the tip retracts to a predefined position, moves to the next point and prepares for another approach (experiment). Further details are described in each chapter in below.

2.6 References

1. Kim, K. K., et al., Synthesis of Monolayer Hexagonal Boron Nitride on Cu Foil Using Chemical Vapor Deposition. *Nano Letters* **2012**, *12*, 161-166.

2. Novoselov, K. S.; Geim, A. K.; Morozov, S. V.; Jiang, D.; Zhang, Y.; Dubonos, S. V.; Grigorieva, I. V.; Firsov, A. A., Electric Field Effect in Atomically Thin Carbon Films. *Science* **2004**, *306*, 666.

3. Tan, S. M.; Ambrosi, A.; Sofer, Z.; Huber, Š.; Sedmidubský, D.; Pumera, M., Pristine Basal-and Edge-Plane-Oriented Molybdenite MoS_2 Exhibiting Highly Anisotropic Properties. *Chemistry–A European Journal* **2015**, *21*, 7170-7178.

4. Bentley, C. L.; Perry, D.; Unwin, P. R., Stability and Placement of Ag/AgCl Quasi-Reference Counter Electrodes in Confined Electrochemical Cells. *Analytical Chemistry* **2018**, *90*, 7700-7707.

Chapter 3. Metal Support Effects in Electrocatalysis at Hexagonal Boron Nitride

A scanning electrochemical droplet cell technique was employed to screen the intrinsic electrocatalytic hydrogen evolution reaction (HER) activity of hexagonal boron nitride (h-BN) nanosheets supported on different metal substrates (Cu and Au). Local (spatially-resolved) voltammetry and Tafel analysis reveal that electronic interaction with the underlying metal substrate plays a significant role in modulating the electrocatalytic activity of h-BN, with Au-supported h-BN exhibiting significantly enhanced HER charge-transfer kinetics (exchange current is *ca.* two orders of magnitude larger) compared to Cu-supported h-BN, making the former material the superior support in a catalytic sense.

This chapter has been published as an article in *Chemical Communications* (Dan-Qing Liu, **Binglin Tao**, Hong-Cheng Ruan, Cameron L. Bentley, and Patrick R. Unwin, *Chem. Commun.* **2019**, 55, 628-631). Dan-Qing Liu designed the experiment and the performed the measurements together with Binglin Tao (this work has already been seen in her thesis, Warwick 2018). Binglin Tao was also responsible for the data processing and manuscript preparation. Hong-Cheng Ruan prepared all the samples (substrates) used in this work. Cameron L. Bentley was a postdoctoral researcher who revised the manuscript.

Metal Support Effects in Electrocatalysis at Hexagonal Boron Nitride

Dan-Qing Liu,[‡a] Binglin Tao,[‡a] Hong-Cheng Ruan,[‡b] Cameron L. Bentley,[*a] and Patrick R. Unwin[*a]

[a] Department of Chemistry, University of Warwick, Gibbet Hill Road, Coventry, UK

[b] School of Information and Safety Engineering, Zhongnan University of Economics and Law, Wuhan 430073, P.R. China

*** Corresponding Author**

*c.bentley.1@warwick.ac.uk (C.L.B), p.r.unwin@warwick.ac.uk (P.R.U)

‡ These authors contributed equally to this work

3.1 Abstract

Efficient evolution of hydrogen through electrochemical water splitting holds tremendous promise for green energy project in the future, which will ultimately serve as the replacement of traditional fossil fuels. Hydrogen evolution can be readily achieved by employing expensive noble metals (such as Pt), while it is still challenging to develop highly active catalysts based on materials that are more abundant at lower prices. Very recently, as low cost and highly stable two-dimensional material, hexagonal boron nitride (h-BN) has attracted much attention in electrocatalysis. A scanning electrochemical droplet cell technique has been employed to screen the intrinsic electrocatalytic hydrogen evolution reaction (HER) activity of hexagonal boron nitride (h-BN) nanosheets supported on different metal substrates (Cu and Au). Local (spatially-resolved) voltammetry and Tafel analysis reveals that electronic interaction with the underlying metal substrate plays a significant role in modulating the electrocatalytic activity of h-BN, with Au-supported h-BN exhibiting significantly enhanced HER charge-transfer kinetics (exchange current is *ca.* two orders of magnitude larger) compared to Cu-supported h-BN.

3.2 Introduction

Electrochemical water splitting is widely recognized as the most sustainable method for generating hydrogen (H_2), a fuel that is in growing demand[1] for use in green energy technologies (*e.g.*, fuel cells) as the world moves towards a decarbonized future.[2] Noble metal based materials (*e.g.*, Pt) are the most efficient HER electrocatalysts in aqueous acid media, with fast reaction kinetics resulting in low overpotentials.[3] However, due to the high cost and relative scarcity of these materials, there is an ongoing search for cheap, earth-abundant HER electrocatalysts, for example, two-dimensional (2D) materials such as transition metal dichalcogenides,[4] carbon nitride,[5] and sandwich structures based on 2D crystals,[6] which in recent years have shown great promise, with certain classes exhibiting considerable catalytic activity and high (electro)chemical stability.[7] Although it is intrinsically insulating (*i.e.*, band gap of 3.6 to 7.1 eV),[8] hexagonal boron nitride (h-BN) has attracted considerable attention in oxygen reduction reaction (ORR)[9-10] and hydrogen evolution reaction (HER) catalysis.[11] This is because the band gap of monolayer h-BN can be considerably reduced by introducing defects such as B/N vacancies and impurities,[12] and tuned to an extent through decoration with hydrogen atoms.[13] Moreover, as electron tunnelling through ultrathin h-BN layers is possible,[14] electronic interaction with the underlying metal support substrate (*i.e.*, through mixing of the d_z^2 metal orbitals with the N-p_z and B-p_z orbitals of h-BN) can tune electrochemical (electrocatalytic) activity.[15]

3.3 Experimental Section

3.3.1 Chemicals and Materials

Copper foil was purchased from Alfa Aesar (purity 99.8 %, 0.025 mm thick). Perchloric acid ($HClO_4$, 70%) and ammonia borane (NH_3-BH_3, 97%) were purchased from Sima-Aldrich and used as received. All aqueous solutions were prepared from ultrapure water (18.2 MΩ cm resistivity at 25 °C) produced by a Purite Integra HP system (U.K.). The silver/silver chloride (Ag/AgCl) quasi reference counter electrode (QRCE) was prepared by anodic polarization of an Ag wire (0.125 mm diameter, Goodfellow, 99.99 %) in saturated KCl solution. The QRCE potential was calibrated against a commercial saturated calomel electrode (SCE) in 0.1 M

$HClO_4$ solution after each experiment, and was found to possess a stable potential of *ca.* 0.21 V vs. SCE.

3.3.2 Preparation of h-BN

Hexagonal boron nitride (h-BN) was grown on polycrystalline Cu foil with a thickness of 25 μm by the atmospheric pressure CVD method. In order to achieve this, the Cu foil was first chemically polished using a solution of 0.4 M $FeCl_3$ in 0.8 M HCl. After drying with compressed N_2 gas, the polished foil was loaded into the center of a 25 mm diameter tube furnace, before being pumped to a pressure of 15 mTorr. After pre-annealing at 1015 °C for 30 min with a mixture gas of 16 standard cubic centimeters (sccm) of H_2 (99.99 %) and 260 sccm of Ar (99.99%), 1 mg ammonia borane was placed in a specially designed boat and loaded in the upstream of the CVD growth tube as the precursor of h-BN. The precursor temperature was controlled by a heating belt around the tube, separated from the heating zone of the furnace. The growth of h-BN was achieved in 60 min at 1065 °C. After growth, the system was quickly cooled down to <200 °C under the same gas flow. The rear surface of the sample was fixed to an evaporated Au (300 nm) film on SiO_2/Si wafer by using silver paint (Agar Scientific, Ltd, U.K.). The whole sample was then connected to a copper wire for subsequent electrochemical measurements.

For preparing the transferred h-BN/Au using polymethyl-methacrylate (PMMA) method, a PMMA (AR-P. 679.04, ALLRESIST, GmbH) layer was spin-coated on the surface of as-grown h-BN on Cu foil at 4000 rpm for 50 s. The h-BN film is released by protecting the h-BN with PMMA and etching the underlying Cu foil with an aqueous solution of 0.4 M $FeCl_3$ for 5 h. After that, the film was washed by floating on deionized water. Subsequently, the film could be transferred on the Au substrate, which consisted of an evaporated Au film (300 nm) on SiO_2/Si. The sample was then heated to 150 ℃ to remove any adventitious water, as well as promote good adhesion of the film to the Au substrate. Following this, the sample was immersed in acetone solution to dissolve the PMMA layer and was then annealed under nitrogen gas at 350 ℃ for 5 min." Similar to above, the sample was connected to a copper wire for electrochemical characterization. After scanning (see below), the h-BN/Cu and h-BN/Au substrates were imaged using a ZEISS GEMINI 500 FE-SEM, at 2K eV with the InLens mode.

3.3.3 Fabrication and Characterization of Nanopipettes

Single-barrel nanopipettes were pulled from glass capillaries (GC120F-10, Friedrich & Dimmock, Inc, U.S.A., with filament) using a P-2000 laser puller (Sutter Instruments, USA) with a two-step protocol. For the first step, the parameters were heat 330, filament 3, velocity 30 and delay 220. For the second step, the parameters were heat 350, filament 3, velocity 40, delay 180 and pull 120. The dimensions of the nanopipette orifice were measured using field emission scanning electron microscopy (FE-SEM) on a Zeiss Supra 55VP system, which was operated at an accelerating voltage of 2 kV. Representative images of the nanopipette probes used in this work are shown in Supporting Information, **Figure 3.4**. After fabrication, the nanopipette probes were back filled with 0.1 M $HClO_4$ solution and a layer of silicone oil (DC 200, Fluka) sequentially using a MicroFil syringe (World Precision Instrument Inc., U.S.A.), before inserting the Ag/AgCl QRCE (detailed above) for electrochemical measurement.

3.3.4 Instrumentation and Data Processing

The instrumental setup of single-barrel SECCM has previously been reported and is shown in the main text, **Figure 3.1a**. During operation, the prepared nanopipette probe (detailed above) was mounted on a *z*-piezoelectric positioner (P-753.3CD, Physik Instrumente), and the substrate (*i.e.*, h-BN/Cu or h-BN/Au) was mounted on an *xy*-piezoelectric positioner (P-622.2CD, Physik Instrumente). SECCM was operated in the voltammetric hopping mode, as previously reported. In this mode, the nanopipette probe is approached to the surface of interest at a series of pre-defined locations in a grid. During *z*-approach, contact between the meniscus (droplet) cell located at the end of the nanopipette probe and substrate surface (note that the nanopipette itself did not make contact) was detected through surface current (i_{surf}) feedback, using a threshold current of 1 pA herein. Upon each landing, a linear-sweep voltammetry (LSV) measurement was carried out at a voltammetric scan rate (v) of 1 V/s. After each measurement, the nanopipette probe was retracted and moved laterally (*i.e.*, in *xy* space) to the next point that was located at a pre-defined distance away ('hopping distance', equal to 500 nm herein), where the same procedure was implemented. The potential applied ($-E_{app}$) to the QRCE (with respect to the ground) was controlled, and h-BN sample (working electrode, ground) current, namely i_{surf}, was detected. The current was measured every 4 μs, which was averaged 513 times to give a

data acquisition rate of 2052 µs per point. The current signal was filtered using an 8th order low-pass filter at a time constant of 2 ms.

To perform LSV measurements using SECCM in the absence of air, the nanopipette tip and h-BN/Cu sample were placed in an environmental chamber that was constantly purged with humidified argon gas, as previously reported.

Data acquisition and fine control of all the instruments were obtained by using an FPGA card (PCIe-7852R) controlled by a LabVIEW 2016 (National Instrument, U.S.A.) interface running the Warwick Electrochemical Scanning Probe Microscopy (WEC-SPM, www.warwick.ac.uk/electrochemistry) software. After collection, the raw data were processed with Matlab R2015b and OriginPro 2016 software packages.

3.4 Results and Discussion

In this study, we explore the tunable electronic properties of h-BN in the context of (electro)catalysis by considering the HER activity of as-grown h-BN nanosheets supported on Cu (denoted as h-BN/Cu) and Au (denoted as h-BN/Au) substrates. The intrinsic electrocatalytic properties of h-BN have been probed using scanning electrochemical cell microscopy (SECCM, see **Figure 3.1a**),[16-17] a scanning droplet cell technique that allows characteristic surface sites (*e.g.*, h-BN vs. metal substrate surface, herein) to be targeted and electrochemically characterized at the 'single-entity' level.[17-18] SECCM has been deployed in the voltammetric hopping mode,[18-20] where the droplet (meniscus) cell formed at the end of an electrolyte-filled (0.1 M $HClO_4$, herein) nanopipette (tip diameter, d_t = 150 to 300 nm, herein) is approached to (contacted with) the sample (working electrode) surface sequentially at a series of predefined locations, and upon each landing a spatially-resolved linear-sweep voltammogram (LSV) is recorded. In other words, in a single SECCM experiment, thousands of spatially-independent nano-electrochemical cells are formed, with the probed area defined by the footprint of the meniscus (droplet) cell, allowing the HER activity of individual h-BN nanosheets to be compared and visualized directly, providing new insights into the catalytic properties of these promising non-precious metal electrocatalysts.

As detailed in the experimental section, the h-BN nanosheets were grown on polycrystalline Cu foils (h-BN/Cu) by an atmospheric pressure chemical vapour deposition

(CVD) method.[21] The as-grown h-BN was subsequently transferred onto the Au substrate (h-BN/Au) by the polymethyl-methacrylate (PMMA) method.[22] The morphologies of as-grown h-BN/Cu and transferred h-BN/Au were observed directly by field emission scanning electron microscopy (FE-SEM), as depicted in **Figure 3.1b** and **c**. Considering **Figure 3.1b**, the h-BN nanosheets are triangular in shape and show a much darker contrast compared than the underlying Cu support, with sizes ranging from *ca.* 5 to 12 µm, in agreement with previous reports.[23] It should be noted that the white particles on the h-BN/Cu surface are comprised of borazine, arising from the decomposition of the ammonium borane precursors.[24] Considering **Figure 3.1c**, the morphology of transferred h-BN/Au is quite similar with that of h-BN/Cu, with h-BN nanosheets (dark regions in **Figure 3.1c**) of approximately *ca.* 5 µm in size dispersed on the underlying Au support (light regions in **Figure 3.1c**).

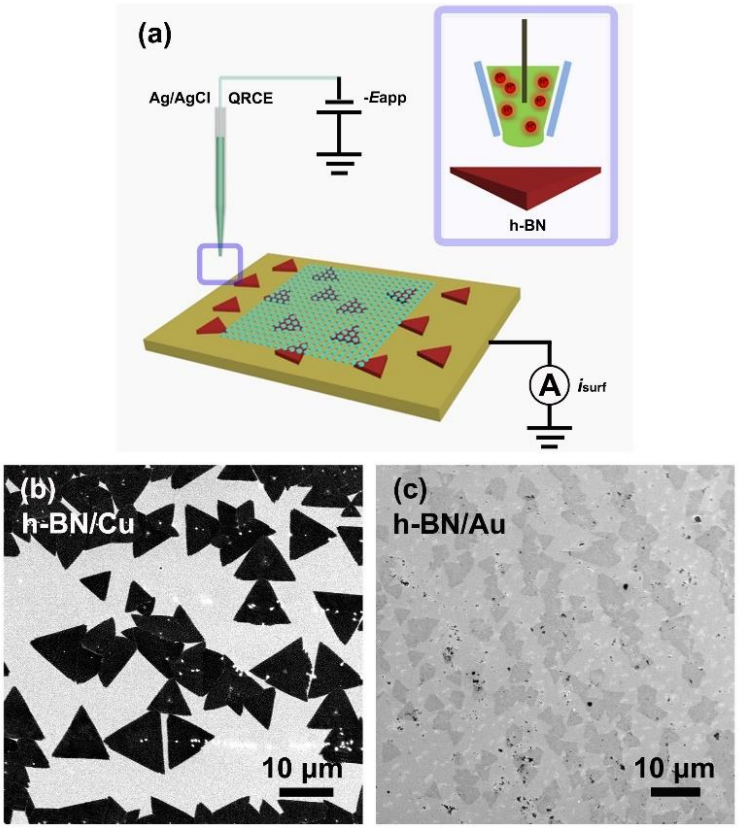

Figure 3.1 (a) Schematic showing the scanning electrochemical cell microscopy (SECCM) set up used to screen the catalytic activity of h-BN at the nanoscale. Potential, $-E_{app}$, is applied the Ag/AgCl quasi-reference counter electrode (QRCE) in the nanopipette probe and current, i_{surf}, is measured at the substrate (working electrode). Inset is an enlarged diagram of the

probed h-BN interface during a single 'hop' of a scanning experiment. FE-SEM images of **(b)** as-grown h-BN/Cu and **(c)** transferred h-BN/Au.

The electrocatalytic activity of h-BN/Cu towards the HER was screened using voltammetric SECCM, where hundreds of local (spatial resolution or 'hopping distance' of 500 nm) LSV measurements were performed with a nanopipette probe of $d_t \approx 300$ nm (see **Figure 3.4a** of the Supporting Information). Note that the ORR was found to make a negligible contribution to the electrocatalytic current measured on the basal surface of h-BN/Cu during cathodic polarization, revealed by performing point measurements in an environmental chamber under an inert (argon) atmosphere (*i.e.*, in the presence and absence of air),[25-26] as explored in the Supporting Information, **Figure 3.5**. For this reason, all SECCM experiments were carried out without environmental control (*i.e.*, in the presence of air), and the electrocatalytic current can be attributed to the HER alone. An FE-SEM image of the area scanned with SECCM is shown in **Figure 3.2a**; the individual droplet 'footprints' are visible on the h-BN surface (light regions), as are exposed regions of the underlying Cu support (dark regions with sharp outlines). Representative LSVs, taken from 45 points across the h-BN surface and normalized by the area of individual footprints (shown in **Figure 3.2a**), as well as the average LSV recorded from all points on the surface of the h-BN nanosheets (684 individual measurements) are shown in **Figure 3.2b**. The LSVs measured at h-BN/Cu are highly reproducible, reflected in the histogram constructed from the current density (j) measured at -0.688 V *vs.* the reversible hydrogen electrode (RHE), shown in **Figure 3.2c**, which is Gaussian in shape ($N = 684$), with a peak (mean) value of 10 (± 2) mA cm^{-2}.

The overpotential (η) required to achieve a j of 20 mA cm^{-2} (termed η_{20}) at h-BN/Cu is *ca.* 0.77 V, indicating that the HER is kinetically sluggish on this material. Although this value is much larger than literature values for HER nanocatalysts such as metallic WS_2 nanosheets on graphite[27] and nanocrystalline MoS_2 on Au,[4] such measurements were performed exclusively by bulk (macroscopic) measurements on ensembles of material, where the number (*i.e.*, surface area) and type (*i.e.*, basal plane vs. edge plane) of exposed surface site is not known, making normalization to the true electrochemical surface area (ECSA) impossible. This is an important advantage of SECCM over macroscopic (bulk) voltammetry, as particular surface sites can be targeted (*i.e.*, the basal surface of h-BN), with the exposed

surface area accurately known from the droplet 'footprint' (**Figure 3.2a**), allowing the true intrinsic catalytic activity to be extracted by semi-quantitative Tafel analysis (*vide infra*).[19] In any case, it is worth noting that the η_{20} value measured at h-BN/Cu (0.77 V) is much lower than the reported value of a BN-modified graphite electrode (1.15 V),[28] indicating the underlying Cu substrate can promote the HER performance of h-BN, which is usually considered to be an insulator.

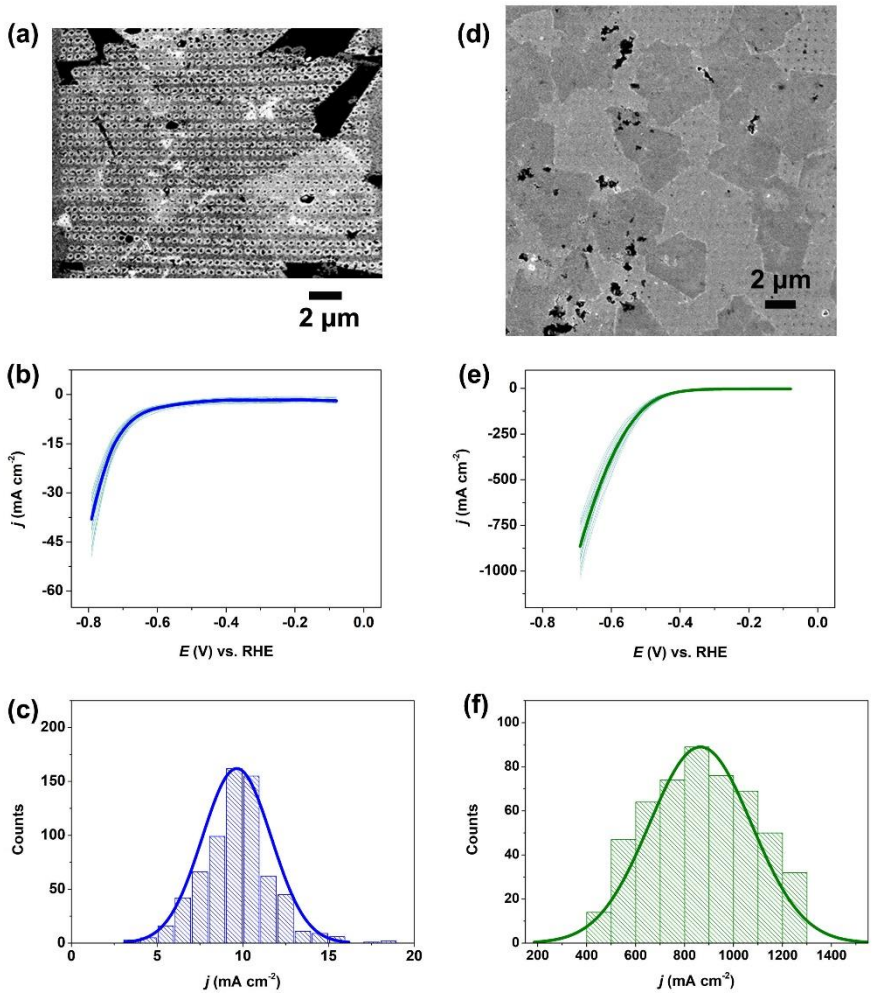

Figure 3.2 (a) FE-SEM image of an area of the h-BN/Cu scanned using SECCM (individual droplet footprints are visible). **(b)** Representative LSVs (transparent) obtained from 45 points across the surface of h-BN/Cu and average LSV (blue) obtained from all points on h-BN/Cu (684 individual measurements). **(c)** Histogram (N = 684) showing the distribution in j values measured at the surface of h-BN/Cu at an applied potential of -0.688 V $vs.$ RHE. **(d)** FE-SEM image of an area of the h-BN/Au scanned using SECCM (individual droplet footprints are visible). **(e)** Representative LSVs (transparent) obtained from 35 points across the surface of

h-BN/Au and average LSV (green) obtained from all points on h-BN/Au (515 individual measurements). **(f)** Histogram (N = 515) showing the distribution in j values measured at the surface of h-BN/Au at an applied potential of -0.688 V vs. RHE. All LSVs were obtained from a 0.1 M $HClO_4$ solution at a voltammetric scan rate (v) of 1 V s^{-1}.

The electrocatalytic activity of h-BN/Au towards the HER was also screened using voltammetric SECCM (d_t ≈ 150 nm, see **Figure 3.4b** of the Supporting Information); an FE-SEM image of the scan area is shown in **Figure 3.2d**. The dark regions represent the surface of the individual h-BN nanosheets, while the light regions correspond to exposed Au substrate (droplet 'footprints' also seen in the image). Representative LSVs, taken from 45 points across the surface of the h-BN nanosheets, as well as the average LSV recorded from all points on the surface of h-BN/Au (515 individual measurements) are shown in **Figure 3.2e**. Evidently, the electrocatalytic activity of h-BN/Au for the HER is much higher than that of h-BN/Cu (albeit, still lower than the underlying Au support, **Figure 3.6** in the Supporting Information), with an η_{20} value of 0.47 V for the former, compared to 0.77 V for the latter (*vide supra*). This is also reflected in the histogram constructed from the *j* values measured on h-BN/Au at -0.688 V *vs.* RHE, shown in **Figure 3.2f**, which is also Gaussian in shape (*N* = 515), with a peak (mean) value of 900 (± 200) mA cm^{-2}, approximately two orders of magnitude larger than that measured at h-BN/Cu. These results unequivocally demonstrate that interaction with the underlying metal support can have a significant effect on the electronic properties of h-BN, evident from the vastly different HER catalytic activities measured when supported on Au and Cu.

A direct comparison of the average area normalized LSVs measured on h-BN/Cu, h-BN/Au and the Au substrate is shown in **Figure 3.3a**. Evidently, while the measured *j* at a given potential is *ca.* 2 orders of magnitude larger on h-BN/Au compared to h-BN/Cu (*e.g.*, *j* = 10 and 900 mA cm^{-2} at -0.688 V vs. RHE on h-BN/Cu and h-BN/Au, respectively), the former material is still less active than underlying Au substrate (*i.e.*, *j* ≈ 1600 mA cm^{-2} at 0.688 V *vs.* RHE on Au). This was confirmed by semi-quantitative Tafel analysis, as shown in **Figure 3.3b**. All materials possess similar Tafel slopes of *ca.* 120 mV per decade (136, 108 and 130 mV per decade at h-BN/Cu, h-BN/Au and Au, respectively), which is consistent with rate determining step being the initial discharge of H^+ at the electrode surface (termed the Volmer step in the classical Volmer-Tafel-Heyrovsky mechanism of hydrogen evolution), although this

conclusion should be treated *cum grano salis*, as the specific mechanism of the HER cannot be unambiguously determined from the Tafel slope alone.[19]

The exchange current density (j_0), estimated directly by extrapolation of the linear Tafel region, reflects the relative catalytic activity of the materials, with values of *ca.* 4×10^{-8} A cm^{-2}, 1×10^{-6} A cm^{-2}, and 4×10^{-6} A cm^{-2} measured at h-BN/Cu, h-BN/Au and Au, respectively. As noted above, making a meaningful comparison between these data and literature data on h-BN is difficult, as the quantity and type of exposed surface site is often not known in macroscopic ensemble-type studies. Nevertheless, the Tafel slope and j_0 values measured in this study are far less favorable (in the catalytic sense) compared to those previously measured at macroscopic h-BN/Au ensembles, where optimal values of *ca.* 30 mV per decade and 4.6×10^{-5} A cm^{-2}, respectively were reported.[11] This suggests that the edges of h-BN, which would be exposed in the bulk measurements (as in Ref 11) but not the local ones (as carried out here), are likely to be predominantly responsible for the observed macroscopic activity in h-BN/Au ensembles. In any case, the j_0 of h-BN/Au is orders of magnitude lower than polycrystalline Pt ($j_0 = 3 \times 10^{-3}$ A cm^{-2}),[29] but is comparable to that measured on the basal plane of bulk (natural crystal) MoS_2 ($j_0 = 2.5 \times 10^{-6}$ A cm^{-2})[19] and a monolayer MoS_2 film supported on glassy carbon ($j_0 = 1.1 \times 10^{-6}$ A cm^{-2}).[30]

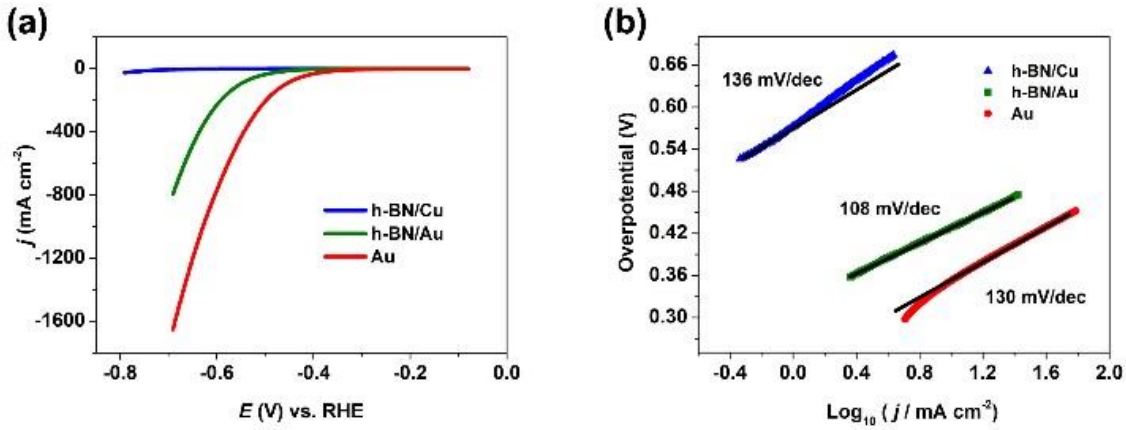

Figure 3.3 (a) LSVs (area normalized) and **(b)** corresponding Tafel plots obtained from the HER on h-BN/Cu (blue curve), h-BN/Au (green curve) and Au substrate (red curve). These data were obtained from a 0.1 M $HClO_4$ solution at v = 1 V s^{-1}. Linear least-squares fit (black traces, slope indicated on plot) are also shown in **(b)**.

As a wide band gap semiconductor, h-BN in its native form is assumed to be electrochemically (and electrocatalytically) inert.[31] In this study, h-BN supported on either Cu or Au substrates exhibit moderate catalytic activity towards the HER, with the enhancement effect of Au being much more pronounced than that of Cu. From this, we conclude that the substrate-dependent HER activity of h-BN is attributable to the interaction with the underlying metal support, which tunes molecular processes such as surface diffusion, adsorption and on-surface (interfacial) reactions.[32] As alluded to above, it has been reported that the strength of chemical bonding at the interface of h-BN and transition metal substrates is determined mainly by the strength of the d and π orbital hybridization.[33-34] On Cu(111), h-BN has previously been shown to be only weakly chemisorbed,[35] evidenced by scanning tunnelling microscopy and spectroscopy experiments.[36] On the other hand, theoretical calculations have predicted a perturbation of the electronic states of h-BN when interacting with an Au substrate.[9] This is consistent with the fact that various forms of BN (nanotubes, nanosheets and sputter deposited BN) have been shown to the significantly lower the overpotential associated with ORR at Au substrates, but have either no or a hindering effect at glassy carbon and Pt electrodes, respectively.[37] It is generally accepted that the ideal HER electrocatalyst should possess a near thermoneutral free energy of adsorbed atomic hydrogen, that is, $\Delta G_{\mathrm{H}^*} \approx 0$ eV.[38] We postulate that the significantly different HER activities of h-BN/Cu and h-BN/Au likely arise from different ΔG_{H^*} values at these two substrates. In other words, electronic coupling of h-BN and Au might result in more optimal adsorption-desorption processes (*i.e.*, $\Delta G_{\mathrm{H}^*} \rightarrow 0$), greatly facilitating the HER. On this basis, we propose that further theoretical studies of metal-support effects on ΔG_{H^*} at h-BN could be very interesting and usefully aid understanding in HER electrocatalysis at this type of nanomaterial.

3.5 Conclusions

In summary, SECCM has been employed to screen the intrinsic electrochemical activity (*i.e.*, HER electrocatalysis) of h-BN supported on Cu and Au substrates. Local voltammetric measurements revealed that the HER charge-transfer kinetics are *ca.* two orders of magnitude larger at the basal surface of h-BN when it is supported at Au (*i.e.*, h-BN/Au) compared to Cu (*i.e.*, h-BN/Cu). This significant enhancement was attributed to differences in the substrate effect between h-BN and Au/Cu, opening up the possibility of tuning reactivity

(*e.g.*, catalytic activity) through the underlying metal support. Overall, these findings pave the way towards rational design of h-BN based electromaterials, with the ultimate goal being the replacement of noble metals with inexpensive and (electro)chemically stable metal-free counterparts in HER electrocatalysis.

3.6 Supporting Information

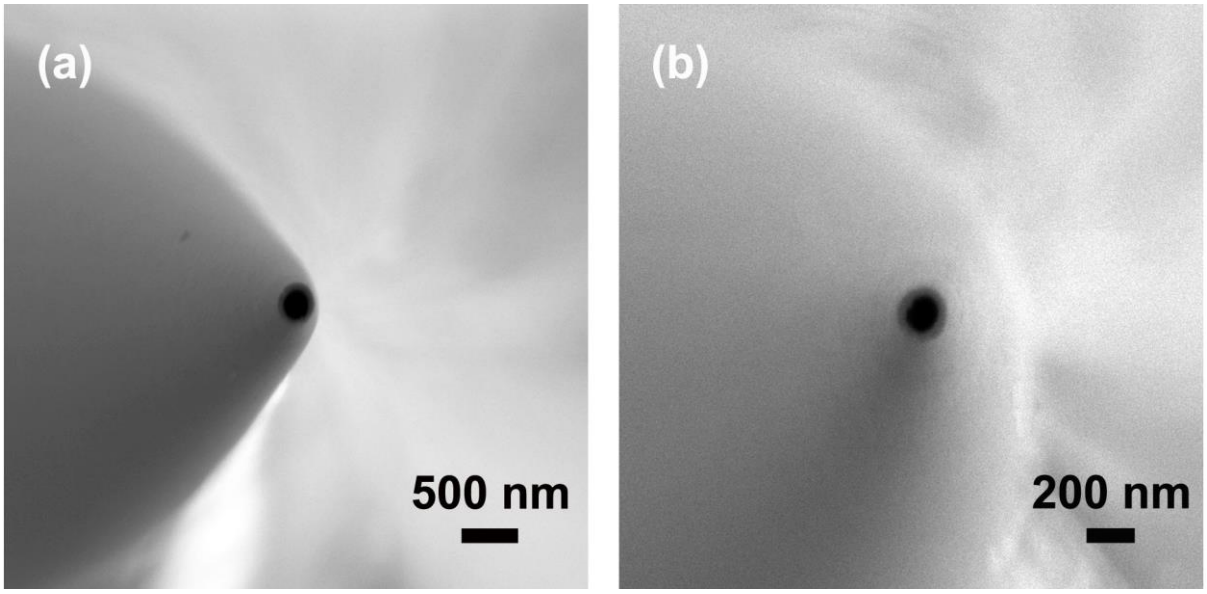

Figure 3.4 Representative FE-SEM images of the end (tip) of single-barrel nanopipettes used in experiments on the **(a)** h-BN/Cu and **(b)** h-BN/Au substrates.

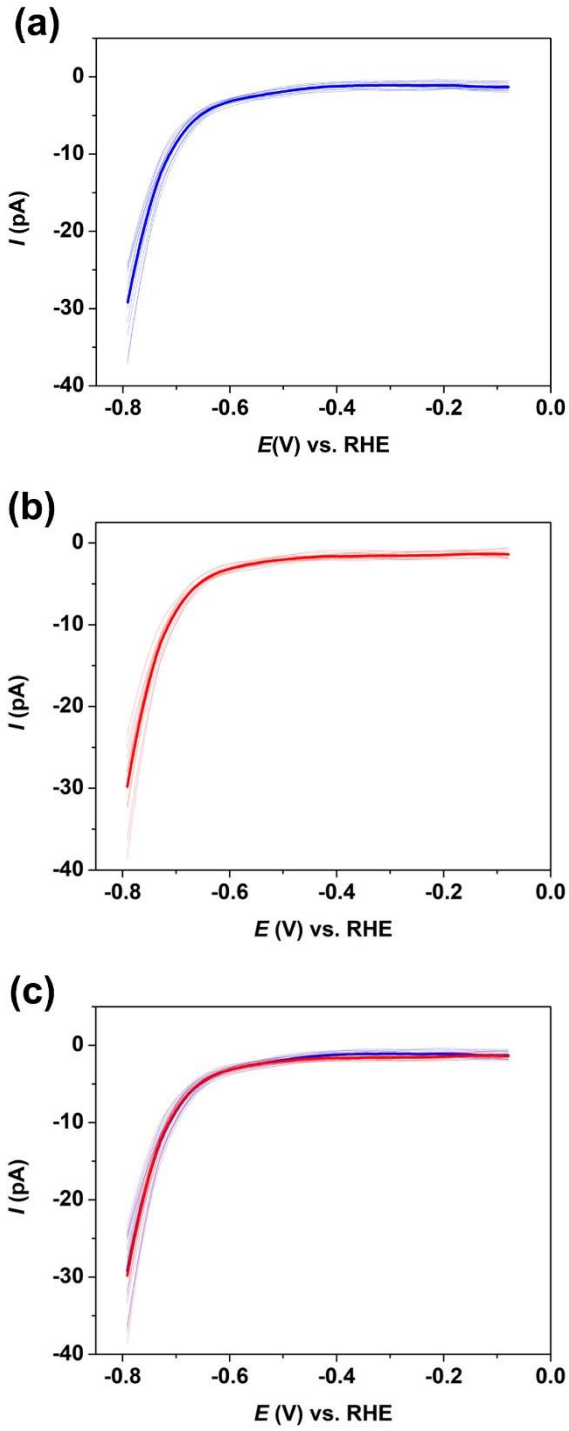

Figure 3.5 Typical LSVs at the surface of h-BN/Cu obtained from the **(a)** 12 points (transparent blue) in the presence of air and representative average LSV (blue), and **(b)** 12 points (transparent red) in the environmental chamber (i.e., absence of air) and representative average LSV (red). **(c)** HER activity comparison between the average LSVs obtained in the presence (blue) and absence (red) of air. Note that all measurements were performed with

the same probe. These LSVs were obtained from a 0.1 M $HClO_4$ solution at a voltammetric scan rate (ν) of 1 V s^{-1}.

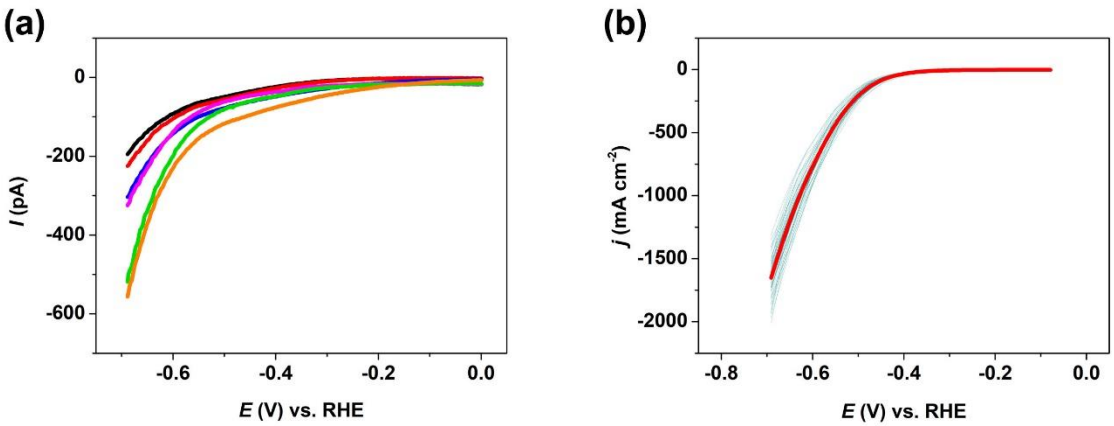

Figure 3.6 Representative linear sweep voltammograms (LSVs) obtained the **(a)** Cu and **(b)** Au support substrates during SECCM. Also shown in (b) is an average LSV (red trace) obtained from all points on exposed Au. These LSVs were obtained from a 0.1 M $HClO_4$ solution at a voltammetric scan rate (ν) of 1 V s^{-1}.

3.7 References

1. Jiao, Y.; Zheng, Y.; Jaroniec, M.; Qiao, S. Z., Design of Electrocatalysts for Oxygen-and Hydrogen-Involving Energy Conversion Reactions. *Chemical Society Reviews* **2015**, *44*, 2060-2086.

2. Gasteiger, H. A.; Marković, N. M., Just a Dream-or Future Reality? *Science* **2009**, *324*, 48-49.

3. Li, Q., *et al.*, New Approach to Fully Ordered Fct-Fept Nanoparticles for Much Enhanced Electrocatalysis in Acid. *Nano Letters* **2015**, *15*, 2468-2473.

4. Jaramillo, T. F.; Jørgensen, K. P.; Bonde, J.; Nielsen, J. H.; Horch, S.; Chorkendorff, I., Identification of Active Edge Sites for Electrochemical H_2 Evolution from MoS_2 Nanocatalysts. *Science* **2007**, *317*, 100-102.

5. Zheng, Y.; Jiao, Y.; Zhu, Y.; Li, L. H.; Han, Y.; Chen, Y.; Du, A.; Jaroniec, M.; Qiao, S. Z., Hydrogen Evolution by a Metal-Free Electrocatalyst. *Nature Communications* **2014**, *5*, 3783.

6. Yang, J.; Voiry, D.; Ahn, S. J.; Kang, D.; Kim, A. Y.; Chhowalla, M.; Shin, H. S., Two-Dimensional Hybrid Nanosheets of Tungsten Disulfide and Reduced Graphene Oxide as Catalysts for Enhanced Hydrogen Evolution. *Angewandte Chemie* **2013**, *125*, 13996-13999.

7. Deng, D.; Novoselov, K. S.; Fu, Q.; Zheng, N.; Tian, Z.; Bao, X., Catalysis with Two-Dimensional Materials and Their Heterostructures. *Nature Nanotechnology* **2016**, *11*, 218-230.

8. Solozhenko, V. L.; Lazarenko, A. G.; Petitet, J. P.; Kanaev, A. V., Bandgap Energy of Graphite-Like Hexagonal Boron Nitride. *Journal of Physics and Chemistry of Solids* **2001**, *62*, 1331-1334.

9. Uosaki, K.; Elumalai, G.; Noguchi, H.; Masuda, T.; Lyalin, A.; Nakayama, A.; Taketsugu, T., Boron Nitride Nanosheet on Gold as an Electrocatalyst for Oxygen Reduction Reaction: Theoretical Suggestion and Experimental Proof. *Journal of the American Chemical Society* **2014**, *136*, 6542-6545.

10. Koitz, R.; Nørskov, J. K.; Studt, F., A Systematic Study of Metal-Supported Boron Nitride Materials for the Oxygen Reduction Reaction. *Physical Chemistry Chemical Physics* **2015**, *17*, 12722-12727.

11. Uosaki, K.; Elumalai, G.; Dinh, H. C.; Lyalin, A.; Taketsugu, T.; Noguchi, H., Highly Efficient Electrochemical Hydrogen Evolution Reaction at Insulating Boron Nitride Nanosheet on Inert Gold Substrate. *Scientific Reports* **2016**, *6*, 32217.

12. Azevedo, S.; Kaschny, J. R.; de Castilho, C. M. C.; de Brito Mota, F., Electronic Structure of Defects in a Boron Nitride Monolayer. *The European Physical Journal B* **2009**, *67*, 507-512.

13. Zhou, J.; Wang, Q.; Sun, Q.; Jena, P., Electronic and Magnetic Properties of a Bn Sheet Decorated with Hydrogen and Fluorine. *Physical Review B* **2010**, *81*, 085442.

14. Britnell, L., et al., Electron Tunneling through Ultrathin Boron Nitride Crystalline Barriers. *Nano Letters* **2012**, *12*, 1707-1710.

15. Gao, M.; Lyalin, A.; Taketsugu, T., Oxygen Activation and Dissociation on H-Bn Supported Au Atoms. *International Journal of Quantum Chemistry* **2013**, *113*, 443-452.

16. Ebejer, N.; Güell, A.; Lai, S.; McKelvey, K.; Snowden, M.; Unwin, P., Scanning Electrochemical Cell Microscopy: A Versatile Technique for Nanoscale Electrochemistry and Functional Imaging. *Annual review of analytical chemistry (Palo Alto, Calif.)* **2013**, *6*.

17. Bentley, C. L.; Kang, M.; Unwin, P. R., Scanning Electrochemical Cell Microscopy: New Perspectives on Electrode Processes in Action. *Current Opinion in Electrochemistry* **2017**, *6*, 23-30.

18. Bentley, C. L.; Kang, M.; Unwin, P. R., Nanoscale Structure Dynamics within Electrocatalytic Materials. *Journal of the American Chemical Society* **2017**, *139*, 16813-16821.

19. Bentley, C. L.; Kang, M.; Maddar, F. M.; Li, F.; Walker, M.; Zhang, J.; Unwin, P. R., Electrochemical Maps and Movies of the Hydrogen Evolution Reaction on Natural Crystals of Molybdenite (MoS_2): Basal Vs. Edge Plane Activity. *Chemical Science* **2017**, *8*, 6583-6593.

20. Chen, C. H.; Jacobse, L.; McKelvey, K.; Lai, S. C. S.; Koper, M. T. M.; Unwin, P. R., Voltammetric Scanning Electrochemical Cell Microscopy: Dynamic Imaging of Hydrazine Electro-Oxidation on Platinum Electrodes. *Analytical Chemistry* **2015**, *87*, 5782-5789.

21. Stehle, Y.; Meyer, H. M.; Unocic, R. R.; Kidder, M.; Polizos, G.; Datskos, P. G.; Jackson, R.; Smirnov, S. N.; Vlassiouk, I. V., Synthesis of Hexagonal Boron Nitride Monolayer: Control of Nucleation and Crystal Morphology. *Chemistry of Materials* **2015**, *27*, 8041-8047.

22. Li, X.; Zhu, Y.; Cai, W.; Borysiak, M.; Han, B.; Chen, D.; Piner, R. D.; Colombo, L.; Ruoff, R. S., Transfer of Large-Area Graphene Films for High-Performance Transparent Conductive Electrodes. *Nano Letters* **2009**, *9*, 4359-4363.

23. Guo, N.; Wei, J.; Fan, L.; Jia, Y.; Liang, D.; Zhu, H.; Wang, K.; Wu, D., Controllable Growth of Triangular Hexagonal Boron Nitride Domains on Copper Foils by an Improved Low-Pressure Chemical Vapor Deposition Method. *Nanotechnology* **2012**, *23*, 415605.

24. Chang, R. J.; Wang, X.; Wang, S.; Sheng, Y.; Porter, B.; Bhaskaran, H.; Warner, J. H., Growth of Large Single-Crystalline Monolayer Hexagonal Boron Nitride by Oxide-Assisted Chemical Vapor Deposition. *Chemistry of Materials* **2017**, *29*, 6252-6260.

25. Aaronson, B. D.; Lai, S. C.; Unwin, P. R., Spatially Resolved Electrochemistry in Ionic Liquids: Surface Structure Effects on Triiodide Reduction at Platinum Electrodes. *Langmuir* **2014**, *30*, 1915-1919.

26. Chen, C. H.; Meadows, K. E.; Cuharuc, A.; Lai, S. C.; Unwin, P. R., High Resolution Mapping of Oxygen Reduction Reaction Kinetics at Polycrystalline Platinum Electrodes. *Physical Chemistry Chemical Physics* **2014**, *16*, 18545-18552.

27. Lukowski, M. A.; Daniel, A. S.; English, C. R.; Meng, F.; Forticaux, A.; Hamers, R. J.; Jin, S., Highly Active Hydrogen Evolution Catalysis from Metallic WS_2 Nanosheets. *Energy & Environmental Science* **2014**, *7*, 2608-2613.

28. Wirth, S.; Harnisch, F.; Weinmann, M.; Schröder, U., Comparative Study of IVB–VIB Transition Metal Compound Electrocatalysts for the Hydrogen Evolution Reaction. *Applied Catalysis B: Environmental* **2012**, *126*, 225-230.

29. Greeley, J.; Jaramillo, T. F.; Bonde, J.; Chorkendorff, I.; Nørskov, J. K., Computational High-Throughput Screening of Electrocatalytic Materials for Hydrogen Evolution. *Nature Materials* **2006**, *5*, 909-913.

30. Yu, Y.; Huang, S. Y.; Li, Y.; Steinmann, S. N.; Yang, W.; Cao, L., Layer-Dependent Electrocatalysis of MoS_2 for Hydrogen Evolution. *Nano Letters* **2014**, *14*, 553-558.

31. Yang, G. H.; Shi, J. J.; Wang, S.; Xiong, W. W.; Jiang, L. P.; Burda, C.; Zhu, J. J., Fabrication of a Boron Nitride-Gold Nanocluster Composite and Its Versatile Application for Immunoassays. *Chemical Communications* **2013**, *49*, 10757-10759.

32. Auwärter, W., Hexagonal Boron Nitride Monolayers on Metal Supports: Versatile Templates for Atoms, Molecules and Nanostructures. *Surface Science Reports* **2019**, *74*, 1-95.

33. Rokuta, E.; Hasegawa, Y.; Suzuki, K.; Gamou, Y.; Oshima, C.; Nagashima, A., Phonon Dispersion of an Epitaxial Monolayer Film of Hexagonal Boron Nitride on Ni (111). *Physical Review Letters* **1997**, *79*, 4609-4612.

34. Preobrajenski, A. B.; Vinogradov, A. S.; Mårtensson, N., Ni 3d-BN π Hybridization at the *h*-BN/Ni (111) Interface Observed with Core-Level Spectroscopies. *Physical Review B* **2004**, *70*, 165404.

35. Preobrajenski, A. B.; Vinogradov, A. S.; Mårtensson, N., Monolayer of H-Bn Chemisorbed on Cu (111) and Ni (111): The Role of the Transition Metal 3d States. *Surface Science* **2005**, *582*, 21-30.

36. Joshi, S., et al., Boron Nitride on Cu (111): An Electronically Corrugated Monolayer. *Nano Letters* **2012**, *12*, 5821-5828.

37. Elumalai, G.; Noguchi, H.; Uosaki, K., Electrocatalytic Activity of Various Types of H-BN for the Oxygen Reduction Reaction. *Physical Chemistry Chemical Physics* **2014**, *16*, 13755-13761.

38. Hellstern, T. R.; Kibsgaard, J.; Tsai, C.; Palm, D. W.; King, L. A.; Abild-Pedersen, F.; Jaramillo, T. F., Investigating Catalyst-Support Interactions to Improve the Hydrogen Evolution Reaction Activity of Thiomolybdate $[Mo_3S_{13}]^{2-}$ Nanoclusters. *ACS Catalysis* **2017**, *7*, 7126-7130.

Chapter 4. Nanoscale Variations in the Electrocatalytic Activity of Layered Transition Metal Dichalcogenides

Hydrogen has been recognized as one of the cleanest fuels, with zero emission to the environment when combusted, which could be an ideal next generation energy source. Electrochemical splitting is a high-efficient way to obtain high purity hydrogen from water, especially when compared with the traditional method in industry at present (methane-steam reforming). To date, transition metal dichalcogenides, such as MoS_2, and WS_2 have been extensively studied as potential hydrogen evolution reaction catalysts, as substitutes for the well-known expensive, rare metal of platinum. Although it is very promising, most of the literatures are material-synthesis oriented, which emphasis the importance of morphological control (or rational design) to expose more active sites or combine with other components (*e.g.*, reduced graphene oxide or other carbon materials) to achieve the "synergistic effects", while ignore the electrocatalytic activity of pristine transition metal dichalcogenides themselves.

This chapter contains the manuscript and supporting information from an article which has been published as a full article in *The Journal of Physical Chemistry C* (**Binglin Tao**, Patrick R. Unwin, and Cameron L. Bentley, *J. Phys. Chem. C.* **2020**, 124, 1, 789-798). In this chapter, the hydrogen evolution reaction activities of pristine MoS_2 and WS_2 (including the basal and edge plane, surface defects, and aging influence) have been studied at the nanoscale via scanning electrochemical cell microscopy. Binglin Tao was responsible for the experiment design, data processing and preparation of the manuscript. Cameron L. Bentley supervised on this project and revised the manuscript.

Nanoscale Variations in the Electrocatalytic Activity of Layered Transition Metal Dichalcogenides

Binglin Tao, Patrick R. Unwin* and Cameron L. Bentley*

Department of Chemistry, University of Warwick, Gibbet Hill Road, Coventry, UK

*** Corresponding Author**

p.r.unwin@warwick.ac.uk (P.R.U), *c.bentley.1@warwick.ac.uk (C.L.B)

4.1 Abstract

Layered transition metal dichalcogenides (TMDs), such as molybdenum disulfide (MoS_2) and tungsten disulfide (WS_2) have attracted considerable interest as alternatives to platinum in hydrogen evolution reaction (HER) electrocatalysis. It is generally accepted that the edge planes of 2H phase MS_2 (where M = Mo or W) are catalytically active, while the basal planes are said to be "catalytically inert", which has inspired the rational design/synthesis of defect-rich nanomaterials with an abundance of exposed edge sites. The intrinsic electrochemical properties of pristine MoS_2/WS_2 crystals has been largely overlooked in this materials-driven approach. Herein, nanometer-resolved measurements using scanning electrochemical cell microscopy (SECCM) reveal electrochemical activity at the basal plane, including spatial variations attributed to the localized folding of the surface (*e.g.* mechanical strain) or variations in electronic structure (*e.g.*, defect density) throughout the crystal. Such effects are particularly evident in synthetic WS_2 compared to natural crystal of MoS_2. Catalytic activity for the HER is greatly enhanced at macroscopic surface defects on both materials, measured directly where the active edge plane is exposed (*e.g.*, crevices, holes, cracks, *etc.*) with single-layer sensitivity. Aging the crystals under ambient conditions (*i.e.*, exposed to the ambient atmosphere for 30 days) substantially decreases the HER activities of MoS_2 and WS_2, attributable to the presence of adventitious adsorbates or surface oxidation, which particularly affects at the active edge plane. Overall, this work presents previously unseen electrochemical phenomena at TMD electrodes, highlighting how subtle changes in sample source, structure, and history can alter the catalytic activity drastically, and emphasizing the care that must be taken when interpreting conventional macroscopic electrochemical data.

This study further demonstrates the advantage of probe-based electrochemical mapping for establishing structure-function relationships in electromaterials science.

4.2 Introduction

Electrochemical water splitting is widely seen as the most promising method for sustainable hydrogen (H_2) generation.[1-2] Although platinum (Pt) is the most efficient electrocatalyst for the purpose, its high price and low abundance presently restricts widespread application.[3] The realization of the "hydrogen economy" will require efficient, stable and low-cost catalysts to promote the hydrogen evolution reaction (HER).[4-5] Layered transition metal dichalcogenides (TMDs) have previously found application in the fields of advanced energy conversion,[6] storage,[7] optical imaging[8] and sensing.[9] More recently, TMDs of the form MS_2 (*e.g.*, where M = Mo or W) have been verified as promising earth abundant and low-cost electrocatalysts towards the HER, which could serve as appropriate substitutes for Pt in water splitting technologies.[10] Molybdenum disulfide (MoS_2) is the most widely explored TMD in this application, where both experiment[11-12] and theory[13-14] have suggested that the edge plane (particularly the Mo-edge versus the S-edge) is electrocatalytically active towards the HER in acid media, whereas the basal plane is said to be "catalytically inert". Tungsten disulfide (WS_2) has been explored to a lesser extent, but has also been suggested to have an active edge plane (Mo-edge and S-edge are comparable) and relatively inactive basal plane.[13]

The strong promise of TMDs in HER catalysis has inspired a large body of research, where rational materials design/synthesis (*e.g.*, control of morphology, phase, crystallinity, facets, *etc.*) is combined with complementary surface characterization tools, such as atomic force microscopy (AFM), scanning electron microscopy (SEM), transmission electron microscopy (TEM), X-ray diffraction (XRD), *etc.*, attempting to reveal the electrochemical properties of MS_2 catalysts in relation to their structure/composition.[15-18] Although structure and composition are well-characterized down to the nm-scale in this approach, electrochemical measurements are almost exclusively performed on the macroscale, with (semi)identified amounts of specific features under investigation (*i.e.*, the ratio of edge to basal plane). In these "bulk" electrochemical approaches, only the "average" properties of the electrode under investigation (*e.g.*, ensembles of nanomaterials) are revealed, with no local or direct information obtained from the featured areas.[19-21] The bulk electrochemical

response can depend on a number of factors, including the synthesis conditions, properties of the electrode support, loading amounts of active materials, role of conductive additives (*e.g.*, graphene), *etc.*, complicating the assignment of the reaction mechanism,[22] particularly when only considering the Tafel slope and exchange current.[23]

Despite extensive research from the rational materials synthesis and characterization perspective, a general literature search reveals a comparative lack of basic understanding on the intrinsic electrochemical properties of TMDs in their bulk form.[24] One particularly powerful strategy to for resolving structure-function relationships (especially for pristine materials) is using scanning electrochemical probe microscopy (SEPM).[19-20, 25-26] In this family of techniques, an electrode [*e.g.*, ultra-microelectrode (UME),[27] nanopipette,[28-31] functionalized AFM cantilever,[32-34] *etc.*] is used as a physical probe to map electrochemical fluxes with high spatial resolution. In this way, characteristic surface sites (from μm scale[35-36] to nm scale[37]) can be targeted, and, when taken with complementary structural information from co-located microscopy/spectroscopy in a *correlative electrochemical multi-microscopy approach*, allows nanoscale structure-function relationships to be assigned.[19-20] For example, we have recently employed scanning electrochemical cell microscopy (SECCM), a meniscus (droplet) cell-based SEPM technique, to show that the basal plane of bulk MoS_2 (natural crystal, molybdenite) is in fact supportive for the HER,[37-39] contrary to many previous reports that observe the kinetics to be ultra-slow to negligible at the macroscale.[24] The SECCM approach has also been recently been extended to investigate the electrochemical activity of single nanoparticles, including active Li-ion battery cathode materials (*i.e.*, $LiMn_2O_4$)[20] and synthetic oxygen evolution reaction (OER) catalysts (*i.e.*, metal organic frameworks, MOF-derived nanocomposites).[40]

Herein, we expand our study of the electrocatalytic activities of commercially available, pristine 2H phase MS_2 crystals (M = Mo or W), using SECCM to perform nm-resolved linear-sweep voltammetry measurements. Benefiting from this local and direct method, the basal planes of a large number of freshly exfoliated MoS_2 and WS_2 crystals were shown possess spatially dependent activity that varies from surface-to-surface. In addition, the presence of surface defects (*i.e.*, crevices, holes, cracks, *etc.*, where the active edge plane is exposed), as

well as the surface conditioning/age (*i.e.*, time after cleavage) were both shown to play important roles in modulating the HER activity of MS_2 crystals.

4.3 Experimental Section

4.3.1 Chemical Reagents and Electrode Preparation

Perchloric acid ($HClO_4$, Sigma-Aldrich, 70 %) and potassium chloride (KCl, Sigma-Aldrich) were used as received from the manufacturer. Deionized water (resistivity ≈18.2 MΩ·cm at 25°C) was produced by a Purite Integra HP (U. K.) system. A solution of 0.1 M $HClO_4$ was prepared and used in the nanopipette probe for all SECCM experiments. The natural crystal molybdenum disulfide (MoS_2) was purchased from Manchester Nanomaterials Ltd (U. K.) and the synthetic crystal of tungsten disulfide (WS_2) was obtained from Sigma-Aldrich. Prior to use as electrode materials, bulk crystals of MS_2 were fixed on a glass substrate using carbon tape and then mechanically cleaved through the "scotch-tape method".[41] In order to ensure electrical connection, the freshly cleaved MS_2 flakes were electrically connected through top contact with adhesive copper tape. For the fresh surfaces, all the experiment were completed right after cleavage in order to avoid deterioration from exposure to the ambient atmosphere.

Silver-silver chloride (Ag/AgCl), comprising AgCl coated Ag wire, which was prepared by anodizing 0.125 mm diameter polished silver wire (Goodfellow, U.K., 99.99 %) in a saturated KCl solution at +5 V (versus a Pt counter electrode), was used as quasi-reference counter electrode (QRCE). Ag/AgCl has previously been shown to possess a very stable reference potential in 0.1 M $HClO_4$, when used in confined electrochemical cells such as nanopipettes.[42] The QRCE potential was calibrated against a commercial saturated calomel electrode (SCE) in 0.1 M $HClO_4$ solution before and after each experiment, and then converted to potential vs. the reversible hydrogen electrode (RHE). In 0.1 M $HClO_4$, E (RHE) = E (SCE) + 0.241 + 0.059 V. The Ag/AgCl QRCEs were found to consistently possess a potential of 0.5 ± 0.05 V vs. RHE.

The nanopipettes were pulled from commercial capillaries using a CO_2 laser puller (P-2000, Sutter Instruments, U. S. A.). Two different sizes of single channel probes have been used in the work featured in the main text. Specifically, borosilicate glass capillaries (GC120F-10, Harvard Apparatus, U. S. A.) were pulled using the following two step program: Line 1

(heat 350, filament 3, velocity 30 and delay 220), Line 2 (heat 350, filament 3, velocity 40, delay 180 and pull 120). This program consistently pulled nanopipettes with a diameter of 150 ± 10 nm (Supporting Information, **Figure 4.7a**), measured using scanning transmission electron microscopy (STEM) on a Zeiss Gemini 500 system, which was operated at an accelerating voltage of 20 kV. Assuming the probed area in SECCM on MS_2 is commensurate with dimensions of the probe tip,[37] active electrode areas of $\pi \cdot (0.07)^2$ = 0.015 μm^2 and $\pi \cdot (0.08)^2$ = 0.020 μm^2 are calculated from probes with diameters of 140 and 160 nm, respectively. Therefore, given that each SECCM scan is performed with a fresh probe, the active electrode area may vary by up to ≈30 % from scan-to-scan, which is relatively insignificant compared to the variation observed due to intrinsic differences in HER kinetics (*vide supra*). Quartz capillaries (QTF120-90-100, Friedrich & Dimmock Inc., U.S.A.) were pulled using the following two step program: Line 1 (heat 750, filament 4, velocity 30 delay 150 and pull 80), Line 2 (heat 650, filament 3, velocity 40, delay 135 and pull 120). This program consistently pulled nanopipettes with a diameter of *ca.* 30 nm (Supporting Information, **Figure 4.7b**), as previously reported.[29, 37-38]

4.3.2 Instrumentation

SECCM was carried out on a previously reported custom SEPM platform,[29, 37] located in an aluminum Faraday cage, which was installed on an optical table (RS2000, Newport, U. S. A.) with automatic leveling isolators (Newport, S-2000A-423.5) to minimize noise and vibration. Probe movement normal to the substrate was controlled using a piezoelectric positioning stage with a travel range of 38 μm (P-753.3CD, Physik Instrumente), while lateral movement of the substrate for XY positioning was achieved using a two-axis piezoelectric positioning stage with a travel range of 100 μm (P-622.2CD, Physik Instrumente). The QRCE potential was controlled using a home-built bipotentiostat and the substrate (working electrode) current was measured using a home-built electrometer with 8th order brick-wall filter unit (low pass, with time constant = 2 ms). Instrumental control and data collection was achieved using a custom-written LabVIEW 2016 program (WEC-SPM, www.warwick.ac.uk/electrochemistry) through an FPGA card (PCIe-7852R, National Instruments). During approach, surface current was used as feedback to detect when the meniscus at the end of the nanopipette had made contact with the working electrode surface (MoS_2 or WS_2). Herein, the threshold current was

set at 1.25 pA, which was slightly higher than the background noise level (*ca.* ± 0.8 pA). It should be noted that the nanopipette itself did not make physical contact with the substrate surface. Data processing and analysis was carried out using the SPIP v. 6.0.14, Matlab R2015b and OriginPro 2016 software packages.

4.3.3 Simultaneous Topography and Electrochemical Mapping

To simultaneously image topography and electrochemical activity, the nanopipette was approached towards to the surface of interest at a series of predefined positions. Upon each landing, an LSV measurement was carried out, following which the nanopipette was retracted 3 µm from the surface. The nanopipette probe was then moved to next predefined pixel, which was located 50 or 200 nm from the previous point, set by the predefined 'hopping distance'. At each pixel, the vertical extension of the nanopipette (z-coordinate) and electrochemical signals (*E* and *i*) were recorded synchronously, building up topographical and voltammetric 'activity' maps, respectively, as previously reported.[37-38] The LSV curve on the basal plane was obtained by averaging 30 random pixels for each scan, while the LSV curves on the edge plane was obtained by averaging all of the 'active' pixels.

4.3.4 Estimating the Wetted Meniscus Area on Freshly Cleaved and Aged MS_2

In our previous study, it was shown that the (macroscopic) water contact angle on MoS_2 changes drastically with surface aging on the weeks-to-months' timescale.[37] Thus, in order to check whether the meniscus cell wets the MS_2 surfaces differently with surface aging, a chronoamperometric (current time curve, *I-t*) scan-hopping experiment was performed at -1.25V *vs.* Ag/AgCl for 0.1s on both the freshly cleaved (less than 3 hours) and aged (in air for 30 days) surfaces of WS_2. To enable imaging of the droplet footprints, post-scan with scanning electron microscopy (SEM), larger SECCM probes (diameter of *ca.* 2 µm, as shown in Supporting Information, **Figure 4.8a**) were employed. Borosilicate glass capillaries (GC120F-10, Harvard Apparatus, U. S. A.) were pulled using the following a one step program: Line 1 (heat 350, filament 4, velocity 40 and delay 200) to make these probes. After the experiment, the footprints of both the freshly cleaved and aged surfaces were measured using (SEM) on a Zeiss Gemini 500 system, which was operated at an accelerating voltage of 0.8 kV. As depicted in **Figure 4.8** (see Supporting Information), the average diameters of the footprints on the

freshly cleaved and aged surfaces were 2.25 ± 0.02 μm and 2.23 ± 0.04 μm (*i.e.*, commensurate with the probe dimensions), which corresponds to the active electrode areas of $\pi \cdot (1.13 \pm 0.01)^2 = 4.01 \pm 0.07$ μm^2 and $\pi \cdot (1.12 \pm 0.02)^2 = 3.94 \pm 0.14$ μm^2, respectively. Interestingly, while the macroscopic water contact angle changes significantly on this timescale,[37] the area wetted by the SECCM meniscus cell during scanning does not, suggesting that the tip and/or electrified nature of the interface are important factors. In any case, the variation in activity between the fresh and aged surfaces cannot be attributed to differences in surface wetting, which decreased by less than 3% after aging for 1 month.

4.4 Results and Discussion

4.4.1 Electrochemical Mapping of HER Activity on MS_2 with SECCM

The instrumentation and working principles of the SECCM setup used herein are summarized in **Figure 4.1a** (labeled schematic is shown in the Supporting Information, **Figure 4.9**).[43] In brief, a single-channeled nanopipette filled with 0.1 M $HClO_4$ and equipped with an Ag/AgCl quasi-reference counter electrode (QRCE) was approached to the substrate surface to make meniscus contact at a series of predefined locations.[44] Upon each landing, local electrochemistry (*i.e.*, a linear sweep voltammogram, LSV) was performed within the confined area defined by the meniscus cell (created between the nanopipette tip and substrate) by applying potential directly at the QRCE. **Figure 4.1b** and **c** depict optical micrographs of freshly cleaved MoS_2 and WS_2 surfaces, which are predominantly basal plane, interrupted by macroscopic step features, where the edge plane is exposed, as explored below.

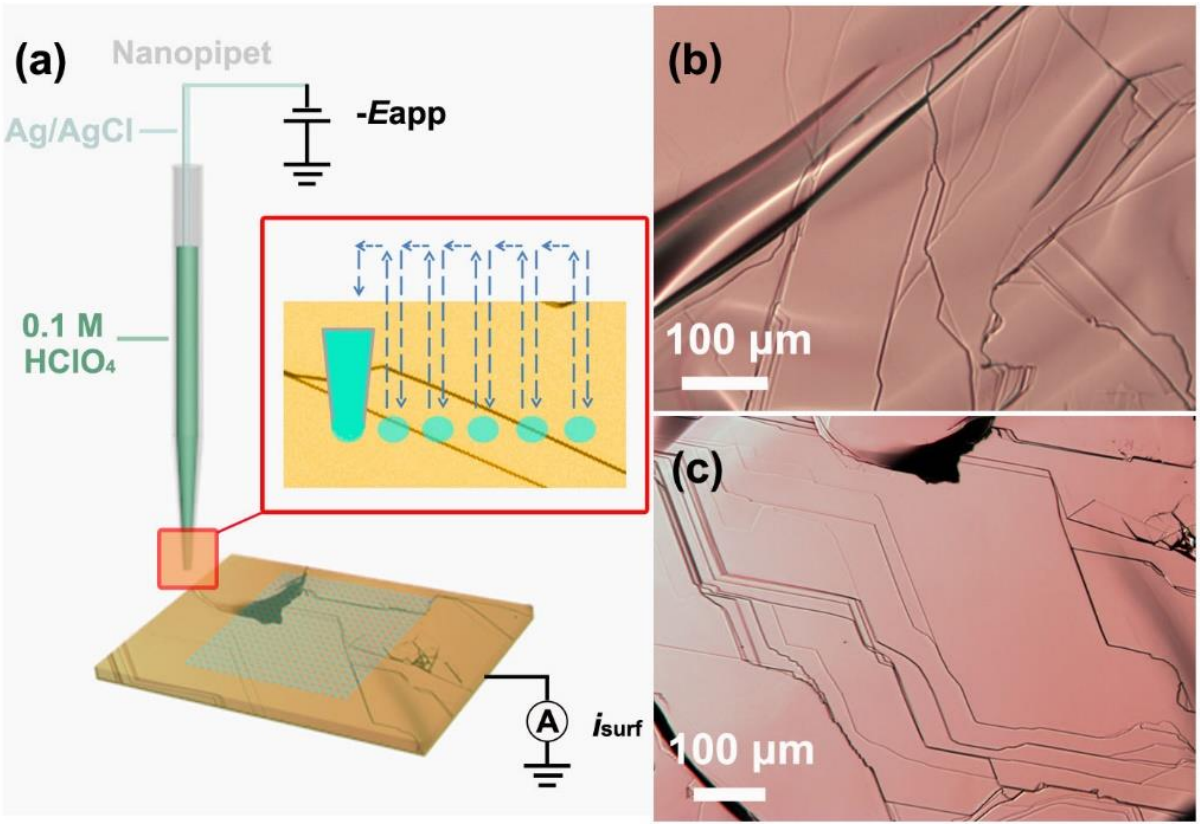

Figure 4.1 (a) Schematic showing the scanning electrochemical cell microscopy (SECCM) setup used to perform nm-resolved catalytic activity measurements on bulk MoS_2 and WS_2 crystals. During operation, a potential, $-E_{app}$, is applied on the Ag/AgCl quasi-reference counter electrode (QRCE) located in the nanopipette probe and the electrochemical surface current, i_{surf}, is measured at the substrate (working electrode). Inset shows the movement of the probe along the sample surface, where the arrows indicate the direction of movement. **(b)** and **(c)** Optical micrograph of the surface of bulk MoS_2 and WS_2, respectively, fresh after mechanical exfoliation.

HER activity at freshly cleaved MS_2 (M = Mo or W) was first investigated using a single-barreled probe of diameter *ca.* 150 nm (as shown in Supporting Information, **Figure 4.7a**) and a hopping distance of 200 nm to ensure each local LSV was independent of the last (*i.e.*, no overlap between the probed areas). Note that this tip size is in-between the previously reported 500 nm[37] and 30 nm[38-39] probes, which allows us to achieve superior spatial-resolution to the former, and probe larger surface features (*e.g.*, step defects) than the latter (*vide infra*). A spatially-resolved equipotential image of MoS_2 taken at -0.704 V vs. the reversible hydrogen electrode (RHE) is shown in **Figure 4.2a** (spatially-resolved LSV-SECCM

movie of the full potential range is shown in the Supporting Information, Movie S1). The two uniformly active areas of basal plane (blue areas in **Figure 4.2a**) are separated by a line of high activity (*i.e.*, yellow line traversing from top left to bottom right in **Figure 4.2a**), which, upon comparison to the corresponding topographical map in **Figure 4.2b** (obtained synchronously, as previously reported[19, 39]), is revealed to be a macroscopic step feature, *ca.* 70 nm in height and 600 nm (*i.e.*, 3 pixels) in width. The coincidence between the surface features and HER activity, derived directly from the line-scan profiles (indicated by the red dashed lines in Supporting Information, **Figure 4.10a** and **4.10b**) of topography and i_{surf} in **Figure 4.10c**, demonstrates that the active edge plane is exposed at this macroscopic defect, giving rise to the relatively high current densities (*vide infra*), which is also in agreement with our previous work.[37] It is worth noting that the gradient transition of surface height and current across this step feature is better described as a "gentle slope" rather than a "sheer cliff" on the scale of the nanopipette probe, which explains the wide distribution of edge plane currents shown in **Figure 4.10d** (*i.e.*, the meniscus cell, 150 nm diameter, encapsulates different amounts of edge plane as it traverses this feature, with minimal spreading[45]). These images directly and unambiguously demonstrate that the basal plane possesses relatively sluggish HER kinetics compared to the edge plane, with average currents of *ca.* 2.83 pA and 28.5 pA (E_{app} = -0.704 V vs. RHE) measured for the former and latter, respectively. This is also evident from the pixel-averaged LSVs curves obtained at the basal surface and edge feature, as shown in **Figure 4.2c**.

It is worth noting that given the small size of the probed area (typically commensurate with the dimensions of the nanopipette tip, *ca.* = $\pi \cdot 0.075^2$ μm^2 = 0.018 μm^2, discussed in the Experimental Section), 2.83 pA (*i.e.*, HER on the basal plane) corresponds to a current density of *ca.* 15 mA/cm^2. This has two important implications. The first being that the HER kinetics herein appear to be much more facile compared to what has been reported on bulk MoS_2,[24] both at the basal and edge planes. This is because the small currents measured in SECCM makes this method relatively immune to the ohmic (*iR*) drop that is expected to distort macroscopic electrochemical measurements on this semiconductive material, as previously discussed.[37] The second is that the range of current densities normally considered during bulk measurements (*i.e.*, 0.01 to 10 mA/cm^2) are not readily accessible (0.01 mA/cm^2 corresponds to ≈ 2 fA), and thus no attempt has been made herein to perform spatially-resolved Tafel analysis, as previously reported with larger SECCM probes.[37, 46]

Similarly, a spatially resolved equipotential image of WS_2 taken at -0.704 V vs. RHE is shown in **Figure 4.2d** (spatially-resolved LSV-SECCM movie of the full potential range is shown in the Supporting Information, Movie S2). Again, the activity of the basal plane is relatively uniform (blue areas in **Figure 4.2d**), with two distinct surface defects labeled (i) and (ii) traversing the scan area from bottom left to top right. Step (ii) gives rise to a larger current than for step (i), which, upon comparison with the corresponding topographical map in **Figure 4.2e**, correlates with the relative height of the features (*i.e.*, the number of exposed edge plane layers), in agreement with previous SECCM studies on MoS_2.[37-38] Again, there is coincidence between the topographical features and elevated HER currents, as shown in the line-scan profiles (indicated by the red dashed lines in Supporting Information, **Figure 4.11a** and 4.11b) of topography and i_{surf} in **Figure 4.11c**. Average LSVs extracted from pixels located on the basal plane, defect (i) and defect (ii) are shown in **Figure 4.2f** (also shown in **Figure 4.11d**), with HER catalytic current increasing in the order of basal plane < defect (i) < defect (ii), reflecting the electrochemical map in **Figure 4.2d**. It is worth noting that defect (i) is hardly detectable from the topography with a probe of this size (**Figure 4.2e**), while the SECCM technique possesses the capability to discern the electrochemical activity of these edge sites, which is comprised of only a few layers of WS_2.

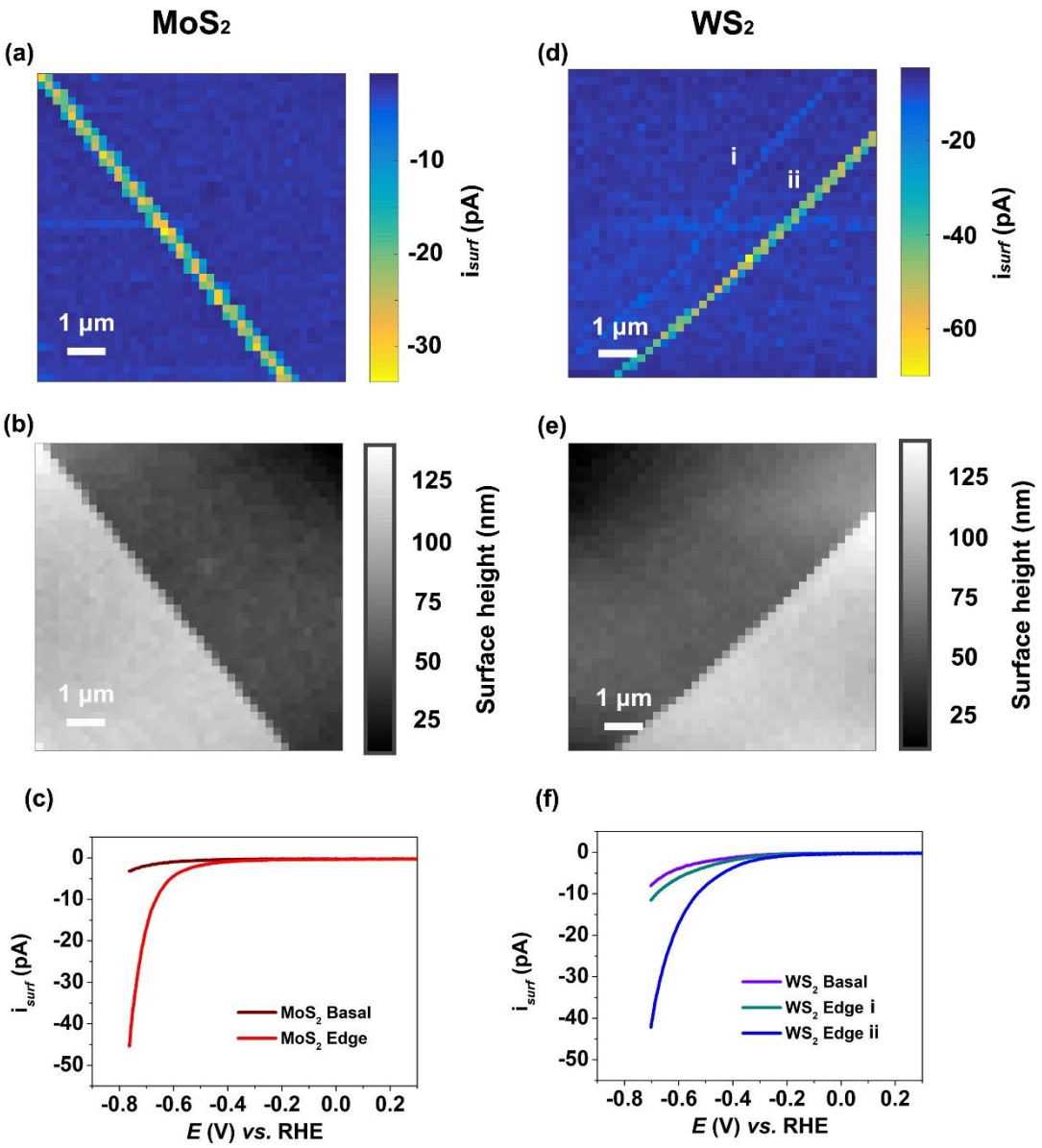

Figure 4.2 Spatially-resolved **(a, d)** electrochemical activity (-0.704 V vs. RHE) and **(b, e)** topographical maps (1600 pixels over an 8×8 µm scan area) obtained on freshly cleaved samples with a voltammetric hopping mode protocol. **(c, f)** Average linear-sweep voltammograms (scan rate, υ = 1 V/s) extracted from the basal surface and edge planes, corresponding to the low-activity (small current magnitude) and high-activity (large current magnitude) traces, respectively. **(a-c)** and **(d-f)** were obtained from MoS_2 and WS_2 crystals, respectively. These experiments were carried out with a nanopipette of diameter ≈150 nm, containing a solution of 0.1 M $HClO_4$, and a hopping distance of 200 nm. Note that there is no interpolation of any of the SECCM data (neither topography nor electrochemical activity). The

associated spatially-resolved LSV-SECCM movies obtained on **(a)** MoS_2 and **(d)** WS_2 are shown in the Supporting Information, Movies S1 and S2, respectively.

4.4.2 Spatial Variations in Local HER Activity on the Basal Plane of MS_2

The activity of the MS_2 basal planes in **Figure 4.2a** and d appear to be relatively homogeneous, implying that the crystals are pristine (*e.g.*, free from impurities or macroscopic structural defects), or at least possess a uniform point defect (*i.e.*, sulfur vacancy) density on this length scale. Although this was observed with most scanned areas of the MS_2 crystals (*vide infra*), a small number were found to exhibit non-uniform HER activity on the µm length scale, as illustrated in **Figure 4.3a** (spatially-resolved LSV-SECCM movie of the full potential range is shown in the Supporting Information, Movie S3). On this area of the crystal, the basal surface can be roughly divided into regions (i) and (ii) (delineated by dashed red lines in **Figure 4.3a**), with the former exhibiting smaller currents (lower activity) than the latter. Importantly, there is no enhancement in the HER activity on the border separating regions (i) and (ii), indicating that there is no step between them.

Figure 4.3b depicts the corresponding topographical map of the scanned area, where region (ii) (marked in **Figure 4.3a**) is seen to be slightly elevated (*ca.* 3 nm) with respect to region (i), suggesting the existence of a ridge-like or folded structure (again, the lack of HER activity enhancement at the border in **Figure 4.3a** suggests no exposed edge plane, ruling out the presence of a step edge). **Figure 4.3c** compares the pixel-averaged LSVs obtained on the basal planes and step feature of MoS_2 (**Figure 4.3a**). Clearly, regions (i) and (ii) exhibit different HER kinetics, with average currents of *ca.* 4.9 and 8.1 pA (E_{app} = -0.766 V vs. RHE), respectively, which while lower than the major step feature in this image (*ca.* 44 pA), demonstrates the significant spatial variation in activity that can be found on the structurally-well defined (*i.e.*, nominally single-crystalline) MS_2 basal surface. As expected, an overlapped bimodal distribution was observed in the surface current distribution histogram (as shown in Supporting Information, **Figure 4.12a**), attributable to the two distinct regions of basal plane activity in **Figure 4.3a**.

Different regions with variable activities were also observed in a small number of WS_2 samples, as shown in the current map of **Figure 4.3d**, also taken at potential of -0.766 V vs.

RHE (spatially-resolved LSV-SECCM movie of the full potential range is shown in the Supporting Information, Movie S4). In this case, the HER activity of region (ii) is marginally higher than that of region (i), while the topography map in **Figure 4.3e** shows that there are no significant topographical variations between the distinct regions. This is also reflected in the averaged LSVs shown in **Figure 4.3f**, where the magnitude of the catalytic currents measured in region (ii) are slightly higher than in region (i) (4.0 *vs.* 3.0 pA at E_{app} = -0.766 V vs. RHE). Again, an overlapped bimodal distribution is observed in the surface current distribution histogram (**Figure 4.12b**). The unique patterns of reactivity observed in **Figure 4.3a** and **d** might arise from spatially-dependent physical deformation of the basal surface of MoS_2 and WS_2 during the mechanical exfoliation (cleavage) process, which could alter the local electronic structure of the basal plane, *e.g.*, by inducing surface strain, which is known to modulate the HER activity of 2H MoS_2, or delamination of the top-most MS_2 layers (as previously proposed for graphitic materials).[47] Alternatively, physical deformation may affect the local conductivity of the basal plane (*e.g.*, through folding), leading to apparently layer-dependent HER kinetics.[48]

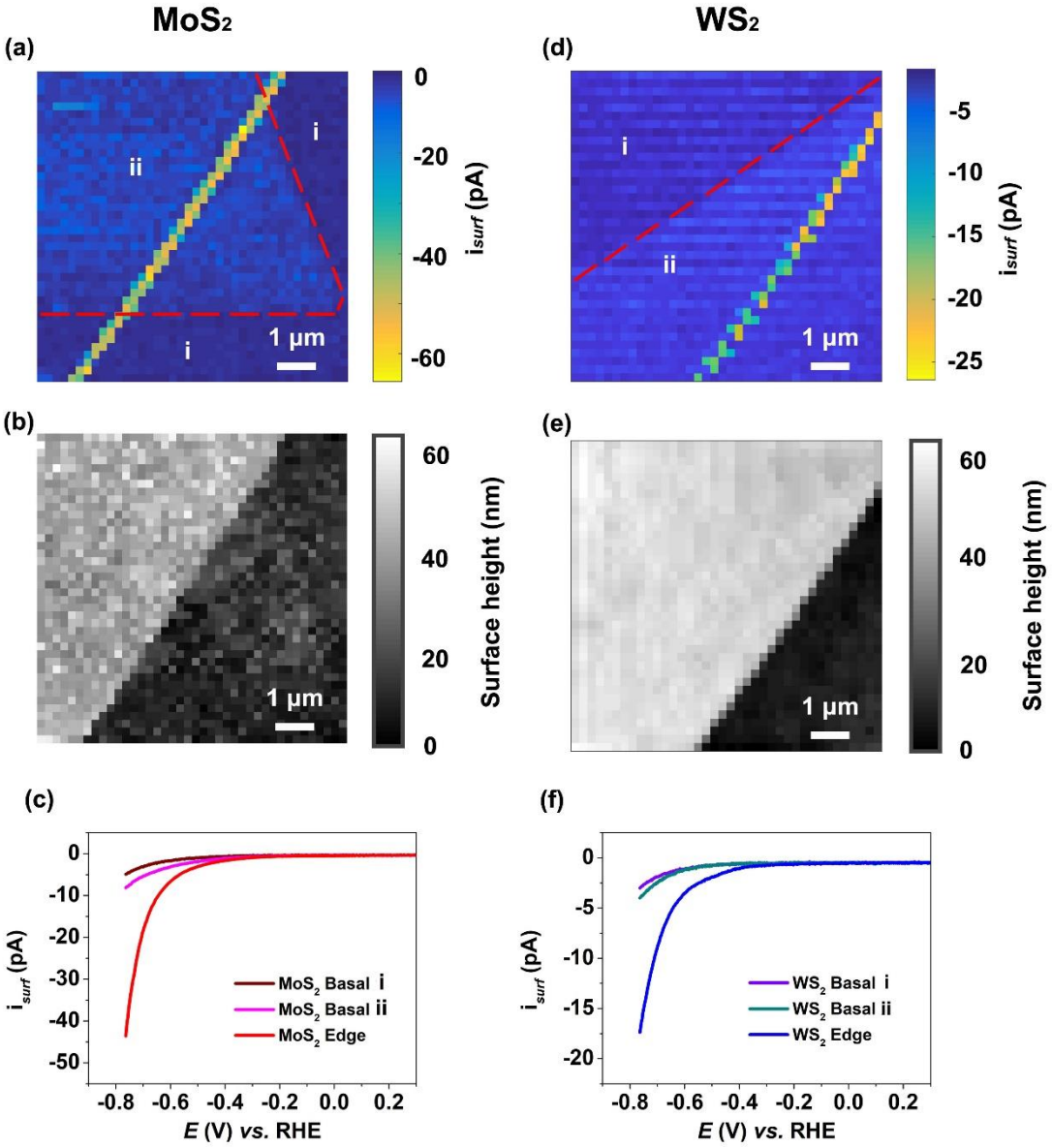

Figure 4.3 Spatially-resolved **(a, d)** electrochemical activity (-0.766 V vs. RHE) and **(b, e)** topographical maps (1600 pixels over an 8×8 μm scan area) obtained on freshly cleaved samples with a voltammetric hopping mode protocol. **(c, f)** Average linear-sweep voltammograms (υ = 1 V/s) extracted from two distinct areas of the basal plane [labeled i and ii in **(a)** and **(d)**] and edge planes, corresponding to the low-activity (small current magnitude) and high-activity (large current magnitude) traces, respectively. **(a-c)** and **(d-f)** were obtained from MoS_2 and WS_2 crystals, respectively. These experiments were carried out with a nanopipette of diameter ≈150 nm, containing a solution of 0.1 M $HClO_4$, and a hopping distance of 200 nm. Note that the red dashed lines in (**a, d**) were added to guide the eye in

delineating the two distinct regions of different activity on the basal surface. Note that there is no interpolation of any of the SECCM data (neither topography nor electrochemical activity). The associated spatially-resolved LSV-SECCM movies obtained on **(a)** MoS_2 and **(d)** WS_2 are shown in the Supporting Information, Movies S3 and S4, respectively.

The two areas mapped on each of the MoS_2 (**Figure 4.2a** and **4.3a**) and WS_2 (**Figure 4.2d** and **4.3d**) crystals demonstrate that these well-defined, nominally single-crystalline surfaces exhibit heterogeneity, evidenced by spatially-dependent HER activities at the nanoscale. In order to delve into this further, ten freshly cleaved areas of each of MoS_2 and WS_2 (*i.e.*, 10 on each material, giving 20 scans total) were scanned using SECCM (the corresponding electrochemical activity maps are shown in Supporting Information, **Figure 4.13** and **4.14**, respectively); histograms showing the distribution in i_{surf} (*i.e.*, catalytic HER current) at a potential of –0.704 V vs. RHE on the basal plane are shown in **Figure 4.4**. It should be noted that each LSV-SECCM scan is made up of 1600 pixels, meaning that each histogram comprises >10000 independent *i*–*E* measurements, demonstrating the high throughput capability of this technique. On MoS_2 (**Figure 4.4a**), the $\log_{10}(i_{surf})$ values are normally distributed, with mean values falling in the range of 1.6 to 5.0 pA at an applied potential of -0.704 V vs. RHE. Note that this variation in surface current is much larger than the ≈30 % expected from variations in wetted area arising from differences in the probe dimensions between different scans (*i.e.*, d_{probe} = 140 to 160 nm, therefore A_{probe} = 0.015 to 0.02 μm^2, further details in the Experimental Section). Thus, the variation is attributed to spatially-dependent variations in the HER kinetics, rather than variations in electrode area (*i.e.*, meniscus size or wetted area) scan-to-scan. The $\log_{10}(i_{surf})$ values are also normally distributed on WS_2 (**Figure 4.4b**), with mean values falling in the range of 2.0 to 15.8 pA at an applied potential of -0.704 V vs. RHE. Comparing **Figure 4.4a** and **b**, it is clear that: (1) there is significantly more variation in HER activity across the basal surface of the synthetic WS_2 crystal compared to the natural MoS_2 crystal and (2) the basal plane of this WS_2 crystal is, on average, more active for the HER than that of this MoS_2 crystal.

Density functional theory (DFT) calculations predict that the pristine MoS_2 basal plane should possess higher HER catalytic activity than that of WS_2, owing to the former having a hydrogen adsorption free energy (ΔG_{H^*}) that is closer to thermoneutral (*i.e.*, 1.92 and 2.23 eV

for MoS_2 and WS_2, respectively).[13, 49] Our results indicate the contrary, and an explanation would be that the basal plane of the synthetic WS_2 crystal used herein is relatively defective compared to that of natural MoS_2. While SECCM has effectively isolated the response of basal plane (*i.e.*, blue areas in **Figure 4.2d** and **4.3d**) from that of the macroscopic (multistep) defect where the edge plane is exposed (*i.e.*, yellow lines in **Figure 4.2d** and **4.3d**), the probed areas are still expected to contain point defects (*e.g.*, sulfur vacancies), which are well-known active sites for the HER.[27, 47, 50-51] It has been reported that synthetic crystals of TMDs can be defect rich (*e.g.*, nanoscale holes and impurities), owing to the relatively fast preparation process.[52-53] It has also been shown that the electronic structure (*i.e.*, p-/n-type character) and surface defect density of TMDs, natural or synthetic, can vary significantly from crystal-to-crystal, or even across the same exfoliated basal surface.[54] These two points would be reasonable explanations for the higher activity of the WS_2 basal surface compared to that of MoS_2 (*i.e.*, compare **Figure 4.4a** and **b**) herein, as well as the dispersion in activity across the same exfoliated basal surface (*i.e.*, compare the individual areas within **Figure 4.3a** or **d**).

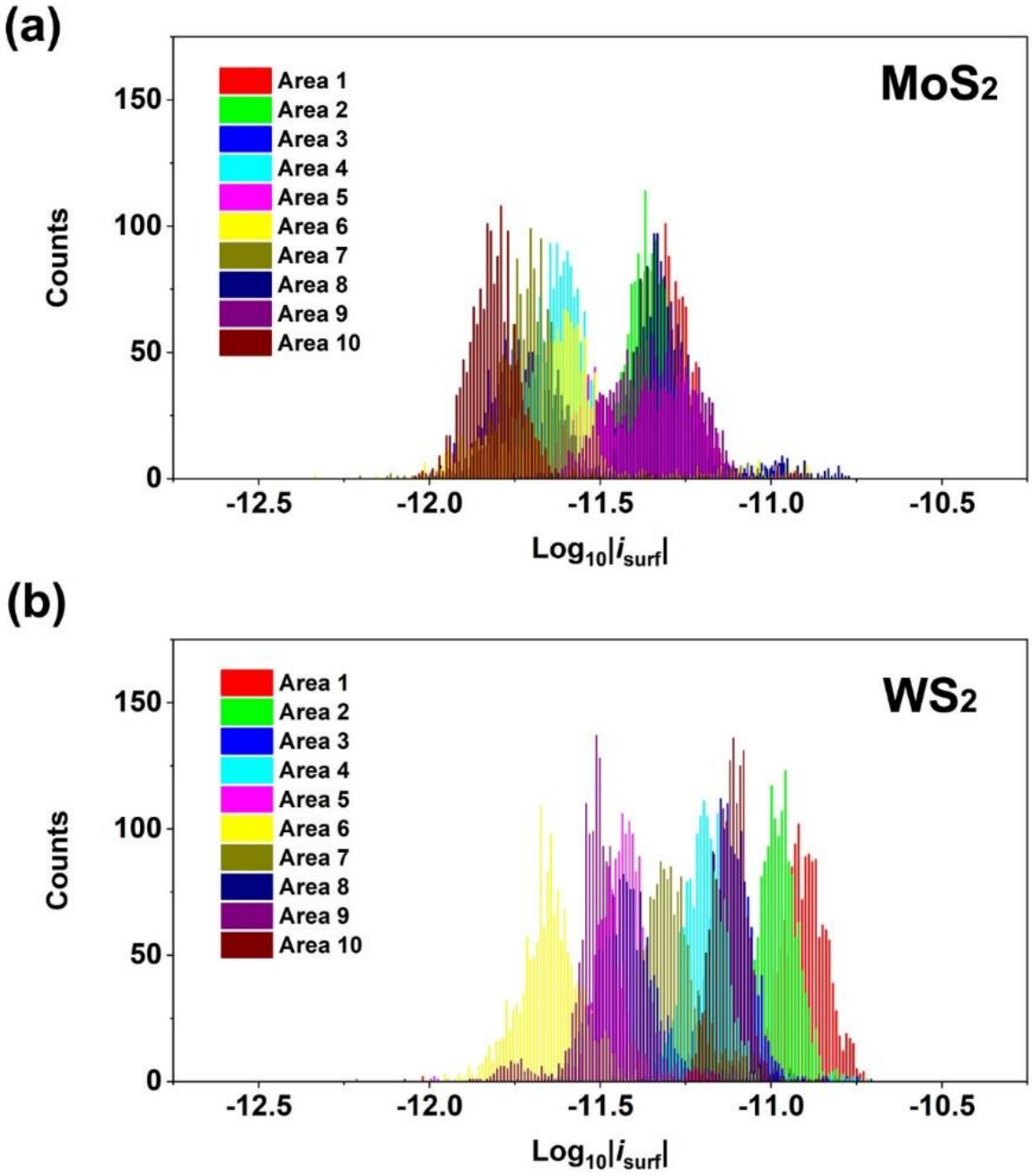

Figure 4.4 Histograms showing the distribution in the logarithm of surface currents (i_{surf}), which were extracted from the HER on each of 10 freshly cleaved **(a)** MoS_2 and **(b)** WS_2 samples at a potential of - 0.704 V vs. RHE, respectively (all the bin sizes were set as 0.01). Note that only pixels on the basal plane were considered in these scans. All the experiments were performed in 0.1 M $HClO_4$ solution with scan rate of 1 V s^{-1}, using single-barreled probes with diameter of *ca.* 150 nm and a hopping distance of 200 nm.

4.4.3 Probing the HER Activity of Nanoscale Surface Defects

High spatial-resolution measurements were performed on freshly cleaved MS_2 surfaces using a *ca.* 30 nm diameter nanopipette (shown in Supporting Information, **Figure 4.7b**) in order to probe the activity of surface defects more directly. As shown in **Figure 4.5a**, at an applied potential of -0.763 V vs. RHE (spatially-resolved LSV-SECCM movie of the full potential range is shown in the Supporting Information, Movie S5), the MoS_2 basal surface appears to possess relatively uniform activity, with one active defect traversing the scan area from bottom-left to top-right. When driven to more negative potentials (-1.053 V vs. RHE, **Figure 4.5b**), a series of six small steps become apparent on the basal surface, all running parallel to the macroscopic defect (bottom-left to top-right). These small step features are hardly detectable in the corresponding topography map, as shown in **Figure 4.5c**. Given that we have previously shown that topographical features as small *ca.* 2 nm can be resolved using SECCM with probes of this size,[38] these step features are likely to be comprised of few layer MoS_2 (≤4, theoretical thickness of monolayer MoS_2 = 0.68 nm).[55-56] Comparing the average LSVs extracted from each unique surface feature (**Figure 4.15**), steps (i), (ii), (iii), (v) and (vi) possess roughly equal activities, while step (vii) is approximately twice as active, indicating that the former are approximately half the size of the latter.

In addition to step edge features (**Figure 4.2d**, **4.3d** and **4.5d**), the synthetic WS_2 surface was also found to frequently possess randomly distributed local activity "hotspots" at strong driving potentials, as shown in **Figure 4.5d – e**. Similar to MoS_2, at an applied potential of -0.763 V vs. RHE (**Figure 4.5d**), the WS_2 basal surface appears to possess relatively uniform activity. At an applied potential of -1.053 V vs. RHE (**Figure 4.5e**), however, specific pixels on the basal surface "light up" (labeled with red circles in Supporting Information, **Figure 4.16a**), indicating locally enhanced HER activity (spatially-resolved LSV-SECCM movie of the full potential range is shown in the Supporting Information, Movie S6). This is also clear in the surface averaged LSVs taken from these features, relative to the pristine basal surface (as shown in Supporting Information, **Figure 4.16b**). Again, these features, which we assign to point (sub 30 nm) defects, are not evident in the topographical map (**Figure 4.5f**). As alluded to above, this kind of activity enhancement is likely attributable to the presence of surface

defect sites (*e.g.*, holes and impurities) on the synthetic WS_2 crystal basal surface, arising from the relatively fast synthesis process.[52-53]

Hitherto, macroscale electrochemical measurements have predominantly been used to study the HER activity of 2D TMDs (*e.g.*, supported nanomaterials), which provide activity averaged over a wide range of interacting surface "active" sites (*e.g.*, basal surface, edge plane, support, auxiliary components *etc.*). The results presented here demonstrate that such an approach has serious limitations, as there are many reasons why the surface activity cannot be considered as uniform, even for these structurally well-defined, nominally single crystalline MS_2 crystals. For instance, exposed edge plane (step edges, **Figure 4.2 - 4**), ridge-like or folded structures (**Figure 4.3**), holes, and impurities (**Figure 4.5**) all give rise to unique patterns of surface reactivity, which would be overlooked in macroscopic measurements, emphasizing the importance of interrogating electrochemical activity at a commensurate scale to structural/compositional characterization (*i.e.*, the nanoscale).

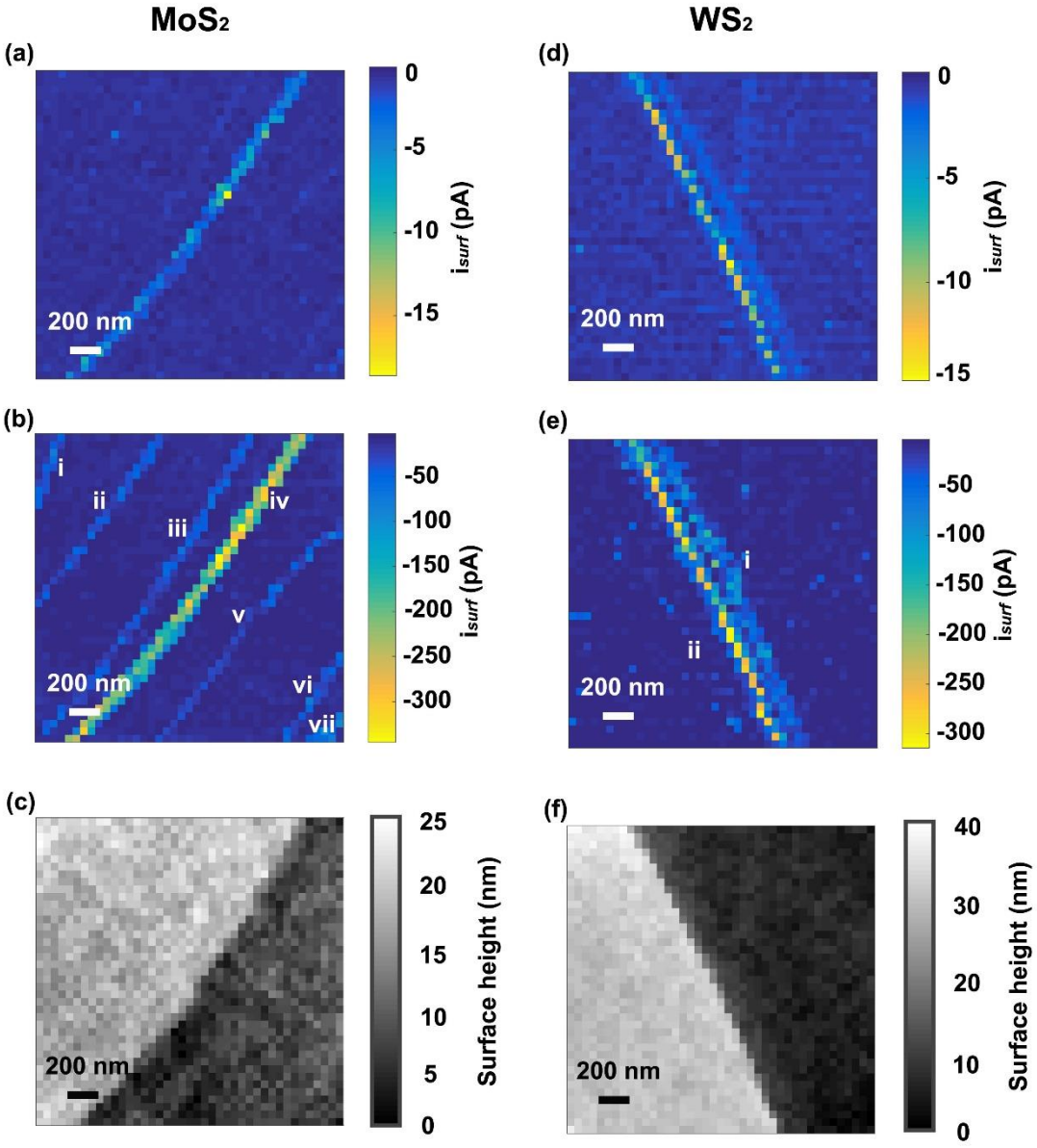

Figure 4.5 Spatially-resolved electrochemical activity maps **(a, d)** at -0.763 V vs. RHE and **(b, e)** at -1.053 V vs. RHE, and **(c, f)** topographical maps (1600 pixels over a 2×2 µm scan area) obtained on freshly cleaved samples with voltammetric hopping mode protocol. (a-c) and (d-f) were obtained from MoS_2 and WS_2 crystals, respectively. These experiments were carried out with a nanopipette of diameter ≈30 nm, containing a solution of 0.1 M $HClO_4$, and a hopping distance of 50 nm. Note that there is no interpolation of any of the SECCM data (neither topography nor electrochemical activity). The associated spatially-resolved LSV-SECCM movies obtained on **(a-b)** MoS_2 and **(d-e)** WS_2 are shown in the Supporting Information, Movies S5 and S6, respectively.

4.4.4 Deterioration in HER Activity with Surface Aging

The final aspect of MS_2 surface activity to be investigated was the influence of surface aging on (HER) electrocatalysis. In order to minimize the influence of local variations in surface structure (*i.e.*, strain and/or defect density, discussed above), a single macroscopic surface (step) feature was targeted, with subsequent scans performed along the step defect (*i.e.*, the "fresh" and "aged" scan areas were only separated by *ca.* 20 μm in distance but 30 days in time on the *same surface*). Note that this timescale is significantly longer than in our previous study,[37] where no differences in MoS_2 basal activity were observed on the 1 to 48 hour timescale. As shown in **Figure 4.6a** and **d**, the freshly cleaved surfaces of MoS_2 and WS_2, respectively, possess a relatively inactive basal plane (blue areas) of uniform activity and a highly active edge plane, exposed at a macroscopic, multilayer step edge feature (*ca.* 32 and 53 nm in height on MoS_2 and WS_2, respectively, see **Figure 4.17a** and **c**), consistent with the results discussed above (spatially-resolved LSV-SECCM movies of the full potential range on freshly cleaved MoS_2 and WS_2 are shown in the Supporting Information, Movie S7 and S8, respectively). After aging under ambient conditions for 30 days (details in the Experimental Section), the MoS_2 and WS_2 surfaces were scanned again using an identical SECCM protocol; the results are shown in **Figure 4.6b** and **e**, respectively (spatially-resolved LSV-SECCM movies of the full potential range on aged MoS_2 and WS_2 are shown in the Supporting Information, Movie S9 and S10, respectively). The catalytic activity of both surfaces deteriorated, with smaller catalytic currents measured at the basal plane, as well as the edge plane exposed at the macroscopic multilayer step edge feature (again, *ca.* 31 and 45 nm in height on MoS_2 and WS_2, respectively, see Supporting Information, **Figure 4.17b** and **d**). This is also reflected in the surface averaged LSVs, as shown in **Figure 4.6c** and **f**. Note that the variation in activity between the fresh and aged surfaces cannot be explained by differences in surface wetting, as contact areas of the meniscus cell on both of the freshly cleaved and aged MS_2 sample are commensurate, confirmed by measuring the droplet "footprint" left by a *ca.* 2 μm probe on WS_2 before and after aging, as shown in **Figure 4.8** (details in the Experimental Section).

Degradation in the surface activity may arise due to a number of reasons, including the adsorption of adventitious impurities (*e.g.*, airborne hydrocarbons[6]) and/or surface oxidation (*e.g.*, from atmospheric oxygen[57]). Layers of surface adsorbate and/or oxidized

species are expected to build up with time, resulting in partial inhibition of the HER, particularly the formation of adsorbed hydrogen (H_{ads}) in the classical Volmer reaction.[58-59] The edge plane activity is degraded more than the basal plane on both MoS_2 (decreases in HER catalytic current of 29% and 54% at -0.7 V vs. RHE on the basal and edge planes, respectively) and WS_2 (decreases in HER catalytic current of 42% and 69% at -0.7 V vs. RHE on the basal and edge planes, respectively), as summarized in Supporting Information, Table 1. This is perhaps unsurprising, as the under-coordinated Mo or W sites at the edge plane (or sulfur vacancy active sites) are much more liable to be oxidized than the saturated S sites on the basal plane. In addition, it seems that the degradation of WS_2 is more significant than that of MoS_2, likely related to the initially higher abundance of under-coordinated defect sites in this synthetic crystal, as described above. All in all, the results clearly demonstrate that the pristine MS_2 crystals (MoS_2 and WS_2) are not stable for long-term storage under ambient conditions (*i.e.*, obvious degradation in air for only 30 days). This has important ramifications for the application of TMDs such as MoS_2 and WS_2 in HER electrocatalysis, where the bulk of studies employ “aged” nanomaterials that have an unknown surface state (*i.e.*, surface cleanliness and oxidation state) due to uncontrolled exposure to air and solvents during the active material synthesis and electrode preparation process.

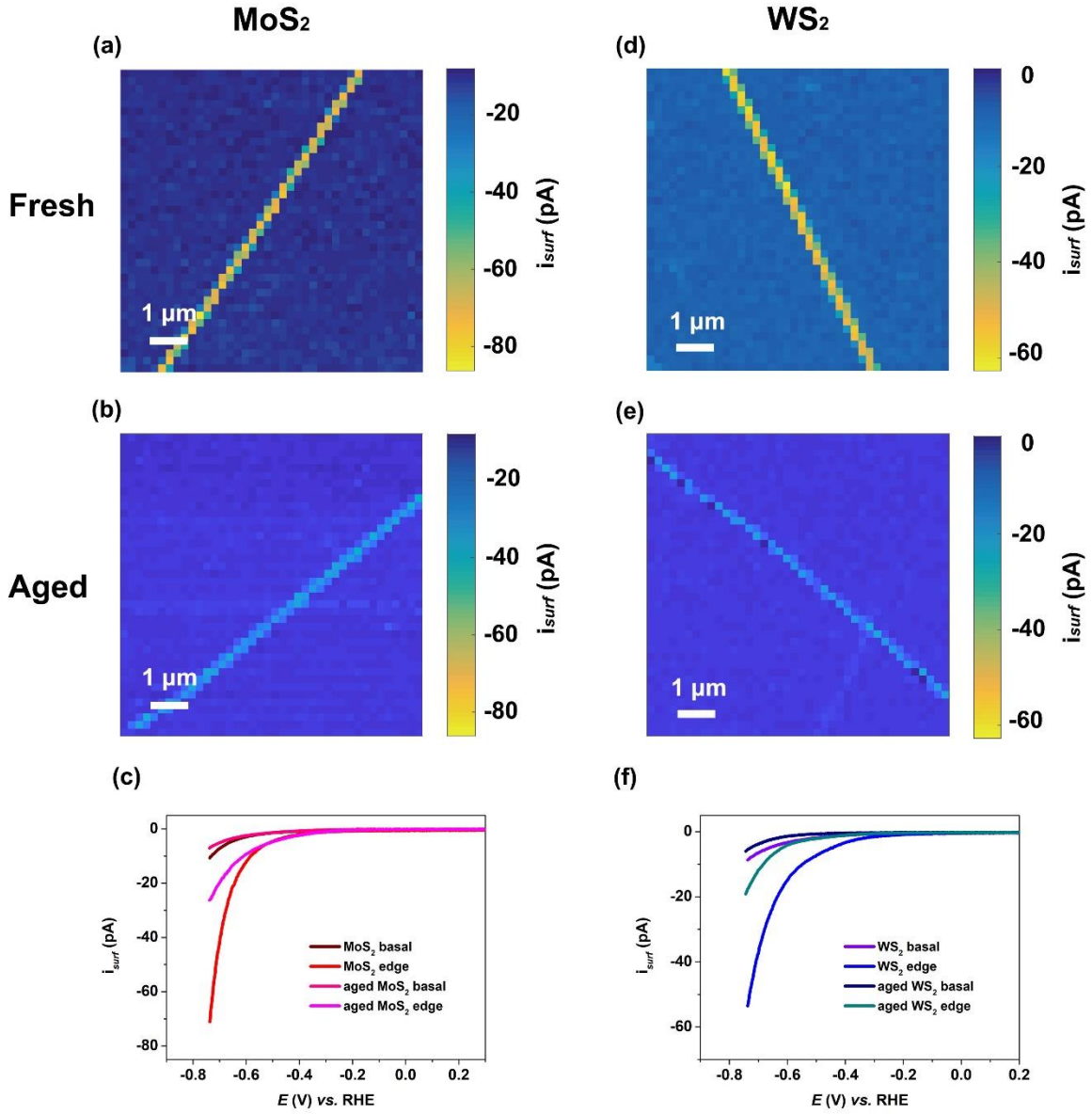

Figure 4.6 Spatially-resolved electrochemical activity maps obtained on **(a, d)** freshly cleaved and **(b, e)** aged samples with voltammetric hopping mode protocol (1600 pixels over an 8×8 µm scan area). **(c, f)** Average linear-sweep voltammograms (scan rate, υ = 1 V/s) extracted from the basal surface and edge planes, corresponding to the low-activity (small current magnitude) and high-activity (large current magnitude) traces, respectively. **(a-c)** and **(d-f)** were obtained from MoS_2 and WS_2 crystals, respectively. These experiments were carried out with a nanopipette of diameter ≈150 nm, containing a solution of 0.1 M $HClO_4$, and a hopping distance of 200 nm. Note that there is no interpolation of any of the SECCM data (electrochemical activity). The associated spatially-resolved LSV-SECCM movies obtained on

(a) freshly cleaved MoS_2, **(b)** aged MoS_2, **(d)** freshly cleaved WS_2 and **(e)** aged WS_2 are shown in the Supporting Information, Movies S7, S9, S8 and S10, respectively.

4.5 Conclusions

A major outcome of this study has been to show that the electrocatalytic activities of the bulk forms of two TMDs, MoS_2 and WS_2 toward the HER vary considerably across the electrode surface at the nanoscale. The basal plane of 2H phase MS_2 (where M = Mo or W) was shown to support the HER (albeit at lower rates than the edge plane), with kinetics that varied across the basal surface of the crystal, attributed to localized folding (*e.g.*, mechanical stress) or variations in the electronic structure (*e.g.*, point defect density). The presence of more significant surface disorder (*e.g.*, crevices, cracks, steps and holes) on the bulk MS_2 crystal was directly shown to greatly enhance the kinetics of the HER with single-edge sensitivity, detectable by SECCM. This is attributed to the local-exposure of the catalytically active edge plane at these sites.

Sample history was also shown to be a very important factor in the evaluation of the intrinsic activity of MS_2 materials, for example, aging in ambient conditions deteriorated the catalytic activity, attributed to the build-up of adventitious adsorbates or surface oxidation products, particularly at the catalytically active edge plane. All-in-all, the important insights in this work are of immediate application to electromaterials research, highlighting not only that care needs to be taken during the (electro)materials synthesis, storage and performance evaluation process, but also demonstrating the power of spatially-resolved electrochemical techniques to reveal the unique patterns of surface reactivity that remain “invisible” to conventional macroscopic (bulk) electrochemical techniques.

4.6 Supporting Information

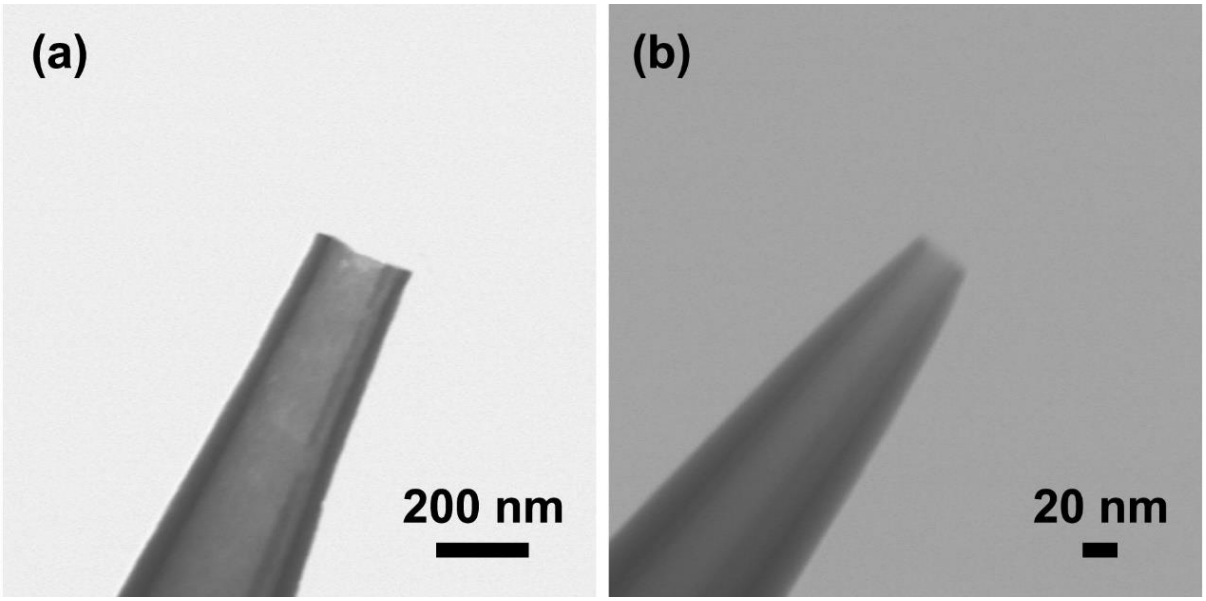

Figure 4.7 Scanning transmission electron microscopy (STEM) images of the representative nanopipette probes with diameter of ca. 150 nm **(a)** and ca. 30 nm **(b)**.

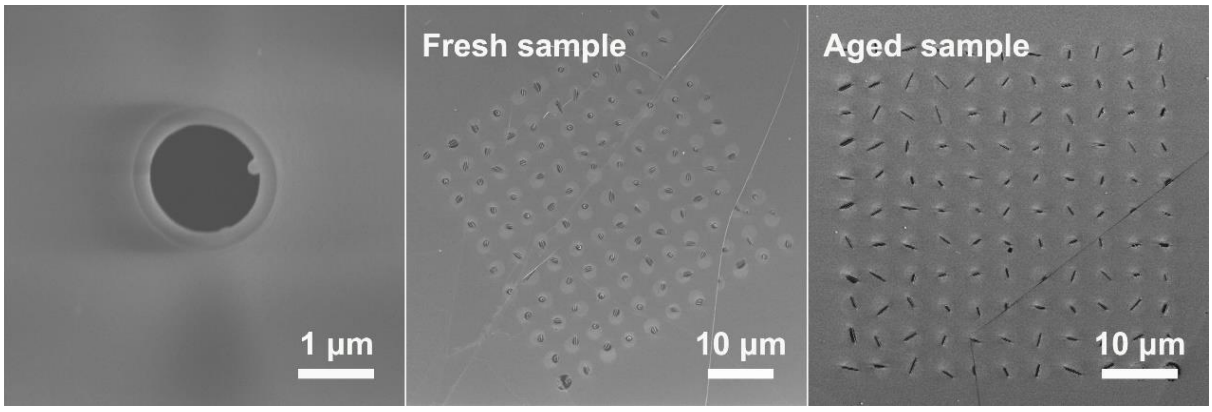

Figure 4.8 (a) Scanning electron microscopy (SEM) images of a representative nanopipette probe with diameter of ca. 2 um. **(b)** and **(c)** SEM images of the droplet (meniscus cell) "footprints" left on the fresh and aged WS_2 sample, respectively. Note that the diameters of the footprints on the freshly cleaved and aged surfaces are 2.25 ± 0.02 µm and 2.23 ± 0.04 µm, respectively, calculated by taking the average diameters of 10 different residues in each case.

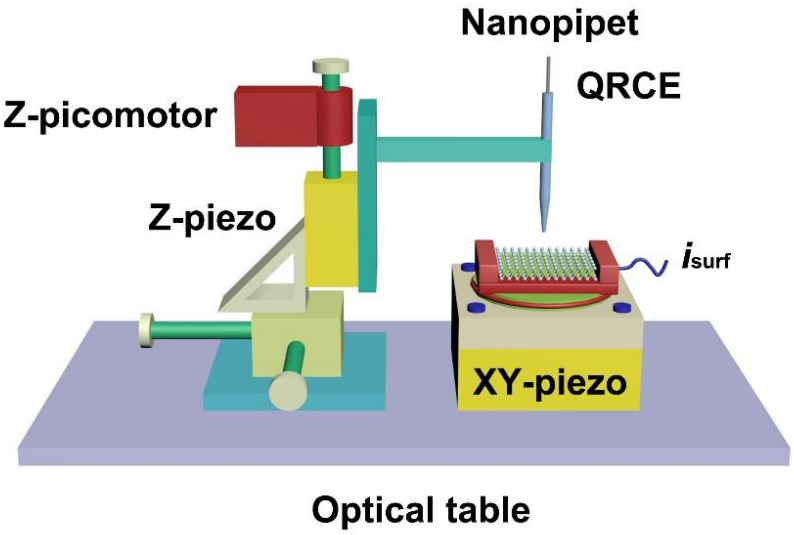

Figure 4.9 Labeled schematic of SECCM setup employed herein. The nanopipette probe was fixed to a z-piezoelectric positioner (fine movement, labeled z-piezo in the image), which was mounted on a z-picomotor and xy-micropositioners for coarse movement. The sample was mounted on a xy-piezoelectric positioner (labeled xy-piezo in the image) for fine control of lateral position. Electrochemical experiments were performed by applying a potential at the quasi-reference counter electrode (QRCE) in the nanopipette barrel, while measuring current (i_{surf}) at the substrate surface.

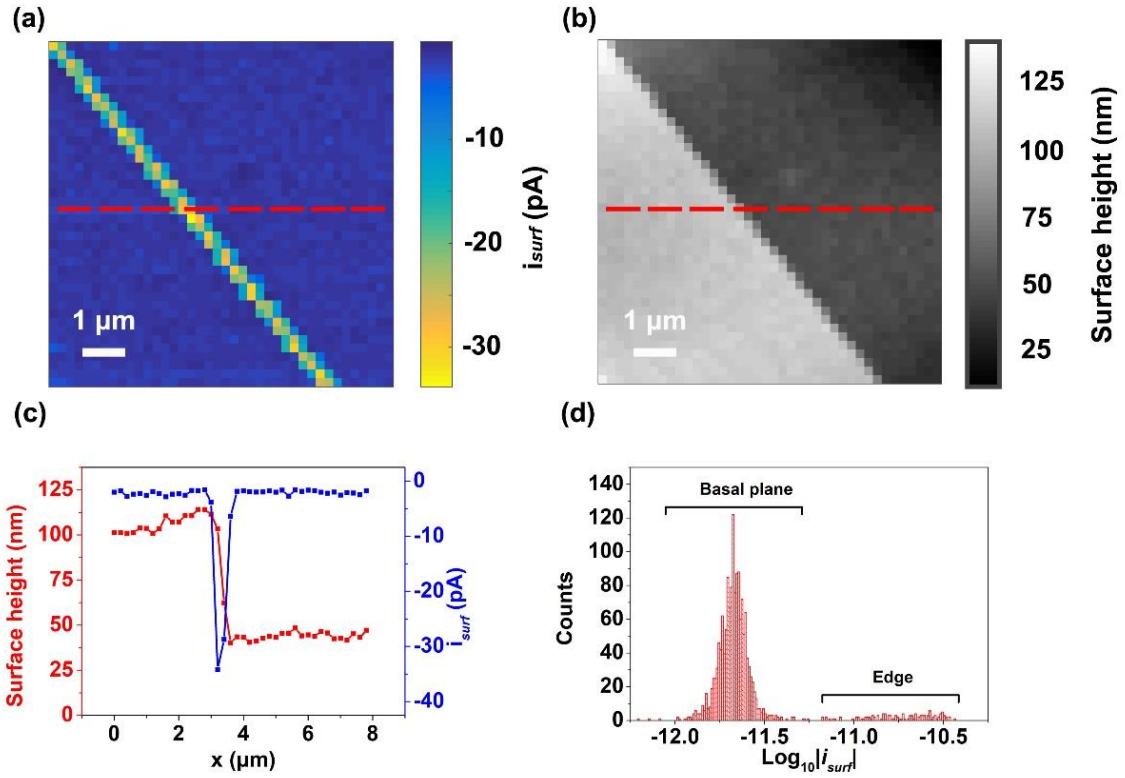

Figure 4.10 Spatially-resolved **(a)** electrochemical activity (-0.704 V vs. the reversible hydrogen electrode, RHE) and **(b)** topographical maps (1600 pixels over an 8×8 µm scan area) obtained on a freshly cleaved MoS_2 surface with voltammetric hopping mode protocol. **(c)** Z-position (red trace) and i_{surf} (blue trace) line scan profiles, indicated by the red dashed lines in **(a)** and **(b)**. **(d)** Histogram showing the distribution of the logarithm of surface current (i_{surf}), extracted from **(a)**. Note that there is no interpolation of any of the SECCM data (neither topography nor electrochemical activity).

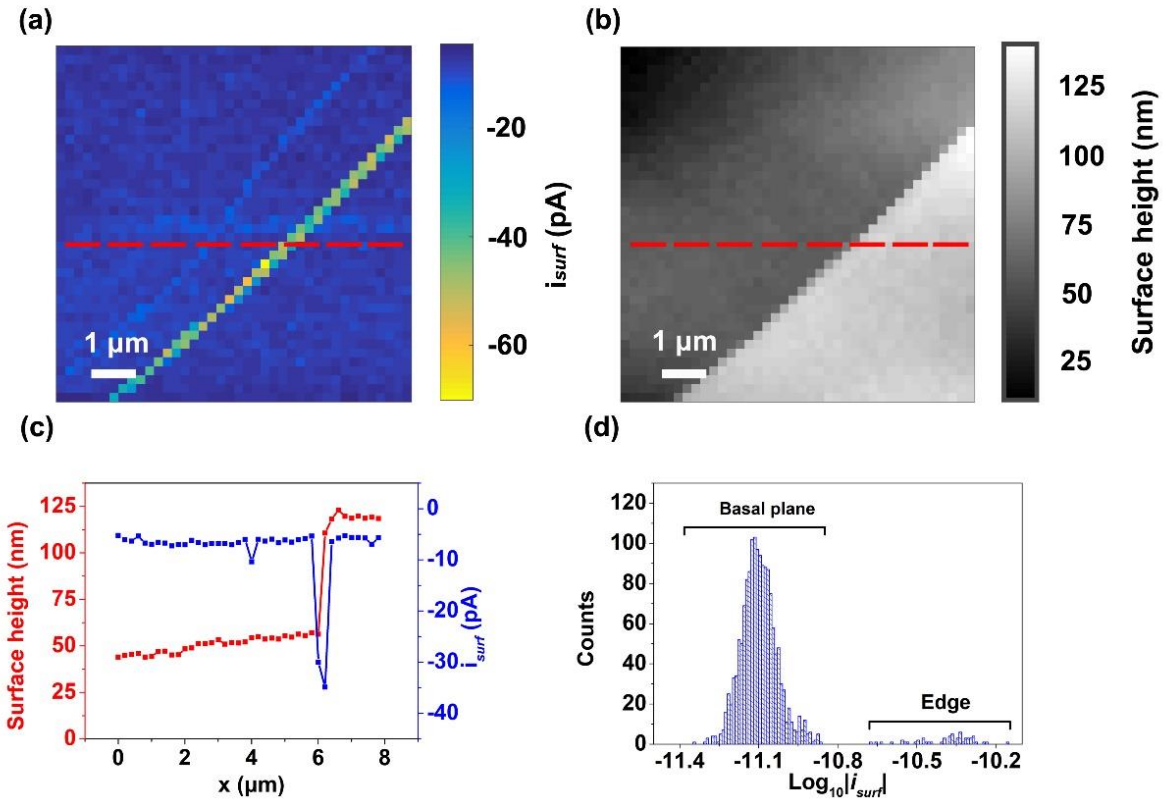

Figure 4.11 Spatially-resolved **(a)** electrochemical activity (-0.704 V vs. the reversible hydrogen electrode, RHE) and **(b)** topographical maps (1600 pixels over an 8×8 µm scan area) obtained on a freshly cleaved WS_2 surface with voltammetric hopping mode protocol. **(c)** Z-position (red trace) and i_{surf} (blue trace) line scan profiles, indicated by the red dashed lines in **(a)** and **(b)**. **(d)** Histogram showing the distribution of $\log_{10}|i_{surf}|$, extracted from (a). These experiments were carried out with a nanopipette of diameter ≈150 nm (0.1 M $HClO_4$), with voltammetric scan rate, υ = 1 V/s and a hopping distance of 200 nm. Note that there is no interpolation of any of the SECCM data (neither topography nor electrochemical activity).

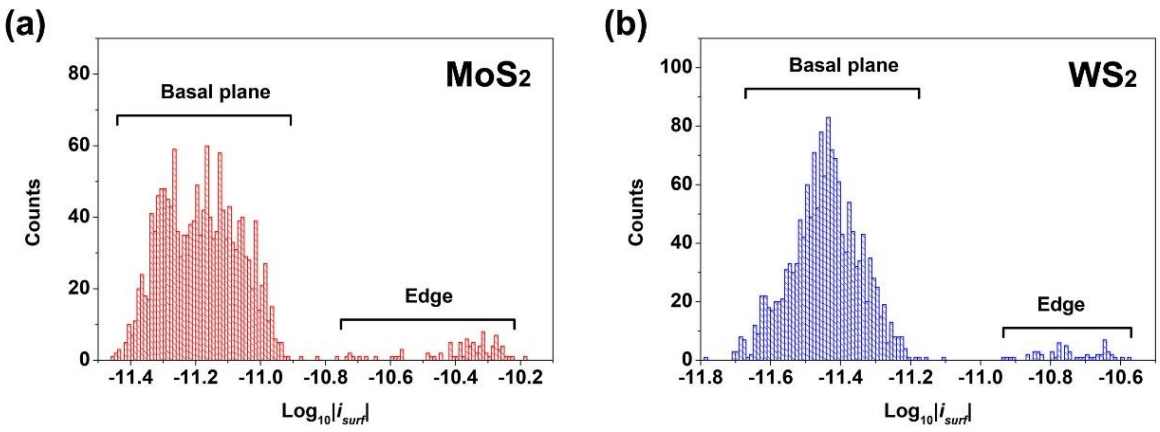

Figure 4.12 Histogram (1600 pixels, -0.7656V vs. RHE) showing the distribution of $\log_{10}|i_{surf}|$, extracted from the **(a)** MoS_2 and **(b)** WS_2 surfaces shown in the main text, Figure 3a and d, respectively. These experiments were carried out with a nanopipette of diameter ≈150 nm (0.1 M $HClO_4$), with υ = 1 V/s and a hopping distance of 200 nm.

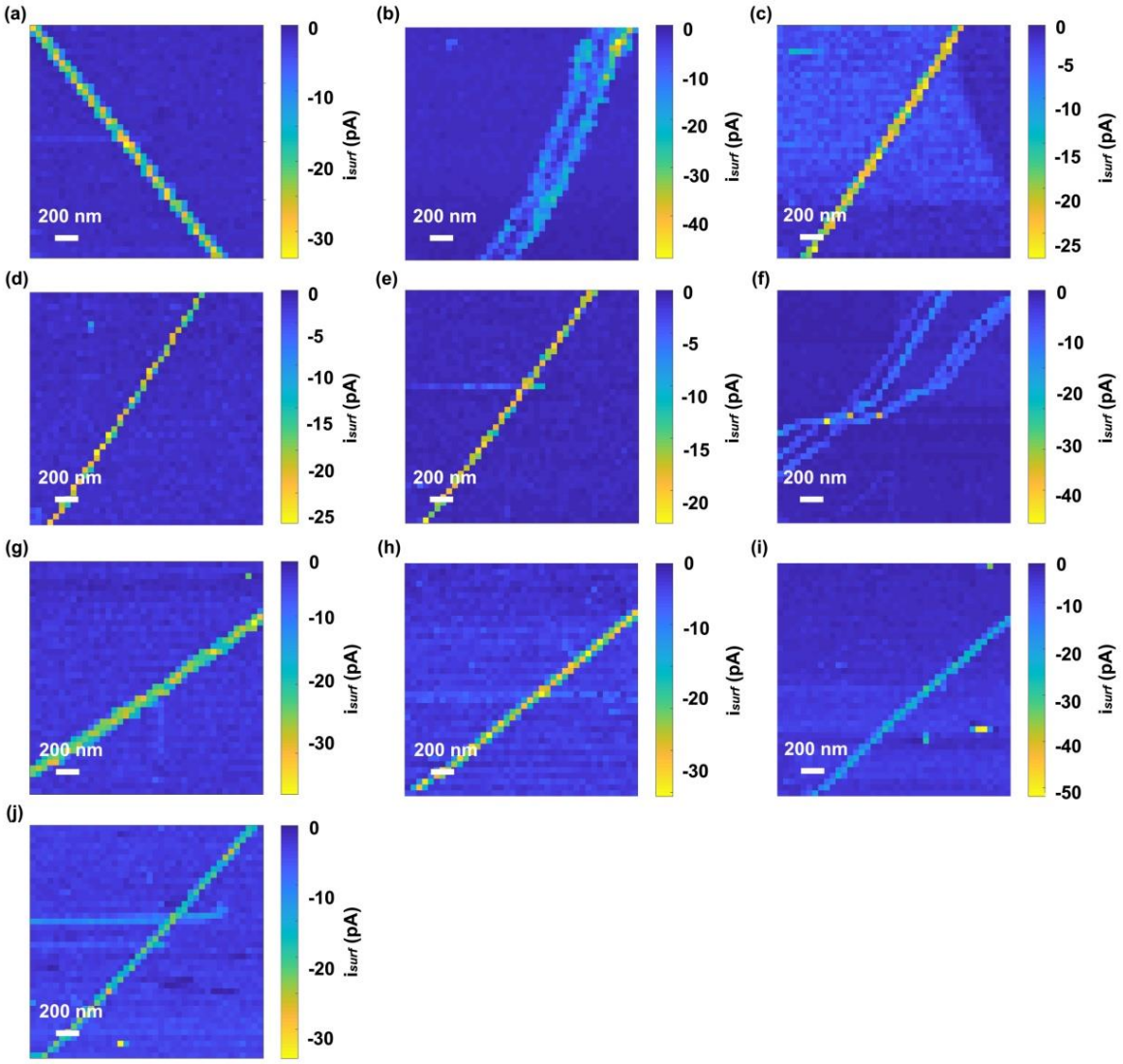

Figure 4.13 Spatially-resolved electrochemical activity maps (1600 pixels over an 8×8 µm scan area, -0.704 V vs. RHE), obtained on ten different areas of freshly cleaved MoS_2 with the voltammetric hopping mode protocol. These experiments were carried out with a nanopipette of diameter ≈150 nm (0.1 M $HClO_4$), with υ = 1 V/s and a hopping distance of 200 nm. Note that there is no interpolation of any of the SECCM data (electrochemical activity).

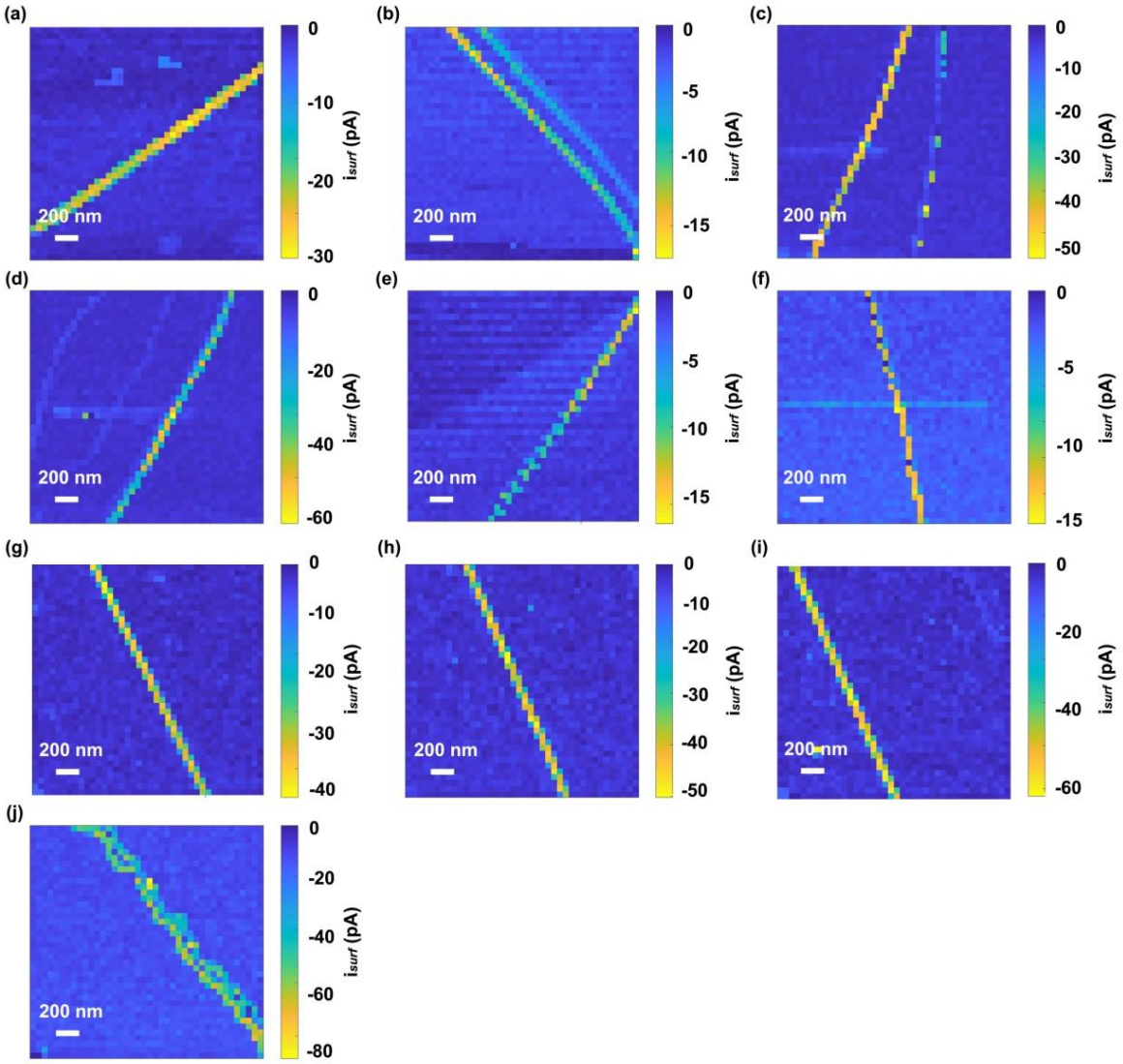

Figure 4.14 Spatially-resolved electrochemical activity maps (1600 pixels over an 8×8 µm scan area, -0.704 V vs. RHE), obtained on ten different areas of freshly cleaved WS_2 with the voltammetric hopping mode protocol. These experiments were carried out with a nanopipette of diameter ≈150 nm (0.1 M $HClO_4$), with υ = 1 V/s and a hopping distance of 200 nm. Note that there is no interpolation of any of the SECCM data (electrochemical activity).

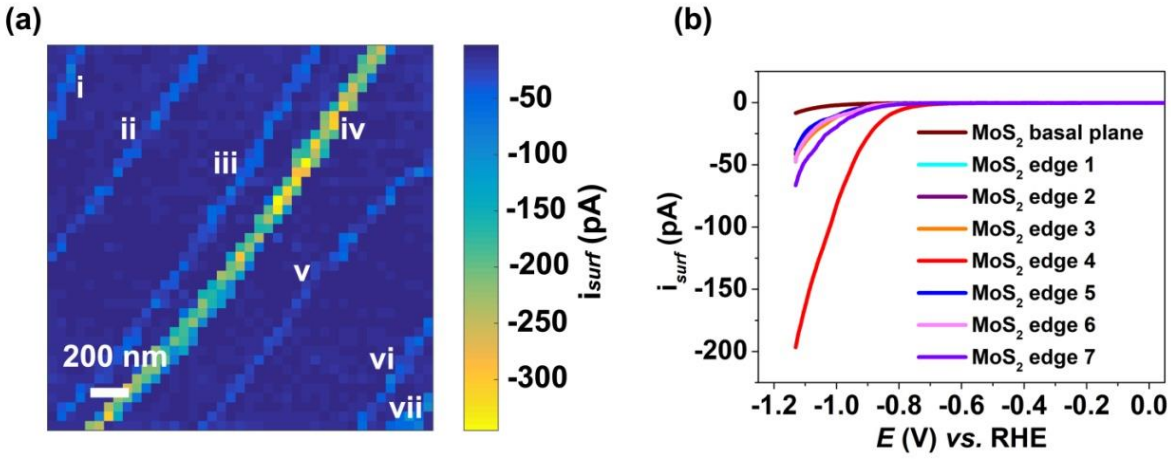

Figure 4.15 (a) Spatially-resolved electrochemical activity map at -1.053 V vs. RHE (1600 pixels over a 2×2 µm scan area, Figure 5b, main text) obtained on a freshly cleaved MoS_2 surface using the voltammetric hopping mode protocol. **(b)** Linear sweep voltammograms (LSVs) extracted from the basal surface, and seven step features labeled i – vii in (a). These experiments were carried out with a nanopipette of diameter ≈150 nm (0.1 M $HClO_4$), with υ = 1 V/s and a hopping distance of 200 nm.

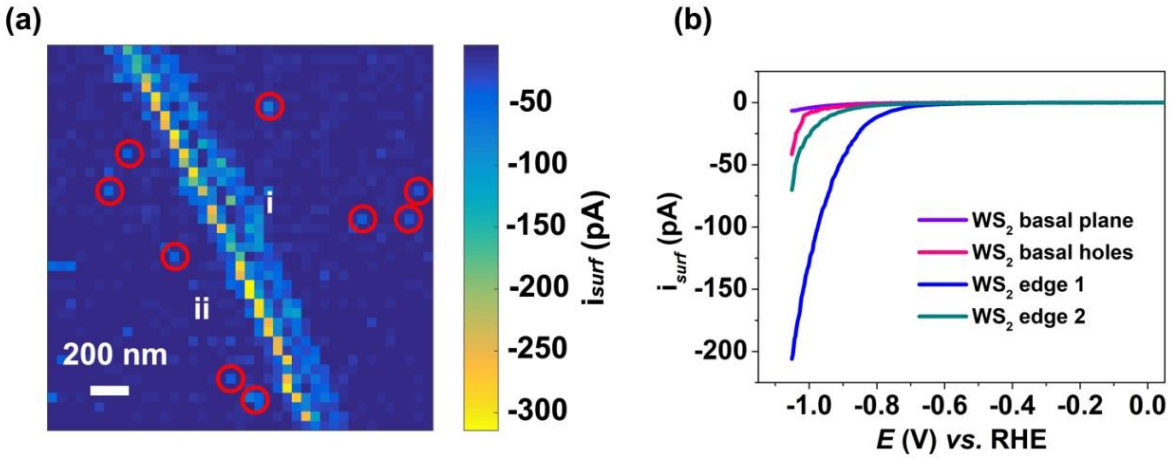

Figure 4.16 (a) Spatially-resolved electrochemical activity map at -1.053 V vs. RHE (1600 pixels over a 2×2 µm scan area, Figure 5e, main text) obtained on a freshly cleaved WS_2 surface using the voltammetric hopping mode protocol. **(b)** LSVs extracted from the basal surface, point defect sites and step feature, labeled in **(a)**. These experiments were carried out with a nanopipette of diameter ≈150 nm (0.1 M $HClO_4$), with υ = 1 V/s and a hopping distance of 200 nm.

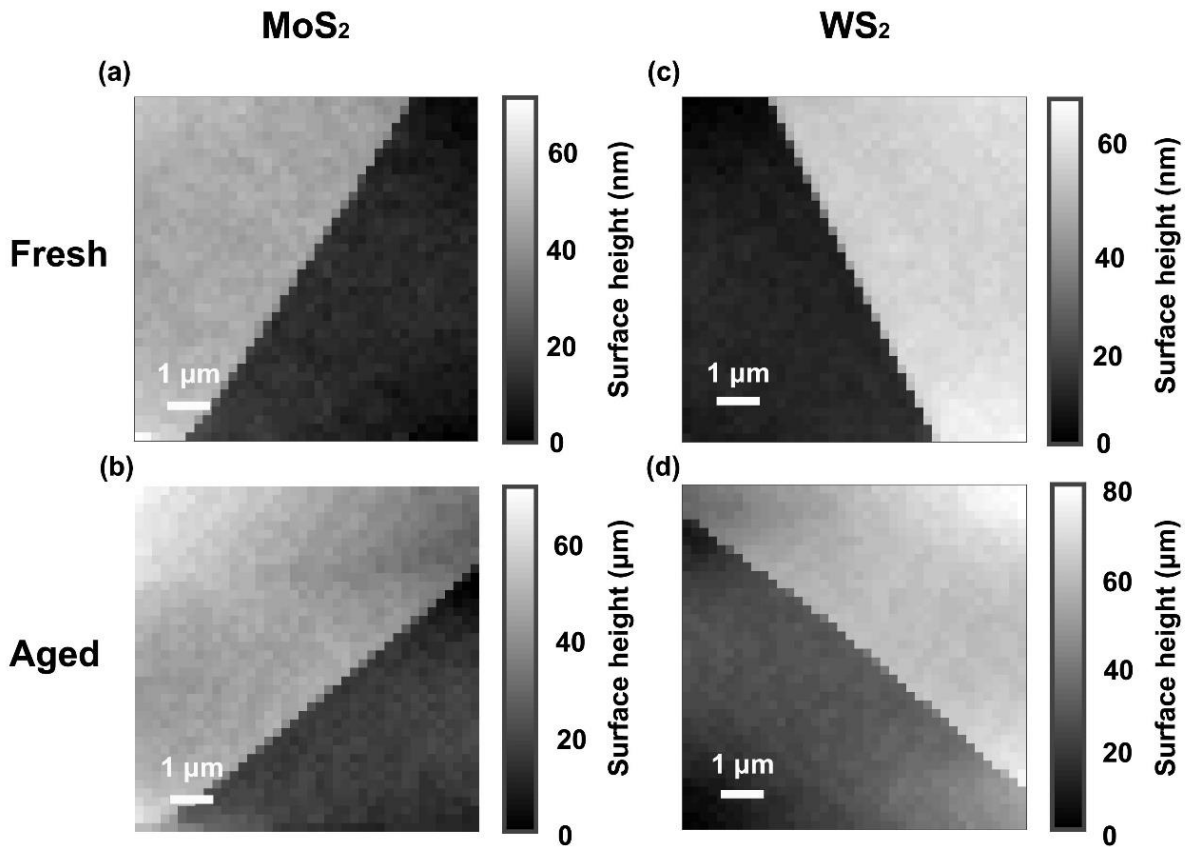

Figure 4.17 (a), **(b)** and **(c), (d)** Topographical maps of freshly cleaved and aged MoS_2 and WS_2, respectively.

Table 4.1 Comparison of electrochemical activities between freshly cleaved and aged MS_2 sample.

Sample		MoS_2		WS_2	
		Basal plane	Edge	Basal plane	Edge
At the potential of -0.5 V vs. RHE	Fresh sample activity/pA	1.4	4.7	1.9	7.3
	Aged sample Activity/pA	1.4	4.7	0.69	2.1
	Decreasing rate %	0	0	63.7	71.2
At the potential of -0.5 V vs. RHE	Fresh sample activity/pA	2.9	12.2	3.4	15.0
	Aged sample Activity/pA	2.5	9.3	1.4	4.1
	Decreasing rate %	13.8	23.8	58.8	72.7
At the potential of -0.7 V vs. RHE	Fresh sample activity/pA	7.2	42.5	6.5	37.5
	Aged sample Activity/pA	5.0	19.7	3.8	11.8
	Decreasing rate %	29.2	53.6	41.5	68.5

4.7 References

1. Ma, T. Y.; Dai, S.; Qiao, S. Z., Self-Supported Electrocatalysts for Advanced Energy Conversion Processes. *Mater. Today* **2016**, *19*, 265-273.

2. Xie, J.; Xie, Y., Structural Engineering of Electrocatalysts for the Hydrogen Evolution Reaction: Order or Disorder? *ChemCatChem* **2015**, *7*, 2568-2580.

3. Cheng, N.; Stambula, S.; Wang, D.; Banis, M. N.; Liu, J.; Riese, A.; Xiao, B.; Li, R.; Sham, T. K.; Liu, L. M., et al., Platinum Single-Atom and Cluster Catalysis of the Hydrogen Evolution Reaction. *Nat. Comm.* **2016**, *7*, 13638.

4. Seh, Z. W.; Kibsgaard, J.; Dickens, C. F.; Chorkendorff, I.; Nørskov, J. K.; Jaramillo, T. F., Combining Theory and Experiment in Electrocatalysis: Insights into Materials Design. *Science* **2017**, *355*, eaad4998..

5. Zou, X.; Zhang, Y., Noble Metal-Free Hydrogen Evolution Catalysts for Water Splitting. *Chem. Soc. Rev.* **2015**, *44*, 5148-5180.

6. Kozbial, A.; Gong, X.; Liu, H.; Li, L., Understanding the Intrinsic Water Wettability of Molybdenum Disulfide (MoS_2). *Langmuir* **2015**, *31*, 8429-8435.

7. Chen, D.; Ji, G.; Ding, B.; Ma, Y.; Qu, B.; Chen, W.; Lee, J. Y., In Situ Nitrogenated Graphene–Few-Layer WS_2 Composites for Fast and Reversible Li^+ Storage. *Nanoscale* **2013**, *5*, 7890-7896.

8. Rong, Y.; He, K.; Pacios, M.; Robertson, A. W.; Bhaskaran, H.; Warner, J. H., Controlled Preferential Oxidation of Grain Boundaries in Monolayer Tungsten Disulfide for Direct Optical Imaging. *ACS Nano* **2015**, *9*, 3695-3703.

9. Wu, S.; Zeng, Z.; He, Q.; Wang, Z.; Wang, S. J.; Du, Y.; Yin, Z.; Sun, X.; Chen, W.; Zhang, H., Electrochemically Reduced Single-Layer MoS_2 Nanosheets: Characterization, Properties, and Sensing Applications. *Small* **2012**, *8*, 2264-2270.

10. Merki, D.; Hu, X., Recent Developments of Molybdenum and Tungsten Sulfides as Hydrogen Evolution Catalysts. *Energy Environ. Mat.* **2011**, *4*, 3878-3888.

11. Jaramillo, T. F.; Jorgensen, K. P.; Bonde, J.; Nielsen, J. H.; Horch, S.; Chorkendorff, I., Identification of Active Edge Sites for Electrochemical H_2 Evolution from MoS_2 Nanocatalysts. *Science* **2007**, *317*, 100-102.

12. Wiensch, J. D.; John, J.; Velazquez, J. M.; Torelli, D. A.; Pieterick, A. P.; McDowell, M. T.; Sun, K.; Zhao, X.; Brunschwig, B. S.; Lewis, N. S., Comparative Study in Acidic and Alkaline

Media of the Effects of pH and Crystallinity on the Hydrogen-evolution Reaction on MoS_2 and $MoSe_2$. *ACS Energy Lett.* **2017**, *2*, 2234-2238.

13. Tsai, C.; Chan, K.; Nørskov, J. K.; Abild-Pedersen, F., Theoretical Insights into the Hydrogen Evolution Activity of Layered Transition Metal Dichalcogenides. *Surf. Sci.* **2015**, *640*, 133-140.

14. Hinnemann, B.; Moses, P. G.; Bonde, J.; Jørgensen, K. P.; Nielsen, J. H.; Horch, S.; Chorkendorff, I.; Nørskov, J. K., Biomimetic Hydrogen Evolution: MoS_2 Nanoparticles as Catalyst for Hydrogen Evolution. *J. Am. Chem. Soc.* **2005**, *127*, 5308-5309.

15. Yang, J.; Shin, H. S., Recent Advances in Layered Transition Metal Dichalcogenides for Hydrogen Evolution Reaction. *J. Mater. Chem. A* **2014**, *2*, 5979-5985.

16. Voiry, D.; Yang, J.; Chhowalla, M., Recent Strategies for Improving the Catalytic Activity of 2D TMD Nanosheets Toward the Hydrogen Evolution Reaction. *Adv. Mater.* **2016**, *28*, 6197-6206.

17. Wu, Z.; Fang, B.; Bonakdarpour, A.; Sun, A.; Wilkinson, D. P.; Wang, D., WS_2 Nanosheets as a Highly Efficient Electrocatalyst for Hydrogen Evolution Reaction. *Appl. Catal., B.* **2012**, *125*, 59-66.

18. Wang, T.; Gao, D.; Zhuo, J.; Zhu, Z.; Papakonstantinou, P.; Li, Y.; Li, M., Size-Dependent Enhancement of Electrocatalytic Oxygen-Reduction and Hydrogen-Evolution Performance of MoS_2 Particles. *Chem.: Eur. J.* **2013**, *19*, 11939-11948.

19. Bentley, C. L.; Kang, M.; Unwin, P. R., Nanoscale Surface Structure–Activity in Electrochemistry and Electrocatalysis. *J. Am. Chem. Soc.* **2018**, *141*, 2179-2193.

20. Tao, B.; Yule, L. C.; Daviddi, E.; Bentley, C. L.; Unwin, P. R., Correlative Electrochemical Microscopy of Li-Ion (De)intercalation at a Series of Individual $LiMn_2O_4$ Particles. *Angew. Chem. Int. Ed.* **2019**, *131*, 4654-4659.

21. Bentley, C. L.; Edmondson, J.; Meloni, G. N.; Perry, D.; Shkirskiy, V.; Unwin, P. R., Nanoscale Electrochemical Mapping. *Anal. Chem.* **2018**, *91*, 84-108.

22. Chen, R.; Yang, C.; Cai, W.; Wang, H.-Y.; Miao, J.; Zhang, L.; Chen, S.; Liu, B., Use of Platinum as the Counter Electrode to Study the Activity of Nonprecious Metal Catalysts for the Hydrogen Evolution Reaction. *ACS Energy Lett.* **2017**, *2*, 1070-1075.

23. Benck, J. D.; Chen, Z.; Kuritzky, L. Y.; Forman, A. J.; Jaramillo, T. F., Amorphous Molybdenum Sulfide Catalysts for Electrochemical Hydrogen Production: Insights into the Origin of Their Catalytic Activity. *ACS Catal.* **2012**, *2*, 1916-1923.

24. Tan, S. M.; Ambrosi, A.; Sofer, Z.; Huber, S.; Sedmidubsky, D.; Pumera, M., Pristine Basal- and Edge-Plane-Oriented Molybdenite MoS_2 Exhibiting Highly Anisotropic Properties. *Chem.: Eur. J.* **2015**, *21*, 7170-7178.

25. Danis, L.; Gateman, S. M.; Kuss, C.; Schougaard, S. B.; Mauzeroll, J., Nanoscale Measurements of Lithium-Ion-Battery Materials using Scanning Probe Techniques. *ChemElectroChem* **2017**, *4*, 6-19.

26. Kalinin, S. V.; Dyck, O.; Balke, N.; Neumayer, S.; Tsai, W. Y.; Vasudevan, R.; Lingerfelt, D.; Ahmadi, M.; Ziatdinov, M.; McDowell, M. T., et al., Toward Electrochemical Studies on the Nanometer and Atomic Scales: Progress, Challenges, and Opportunities. *ACS Nano* **2019**, *13*, 9735-9780.

27. Li, H.; Du, M.; Mleczko, M. J.; Koh, A. L.; Nishi, Y.; Pop, E.; Bard, A. J.; Zheng, X., Kinetic Study of Hydrogen Evolution Reaction over Strained MoS_2 with Sulfur Vacancies Using Scanning Electrochemical Microscopy. *J. Am. Chem. Soc.* **2016**, *138*, 5123-5129.

28. Mariano, R. G.; McKelvey, K.; White, H. S.; Kanan, M. W., Selective Increase in CO_2 Electroreduction Activity at Grain-boundary Surface Terminations. *Science* **2017**, *358*, 1187-1192.

29. Kang, M.; Perry, D.; Bentley, C. L.; West, G.; Page, A.; Unwin, P. R., Simultaneous Topography and Reaction Flux Mapping at and Around Electrocatalytic Nanoparticles. *ACS Nano* **2017**, *11*, 9525-9535.

30. Wang, Y.; Gordon, E.; Ren, H., Mapping the Nucleation of H_2 Bubble on a Polycrystalline Pt via Scanning Electrochemical Cell Microscopy. *J. Phys. Chem. Lett.* **2019**, *10*, 3887-3892.

31. Hill, J. W.; Hill, C. M., Directly Mapping Photoelectrochemical Behavior within Individual Transition Metal Dichalcogenide Nanosheets. *Nano Lett.* **2019**, *19*, 5710-5716.

32. Wang, S.; Liu, Q.; Zhao, C.; Lv, F.; Qin, X.; Du, H.; Kang, F.; Li, B., Advances in Understanding Materials for Rechargeable Lithium Batteries by Atomic Force Microscopy. *Energy Environ. Mat.* **2018**, *1*, 28-40.

33. Kranz, C.; Friedbacher, G.; Mizaikoff, B.; Lugstein, A.; Smoliner, J.; Bertagnolli, E., Integrating an Ultramicroelectrode in an AFM Cantilever: Combined Technology for Enhanced Information. *Anal. Chem.* **2001**, *73*, 2491-2500.

34. Macpherson, J. V.; Unwin, P. R., Noncontact Electrochemical Imaging with Combined Scanning Electrochemical Atomic Force Microscopy. *Anal. Chem.* **2001**, *73*, 550-557.

35. Zhang, G.; Kirkman, P. M.; Patel, A. N.; Cuharuc, A. S.; McKelvey, K.; Unwin, P. R., Molecular Functionalization of Graphite Surfaces: Basal Plane Versus Step Edge Electrochemical Activity. *J. Am. Chem. Soc.* **2014**, *136*, 11444-11451.

36. Kang, M.; Wilson, P.; Meng, L.; Perry, D.; Basile, A.; Unwin, P. R., High Resolution Visualization of the Redox Activity of Li_2O_2 in Non-Aqueous Media: Conformal Layer vs. Toroid Structure. *Chem. Comm.* **2018**, *54*, 3053-3056..

37. Bentley, C. L.; Kang, M.; Maddar, F. M.; Li, F.; Walker, M.; Zhang, J.; Unwin, P. R., Electrochemical Maps and Movies of the Hydrogen Evolution Reaction on Natural Crystals of Molybdenite (MoS_2): Basal Vs. Edge Plane Activity. *Chem. Sci.* **2017**, *8*, 6583-6593.

38. Bentley, C. L.; Kang, M.; Unwin, P. R., Nanoscale Structure Dynamics within Electrocatalytic Materials. *J. Am. Chem. Soc.* **2017**, *139*, 16813-16821.

39. Bentley, C. L.; Unwin, P. R., Nanoscale Electrochemical Movies and Synchronous Topographical Mapping of Electrocatalytic Materials. *Faraday Discuss.* **2018**, *210*, 365-379.

40. Tarnev, T.; Aiyappa, H. B.; Botz, A.; Erichsen, T.; Ernst, A.; Andronescu, C.; Schuhmann, W., Scanning Electrochemical Cell Microscopy Investigation of Single ZIF-Derived Nanocomposite Particles as Electrocatalysts for Oxygen Evolution in Alkaline Media. *Angew. Chem. Int. Ed.* **2019**, *58*, 14265 –14269.

41. Novoselov, K. S.; Geim, A. K.; Morozov, S. V.; Jiang, D.; Zhang, Y.; Dubonos, S. V.; Grigorieva, I. V.; Firsov, A. A., Electric Field Effect in Atomically Thin Carbon Films. *Science* **2004**, *306*, 666-669.

42. Bentley, C. L.; Perry, D.; Unwin, P. R., Stability and Placement of Ag/AgCl Quasi-Reference Counter Electrodes in Confined Electrochemical Cells. *Anal. Chem.* **2018**, *90*, 7700-7707.

43. Snowden, M. E.; Guell, A. G.; Lai, S. C.; McKelvey, K.; Ebejer, N.; O'Connell, M. A.; Colburn, A. W.; Unwin, P. R., Scanning Electrochemical Cell Microscopy: Theory and Experiment for Quantitative High Resolution Spatially-Resolved Voltammetry and Simultaneous Ion-Conductance Measurements. *Anal. Chem.* **2012**, *84*, 2483-2491.

44. Williams, C. G.; Edwards, M. A.; Colley, A. L.; Macpherson, J. V.; Unwin, P. R., Scanning Micropipet Contact Method for High-Resolution Imaging of Electrode Surface Redox Activity. *Anal. Chem.* **2009**, *81*, 2486-2495.

45. Alzahrani, H.; Bentley, C.; Burrows, R.; Cao, C.; Cai, Q.; Chikere, C.; Crooks, R. M.; Dunevall, J.; Edwards, M.; Ewing, A., et al., Dynamics of Nanointerfaces: General Discussion. *Faraday Discuss.* **2018**, *210*, 451-479.

46. Sharel, E.; Kim, Y.-R.; Perry, D.; Bentley, C. L.; Unwin, P. R., Nanoscale Electrocatalysis of Hydrazine Electro-oxidation at Blistered Graphite Electrodes. *ACS Appl. Mater. Interfaces.* **2016**, *8*, 30458-30466.

47. Li, H.; Tsai, C.; Koh, A. L.; Cai, L.; Contryman, A. W.; Fragapane, A. H.; Zhao, J.; Han, H. S.; Manoharan, H. C.; Abild-Pedersen, F., Activating and Optimizing MoS_2 Basal Planes for Hydrogen Evolution Through the Formation of Strained Sulphur Vacancies. *Nat. Mater.* **2016**, *15*, 48-53.

48. Yu, Y.; Huang, S. Y.; Li, Y.; Steinmann, S. N.; Yang, W.; Cao, L., Layer-dependent Electrocatalysis of MoS_2 for Hydrogen Evolution. *Nano Lett.* **2014**, *14*, 553-558.

49. Bonde, J.; Moses, P. G.; Jaramillo, T. F.; Nørskov, J. K.; Chorkendorff, I., Hydrogen Evolution on Nano-Particulate Transition Metal Sulfides. *Faraday Discuss.* **2009**, *140*, 219-231.

50. Yin, Y.; Han, J.; Zhang, Y.; Zhang, X.; Xu, P.; Yuan, Q.; Samad, L.; Wang, X.; Wang, Y.; Zhang, Z., et al., Contributions of Phase, Sulfur Vacancies, and Edges to the Hydrogen Evolution Reaction Catalytic Activity of Porous Molybdenum Disulfide Nanosheets. *J. Am. Chem. Soc.* **2016**, *138*, 7965-7972.

51. Li, G.; Zhang, D.; Qiao, Q.; Yu, Y.; Peterson, D.; Zafar, A.; Kumar, R.; Curtarolo, S.; Hunte, F.; Shannon, S., All the Catalytic Active Sites of MoS_2 for Hydrogen Evolution. *J. Am. Chem. Soc.* **2016**, *138*, 16632-16638.

52. Choi, C. L.; Feng, J.; Li, Y.; Wu, J.; Zak, A.; Tenne, R.; Dai, H., WS_2 Nanoflakes from Nanotubes for Electrocatalysis. *Nano Res.* **2013**, *6*, 921-928.

53. Zhang, Y.; Shi, J.; Han, G.; Li, M.; Ji, Q.; Ma, D.; Zhang, Y.; Li, C.; Lang, X.; Zhang, Y., Chemical Vapor Deposition of Monolayer WS_2 Nanosheets on Au Foils Toward Direct Application in Hydrogen Evolution. *Nano Res.* **2015**, *8*, 2881-2890.

54. Addou, R.; Colombo, L.; Wallace, R. M., Surface Defects on Natural MoS_2. *ACS Appl. Mater. Interfaces.* **2015**, *7*, 11921-11929.

55. Radisavljevic, B.; Radenovic, A.; Brivio, J.; Giacometti, i. V.; Kis, A., Single-Layer MoS_2 transistors. *Nat. Nanotechnol.* **2011**, *6*, 147-150.

56. Li, J.; Zhan, G.; Yu, Y.; Zhang, L., Superior Visible Light Hydrogen Evolution of Janus Bilayer Junctions via Atomic-level Charge Flow Steering. *Nat. Comm.* **2016**, *7*, 11480.

57. Voiry, D.; Salehi, M.; Silva, R.; Fujita, T.; Chen, M.; Asefa, T.; Shenoy, V. B.; Eda, G.; Chhowalla, M., Conducting MoS_2 Nanosheets as Catalysts for Hydrogen Evolution Reaction. *Nano Lett.* **2013**, *13*, 6222-6227.

58. Voiry, D.; Yamaguchi, H.; Li, J.; Silva, R.; Alves, D. C.; Fujita, T.; Chen, M.; Asefa, T.; Shenoy, V. B.; Eda, G., et al., Enhanced Catalytic Activity in Strained Chemically Exfoliated WS_2 Nanosheets for Hydrogen Evolution. *Nat. Mater.* **2013**, *12*, 850-855.

59. Eng, A. Y.; Ambrosi, A.; Sofer, Z.; Simek, P.; Pumera, M., Electrochemistry of Transition Metal Dichalcogenides: Strong Dependence on the Metal-to-Chalcogen Composition and Exfoliation Method. *ACS Nano* **2014**, *8*, 12185-12198.

Chapter 5. Correlative electrochemistry-microscopy of Li-ion (de)intercalation at series of individual $LiMn_2O_4$ particles

Lithium-ion batteries power all kinds of portable electronics, such as laptops, mobile phones, camera, etc., which greatly facilitate our daily life. Understanding the phenomena and fundamentals inside the battery, *e.g.*, the lithium-ion intercalation in the electrode materials are important and necessary for promoting the battery performance to a high level. Correlating microscopy with electrochemical data (cyclic voltammetry, galvanostatic charge/discharge, *etc.*) obtained on the same sample (same area, or even same particle) can avoid sample heterogeneity and uncertainty, allowing a direct structure-and-function relationship to be built, especially when electrochemistry can be performed at the nanoscale.

This chapter contains the manuscript and supporting information from a short *Communication* published in *Angewandte Chemie* (**Binglin Tao**, Lewis C. Yule, Enrico Daviddi, Cameron L. Bentley, and Patrick R. Unwin, *Angew. Chem. Int. Ed.* **2019**, 131, 4654-4659), where the electrochemical activities (both cyclic voltammetry and galvanostatic charge and discharge) of individual $LiMn_2O_4$ particles have been measured. Binglin Tao was responsible for design the experiment, collection of data and preparation of the manuscript. Lewis C. Yule helped with the Matlab script to process the data. Enrico Daviddi supported with the galvanostatic charge-discharge technique. Cameron L. Bentley was a postdoctoral researcher supervising on this project and revised the manuscript in this chapter.

Correlative electrochemistry-microscopy of Li-ion (de)intercalation at series of individual $LiMn_2O_4$ particles

Binglin Tao, Lewis C. Yule, Enrico Daviddi, Cameron L. Bentley* and Patrick R. Unwin*

Department of Chemistry, University of Warwick, Gibbet Hill Road, Coventry, UK

***Corresponding Author**

c.bentley.1@warwick.ac.uk, p.r.unwin@warwick.ac.uk

5.1 Abstract

The redox activity (Li-ion intercalation/deintercalation) of a series of individual $LiMn_2O_4$ particles of known geometry and (nano)structure, within an array, is determined using a correlative electrochemical microscopy strategy. Cyclic voltammetry (current voltage curve, *I*-*E*) and galvanostatic charge/discharge (voltage time curve, *E*-*t*) is applied at the single particle level, using scanning electrochemical cell microscopy (SECCM), together with co-location scanning electron microscopy that enables the corresponding particle size, morphology, crystallinity, and other factors to be visualized. This study identifies a wide spectrum of activity of nominally similar particles, and highlights how subtle changes in particle form can greatly influence electrochemical properties. SECCM is well suited to assessing single particles and constitutes a combinatorial method that will enable the rational design and optimization of battery electrode materials.

5.2 Introduction

As a promising Li-ion battery cathode material in both aqueous and organic electrolytes, spinel $LiMn_2O_4$ has attracted much attention in recent years due to its large theoretical capacity, high abundance and nontoxicity,[1] although a number of problems remain to be resolved.[2-4] As with much research in electrochemistry, macroscale electrochemical measurements have mainly been used to study battery materials, which for complex composite electrodes include contributions from the conductive agent, adhesive, as well as the active material.[5-6] Local structure-activity relationships for battery materials are still somewhat unexplored in regards to individual active particles or particle agglomerates.[7]

Indeed, the dispersion in activity among particles, and the relation to particle topology and structure, has largely remained elusive. This paper addresses this issue head on, through the use of a strategy that enables the structure and electrochemical activity of individual particles to be measured and compared directly.

In order to rationally design battery electrodes, and electroactive materials in general, strategies that enable local redox activity and electrode structure to be related directly are highly valuable.[8-9] In addition to some optical approaches (*e.g.*, plasmonic imaging[10-11]) emerging *in situ* scanning electrochemical probe microscopy (SEPM)[12] techniques are also promising in being able to provide insight into the structural factors controlling the electrochemical behaviour of battery electrode materials. Within the SEPM family, scanning electrochemical microscopy (SECM) has been the most widely used in Li-ion battery research, especially for probing the electrically insulating solid electrolyte interphase (SEI), although mainly on the scale of tens microns.[13-14] Scanning ion conductance microscopy (SICM) offers much higher spatial resolution and has been used to visualize ion flux spatial-heterogeneities in tin and silicon anodes in Li-ion batteries.[15] It is worth noting that both SECM and SICM collect electrochemical information about an electrode substrate by monitoring the spatially-dependent concentrations/fluxes of reactant, product or intermediates at a scanning electrode tip.

By contrast, in SECCM, electrochemistry is probed *directly and locally* at a substrate electrode, with a spatial resolution defined by the area of meniscus contact, and with the possibility of synchronous co-location topographical mapping.[8, 16] In the context of battery research, this technique has previously been used to electrochemically interrogate thin films of (insulating) Li_2O_2,[17] as well as small populations of $LiFePO_4$ particles (*ca.* 10 particles).[7, 18] In this study, SECCM has been deployed in a single-channel nanopipette configuration to investigate the electrochemical behavior of individual $LiMn_2O_4$ particles within an ensemble, which were visualized, post-experiment, by co-located scanning electron microscopy (SEM).

5.3 Experimental Section

5.3.1 Chemical Reagents and Electrode Preparation

Lithium manganese oxide ($LiMn_2O_4$, electrochemical grade) and lithium chloride (LiCl, ≥ 99 %) were purchased from Sigma-Aldrich, and used as received. Deionized water (resistivity ≥18 MΩ • cm) was produced by a Purite Integra HP system (U.K.). The glassy carbon (GC) plate was purchased from Alfa Aesar, and polished with 0.05 μm diamond suspension (Bueler, U.S.A.) prior to use. To prepare the working electrode, $LiMn_2O_4$ was sonicated in deionized water for 10 min, and then 1 μL of the suspension was drop casted onto the GC substrate. The silver/silver chloride (Ag/AgCl) quasi reference counter electrode (QRCE) was prepared by anodic polarization of an Ag wire (0.125 mm diameter, Goodfellow, 99.99 %) in saturated KCl solution. The QRCE potential was calibrated against a commercial saturated calomel electrode (SCE) in 1.0 M LiCl solution before and after each experiment, and was found to possess a stable reference potential of ± 0.005 V *vs.* SCE.

The composite battery macro-electrode (working electrode) was prepared as follows: active material (85 wt%), acetylene black (10 wt%)and polytetrafluoroethylene (PTFE, 5 wt%) aqueous suspension were mixed together, followed by sonication treatment for 20 min and drying for 1 h. Approximately 2.8 mg of the mixture was impregnated into a stainless titanium grid with area of 1 cm^2 and then pressed under 5 MPa pressure to fabricate the electrode. The working electrode was soaked with 1.0 M LiCl solution (electrolyte) overnight, prior to use to ensure completing wetting.[19]

5.3.2 Instrumentation

Single channel nanopipettes with diameter of 500 nm and 8 μm were prepared using a CO_2 laser puller (P-2000, Sutter Instruments, U.S.A.). The former were pulled from glass capillaries (GC120F-10 1.2OD×0.69×100 mm, Harvard Apparatus, U.S.A.) with a two-step protocol. For the first step, the parameters were heat 350, filament 3, velocity 40 and delay 220. For the second step, the parameters were heat 350, filament 3, velocity 40, delay 180 and pull 100. The dimensions of the nanopipette orifice were measured using scanning electron microscopy (SEM) on a Zeiss Supra 55VP system, which was operated at an accelerating

voltage of 2 kV. Typically, the diameter of the nanopipette probe was 500-600 nm. The latter were pulled from glass capillaries (GC120F-10 1.0OD×0.58×100 mm, Harvard Apparatus, U.S.A.), and a one-step protocol was exploited. The parameters were heat 350, filament 3, velocity 40 and delay 220. Single channel nanopipettes with diameter of 50 µm were pulled from glass capillaries (GC120F-10 1.0OD×0.58×100 mm, Harvard Apparatus, U.S.A.) using a PC-10 puller (Narishige Group, Japan) with a two-step protocol. For the first step, the parameters were heater 70, weight 3, and slider 8. For the second step, the parameters were heater 55, weight 3, and slider 4. After pulling, the nanopipette probes were filled with a 1 M LiCl solution using a MicroFil syringe (World Precision Instrument Inc., U.S.A.), and a QRCE was inserted from the back.

Macroscale 'bulk' electrochemical experiments were carried out in the 3-electrode format (graphite rod and commercial Ag/AgCl reference electrodes for counter and reference electrodes, respectively) on a CHI 660D electrochemical work station. All experiments in the SECCM configuration were carried out on a home-built scanning electrochemical probe microscopy (SEPM) platform.[17, 20] As shown schematically in **Figure 5.5**, in this configuration, the prepared nanopipette probe and substrate of interest were mounted on a z-(P-753.3CD, Physik Instrumente, Germany) and *xy*-(P-622.2CD, Physik Instrumente) piezoelectric positioners, respectively, which were controlled by amplifier modules (E-665 and E-500, respectively). Coarse and fine control of the nanopipette probe with respect to the substrate surface was achieved with micropositioners and piezoelectric positioners (detailed above), respectively. The SECCM cell and all piezoelectric positioners were placed in an aluminum Faraday cage, which was installed on an optical table (RS2000, Newport, U.S.A.) with automatic leveling isolators (Newport, S-2000A-423.5).During experiments, the current was measured every 4 µs, and averaged 513 times to give a data acquisition rate of 2.052 ms per point. This current signal was typically filtered using an 8th order low-pass filter at a time constant of 2 ms. Data acquisition and fine control of the whole system was achieved on a Field Programmable Gate Array (FPGA) board (PCIe-7852R) controlled by a Labview 2016 (National Instruments, U.S.A.) interface running the Warwick Electrochemical Scanning Probe Microscopy (WEC-SPM,www.warwick.ac.uk/electrochemistry) software.

5.3.3 Scanning Protocols

Electrochemical measurements on the substrate (working electrode) were performed using three different 'scan hopping' modes, including 'scan hopping with cyclic voltammetry', 'scan hopping with current-time' and 'scan hopping with galvanostatic charge-discharge'. Taking 'scan hopping with cyclic voltammetry' as an example (see below, Supporting Information **Figure 5.6**), the nanopipette (meniscus cell) was approached to the surface of interest at an approach rate of 3 μm/s, during which the current was monitored constantly. Upon landing, *i.e.*, when an electrochemical cell was formed between the nanopipette and sample surface through the meniscus, the approach was stopped immediately after detecting a threshold current of 1.2 pA (set to be slightly larger than the noise level). It should be noted that the nanopipette probe itself did not physically contact with the substrate. After detecting the surface, a local cyclic voltammetric experiment was performed, following which the nanopipette was retracted 5 μm from the surface. The nanopipette was subsequently moved to next predefined pixel, located 1.5 or 2 μm from the previous point, set by the predefined 'hopping distance'. At each pixel, the vertical extension of the nanopipette (z-coordinate) and electrochemical signals (potential, *E* and current, *i*) were recorded synchronously, effectively building up topographical and voltammetric 'activity' maps, respectively. The working principles of 'scan hopping with current-time' and 'scan hopping with galvanostatic charge-discharge' were very similar, except chronoamperometry or galvanostatic charge-discharge (chronopotentiometry) was carried out as substitutes for cyclic voltammetry at each pixel. After the SECCM scanning experiments, the probed (working electrode) area was determined by imaging the droplet footprint left behind at each pixel with SEM (Zeiss Gemini 500).

5.3.4 Data Processing

After collection, the raw data were processed with Matlab R2015b software package. Sample tilt was removed using SPIP v. 6.0.14 software package. Data plotting was performed using Matlab R2015b and OriginPro 2016 software packages. It should be noted that cyclic voltammograms presented in the main text have been smoothed by averaging with 10 adjacent points.

5.4 Results and Discussion

SECCM was deployed in hopping mode,[8, 21] as shown schematically in **Figure 5.1a** (labelled in Supporting Information, Section 1, **Figure 5.5**). In this configuration, a nanopipette probe, containing 1.0 M aqueous LiCl as the electrolyte and a AgCl-coated Ag wire as a quasi-reference counter electrode (QRCE), was approached to the substrate (working electrode) surface to make meniscus contact at a series of predefined locations in a grid (Supporting Information, **Figure 5.6**). At each landing, local electrochemical measurements (*I*-*E*, or *E*-*t*) were made within the confined area defined by the meniscus cell (the probe itself did not make physical contact with the surface). Herein, the substrate was prepared by drop casting spinel $LiMn_2O_4$ particles onto glassy carbon, GC (see Supporting Information, **Figure 5.7**).

To explore the Li^+ storage mechanism at individual $LiMn_2O_4$ particles, as well as visualize the dispersion in activity within an active ensemble, spatially-resolved cyclic voltammetry was performed on the as-prepared $LiMn_2O_4$/GC electrode. Starting at 0 V *vs.* Ag/AgCl, the potential was swept between 0 to 1.25 V at a rate of 1 V/s. As shown in **Figure 5.1b**, a relatively featureless cyclic voltammogram (CV) was obtained on the GC support, with processes encountered at extreme anodic and cathodic potentials attributable to carbon corrosion[22] and the oxygen reduction reaction (ORR),[23] respectively. Thus, the electrochemical stability window of GC was estimated to be ~1.8 V under these conditions. **Figure 5.1c** depicts a 'representative' CV obtained at a single $LiMn_2O_4$ particle, encapsulated by the meniscus (droplet) cell. Li^+ (de)intercalation chemistry at $LiMn_2O_4$ can be expressed by the following equation

$$LiMn_2O_4 = x\ Li^+ + x\ e^- + Li_{1-x}Mn_2O_4 \quad (1)$$

where typically $0<x<1$.[24] During the charging process (Eq. 1, forward), Li^+ is extracted from the structural framework of $LiMn_2O_4$, coinciding with the oxidation of Mn (III) to Mn (IV). This corresponds to the sweep in the positive direction, where two redox peaks located at 0.89 and 1.01 V *vs.* Ag/AgCl (1.0 M LiCl) can be assigned to Li^+ extraction from tetrahedral lattice sites in the presence and absence of Li-Li interaction, respectively.[24] The reverse processes (Eq. 1, reverse) occurred during discharge, with the two peaks at 0.69 and 0.89 V in the negative sweep corresponding to the respective two different Li^+ insertion processes. In

addition, no undesirable side (parasitic) reactions are observed at high potentials, demonstrating that the oxygen evolution reaction does not occur on $LiMn_2O_4$ in this potential range.[25] It is interesting to note that this scan rate (v) is 2-4 orders-of-magnitude larger than employed in bulk electrochemical experiments with the same material (v = 0.1 to 10 mV/s),[26] and yet the (de)intercalation processes are facile. This indicates that in 'traditional' composite electrode configuration, the achievable (de)intercalation rates are largely governed by the rate of electron transfer between the auxiliary elements (*e.g.*, binder and carbon black) and electroactive components (*vide infra*). Note that low currents passed during measurement in SECCM make it relatively unsensitive to resistance arising from the sample itself (*e.g.*, low intrinsic conductivity or contact resistance), making this technique ideal for the study of a diverse range of (semi)conductive materials.[8, 27]

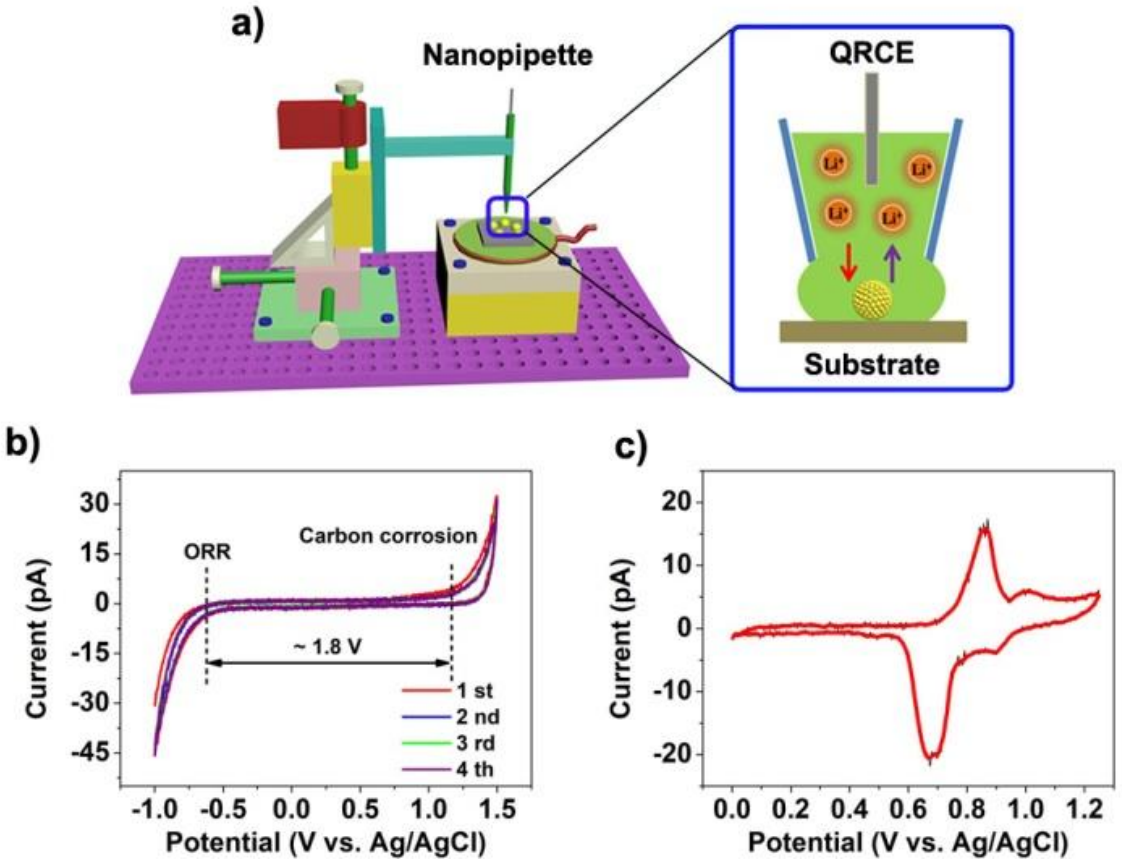

Figure 5.1 (a) Schematic showing the sub-microscale electrochemical measurements performed on single $LiMn_2O_4$ particles using SECCM. On the right is an enlarged diagram of the probe-particle-support interface at a single pixel of a scanning experiment, where an individual $LiMn_2O_4$ particle is fully encapsulated by the meniscus cell. **(b)** Four SECCM CVs

obtained at the GC support and **(c)** a typical CV obtained from a single $LiMn_2O_4$ particle. Experiments performed in 1 M LiCl, with a 500 nm diameter probe, at a scan rate (v) of 1 V/s.

Individual $LiMn_2O_4$ particles within the ensemble were probed in an automated fashion by performing a 'hopping mode' SECCM scan in the voltammetric mode, where each hop corresponds to an independent, spatially-resolved CV experiment.[21, 27] The hopping distance (*i.e.*, distance between each landing/pixel) was 1.5 µm, which ensured each measurement spot was independent of the last. An SEM image of the probed area, post-scan, is shown in **Figure 5.2a** (also shown enlarged in Supporting Information, **Figure 5.8**). Evidently, the probed area is predominantly GC (individual droplet 'footprints' visible in the scan area), with a collection of $LiMn_2O_4$ particles scattered throughout. Comparison with the SECCM topographical (z-height) map in **Figure 5.2b**, 18 pixels with 'elevated' topography have been revealed, each corresponding to an isolated $LiMn_2O_4$ particle or agglomerates (see below). The coincidence between the location of the particles (**Figure 5.2a**) and the higher points in the topography map (**Figure 5.2b**) gives confidence in the SECCM technique in being able to identify particles *in-situ*.

A spatially resolved CV-SECCM movie (current maps as a function of potential) obtained on the $LiMn_2O_4$/GC ensemble electrode (60 × 60 µm^2, 40 × 40 pixels) is shown in the Supporting Information, Movie S1. The magnitude of the anodic and cathodic currents (*i.e.*, 'peak current') obtained at each individual 'active' pixel is comparable throughout, signifying that Li^+ (de)intercalation is relatively reversible (*vide infra*). **Figure 5.2c** and d depict two frames from the movie, taken from the anodic (forward) and cathodic (reverse) sweeps at potentials of 1.0 V and 0.6 V, respectively. Through correlation of the activity maps with the SEM image of the scan area (**Figure 5.2a**) and surface topography map (**Figure 5.2b**), it is obvious that the individual $LiMn_2O_4$ particles exhibit elevated currents compared to the relatively inert GC support. It should be noted that while a CV-scan hopping protocol was employed above, chronoamperometric (current time curve, *I-t*) waveforms can also be applied if only a single potential is of interest, as shown in Supporting Information, **Figure 5.9**.

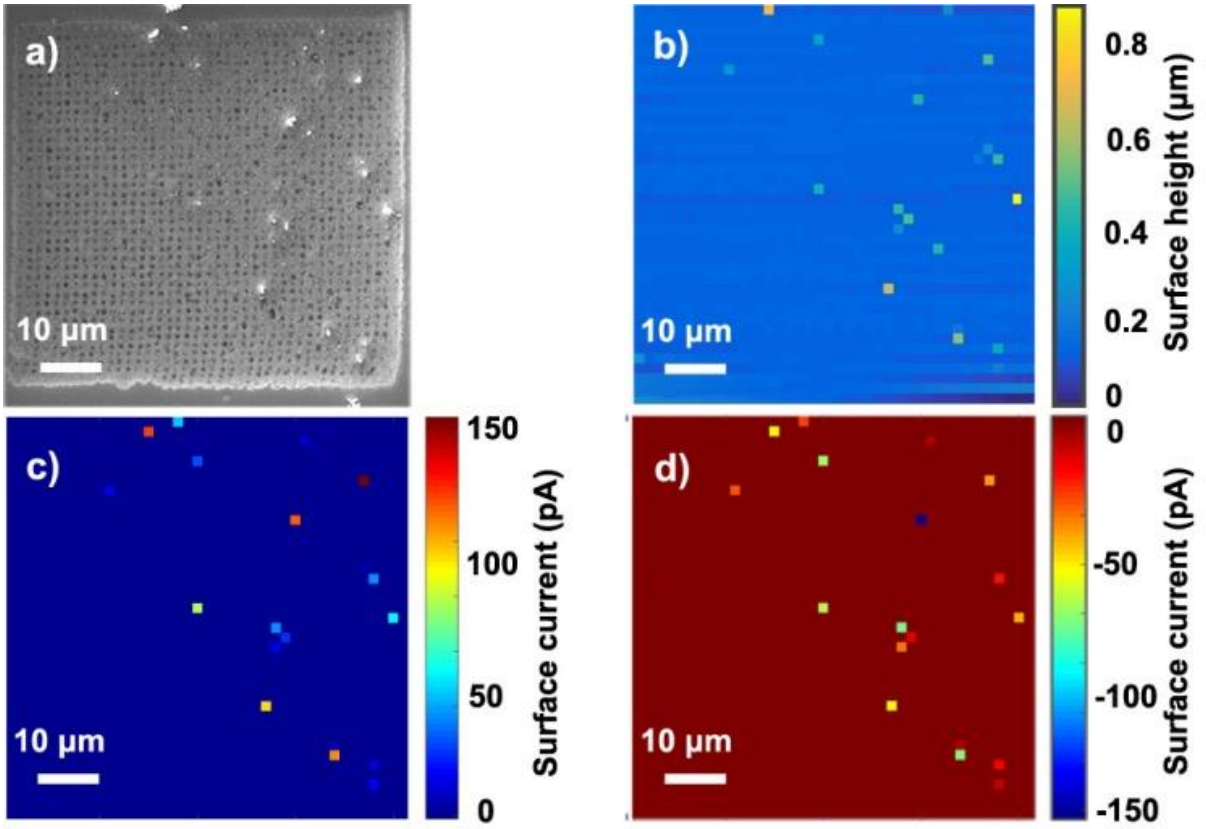

Figure 5.2 SECCM-CV measurements of individual and aggregated $LiMn_2O_4$ particles supported on GC. **(a)** SEM image and **(b)** topography (z-height) of the corresponding scanning area. Surface current maps obtained at **(c)** 1.0 V (forward sweep) and **(d)** 0.6 V (reverse sweep) during the anodic and cathodic scan, respectively.

The individual $LiMn_2O_4$ particles (including primary particles and agglomerated secondary particles) exhibit very different current magnitudes in **Figure 5.2c** and **d**, indicative of heterogeneous size and activity within the ensemble. Indeed, by extracting the individual CVs from each 'active' pixel, as shown in Supporting Information, **Figure 5.10**, it is clear that each particle/agglomerate presents a unique *I-E* profile, attributable to its physical heterogeneities (*e.g.*, particle size, composition, crystallinity, orientation, *etc.*), as demonstrated by the corresponding high-resolution SEM images in **Figure 5.11**. It is worth reemphasizing, the dispersion in *I-E* characteristics ('activity') among superficially similar particles (or agglomerates) is completely invisible in macroscopic (bulk) measurements, which reflect the 'average' response of the ensemble (*vide infra*). As the probed area (indicated by the individual droplet footprints) is only a little bit larger than the tip diameter (500 nm, see Supporting Information, **Figure 5.12**), some $LiMn_2O_4$ agglomerates cannot be fully

encapsulated by the SECCM meniscus. In order to treat the data semi-quantitatively (*i.e.*, active particle surface area is known, *vide infra*), the meniscus cell should totally encapsulate the particle during measurement, as shown schematically in **Figure 5.1a**. Thus, multiple scans were performed on different areas of the $LiMn_2O_4$/GC ensemble and only pixels where particles were small (or sparse) enough to be fully encapsulated by the meniscus were selected for comparison and quantitative analysis, as depicted in **Figure 5.3**. A further indication of the validity of this approach is that the overall peak currents fall within a fairly narrow range of *ca.* 30 - 70 pA, notwithstanding some variation in the peak potentials and overall CV morphology. Note that the size of the nanopipette probe could easily be tailored to accommodate encapsulation of larger particles, or smaller particle-to-particle separations.

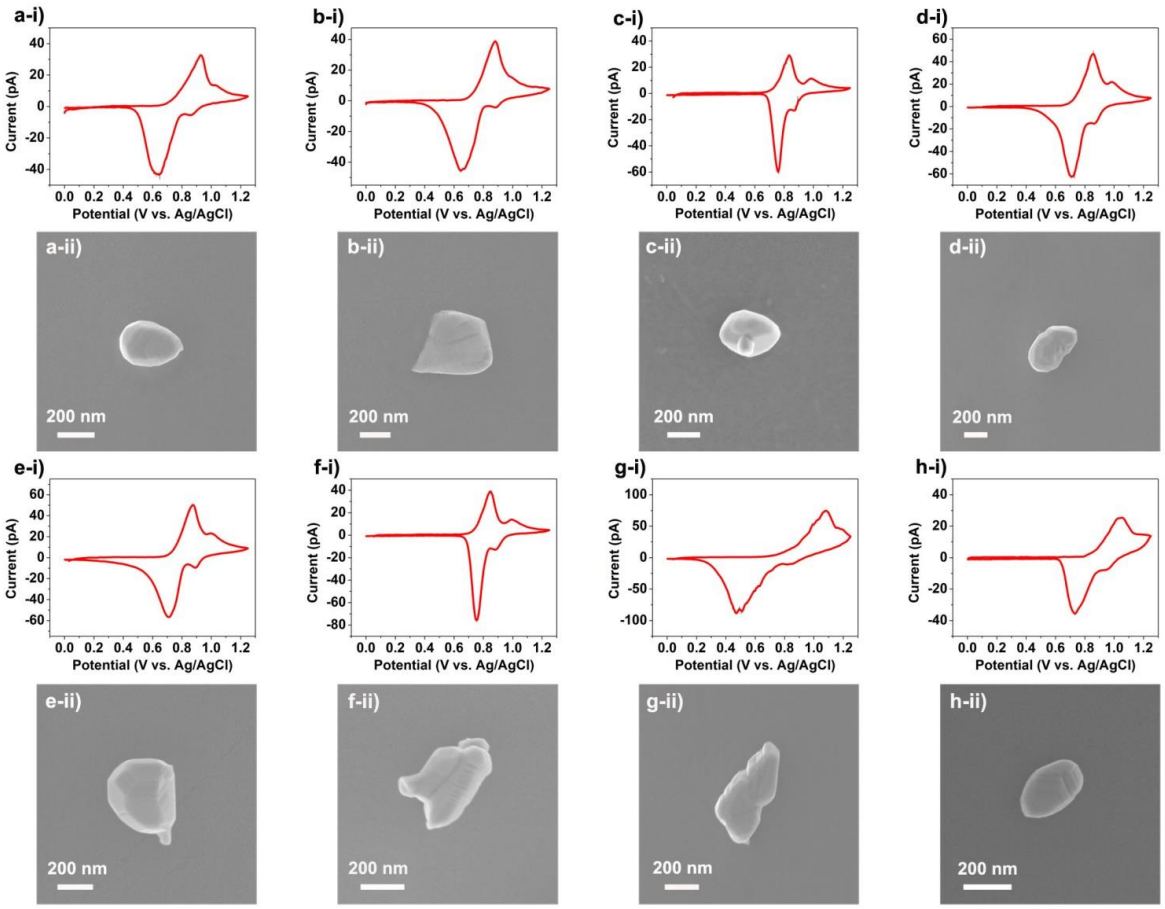

Figure 5.3 (i) CVs and **(ii)** corresponding SEM images from individual $LiMn_2O_4$ particles, **(a)** to **(h)**, supported on GC. The CV measurements (v = 1 V/s) were obtained by local ensemble measurements with SECCM, with a 500 nm diameter probe filled with 1 M LiCl.

The magnitude of the current measured at each pixel is governed by the size (*i.e.*, exposed surface area) of the $LiMn_2O_4$ particle, while the position and shape of the anodic and cathodic peaks, indicative of Li^+ (de)intercalation mechanism and kinetics, is governed by the particular properties (*i.e.*, composition, crystallinity and orientation) of the particle. It is important to note that the electrochemical behaviour of individual $LiMn_2O_4$ particles is highly heterogeneous, with the voltammetric peak morphology (position, separation and width) varying considerably throughout the ensemble. Some particles, such as particles g and h, exhibit very sluggish kinetics (*i.e.*, large peak-to-peak separations), which is not desirable for the application of this material as an active battery material. By comparison, particle c, which appears to be comprised of small crystallographic facets, exhibits fast kinetics, making it the ideal structure that should be pursued through the application of novel design principles. To further illustrate this point, detailed comparisons of the electrochemical properties (voltammetric peak potential and current, total charge and reduction to oxidation charges ratio) of each individual particle in **Figure 5.3** are summarized in the Supporting Information, Table 2. A particularly interesting observation is that the reduction to oxidation charges ratio (calculated by dividing the total reduction charge by the total oxidation charge) is higher than 100 % for all particles, which is ascribed to the Jahn-Teller effect.[28-29] In brief, partial of the Mn^{3+} can be further reduced to Mn^{2+} during the reverse scan (Li^+ intercalation process), which subsequently undergoes dissolution into the electrolyte. Thus, the material is over-reduced, resulting in enhanced cathodic charge and apparent reduction to oxidation charges ratio greater than 100 % during cycling. As the CV measurement only probes the near-surface processes (*i.e.*, only 10-30 % of the total capacity can be used), this phenomenon can carry on for multiple cycles without apparent capacity loss (see Supporting Information, **Figure 5.13**). Besides, the voltammetric peak-to-peak separation (ΔE_p) decreased during the multiple voltammetric cycling, indicating that the (de)intercalation processes become kinetically more facile at the single particle level.

To further clarify the relationship between 'single particle' and conventional 'macroscale' electrochemistry, voltammetry was performed on a composite (*i.e.*, material, binder and conductive additive) $LiMn_2O_4$ electrode (see Supporting Information, **Figure 5.14**). Note that in bulk only a fraction of the total capacity is accessed (e.g., 23 % at 5 mV s^{-1}) and the cathodic-to-anodic charge ratio is greater than 100 %, in agreement with the single-

particle measurements above, as well as previous reports.[25] Viewing these results alongside those from SECCM (**Figure 5.3**), it is very clear that the 'bulk' electrochemical response 'washes out' the unique properties of each individual $LiMn_2O_4$ particle. This contrasts with the SECCM measurements, which reveals the dispersion (heterogeneity) of activity at the single particle level. To illustrate this point further, the eight CVs in **Figure 3** were averaged (see Supporting Information, **Figure 5.15**) to produce a curve that superficially resembles (*i.e.*, two oxidation peaks observed at 0.8 and 1.0 V) the bulk 'ensemble' response. Small disparity can be observed between the averaged and bulk CV curves, as only a relatively small population of particles (N = 8) was probed, and the contribution from the auxiliary components cannot be ignored (*vide infra*). Cyclic voltammetry was also carried out at slow scan rates with large-sized tips (8 and 50 μm, see Supporting Information, **Figure 5.12**), which further explain the relationship between microscale and bulk measurements (see Supporting Information, **Figure 5.16**). At the same time, these results underline the importance of kinetic effects in Li^+ (de)intercalation reactions.

To complete this study, and highlight further the versatility of the SECCM approach, spatially-resolved galvanostatic charge-discharge measurements were performed at the single particle level, with an applied current of ± 5 pA for 1 s at each measurement point. Spatially-resolved, potential-time 'snapshots' (maps) obtained at different times and current polarities are presented in **Figure 5.17a-d**. Again, comparison of the maps with the corresponding SEM image in **Figure 5.17e**, it is clear different particles present different charge/discharge potentials, attributed to unique structural characteristics (*i.e.*, size and morphology). **Figure 5.17f** considers a representative *E-t* curve (galvanostatic charge/discharge profile) extracted from a single $LiMn_2O_4$ particle, where it is clear that the charge/discharge processes occur at a potential of *ca.* 0.75 V *vs.* Ag/AgCl, which is consistent with the peak position in the CVs shown in **Figure 5.3**. By contrast, at GC, the measured potential changes rapidly (nonfaradaic or capacitive charging current) before reaching the electrochemical window 'limits' highlighted in **Figure 5.1b**, as expected for an ideal polarizable electrode system.

Figure 5.4 depicts the galvanostatic charge-discharge measurements performed on individual $LiMn_2O_4$ particles (agglomerates) that again, are small enough to be fully

encapsulated by the SECCM meniscus (electrochemical cell). In line with the CV results above, each particle presents a unique *E-t* profile, with different charge/discharge potentials and ohmic (*IR*, where *R* is resistance) drops (*i.e.*, the potential difference between the charge/discharge plateau), as summarized in Table 1. Again, it needs to be reiterated that the dispersion in activity (*E-t* profiles in **Figure 5.4** or CVs in **Figure 5.3**) among superficially similar $LiMn_2O_4$ particles or agglomerates is a largely unexplored phenomenon that is obscured in traditional macroscopic measurements on composite electrodes. It should also be noted that the *IR* drop values are very low, especially considering the extremely high charge/discharge rates implemented here (*e.g.*, the *IR* drop was only *ca.* 20 mV at a C-rate of 279 C for particle b in **Figure 5.4**). This value is among the highest C-rates reported in the literature, with high rate performance Zn (up to 50 C) and Al (up to 500 C) ion battery electrodes being reported before.[30-31] As alluded to above, this indicates that in the 'traditional' composite electrode configuration, *IR* drop (and hence rate-performance limitation) is largely governed by the rate of electron transfer between the auxiliary elements (*e.g.*, binder and carbon black) and electroactive component(s), rather than Li^+ (de)intercalation into the individual $LiMn_2O_4$ particles. Thus, there remains great potential to further improve the rate capability in battery electrochemistry by new strategies to wire active particles, or by improving the electrode preparation method to enhance the charge transfer kinetics (see above).[32-34] Again, it needs to be reiterated that the timescale of these localized *E-t* experiments are orders-of-magnitude faster than that usually encountered in bulk electrochemical measurements (*i.e.*, 0.1 to 10 C rates), which is explored in detail in the Supporting Information, Section S2.

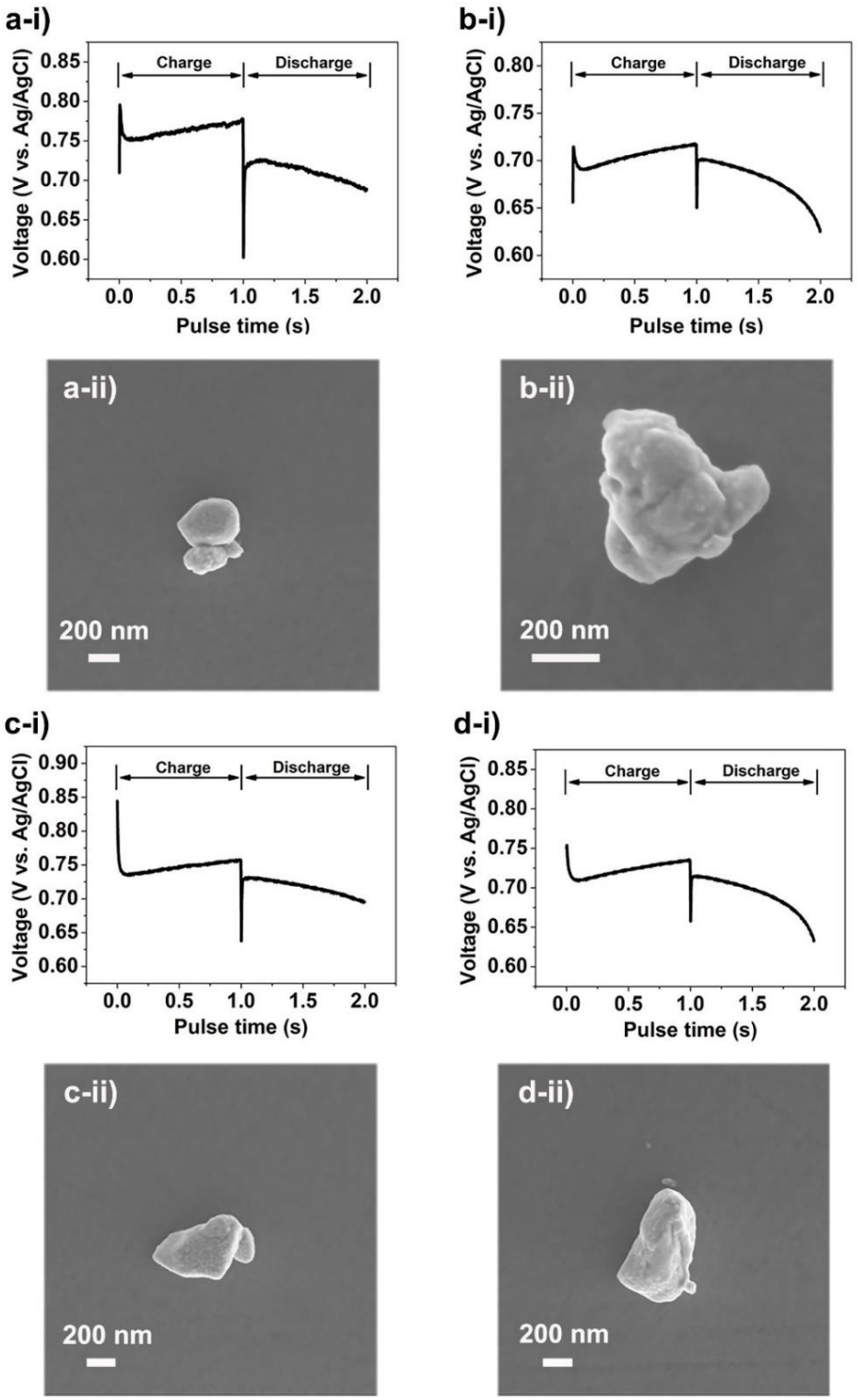

Figure 5.4 (i) Galvanostatic charge-discharge curves and **(ii)** corresponding SEM images from individual $LiMn_2O_4$ particles, **(a)** to **(d)**, supported on GC. The charge-discharge measurements (I = ± 5 pA) were obtained by local ensemble measurements with SECCM, with a 500 nm diameter probe filled with 1 M LiCl.

In summary, using a mobile meniscus cell in the SECCM configuration, we have been able to probe and compare the electrochemical activities of individual particles within an ensemble. This direct and local probe method has enabled characteristic features to be targeted and analysed precisely through a correlative approach with *ex situ* SEM. Specifically, in this work $LiMn_2O_4$, a promising Li-ion battery cathode material, has been revealed to possess significantly heterogeneous electrochemical behaviour [*i.e.*, Li^+ (de)intercalation processes] at the single particle level, attributable to differences between particle size, composition, crystallinity, orientation, *etc*. In addition, the dispersion in electrochemical activity revealed by these sub-microscale (single particle) measurements has allowed us to rationalize the macroscopic 'bulk' electrochemical response of complex composite battery electrodes.

Table 5.1 Physical and electrochemical characteristics of each particle investigated by galvanostatic charge/discharge.

Particle[a]	a	b	c	d
E_{charge} / V	0.763	0.705	0.747	0.723
$E_{discharge}$ / V	0.713	0.685	0.719	0.698
Volume[b] / $cm^3 \times 10^{-14}$	3.3	3.0	7.7	12.9
Capacity[c] / pC	73	64	168	282
C rate	247	279	107	64
IR drop / mV	50	20	28	25

[a] Particle labels correspond to those in **Figure 4**. [b] The volume of each particle was estimated based on the height (estimated from *z*-height topography), width and length (estimated from SEM image) by assuming the particle is an ellipsoid ($V = 4/3\pi abc$). [c] The capacity calculation process can be referenced from the Supporting Information, Section S2.

5.5 Conclusions

In the past few years, a number of *in situ/in operando* analysis tools have been established for the exploration of complex redox processes in battery materials.[35-36] However, to date, there have been relatively few reports of techniques that can provide information at single particle level, or possess the capability to distinguish variations in the electrochemical performance of individual active entities. The work presented herein demonstrates new capabilities of SECCM, which paves the way for the deep-investigation of electrode reaction processes in energy conversion/storage technologies. In the future, we aim to visualize any minute influence of (nano)structure (*e.g.*, crystallographic orientation) on redox activity and (de)intercalation kinetics through a combination of rational materials design and synthesis[37-38] and SECCM. This will be achieved by investigating mono-dispersed particles on TEM grids and then performing characterization by high-resolution analytical TEM.

5.6 Supporting Information

5.6.1 Supporting Figures

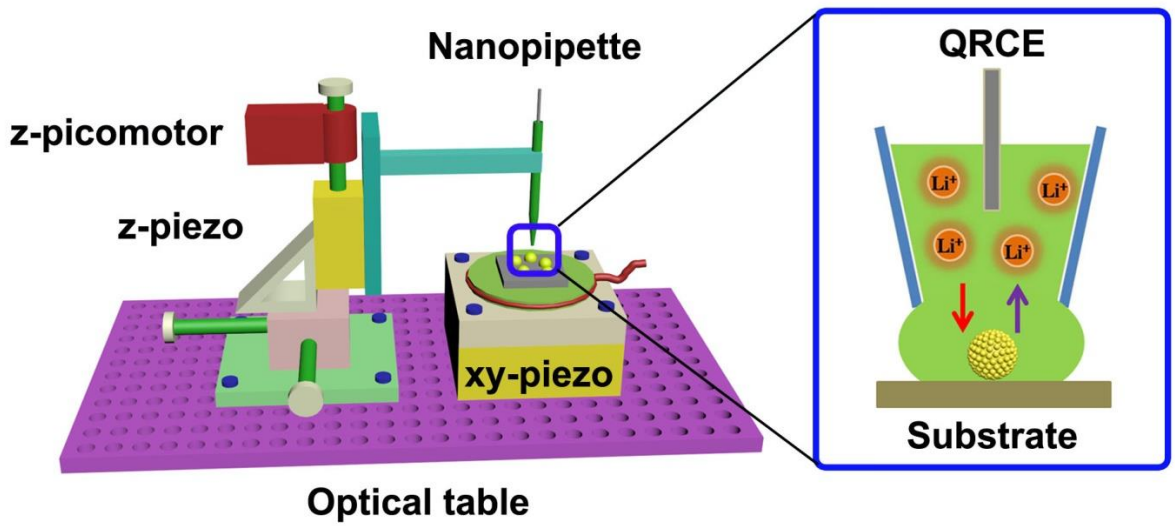

Figure 5.5 Labeled schematic of SECCM setup employed herein. The nanopipette probe is fixed to a z-piezoelectric positioner (fine movement, labelled z-piezo in the image), which is mounted on a z-picomotor and xy micropositioners for coarse movement. The sample is mounted on a xy-piezoelectric positioner (labelled xy-piezo in the image) for fine control of

lateral position. On the right is an enlarged diagram of the probe-particle-support interface during a single 'hop' of a scanning experiment. Electrochemical experiments are performed by applying a potential at the QRCE in the nanopipette barrel (with respect to ground), while measuring the current at the substrate surface (at ground).

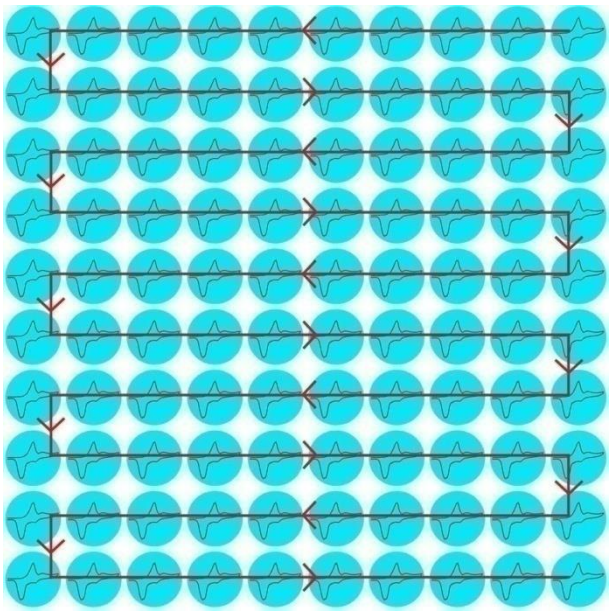

Figure 5.6 Schematic diagram illustrating the scanning route (red arrows) during a 'scan hopping with cyclic voltammetry' experiment. An independent cyclic voltammetric experiment is carried out at each and every point, building up a pixel-resolved activity map of the substrate. The blue circles represent the droplet 'footprint' (i.e., probed area of the meniscus cell).

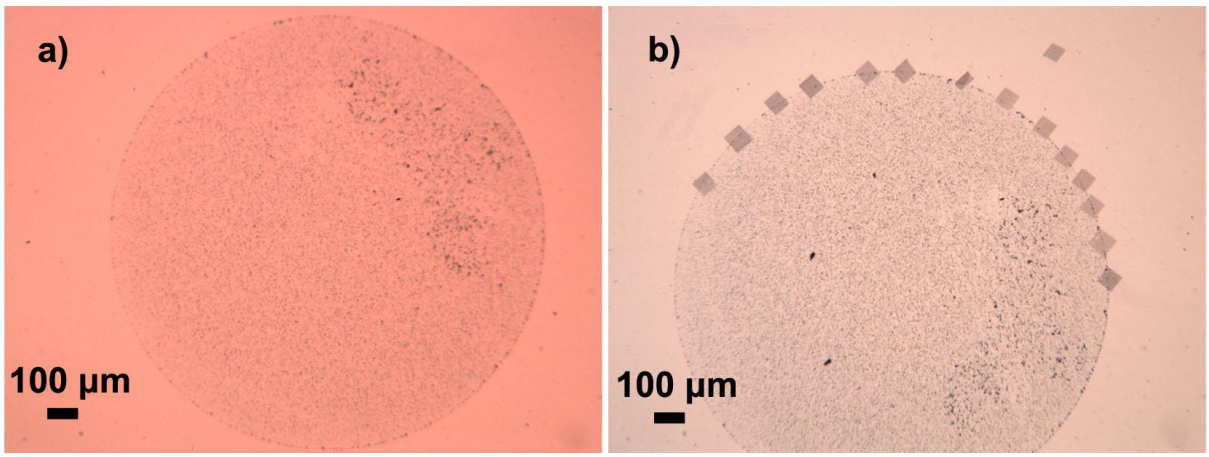

Figure 5.7 Optical micrograph of a $LiMn_2O_4$/GC electrode, which was prepared by drop-casting method. **(a)** and **(b)** were taken before and after SECCM scanning, respectively. Note

that there is a rotation of b, with respect to a by about 40-50°. The 'squares' in b are the arrays of dots of successful SECCM experiments, most of which were carried out at the border between the drop-cast region and GC substrate. One experiment was carried out on GC alone. One scan is rectangular rather than square, indicating an incomplete scan (This scan was stopped manually). Overall, Figure 5.7b, indicates the high success rate of SECCM scanning and the ability to position the tip in a desired area.

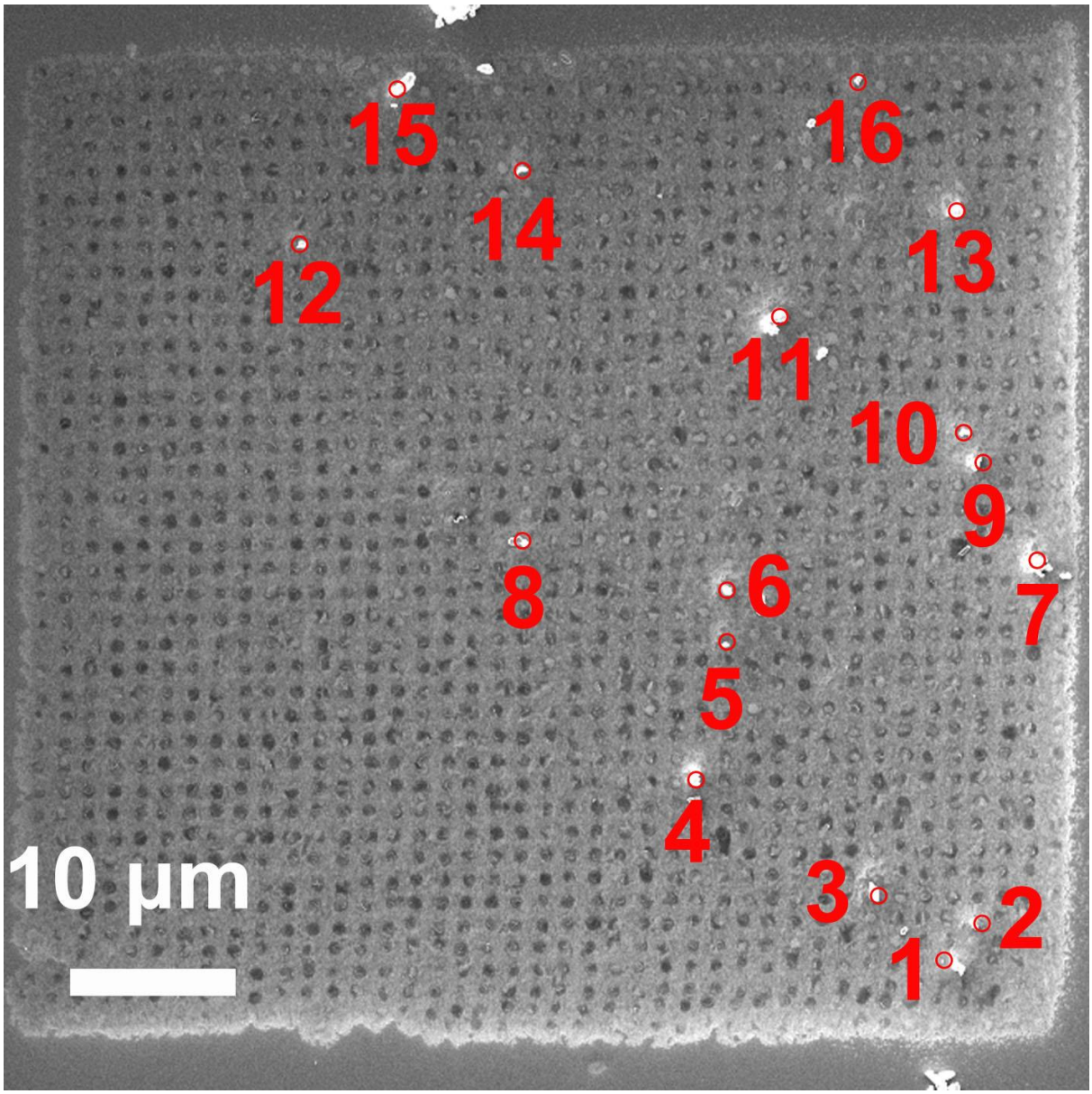

Figure 5.8 SEM image of the scanning area of the cyclic voltammetry measurements, as shown in Figure 5.2 of the main text. The red numbers correspond to the pixel-resolved CVs and corresponding SEM images of the $LiMn_2O_4$ particles, shown in Figure 5.10 and 5.11, respectively.

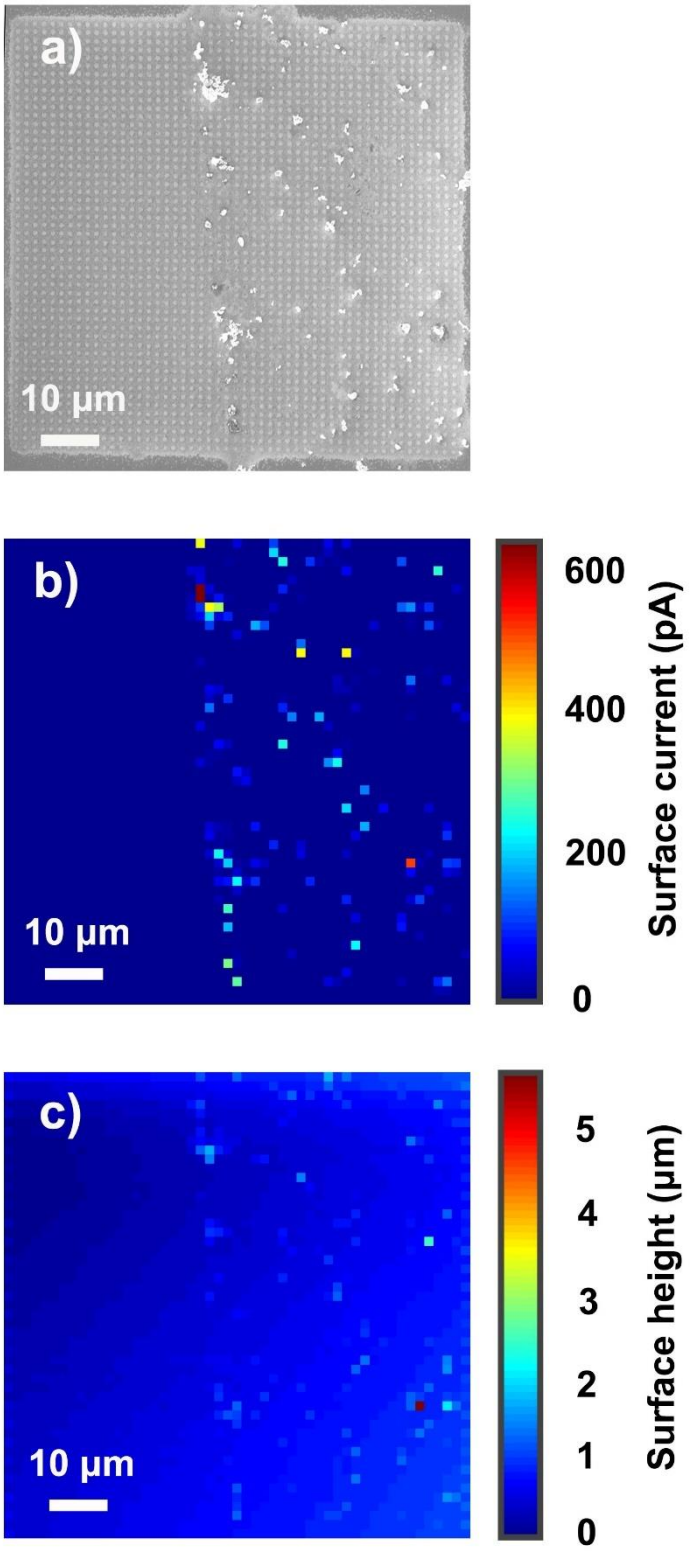

Figure 5.9 Chronoamperometric (I-t) SECCM measurements performed at individual and aggregated $LiMn_2O_4$ particles supported on GC at a fixed potential of +1.0 V vs. Ag/AgCl QRCE and pulse tine lasted for 1s. **(a)** SEM image, **(b)** surface current map at 0.5s and **(c)** topography of the corresponding scanning area.

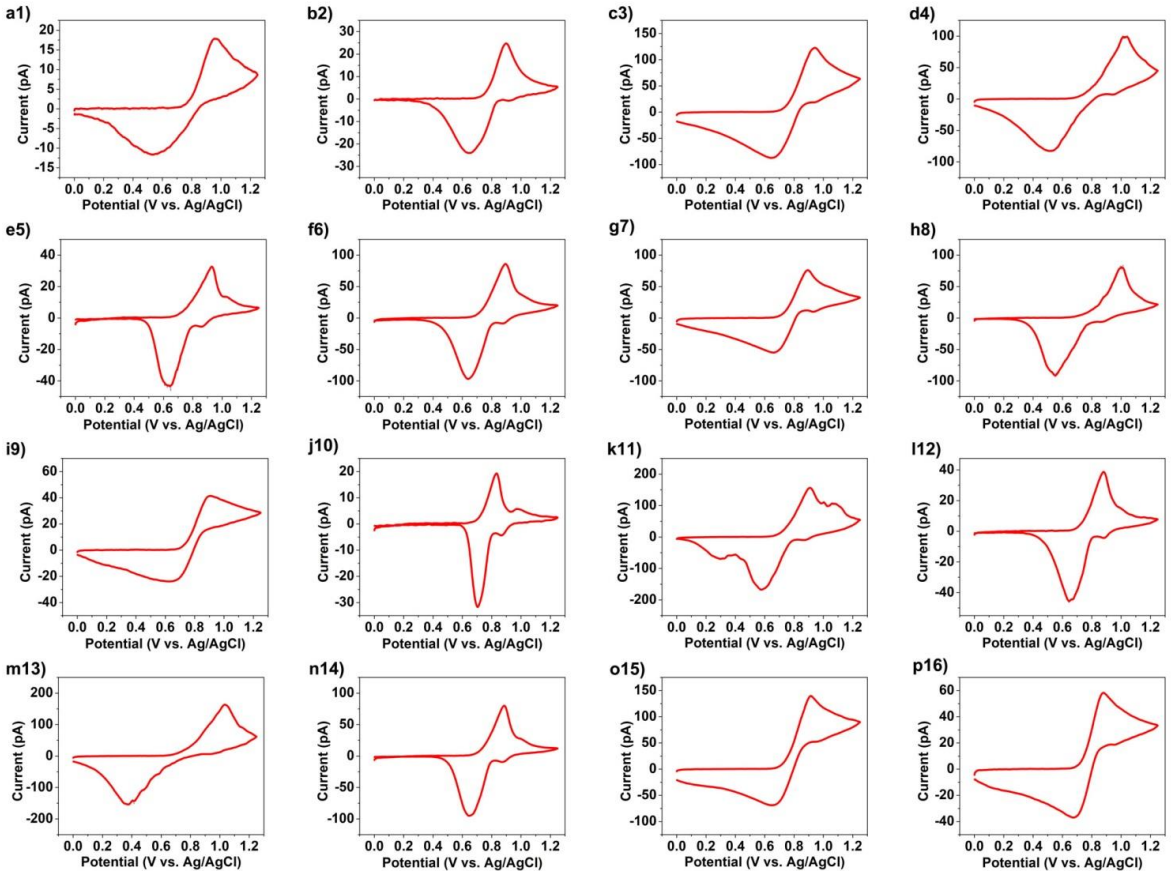

Figure 5.10 Sixteen independent cyclic voltammograms (CVs) obtained at the individual $LiMn_2O_4$ particles labeled in Figure 5.8, with corresponding high resolution SEM images shown in Figure 5.11. Note that these particles (or particle agglomerates) are not necessarily fully encapsulated by the meniscus (droplet) cell during scanning. These experiments were performed in 1 M LiCl, with a 500 nm diameter probe and at a scan rate (v) of 1 V/s.

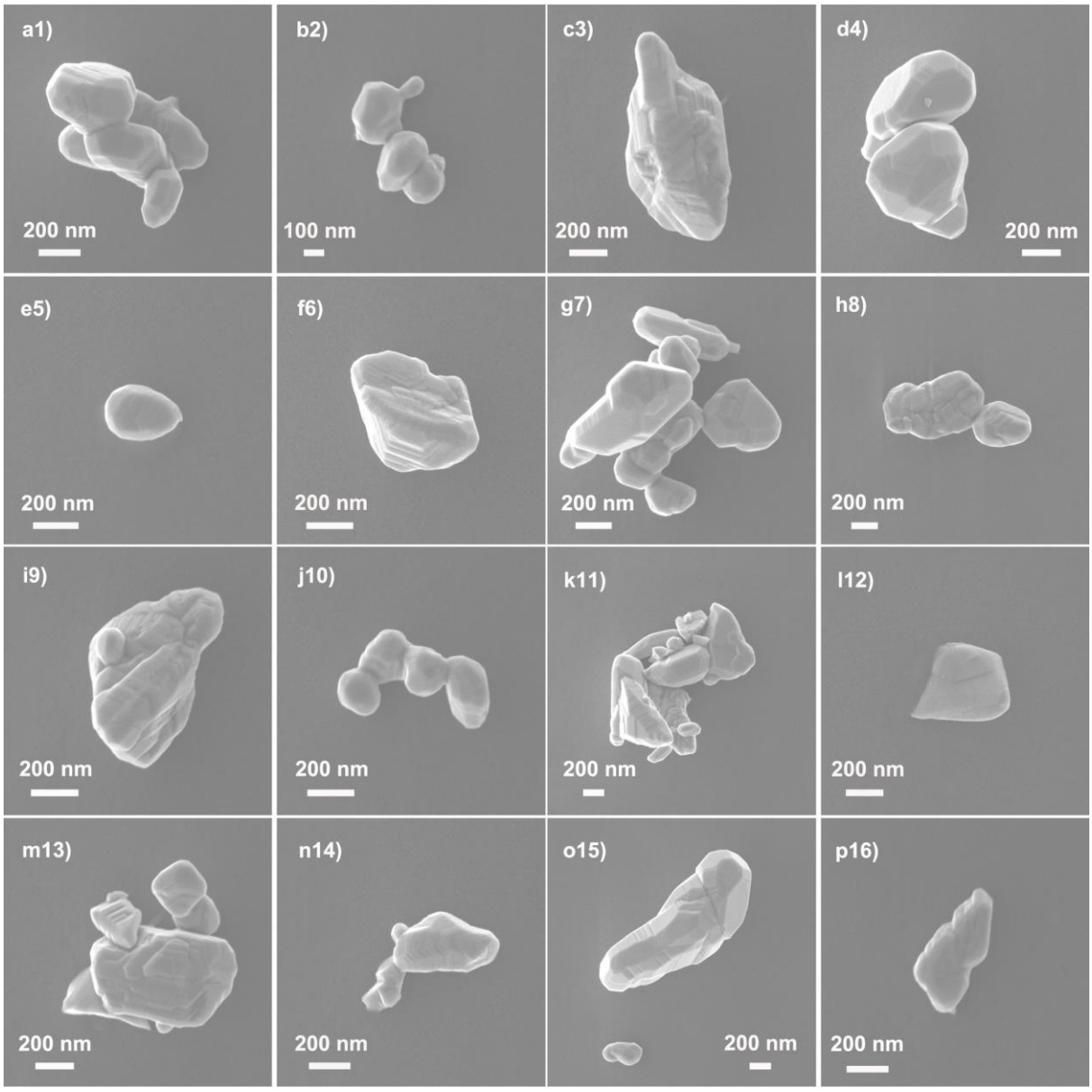

Figure 5.11 High resolution SEM images of individual $LiMn_2O_4$ particles probed with CV-SECCM, as shown in Figure 5.8 and 5.10.

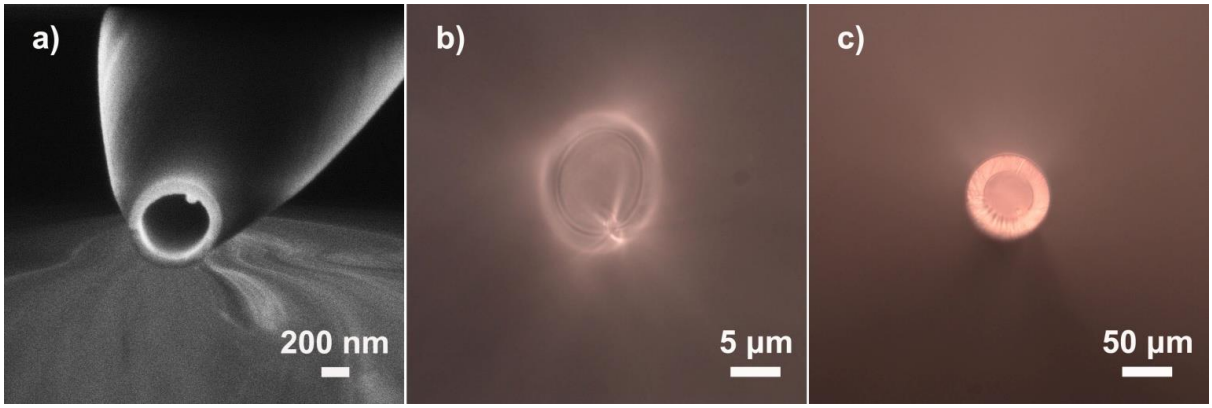

Figure 5.12 (a) SEM image of a representative nanopipette probe. The inner diameter of this tip is about 500 nm, and the inside filament could be observed clearly, indicating the robustness of the two-step pulling protocol. **(b)** and **(c)** Optical microscopic images of representative nanopipette probes with diameters of 8 and 50 µm, respectively.

Table 5.2 Electrochemical characteristics of the 8 $LiMn_2O_4$ particles shown in the main text Figure 5.3 and Supporting Information, Figure 5.13, derived from single-particle cyclic voltammetry measurements.

Particle	Oxidation peak					Reduction peak									
	E_{p1}/V	E_{p2}/V	i_{p1}/pA	i_{p2}/pA	Q/pC	E_{p1}/V	E_{p2}/V	i_{p1}/pA	i_{p2}/pA	Q/pC	ΔE_{p1} /V	ΔE_{p2} /V	Reduction to oxidation charges ratio/%	Volume[a] /cm^3×10^{-14}	Capacity usage/%[b]
a	0.93	1.04	33.00	13.78	6.39	0.64	0.87	43.27	5.41	8.73	0.29	0.17	136.62	1.01	29.1
b	0.88	1.00	38.50	15.25	7.63	0.66	0.89	44.59	4.62	10.00	0.22	0.11	131.06	2.09	16.7
c	0.83	0.98	29.24	11.48	5.14	0.76	0.82	59.74	13.00	6.13	0.07	0.16	119.26	2.28	10.3
d	0.86	0.98	46.92	22.2	9.67	0.71	0.87	62.12	15.04	11.61	0.15	0.11	120.06	2.80	15.8
e	0.87	1.00	50.84	23.26	10.16	0.71	0.89	57.06	9.81	12.92	0.16	0.11	127.17	3.77	12.3
f	0.85	0.99	39.2	14.43	6.79	0.75	0.88	75.56	13.43	7.81	0.10	0.11	115.02	2.41	12.9
g	1.08	0.17	73.74	46.86	15.82	0.47	0.83	86.83	10.36	24.1	0.61	0.34	152.34	4.50	16.1
h	1.04	-	24.94	-	5.63	0.73	0.95	35.62	7.80	6.96	0.31	-	123.62	1.22	21.1

E_p and i_p correspond to peak potential and current, respectively. The subscripts '1' and '2' denote the first and second pair of peaks, respectively. Q is the charge, calculated by integrating the peaks. ΔE_p is the peak-to-peak separation. Reduction to oxidation charge ratio was calculated as follows: $Q_{reduction}/Q_{oxidation} \times 100\%$. [a] The volume of the particle was

estimated based on the height (SECCM topography), length and width (SEM image). [b] Capacity usage = real capacity/theoretical capacity × 100%. The real capacity is calculated from the CV curve, while the theoretical capacity is calculated based on the volume.

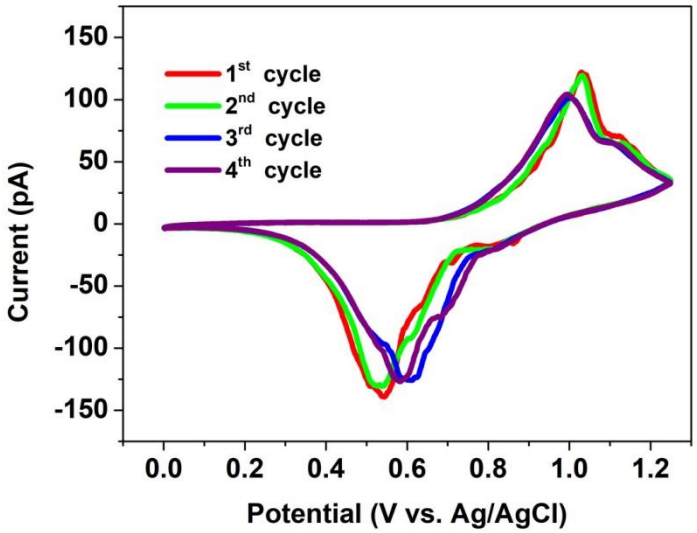

Figure 5.13 First 4 CVs obtained at individual $LiMn_2O_4$ particles. The experiment was performed at a scan rate (v) of 1 V/s. It should be noted that the peak position moved during the 3rd and 4th cycle, indicating the (de)intercalation reaction became much more facile.

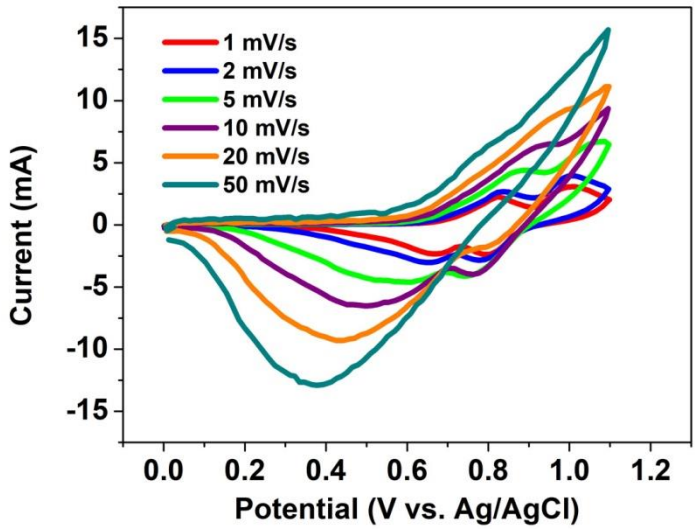

Figure 5.14 Macroscopic CVs obtained from a composite $LiMn_2O_4$ electrode, at scan rates ranging from 1 to 50 mV/s. Two pairs of (de)intercalation peaks can be observed only at slow

scan rates (less than 5 mV/s). This limitation in (de)intercalation kinetics is attributable to sluggish charge transfer within the complex composite electrode matrix, as addressed in the main text.

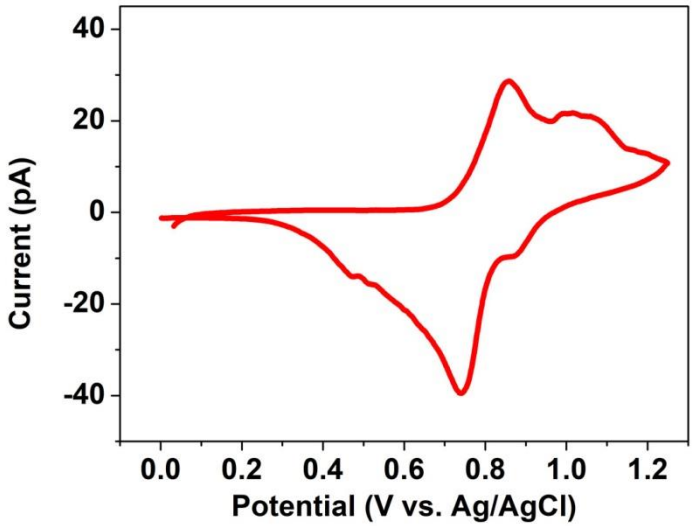

Figure 5.15 Averaged CV profile from 8 independent particles in Figure 5.3

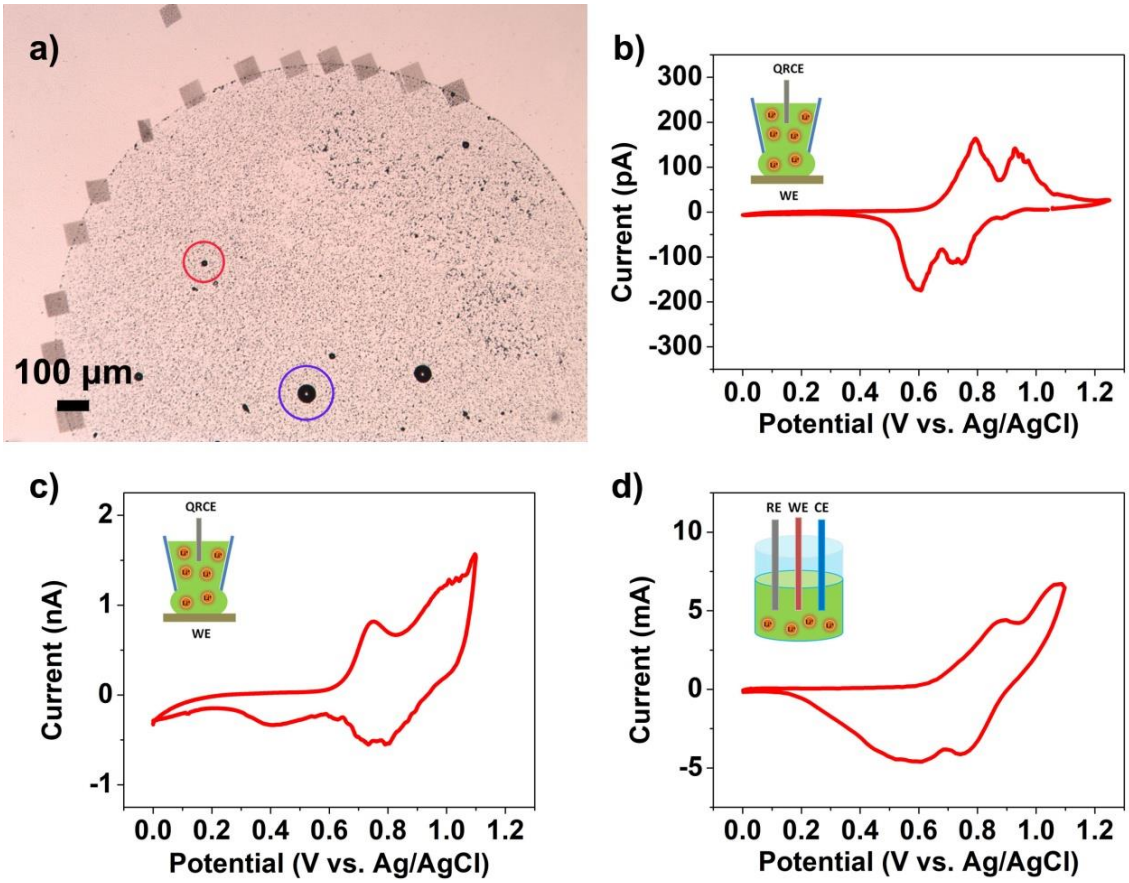

Figure 5.16 (a) Optical micrograph of a $LiMn_2O_4$/GC electrode. The red and blue circle represent the droplet 'footprint' (i.e., probed area of the meniscus cell) of measurements, with tip diameters of 8 and 50 µm, respectively. **(b)** Experiment performed with a tip of 8 µm in diameter, at a scan rate (v) of 20 mV/s. The CV profile shows two pairs of symmetrical peaks, which is almost the same with the bulk measurement at a scan rate of 1 mV/s (shown in Figure 5.14). **(c)** Experiment performed with a tip of 50 µm in diameter, at a scan rate (v) of 5 mV/s. **(d)** Bulk measurement performed at a scan rate (v) of 5 mV/s (extracted from Figure 5.14). The results from both microscale and bulk measurements are in accordance with each other, which rule out the possibility of contamination and underline the importance of kinetic effects in battery research.

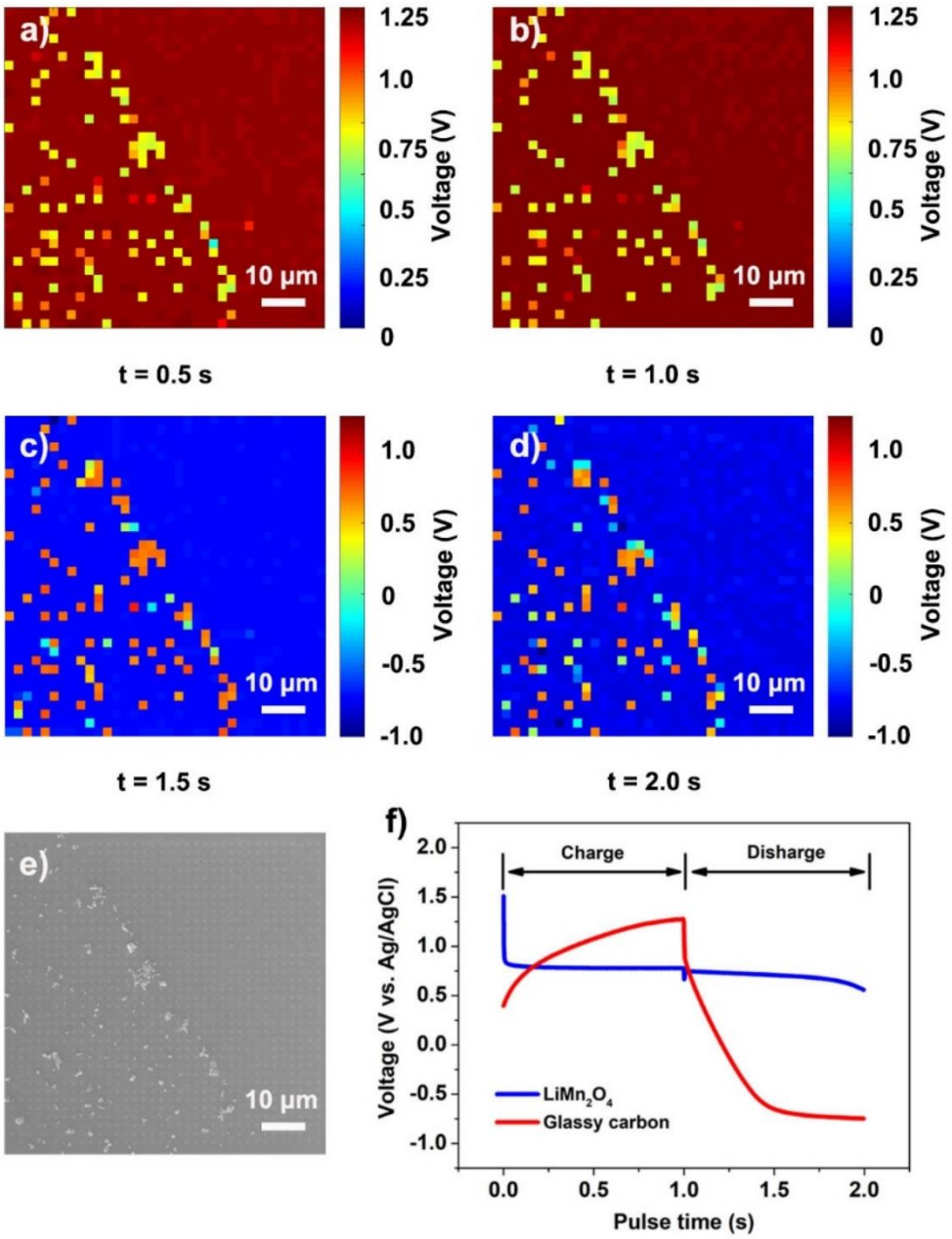

Figure 5.17 Galvanostatic charge-discharge measurements of individual and aggregated $LiMn_2O_4$ particles supported on GC. **(a)**, **(b)**, **(c)** and **(d)** spatially resolved potential images at different times of 0.5, 1.0, 1.5, and 2.0 s during galvanostatic charging-discharge, respectively. **(e)** SEM image of the corresponding scanning area. **(f)** Potential-time characteristics of GC (red) and $LiMn_2O_4$ particle (blue). The galvanostatic charge/discharge measurements were obtained by local ensemble measurements with SECCM, with a 500 nm diameter probe filled with 1 M LiCl.

5.6.2 Galvanostatic Charge/Discharge Process: Explanation and Calculations

Galvanostatic charge/discharge measurements performed in SECCM differ from the convention commonly applied for bulk electrochemical experiments.[39] In this work, if we assume that the $LiMn_2O_4$ particle is roughly spherical with 'average' diameter of 0.5 µm, then the volume of a typical particle would be:

$V=4/3*\pi r^3= 4\div3\times3.14\times (0.25)^3\ \mu m^3 = 0.065\ \mu m^3 =0.65 \times 10^{-13}\ cm^3$

Note that the actual volume of each particle can be estimated based on the height (estimated from z-height topography), width and length (estimated from SEM image) by assuming the particle is an ellipsoid (V = 4/3πabc), as shown in Table 1, main text. Considering the capacity and density are 148 mAh/g and 4.1 g/cm^3, respectively,[40] the theoretical volumetric capacity (C_v) of these $LiMn_2O_4$ particles is *ca.* 600 mAh/cm^3. Thus, if we want to fully charge/discharge each individual particle, the total charges (Q_t) we that we would need to apply are:

$Q_t= 0.65 \times 10^{-13}\ cm^3\times 606.8\ mA\ h/cm^3 = 0.395\times 10^{-10}\ mA\ h = 0.0395\ pA\ h = 142.2\ pA\ s$

In the SECCM configuration, as we only apply a small current and short contact time with the pipette (Q = 5 pA s), the particle are only charged/discharged a small fraction of the total (volumetric) capacity. As a result, a relatively constant *E-t* profile is observed, centred around a potential of *ca.* 0.75 V *vs.* Ag/AgCl. For comparison, in macroscale tests, C-rates ranging from 0.1 C to 10 C (*i.e.*, 10 hours to 0.1 hour charge/discharge time, respectively) are usually performed to fully charge/discharge the battery electrode.[41-42]

5.7 References

1. Amine, K.; Liu, J.; Kang, S.; Belharouak, I.; Hyung, Y.; Vissers, D.; Henriksen, G., Improved Lithium Manganese Oxide Spinel/Graphite Li-Ion Cells for High-Power Applications. *Journal of Power Sources* **2004**, *129*, 14-19.

2. Jang, D. H., Dissolution of Spinel Oxides and Capacity Losses in 4 V $Li/Li_xMn_2O_4$ Cells. *Journal of The Electrochemical Society* **1996**, *143*, 2204.

3. Yamada, A., Lattice Instability in $Li(Li_xMn_{2-x})O_4$. *Journal of Solid State Chemistry* **1996**, *122*, 160-165.

4. Lee, H.W.; Muralidharan, P.; Ruffo, R.; Mari, C. M.; Cui, Y.; Kim, D. K., Ultrathin Spinel Limn2o4 Nanowires as High Power Cathode Materials for Li-Ion Batteries. *Nano Letters* **2010**, *10*, 3852-3856.

5. Huang, H., Correlating Capacity Loss of Stoichiometric and Nonstoichiometric Lithium Manganese Oxide Spinel Electrodes with Their Structural Integrity. *Journal of The Electrochemical Society* **1999**, *146*, 3649.

6. Jaber-Ansari, L., et al., Suppressing Manganese Dissolution from Lithium Manganese Oxide Spinel Cathodes with Single-Layer Graphene. *Advanced Energy Materials* **2015**, *5*, 1500646.

7. Snowden, M. E.; Dayeh, M.; Payne, N. A.; Gervais, S.; Mauzeroll, J.; Schougaard, S. B., Measurement on Isolated Lithium Iron Phosphate Particles Reveals Heterogeneity in Material Properties Distribution. *Journal of Power Sources* **2016**, *325*, 682-689.

8. Bentley, C. L.; Kang, M.; Unwin, P. R., Nanoscale Structure Dynamics within Electrocatalytic Materials. *Journal of the American Chemical Society* **2017**, *139*, 16813-16821.

9. Bentley, C. L.; Kang, M.; Unwin, P. R., Nanoscale Surface Structure–Activity in Electrochemistry and Electrocatalysis. *Journal of the American Chemical Society* **2019**, *141*, 2179-2193.

10. Jiang, D.; Jiang, Y.; Li, Z.; Liu, T.; Wo, X.; Fang, Y.; Tao, N.; Wang, W.; Chen, H.Y., Optical Imaging of Phase Transition and Li-Ion Diffusion Kinetics of Single $LiCoO_2$ Nanoparticles During Electrochemical Cycling. *Journal of the American Chemical Society* **2017**, *139*, 186-192.

11. Wang, W., Imaging the Chemical Activity of Single Nanoparticles with Optical Microscopy. *Chemical Society Reviews* **2018**, *47*, 2485-2508.

12. Hui, J.; Gossage, Z. T.; Sarbapalli, D.; Hernández-Burgos, K.; Rodríguez-López, J., Advanced Electrochemical Analysis for Energy Storage Interfaces. *Analytical Chemistry* **2019**, *91*, 60-83.

13. Bülter, H.; Peters, F.; Schwenzel, J.; Wittstock, G., Spatiotemporal Changes of the Solid Electrolyte Interphase in Lithium-Ion Batteries Detected by Scanning Electrochemical Microscopy. *Angewandte Chemie International Edition* **2014**, *53*, 10531-10535.

14. Zampardi, G.; Ventosa, E.; La Mantia, F.; Schuhmann, W., In Situ Visualization of Li-Ion Intercalation and Formation of the Solid Electrolyte Interphase on TiO_2 Based Paste Electrodes Using Scanning Electrochemical Microscopy. *Chemical Communications* **2013**, *49*, 9347-9349.

15. Lipson, A. L.; Ginder, R. S.; Hersam, M. C., Nanoscale in Situ Characterization of Li-Ion Battery Electrochemistry Via Scanning Ion Conductance Microscopy. *Advanced Materials* **2011**, *23*, 5613-5617.

16. Ebejer, N.; Schnippering, M.; Colburn, A. W.; Edwards, M. A.; Unwin, P. R., Localized High Resolution Electrochemistry and Multifunctional Imaging: Scanning Electrochemical Cell Microscopy. *Analytical Chemistry* **2010**, *82*, 9141-9145.

17. E, S. P.; Kang, M.; Wilson, P.; Meng, L.; Perry, D.; Basile, A.; Unwin, P. R., High Resolution Visualization of the Redox Activity of Li_2O_2 in Non-Aqueous Media: Conformal Layer Vs. Toroid Structure. *Chemical Communications* **2018**, *54*, 3053-3056.

18. Dayeh, M.; Ghavidel, M. R. Z.; Mauzeroll, J.; Schougaard, S. B., Micropipette Contact Method to Investigate High-Energy Cathode Materials by Using an Ionic Liquid. *ChemElectroChem* **2019**, *6*, 195-201.

19. Luo, J.Y.; Cui, W.-J.; He, P.; Xia, Y.Y., Raising the Cycling Stability of Aqueous Lithium-Ion Batteries by Eliminating Oxygen in the Electrolyte. *Nature Chemistry* **2010**, *2*, 760-765.

20. Page, A.; Kang, M.; Armitstead, A.; Perry, D.; Unwin, P. R., Quantitative Visualization of Molecular Delivery and Uptake at Living Cells with Self-Referencing Scanning Ion Conductance Microscopy-Scanning Electrochemical Microscopy. *Analytical Chemistry* **2017**, *89*, 3021-3028.

21. Takahashi, Y., et al., Nanoscale Visualization of Redox Activity at Lithium-Ion Battery Cathodes. *Nature Communications* **2014**, *5*, 5450.

22. Yi, Y.; Weinberg, G.; Prenzel, M.; Greiner, M.; Heumann, S.; Becker, S.; Schlögl, R., Electrochemical Corrosion of a Glassy Carbon Electrode. *Catalysis Today* **2017**, *295*, 32-40.

23. Byers, J. C.; Güell, A. G.; Unwin, P. R., Nanoscale Electrocatalysis: Visualizing Oxygen Reduction at Pristine, Kinked, and Oxidized Sites on Individual Carbon Nanotubes. *Journal of the American Chemical Society* **2014**, *136*, 11252-11255.

24. Hosono, E.; Kudo, T.; Honma, I.; Matsuda, H.; Zhou, H., Synthesis of Single Crystalline Spinel Limn2o4 Nanowires for a Lithium Ion Battery with High Power Density. *Nano Letters* **2009**, *9*, 1045-1051.

25. Wang, Y.G.; Luo, J.Y.; Wang, C.X.; Xia, Y.Y., Hybrid Aqueous Energy Storage Cells Using Activated Carbon and Lithium-Ion Intercalated Compounds. *Journal of The Electrochemical Society* **2006**, *153*, A1425.

26. Luo, J. Y.; Xia, Y. Y., Aqueous Lithium-Ion Battery $LiTi_2(PO_4)_3/LiMn_2O_4$ with High Power and Energy Densities as Well as Superior Cycling Stability. *Advanced Functional Materials* **2007**, *17*, 3877-3884.

27. Bentley, C. L.; Kang, M.; Unwin, P. R., Scanning Electrochemical Cell Microscopy: New Perspectives on Electrode Processes in Action. *Current Opinion in Electrochemistry* **2017**, *6*, 23-30.

28. Chung, K. Y.; Kim, K.B., Investigations into Capacity Fading as a Result of a Jahn–Teller Distortion in 4V $LiMn_2O_4$ Thin Film Electrodes. *Electrochimica Acta* **2004**, *49*, 3327-3337.

29. Xia, Y., Capacity Fading on Cycling of 4 V $Li/LiMn_2O_4$ Cells. *Journal of The Electrochemical Society* **1997**, *144*, 2593.

30. Chen, H.; Guo, F.; Liu, Y.; Huang, T.; Zheng, B.; Ananth, N.; Xu, Z.; Gao, W.; Gao, C., A Defect-Free Principle for Advanced Graphene Cathode of Aluminum-Ion Battery. *Advanced Materials* **2017**, *29*, 1605958.

31. Chao, D., et al., A High-Rate and Stable Quasi-Solid-State Zinc-Ion Battery with Novel 2D Layered Zinc Orthovanadate Array. *Advanced Materials* **2018**, *30*, 1803181.

32. Shen, L.; Che, Q.; Li, H.; Zhang, X., Mesoporous $NiCo_2O_4$ Nanowire Arrays Grown on Carbon Textiles as Binder-Free Flexible Electrodes for Energy Storage. *Advanced Functional Materials* **2014**, *24*, 2630-2637.

33. Zhang, W.; Liu, Y.; Chen, C.; Li, Z.; Huang, Y.; Hu, X., Flexible and Binder-Free Electrodes of Sb/rGO and $Na_3V_2(PO_4)_3$/rGO Nanocomposites for Sodium-Ion Batteries. *Small* **2015**, *11*, 3822-3829.

34. Zhu, X.; Wu, X.; Doan, T. N. L.; Tian, Y.; Zhao, H.; Chen, P., Binder-Free Flexible $LiMn_2O_4$/Carbon Nanotube Network as High Power Cathode for Rechargeable Hybrid Aqueous Battery. *Journal of Power Sources* **2016**, *326*, 498-504.

35. Tripathi, A. M.; Su, W.N.; Hwang, B. J., In Situ Analytical Techniques for Battery Interface Analysis. *Chemical Society Reviews* **2018**, *47*, 736-851.

36. Grey, C. P.; Tarascon, J. M., Sustainability and in Situ Monitoring in Battery Development. *Nature Materials* **2017**, *16*, 45-56.

37. Subramania, A.; Angayarkanni, N.; Vasudevan, T., Effect of PVA with Various Combustion Fuels in Sol–Gel Thermolysis Process for the Synthesis of $LiMn_2O_4$ Nanoparticles for Li-Ion Batteries. *Materials Chemistry and Physics* **2007**, *102*, 19-23.

38. Lee, M.J.; Lee, S.; Oh, P.; Kim, Y.; Cho, J., High Performance $LiMn_2O_4$ Cathode Materials Grown with Epitaxial Layered Nanostructure for Li-Ion Batteries. *Nano Letters* **2014**, *14*, 993-999.

39. Izanzar, I.; Dahbi, M.; Kiso, M.; Doubaji, S.; Komaba, S.; Saadoune, I., Hard Carbons Issued from Date Palm as Efficient Anode Materials for Sodium-Ion Batteries. *Carbon* **2018**, *137*, 165-173.

40. Li, X.; Guo, S.; Deng, H.; Jiang, K.; Qiao, Y.; Ishida, M.; Zhou, H., An Ultrafast Rechargeable Lithium Metal Battery. *Journal of Materials Chemistry A* **2018**, *6*, 15517-15522.

41. Wang, G.; Fu, L.; Zhao, N.; Yang, L.; Wu, Y.; Wu, H., An Aqueous Rechargeable Lithium Battery with Good Cycling Performance. *Angewandte Chemie International Edition* **2007**, *46*, 295-297.

42. Tron, A.; Park, Y. D.; Mun, J., AlF_3-Coated $LiMn_2O_4$ as Cathode Material for Aqueous Rechargeable Lithium Battery with Improved Cycling Stability. *Journal of Power Sources* **2016**, *325*, 360-364.

Chapter 6. Rate Controlling Factors in $LiMn_2O_4$ Cathode: Multiscale Analysis of Contact Resistance and Ensemble Effect

Following the experiment in **Chapter 5**, where electrochemical properties of $LiMn_2O_4$ single particles were scrutinized, this chapter focus on the Li^+ (de)intercalation at a collection of $LiMn_2O_4$ particles. By precisely controlling the position of the micropipette in 3D space, the wetting of different amount of $LiMn_2O_4$ particles, as well as the wetting of supporting electrode can be controlled, allowing ensemble effects and particle-support contact resistance to be studied separately.

This Chapter has been prepared as the format of manuscript and supporting information, which is going to be submitted for peer review. Binglin Tao was responsible for design the experiment, collection of data and preparation of the manuscript. Cameron L. Bentley was a postdoctoral researcher supervising on this project and revised the manuscript in this chapter. Patrick R. Unwin provided the initial idea (conception) and supervise the whole process.

Rate Controlling Factors in $LiMn_2O_4$ Cathode: Multiscale Analysis of Contact Resistance and Ensemble Effect

Binglin Tao, Cameron L. Bentley* and Patrick R. Unwin*

Department of Chemistry, University of Warwick, Coventry CV4 7AL, U.K.

Corresponding authors:

c.bentley.1@warwick.ac.uk, p.r.unwin@warwick.ac.uk

6.1 Abstract

The improvement of the specific power density (rate capability) in Li-ion batteries is a fundamental issue to develop better portable electronics and electrical vehicles. Most of previous research focused on the composite electrodes with corresponding design considerations, while largely overlooked the intrinsic rate performance of the active component itself. Herein, scanning electrochemical cell microscopy (SECCM) is applied to investigate the rate performance of $LiMn_2O_4$ cathode by stripping of the auxiliary component (*e.g.*, binders and conducting additives) in the composite electrodes. Using a series of micropipette probes with graded diameters, rate performance evolution from individual particle to small clusters (*ca.* 5-10 particles) then to ensemble level (*ca.* 100 particles) are investigated, together with precisely control of the wetting of the supporting electrode. Interparticle interactions (ensemble effect) is proved to be the dominant effect in controlling of the rate performance of Li-ion batteries, and the nature of the particle-support contact (*i.e.*, wet vs dry contact) also plays an important role. Overall, SECCM provides a new perspective to understand the electrochemical behaviours (especially rate capability herein) of active particles in battery science, which helps to improve/optimise the performance of electrode by rational design.

6.2 Introduction

The high power demands of modern portable electronics and electrical vehicles (EVs) has driven extensive research into improving the power density (rate capability) of Li-ion batteries.[1-2] Focusing on the cathode, among a host of different metal oxide materials, lithium

manganese oxide ($LiMn_2O_4$) spinel is widely used due to its large theoretical energy capacity, relatively high abundance and environmental benignity.[3-4] While it is reported that the cathode rate capability may be limited by charge-transfer (*i.e.*, ion and/or electron transport) into the $LiMn_2O_4$ particles themselves,[5] few studies explicitly consider the electrochemical properties of said particles in the absence of "matrix effects".[6-8] This is because in practice it is difficult to isolate the response of "a particle" within a complex composite electrode (*i.e.*, active material, binder, conductive agent and current collector), where the influence of contact resistance(s) between the active particles and/or current collector,[9-10] variable wetting of particles,[11-12] and interparticle variations in electrode structure[13] may all contribute to the macroscopic electrochemical response. Thus, there is a great need for new techniques to study matrix effects in complex composite electrodes in a systematic way, *e.g.*, by removing all of the auxiliary elements and only focusing on the electrochemistry of single $LiMn_2O_4$ particles or small ensembles of active particles.[14]

Microelectrode technique has been exploited as an effective method to investigate the electrochemical properties of single particle electrode.[15-17] The beauty of this approach is avoidance the influence of binders and conductive additives for the fabrication of porous electrode, thus revealing the intrinsic properties of active materials. In principle, single particle measured under microelectrode technique exhibits much higher rate capability, as the straightforward current/potential does not "dilute" by the binder and conductive additive.[6] For example, the diffusion coefficient of $LiMn_2O_4$ measured via single particle measurement is 2-5 orders of magnitude higher Li^+ diffusion coefficients compared to its counterpart measured via polycrystalline electrode (10^{-9} - 10^{-6} vs 10^{-11} cm^2 s^{-1}), indicating significant impact of the grain boundaries on the effective diffusivity.[18] In addition, it has been deduced that one of the further battery research directions regarding the rate performance should rather focus on the electrode design/architecture.[6]

More recently, scanning electrochemical cell microscopy (SECCM) has emerged as a powerful technique for probing the electrochemistry of particles down to the single-entity level.[19-20] In SECCM, a fluidic micropipette/nanopipette probe is used to perform electrochemistry within a confined area of an electrode surface, with spatial-resolution defined by the area of meniscus contact.[21] Compared to the particle-by-particle approach

outlined above (microelectrode technique), SECCM probes the electrochemistry of a series of individual particles/clusters in a single high-throughput scanning experiment, which can be further correlated to co-located structural information to assign single-particle structure–function relationship unambiguously.[22-24] For example, very recently our group used this approach to interrogate single $LiMn_2O_4$ particles within an ensemble, revealing heterogeneous activity and superfast charge/discharge rate capability (up to 279 C) at single-particle level.[14]

Built on that study, herein we deploy SECCM to investigate the electrochemical behaviour evolution from individual $LiMn_2O_4$ particles to small clusters (ca. 5-10 particles) then to the ensemble level (ca. 100 particles) by utilization of a series of micropipette probes with graded diameters. Precisely controlling the position of the micropipette in 3D space allows both the number of $LiMn_2O_4$ particles, as well as the wetting of the supporting electrode (glassy carbon, GC, unless otherwise state) to be controlled, allowing ensemble effects and particle-support contact resistance to be studied separately. Experimental results prove that the charge-transfer barrier in $LiMn_2O_4$ ensembles is largely dictated by interparticle interactions, and the nature of the particle-support contact (*i.e.*, wet vs dry contact) also plays an important role.

6.3 Experimental Section

6.3.1 Chemical Reagents and Electrodes Preparation

Lithium manganese oxide ($LiMn_2O_4$, spinel structure, < 0.5 μm particle size) and lithium chloride (LiCl, ≥ 99 %) were both purchased from Sigma-Aldrich and used as received. Deionized water (resistivity ≥18 MΩ • cm) was produced by a Purite Integra HP system (U.K.). The glassy carbon plate (GC, 25×25 mm) was purchased from Alfa Aesar, and cleaned with 0.05 μm Al_2O_3 suspension (Bueler, U.S.A.) prior to use. Highly oriented pyrolytic graphite (HOPG) was purchased from SPI Materials (12×12×2 mm). Before use, HOPG was cleaved to expose the fresh surface using scotch tape. To prepare the working electrodes, $LiMn_2O_4$ particles were sonicated in deionized water for 10 minutes, stood at room temperature for 30 minutes, then 0.6 μL of the supernatant was drop-casted onto different carbon substrates. After dying at ambient conditions (*ca.* 30 minutes), these electrodes were mount on the *xy*-

piezoelectric positioner for further experiment (*vide infra*). The silver/silver chloride (Ag/AgCl) quasi reference counter electrode (QRCE) was prepared by anodic polarization of an Ag wire (0.125 mm diameter, Goodfellow, 99.99 %) at 5 V *vs.* Pt wire in saturated KCl solution. The QRCE potential was calibrated against a commercial saturated calomel electrode (SCE) in 1 M LiCl solution, which possessed a stable reference potential of ± 0.005 V *vs.* SCE.[25]

6.3.2 Instrumentation

Single channel micropipettes with diameter of 2 µm and 5 µm were prepared using a CO_2 laser puller (P-2000, Sutter Instruments, U.S.A.). The former was pulled from glass capillaries (GC 120F-10 1.2OD×0.69×100 mm, Harvard Apparatus, U.S.A.) with a one-step protocol. The parameters were heat 350, filament 4, velocity 40, delay 200 and pull 0. The latter were pulled from quartz capillaries (QTF 120-90-100, Friedrich & Dimmock Inc., U.S.A.), and another one-step protocol was exploited. The parameters were heat 680, filament 4, velocity 45, delay 130 and pull 35. The dimensions of the micropipette orifice were measured using scanning transmission electron microscopy (STEM) on a Zeiss Gemini 500 system, which was operated at an accelerating voltage of 10 kV. This system was also used for the observation of $LiMn_2O_4$ particles morphology via switching to scanning electron microscopy (SEM) mode. Single channel micropipettes with diameter of 70 µm were pulled from glass capillaries (GC 120F-10 1.0OD×0.58×100 mm, Harvard Apparatus, U.S.A.) using a PC-10 puller (Narishige Group, Japan) with a two-step protocol. For the first step, the parameters were heat 65, weight 3, and slider 8. For the second step, the parameters were heat 55, weight 3, and slider 4. The diameter of the tip was measured on an optical microscopy system (BH-2 optical microscope, Olympus, Japan). After pulling, these micropipette probes were filled with 1 M LiCl solution using a MicroFil syringe (World Precision Instrument Inc., U.S.A.), and a lab-made Ag/AgCl QRCE (mentioned above) was inserted from the back of the capillary.

All the experiments were performed on a custom-made scanning electrochemical cell microscopy (SECCM) platform unless specified, which was placed on an automatic leveling isolators (Newport, S-2000A-423.5) to minimize vibration. In the z direction, the micropipette probe was mounted on a *z*-(P-753.3CD, Physik Instrumente, Germany) piezoelectric positioner, which was controlled by an amplifier module (E-665). Similarly, the movement of working electrodes in the horizontal plane were controlled by a *xy*-(P-622.2CD, Physik

Instrumente) piezoelectric positioner, followed by their independent amplifier modules (E-500). Typically, the voltage was biased on the Ag/AgCl QRCE in the micropipette and the current on the working electrode was collected via a custom-made current follower (different sensitivities in different experiments, *vide infra*). It should be noted that all the piezoelectric positioners and electrometer head were placed inside of an aluminum Faraday cage to shield electromagnetic interference. During experiments, the surface current was measured every 4 μs, which was averaged 512 times to give a data acquisition rate of 4 × (512 + 1) = 2052 μs (note that one extra iteration is used to transfer the data to the host computer). To achieve such fast signal sending and data acquisition/processing capability, a field programmable gate array (FPGA) board (PCIe-7852R) from NI (National Instruments, U.S.A.) company was exploited. The whole system was controlled by a LabVIEW 2019 interface running the Warwick Electrochemical Scanning Probe Microscopy software (WEC-SPM, www.warwick.ac.uk/electrochemistry).

6.3.3 Scanning Protocol

For the experiment with small micropipettes (2 and 5 μm), the scanning protocol is exactly the same with our previous report (scan hopping with cyclic voltammetry). Briefly, the micropipette (meniscus cell) was introduced to the surface of interest at an approach rate of 3 μm/s, during which the Ag/AgCl QRCE is biased at - 1.25 V and the current on the working electrode was monitored constantly. Upon landing, *i.e.*, when an electrochemical cell was formed between the micropipette and sample surface through the meniscus, the electric circuit is closed and a threshold current of 2 pA (little bit bigger than the system noise level of ± 1.3 pA, with the ammeter range of ± 1 nA) triggered the tip to stop from further approaching. At this height, a local cyclic voltammetric experiment was performed (from 0 to 1.25 then back to 0 V *vs.* Ag/AgCl QRCE), following which the micropipette was retracted 5 or 10 μm from the surface (depend on the tip size). The micropipette was subsequently moved to next predefined pixel, located 5 or 10 μm from the previous point, set by the predefined 'hopping distance'. At each and every pixel, the electrochemical signals (potential, *E* and current, *i*) were recorded, but only the active pixels (signals different from bare substrate) were analyzed in this work (the way to distinguish active pixels from *in-situ* and *ex-situ* method were detailed in the main text).

Different from the scanning protocol mentioned above, experiments performed with big tip (diameter of 70 µm) were single point based, via a '*step approached cyclic voltammetric measurement*'. To be more specific, the micropipette (meniscus cell) was introduced to the surface of interest at an approach rate of 0.5 µm/s, during which the Ag/AgCl QRCE is biased at - 1.25 V and the current on the working electrode was monitored constantly. Upon landing, a threshold current of 50 pA (system noise level of ± 5 pA, with the ammeter range of ± 10 nA) triggered the tip to stop approaching. At this height, a local cyclic voltammetric experiment was performed (0 to 1.25 V vs. Ag/AgCl QRCE), with the vertical extension of the micropipette (*z*-coordinate) and electrochemical signals (potential, *E* and current, *i*) were recorded. After that, the tip was moved down at a specific distance of 100 nm with the *z*-piezoelectric positioner, and another local cyclic voltammetric experiment was performed. By repeating these steps moving down and cyclic voltammetric measurement for several times, a series of CVs can be recorded, which gave the cross-section diagnostic information until the carbon-based substrate was touched.

6.3.4 Data Processing

After data collection, the raw data were processed with Matlab R2015b software package to extract the 'active pixels' in each experiment. Data plotting was performed using Matlab R2015b and Origin 2018 software packages. It should be noted that there is no interpolation or smooth of any SECCM data presented in this work. All the SEM figures were cropped and typeset with Illustrator 2017.

6.4 Result and Discussion

6.4.1 Experiment Design and Multi-scale Analysis of $LiMn_2O_4$ Particles.

In order to study how interparticle interactions (*e.g.*, ensemble effects) and the particle-support contact (*e.g.*, *wet* vs *dry* contact) influence Li^+ (de)intercalation at $LiMn_2O_4$ electrode, two different series of experiments were designed, as shown schematically in **Figure 6.1**. In the first series of experiments, SECCM was deployed in the voltammetric hopping mode to interrogate the redox activity of a series of individual $LiMn_2O_4$ particles or particle clusters (*i.e.*, <10 particles) supported on GC, as detailed in our previous study. After scanning, the SECCM scan areas were visualized with scanning electron microscopy (SEM), and each

individual cyclic voltammogram (CV) was classified according to the number of particles (*i.e.*, *single* vs *multiple*) and the nature of the electrolyte-particle(s)-GC contact (*i.e.*, *dry* vs *wet* contact), as depicted in **Figure 6.1a**. In contact mode (I), meniscus contact was made with a single $LiMn_2O_4$ particle without touching the underlying GC support (*i.e.*, *single* particle, *dry* particle-support contact). In mode (II), the meniscus fully encapsulates a single $LiMn_2O_4$ particle and further makes contact with the underlying GC support (*i.e.*, *single* particle, *wet* particle-support contact). In mode (III), meniscus contact was made with several $LiMn_2O_4$ particles without touching the underlying GC support (*i.e.*, *multiple* particles, *dry* particle-support contact). Finally, in mode (IV), the meniscus fully encapsulates several $LiMn_2O_4$ particles and further makes contact with the underlying GC support (*i.e.*, *multiple* particles, *wet* particle-support contact). It should be noted that the nature of the probed area (*i.e.*, number of particles and particle-support wetting) was inferred from the *in-situ* electrochemical signals (during scanning, *vide infra*) and ultimately confirmed by *ex-situ* SEM imaging (after scanning).

In the second series of experiments, a relatively large probe (diameter ≈ 70 µm) was employed to perform '*step-approach cyclic voltammetric measurements*' on small ensembles of $LiMn_2O_4$ particles (*ca.* 15 agglomerates or 100 particles). In this experiment, the probe-substrate distance was precisely controlled to manipulate the electrolyte-particle-support wetting, as depicted schematically in **Figure 6.1b**. This process consisted of: (i) initially making meniscus contact with only the tops of the $LiMn_2O_4$ particles (details in the Experimental Section); (ii) recording a CV; (iii) decreasing the probe-substrate distance by 100 nm (*i.e.*, translating the probe 100 nm downwards in the z-direction, towards the support) and; (iv) repeating steps (ii) and (iii) until the meniscus wets the GC support. By employing this 'cross-sectional' approach, three different types of electrolyte-particle-support interaction could be captured. At initial contact, mode (I) in **Figure 6.1b**, only the upper parts of the larger $LiMn_2O_4$ particle(s) were contacted by the meniscus, while the lower parts of these particles, as well as many other small particles and the GC support do not contribute to the measured CV. As the probe is gradually moved down, mode (II) in **Figure 6.1b**, more and more $LiMn_2O_4$ particles were contacted by the meniscus and contribute to the measured CV, while the GC was still excluded (*i.e.*, *dry* particle-support contact). By comparing CVs obtained in modes (I) and (II), the influence of interparticle interactions (*i.e.*, ensemble effects) on Li^+

(de)intercalation at $LiMn_2O_4$ was inferred. The meniscus eventually wetted the support, mode (III) in **Figure 6.1b**, where multiple particles plus the GC substrate contribute to the CV. By comparing CVs obtained in modes (II) and (III), the role of the particle-support interaction (*i.e.*, *wet* vs *dry* contact) in modulating Li^+ (de)intercalation at $LiMn_2O_4$ was inferred. In effect, the experiments devised in **Figure 6.1** probe $LiMn_2O_4$ electrode across length-scales, from the single particle to the ensemble (*ca.* 100 particles) level to identify the multi-scale factors controlling apparent Li^+ (de)intercalation kinetics.

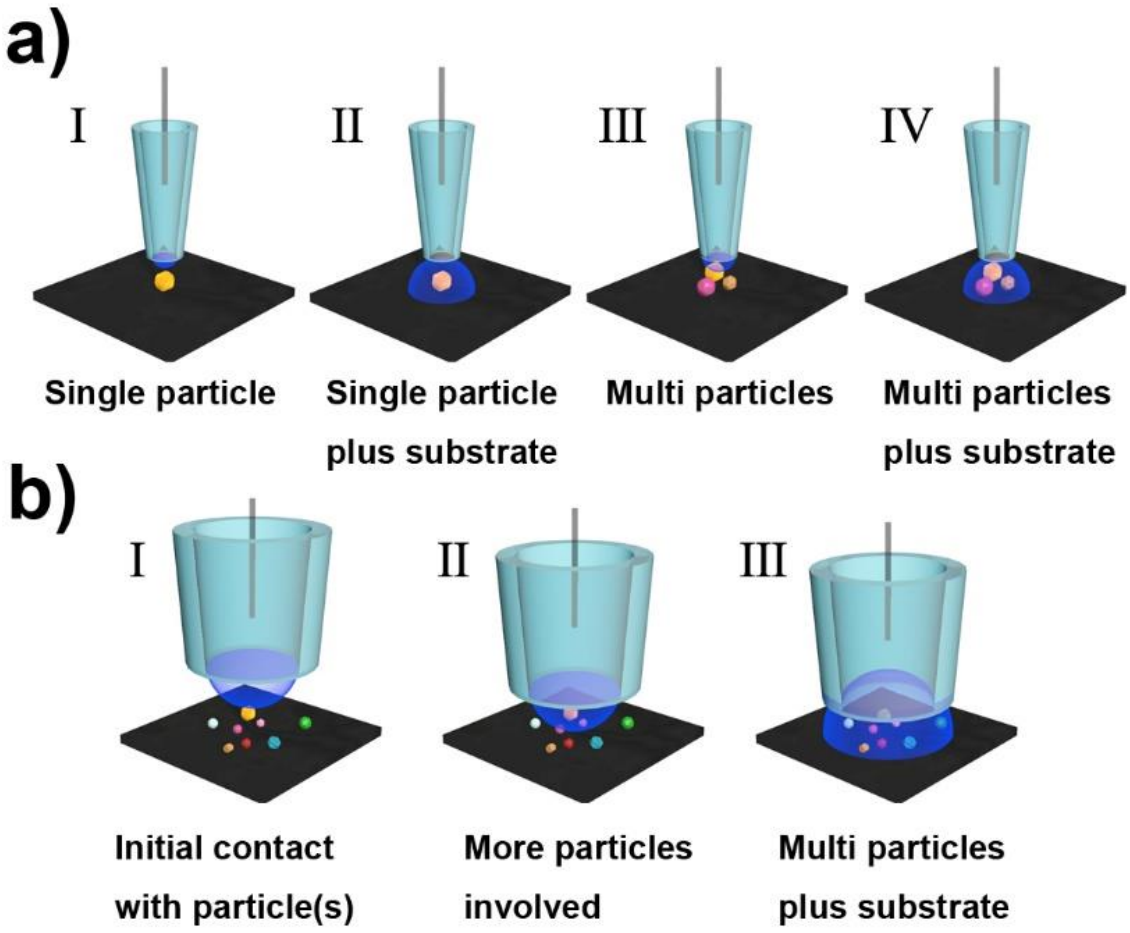

Figure 6.1 Schematic showing the multi-scale cyclic voltammetric measurements performed on $LiMn_2O_4$ particle(s) supported on carbon substrates via SECCM. **(a)** Four different kinds of contact modes when hopping scan protocol was exploited, via using 2 µm (results shown in Figure 6.2) and 5 µm (results shown in Figure 6.3) diameter probes. **(b)** Three different kinds of contact modes at different heights where point-based experiment was performed, via using 70 µm diameter probes (results shown in Figure 6.5 and 6.6). It should be noted that all

the experiments in this work were performed in 1 M LiCl electrolyte, at a scan rate (ν) of 1 V/s.

6.4.2 Li^+ (De)intercalation at 1 − 10 $LiMn_2O_4$ Particles.

Employing the experimental protocol outlined in **Figure 6.1a**, voltammetric hopping mode SECCM was performed on GC-supported $LiMn_2O_4$ particles, initially using a micropipette probe of diameter *ca.* 2 μm (representative STEM image is shown in the Supporting Information, SI, **Figure 6.7a**). Representative CVs obtained for the four different contact modes (*vide supra*, **Figure 6.1a**) are shown in **Figure 6.2**. Shown in **Figure 6.2a-i** is a CV obtained in contact mode (I), *i.e.*, *single* particle with *dry* particle-support contact, evidenced by the lack of electrolyte residue on the GC support, observed with SEM (after SECCM scanning), shown in **Figure 6.2a-ii**. In this case, the electrochemical signal (**Figure 6.2a-i**) arises only from the upper portion of the $LiMn_2O_4$ particle wetted by the meniscus, while the GC substrate and the *dry* particle-support contact simply served as series resistance in the electrical circuit. Thus, the two pairs of redox peaks located at 0.90/0.70 and 1.05/0.89 V correspond to two different Li^+ extraction-insertion processes, which can be assigned to Li^+ extraction from tetrahedral lattice sites in the presence and absence of the Li–Li interaction, respectively.[3] Herein, the scan rate (ν) is 1 V/s, which is 2-4 orders of magnitude larger than that employed in the traditional composite electrode measurement (0.1–10 mV/s) with the identical material.[26-27] It is also important to note that while the CV shown in **Figure 6.2a-i** is considered representative, each individual $LiMn_2O_4$ particle presents a unique *i*–*E* characteristic, as presented in the SI, **Figure 6.8a-f**.

Shown in **Figure 6.2b-i** is a CV obtained in contact mode (II), *i.e.*, *single* particle with *wet* particle-support contact, evidenced by the electrolyte residue present on the GC support, observed with SEM (after SECCM scanning), shown in **Figure 6.2b-ii**. In this case, both the single $LiMn_2O_4$ particle and GC support participated in the electrochemical reactions, and the resulting signal (**Figure 6.2b-i**) is the superimposition of them. Consulting **Figure 6.2b-i**, the pair of peaks located at 0.94/0.55 V corresponds to Li^+ (de)intercalation at $LiMn_2O_4$, while the process at > 1 V arises from corrosion of the GC support,[28] which effectively serves as an *in-situ* indicator of whether the meniscus wetted the support or not. In this context, the signal from GC support can be viewed as a "parasitic process" that does not interfere with the Li^+

(de)intercalation process at $LiMn_2O_4$ (*vide infra*). It is interesting to note that the CV shown in **Figure 6.2b-i** only features a single pair of redox peaks, with a larger peak-to-peak separation, Δ*Ep* (*n.b.* Δ*Ep* is only considered for the first redox process herein) than the corresponding process shown in **Figure 6.2a-i**, indicating apparently less-facile (de)intercalation kinetics at the single-particle level.[29-30] As discussed in detail below, this apparent discrepancy is thought to arise from the contact resistance brought on by the different nature of the particle-support contact, *i.e.*, *dry* vs *wet* contact. Other data with the same contact mode are shown in SI, **Figure 6.9a-b**.

Shown in **Figure 6.2c-i** is a CV obtained in contact mode (III), *i.e.*, *multiple* particles with *dry* particle-support contact. As shown in **Figure 6.2c-ii**, the contacting area (delineated by the red circle) can be estimated according to the nearby droplet footprint residues on the GC support, from the post-scan SEM image. In this case, several $LiMn_2O_4$ particles (5-6 particles shown in **Figure 6.2c-ii**) contribute to the electrochemical signal, with the CV (**Figure 6.2c-i**) being the weighted sum of each individual particle (*i.e.*, depending on the specific particle surface area contacted by the meniscus). This is clear from the multiple overlapping peaks present in the CV, *e.g.*, anodic peaks at 0.99, 1.09 and 1.2 V, and cathodic peaks at 0.56, 0.35 and 0.12 V on the forward and reverse sweep, respectively. Interestingly, **Figure 6.2c-i** features much broader peaks and larger Δ*Ep* values than either **Figure 6.2a-i** or **6.2b-i**, indicating apparently less-facile Li^+ (de)intercalation kinetics at the multiple particle level. As discussed in detail below, this apparent trend may be attributable to interactions (*e.g.*, electronic and/or diffusional coupling) between different $LiMn_2O_4$ particles. Other data with the same contact mode are shown in SI, **Figure 6.10-12**.

Finally, shown in **Figure 6.2d-i** is a CV obtained in contact mode (IV), *i.e.*, *multiple* particles with *wet* particle-support contact, as observed with SEM (after SECCM scanning), shown in **Figure 6.2d-ii**. Unlike the previous cases in **Figure 6.2a-c**, in this case the anodic processes from $LiMn_2O_4$ (*i.e.*, Li^+ deintercalation) overlap with the background signal (*i.e.*, parasitic reactions) from the GC support, meaning that only cathodic peaks are discernible in **Figure 6.2d-i**. This indicates that apparent Li^+ (de)intercalation kinetics is ultra-slow, even though the number of probed particles (5 particles) is the same as that in **Figure 6.2c**. Again, as discussed below, this likely indicates that the '*wet* contact' is much more resistive than the

'*dry* contact' and that Li^+ (de)intercalation may be hindered by the '*wet* contact' resistance at the ensemble level.

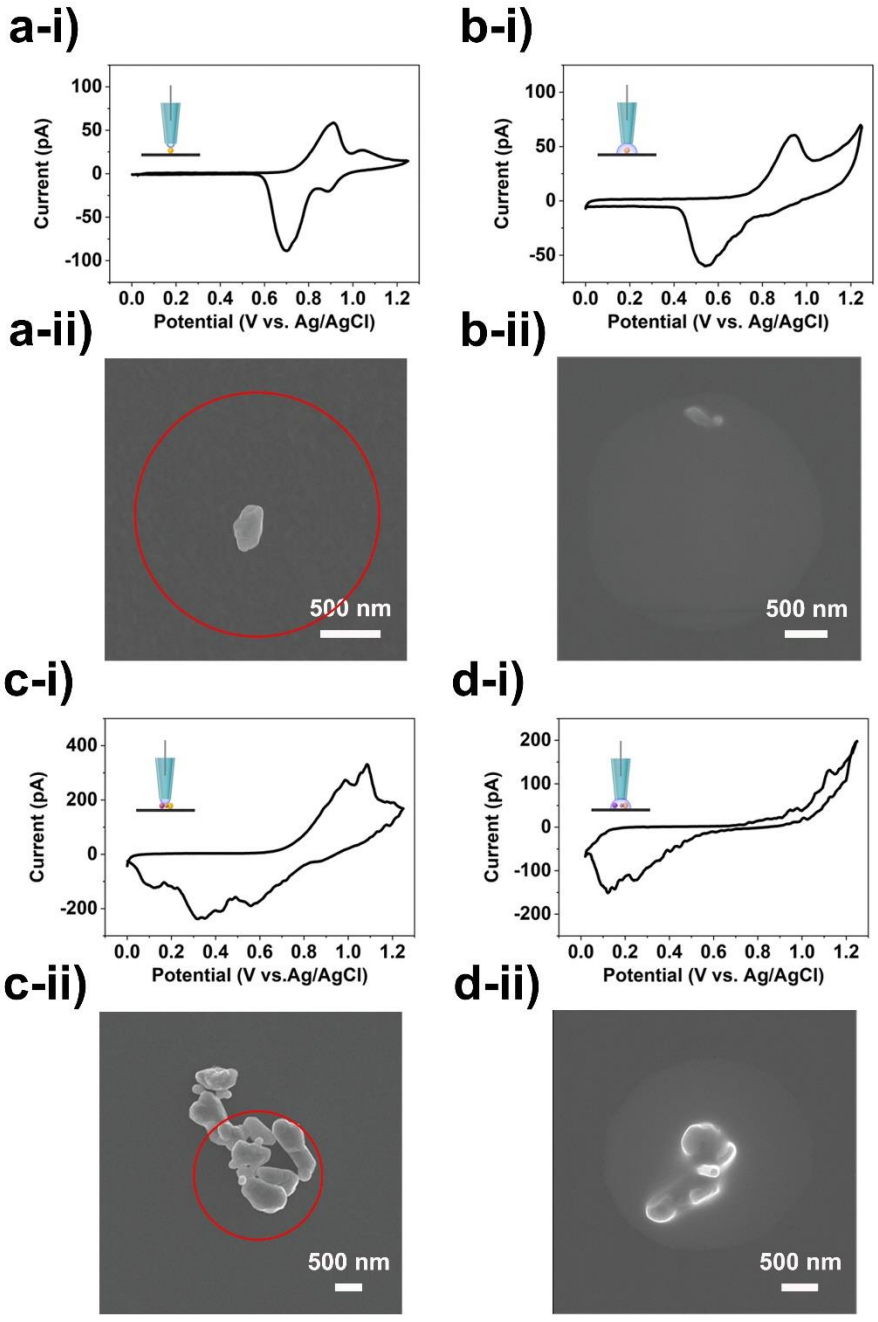

Figure 6.2 (i) CVs and **(ii)** corresponding SEM images from $LiMn_2O_4$ particle(s) supported on GC, the contact interface was made between the meniscus and **(a)** single particle **(b)** single particle plus substrate **(c)** multi-particles **(d)** multi-particles plus substrate. From the SEM image, the contacting area in **(a)** is the top of the whole particle, in **(b)** and **(d)** is confined by the LiCl salt residue on GC, and in **(c)** is on the top of multiple particles (estimated by the

nearby residues), which is marked with the red circle. The CV measurements (v = 1 V/s) were obtained with probes of diameter ca. 2 µm filled with 1 M LiCl solution.

The experiments described in **Figure 6.1a** were repeated with a larger micropipette probe (diameter ≈ 5 µm, see the SI, **Figure 6.7b**); results are shown in **Figure 6.3**. Increasing the size of the micropipette probe has two important consequences: (i) GC makes up a larger proportion of the probed area during single particle or few particles, *wet* contact experiments [*i.e.*, contact modes (II) and (IV) in **Figure 6.1a**] and (ii) a larger number of particles can be simultaneously probed during *multiple* particle experiments [*i.e.*, contact modes (III) and (IV) in **Figure 6.1a**]. In addition, as discussed below, observing the same trends in the apparent Li^+ (de)intercalation kinetics of $LiMn_2O_4$ with regards to the electrolyte-particle(s)-GC contact modes, independent of probe size, effectively demonstrates that the confined electrochemical cell format of SECCM does not affect the CV morphology (*i.e.*, the trends are not due to a measurement artefact).

In contact mode (I), **Figure 6.3a**, two pairs of redox peaks are again discernable in the CV at 0.94/0.68 V and 1.06/0.93 V, attributable to two-stage Li^+ (de)intercalation at $LiMn_2O_4$, described above. Compared with the single particle shown in **Figure 6.2a**, the particle size in **Figure 6.3a** is *ca.* 2-3 times larger in diameter, explaining the higher current magnitude (*ca.* 8-fold different). Comparing the ΔE_p values in **Figure 6.2a** and **6.3a**, particle size appears to have a negligible effect on apparent (de)intercalation kinetics at the single particle level, consistent with our previous report.[14] For this reason, downsizing the active material particle sizes via nanocrystallization method is not an effective way to improve the battery rate performance. In contact mode (II), **Figure 6.3b**, there is again only one pair of redox peaks discernable in the CV at 1.05/0.57 V, superimposed on the background (parasitic) current from the GC support. In contact mode (III), **Figure 6.3c**, multiple particles (*ca.* 10 particles) exhibit a merged oxidation peak at 1.06 V (Li^+ deintercalation) in the forward sweep and a series of reduction peaks at 0.57, 0.62, and 0.73 V in the reverse sweep (Li^+ intercalation). In contact mode (IV), **Figure 6.3d**, the apparent Li^+ (de)intercalation kinetics are again ultra-sluggish, with no discernible oxidation peak and a broad, drawn out reduction peak at *ca.* 0.4 V . Thus, as alluded to above, the trends in apparent (de)intercalation kinetics in **Figure 6.3** agrees with the smaller-probe counterparts in **Figure 6.2**, reiterating the conclusions about

the different contact modes. It should also be re-emphasized that although all data depicted in the main text is considered representative, the full collection of correlative electrochemistry-SEM measurements is available in the SI, **Figure 6.8-14**.

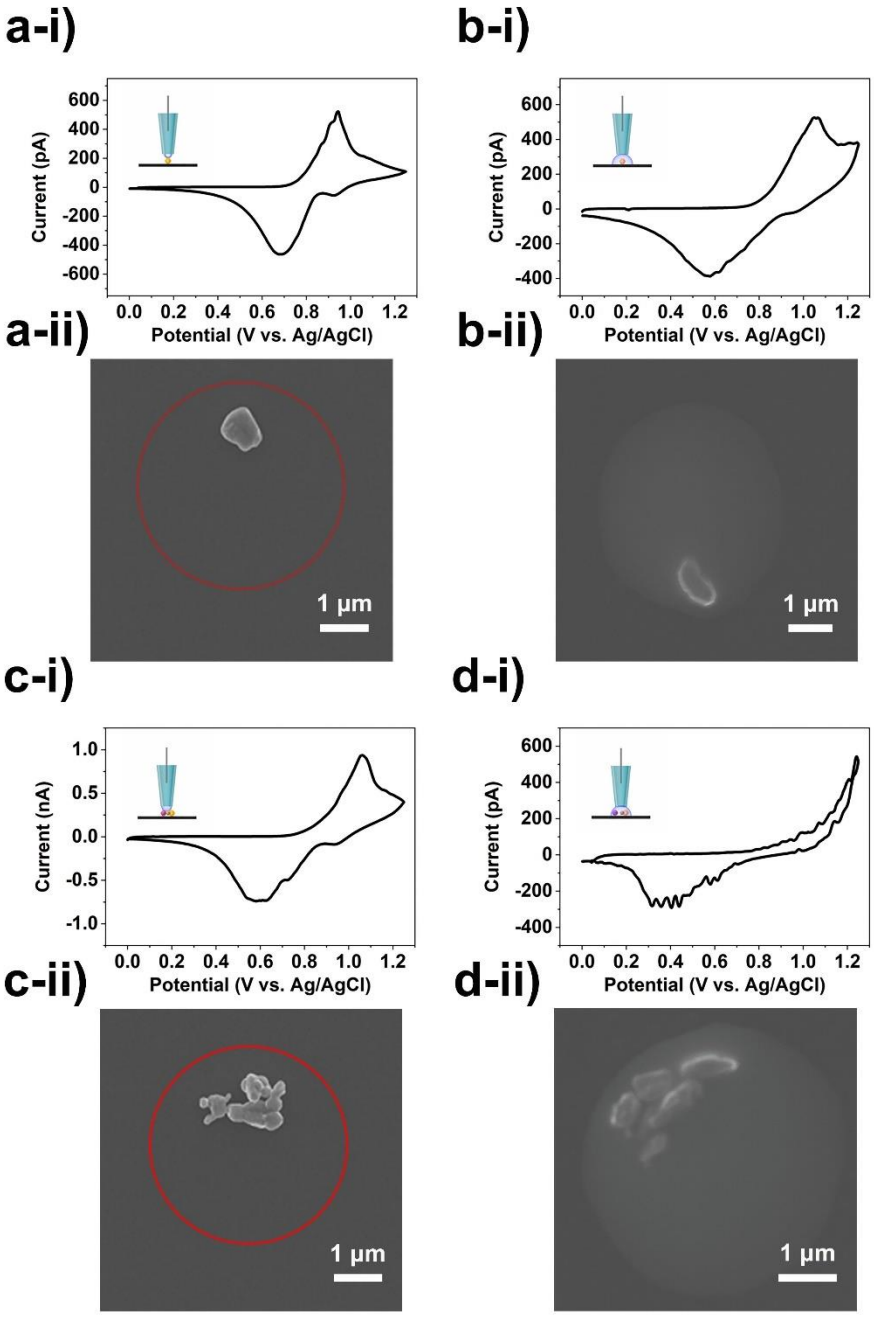

Figure 6.3 (i) CVs and **(ii)** corresponding SEM images from $LiMn_2O_4$ particle(s) supported on GC, the contact interface is made between the meniscus and **(a)** single particle **(b)** single particle plus substrate **(c)** multi-particles **(d)** multi-particles plus substrate. The contacting area in **(a)** and **(c)** is the top of the whole particle(s), which is estimated by the nearby residues

and highlighted with blue circles, in **(b)** and **(d)** is confined by the LiCl salt residue on GC. The CV measurements (v = 1 V/s) were obtained with probes of diameter ca. 5 µm filled with 1 M LiCl solution.

In order to unveil how interparticle interactions (*e.g.*, single vs multiple particles) and the particle-support contact (*e.g.*, *wet* vs *dry* contact) influence apparent Li^+ (de)intercalation kinetics at $LiMn_2O_4$, a plot of ΔE_p values (tabulated in SI, **Table 6.1**) vs contact mode (**Figure 6.1a**) was constructed, as shown in **Figure 6.4a-d**. Evidently, ΔE_p increases in the order of contact mode (I) < (II) ≈ (III) < (IV), with values (mean ± standard deviation) of 0.2 ± 0.067, 0.38 ± 0.19, 0.37 ± 0.2 and 0.79 ± 0.18, respectively. Note that although there are relatively few single-particle measurements herein, the ΔE_p values are consistent with our previous study (as shown in **Figure 6.4e**). Also note that the SECCM probe size (*i.e.*, 2 vs 500 nm and 5 µm diameter) appears to have minimal influence on the measured ΔE_p values, supporting our conclusion above (*i.e.*, compare **Figures 6.2** and **6.3**).

Comparing contact modes (I) to (II) or (III) to (IV), it is clear that the nature of the particle-support contact (*i.e.*, 'dry' vs 'wet') has a strong bearing on the measured ΔE_p values. Evidently, the 'dry' contact modes (I) and (III), gives rise to apparently more facile Li^+ (de)intercalation kinetics than the equivalent 'wet' contact modes (II) and (IV). Another important observation is that there is significantly more spread in the multiple particle data compared to the equivalent single particle data, with standard deviations of 0.19 and 0.067 V for contact modes (III) and (I), respectively (*i.e.*, multiple vs single particle, dry contact). This may be reflective of the fact that a much larger total population of particles was probed in contact mode (III) (59 measurements of *ca.* 5 particles = 295 particles in total) compared to mode (I) (7 particles in total). In addition, complex interparticle interactions, such as electronic or diffusional coupling (*i.e.*, ensemble effects) may also contribute to the data spread in contact mode (III). Indeed, plotting the logarithm of anodic peak current, i_{pa} (proportional to the number of particles probed) vs ΔE_p [indicator of Li^+ (de)intercalation kinetics] reveals a roughly linear relationship, as shown in **Figure 6.4f**. In other words, the more $LiMn_2O_4$ particles encapsulated within the meniscus and contributing to the measured CV, the slower the apparent Li^+ (de)intercalation kinetics. This is thought to be due to the relaxation behaviour of these particles, where Li^+ can de-intercalation from one particle and

re-intercalation into another one until a uniform local potential distribution is reached across the whole electrode.[31] This result obviously has important implications for practical battery electrodes which are comprised of orders-of-magnitude larger ensembles of electronically/diffusionally coupled $LiMn_2O_4$ particles, as explored below.

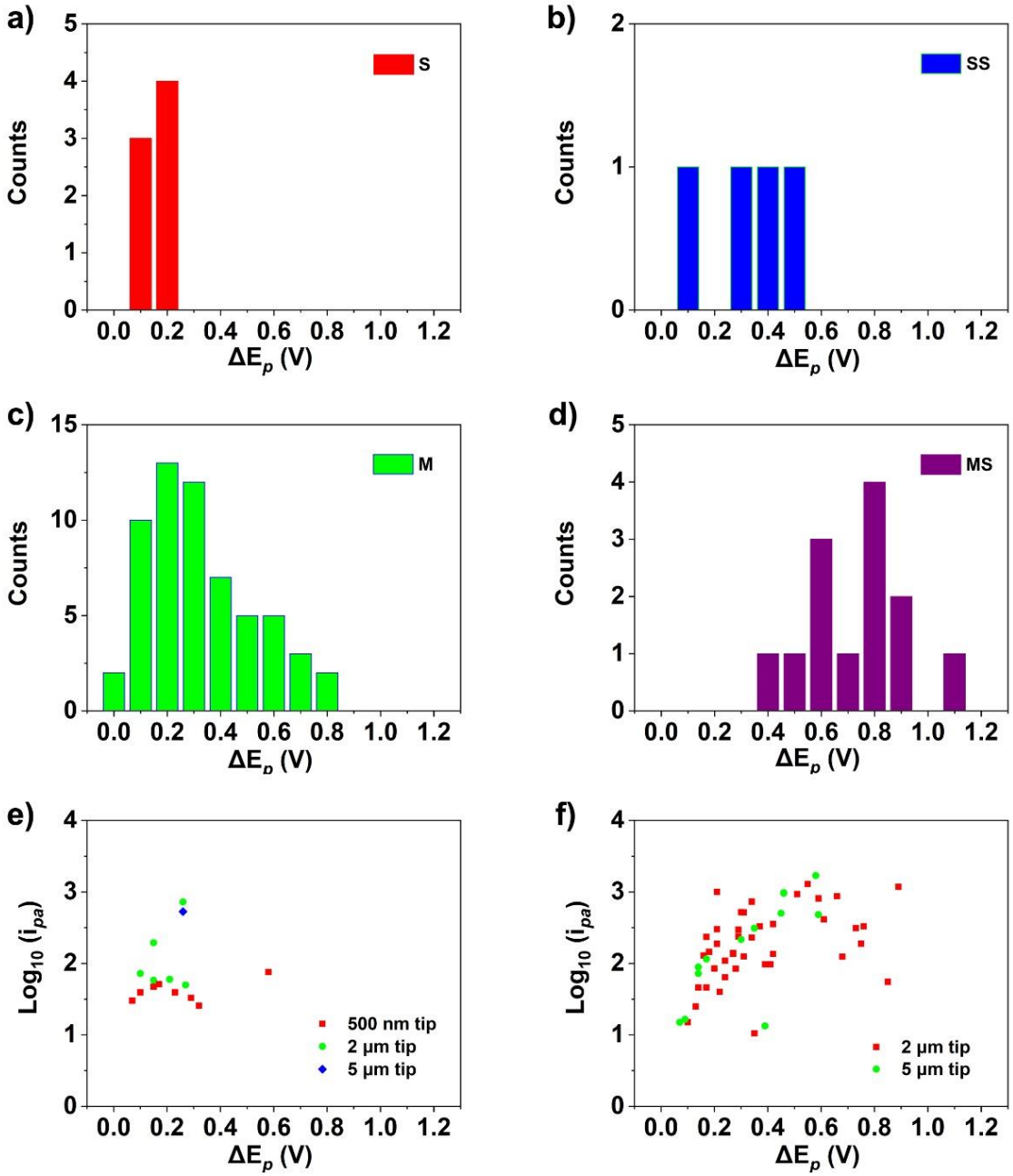

Figure 6.4 Scatter plot of peak separation vs. different electrolyte-particle(s)-glassy carbon contact modes. In **(a)** S stands for single particle, in **(b)** SS stands for single particle plus substrate, in **(c)** M stands for multiple particles and in **(d)** MS stands for multiple particles plus substrate. Scatter plot of log anodic current vs. peak separation. In **(e)** single particle mode

and in **(f)** multi-particles mode, respectively. Most data was extracted from Table 6.1, while 500 nm tip data in **(e)** was extracted from our previous report.

6.4.3 Li^+ (De)intercalation at *ca.* 100 $LiMn_2O_4$ particles.

In order to simulate a "macroscopic" ensemble (real electrode but without binders and conducting additives), a micropipette probe of diameter 70 μm (as shown in SI, **Figure 6.7c**) was used to perform '*step-approach cyclic voltammetric measurements*', as outlined in **Figure 6.1b**. As highlighted above, through precise positioning of the meniscus cell in 3D space, particle-support wetting status can be controlled, allowing the effects of interparticle interaction and contact resistance to be studied at the ensemble (*ca.* 100 particles) level. Different from the above-mentioned scanning experiments, herein the measurements are all single point based. **Figure 6.5a** and **b** depict two of such experiments, performed on GC-supported $LiMn_2O_4$ particles. At initial contact, **Figure 6.5a-i** and **6.5b-i**, both areas exhibit relatively facile Li^+ (de)intercalation responses at $LiMn_2O_4$, with ΔE_p values of 0.17 and 0.36 , respectively, which are on the lower end of the values reported in **Figure 6.4a**. Note that from the magnitude of the currents, it is evident that significantly less $LiMn_2O_4$ particles were contacted in **Figure 6.5a-i** (i_{pa} ≈ 30 pA) compared to **Figure 6.5b-i** (i_{pa} ≈ 700 pA), explaining why the former exhibits apparently more facile kinetics than the latter, consistent with **Figure 6.4b**. By lowering the z-position of the probe, the meniscus cell breaks on the GC support surface, simultaneously encapsulating *ca.* 15 $LiMn_2O_4$ agglomerates or 100 individual particles (shown in **Figure 6.5c**). In both cases, **Figure 6.5a-ii** and **Figure 6.5b-ii**, the anodic peak associated with Li^+ deintercalation at $LiMn_2O_4$ completely overlaps with the background current from the GC support at > 1 V, while the broad cathodic peak associated with Li^+ intercalation occurs at *ca.* 0.5 V on the return sweep. Evidently, contacting additional $LiMn_2O_4$ particles and/or wetting the particle-support contact also hinders Li^+ (de)intercalation at the ensemble level, consistent with the 1 - 10 particles experiments mentioned above.

Due to the relatively hydrophilic nature of the GC support,[32-33] only two wetting stages could be observed in these experiments: initial contact with $LiMn_2O_4$ (**Figure 6.5a-i** and **Figure 6.b-i**) or multiple particles plus wetted support (**Figure 6.5a-ii** and **Figure 6.5b-ii**). In order to deconvolute the effects of interparticle interactions and '*wet*' contact resistance, it is necessary to study the intermediate wetting stages, *i.e.*, where the $LiMn_2O_4$ particles are

gradually encapsulated from top-to-bottom as the probe is lowered incrementally, as depicted in **Figure 6.1b**. HOPG is more hydrophobic than GC,[34-35] and is also more electrochemically inert within the investigated potential range, as shown in the SI, **Figure 6.17**. Thus, an identical set of experiments were carried out using highly oriented pyrolytic graphite (HOPG) as the support, as shown in **Figure 6.6**.

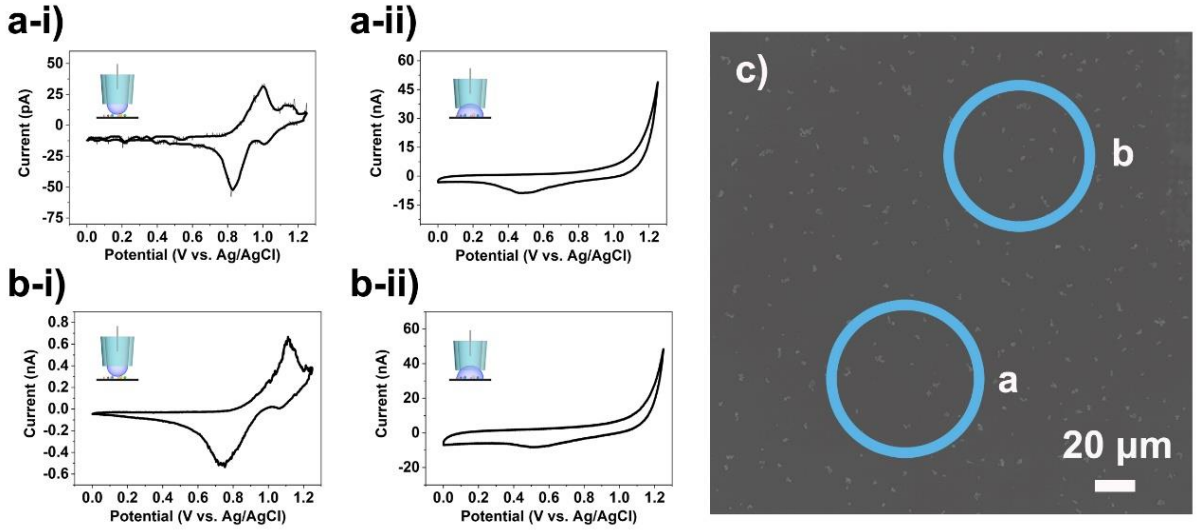

Figure 6.5 CV measurements at different status of **(i)** initial contact and **(ii)** touching both particles and substrate from $LiMn_2O_4$ particle(s) supported on GC, **(a)** and **(b)** are different probing points as indicated by the blue circle in **(c)**. **(c)** Corresponding SEM images from $LiMn_2O_4$ particles supported on GC, and the scanning areas were deduced by comparing the SEM images before and after experiment, as shown in Figure 6.16. The CV measurements (v = 1 V/s) were obtained with probes of diameter ca. 70 µm filled with 1 M LiCl.

A representative CV profile obtained upon initial contact with the HOPG-supported $LiMn_2O_4$ particles is shown in **Figure 6.6a**. The wave shape of the CV is comparable to that measured on GC for a similar current magnitude (*i.e.*, $i_{pa} \approx 400$ pA, comparable to **Figure 6.5b-i**), with a single pair of redox peaks located at 1.16/0.64 V. During this initial measurement, only the upper portions of the largest $LiMn_2O_4$ particles are contacted by the meniscus, as depicted in **Figure 6.1b**, contact mode (I). As shown in **Figure 6.6b**, lowering the z-position of the micropipette probe led to an increase in the magnitude of the measured current due to more particles being contacted [*i.e.*, **Figure 6.1b**, contact mode (II)]. Note that additional 'intermediate' steps in this set of experiments (*i.e.*, between initial contact with $LiMn_2O_4$

particles and ultimately wetting of the HOPG support) are presented in the SI, **Figure 6.18**. Comparing **Figure 6.6a** to 6.**6b**, upon contacting additional $LiMn_2O_4$ particles, ΔE_p increased from 0.52 to 0.67 V (assuming the switch potential of 1.25 V as the deintercalation potential in **Figure 6.6b**, although this reaction did not finish yet), indicating decreased apparent Li^+ (de)intercalation kinetics. As the meniscus was not yet in contact with the HOPG support, this apparent "slowing down" of the (de)intercalation kinetics must be attributable to interparticle interactions (*i.e.*, ensemble effects), rather than particle-support contact resistance. Interestingly, also shown in **Figure 6.6b**, by decreasing the voltammetric sweep rate from 1 V s^{-1} to 0.01 V s^{-1}, the same set of particles exhibit the archetypal two-stage Li^+ (de)intercalation response expected from bulk $LiMn_2O_4$ electrodes (see SI, **Figure 6.19**). Thus, while interparticle interactions within the ensemble hinders Li^+ (de)intercalation at the individual $LiMn_2O_4$ particle level [*e.g.*, compare S and M in **Figure 6.4a**], this charge-transfer barrier can be alleviated to an extent by slowing down the sweep rate, *i.e.*, at the expense of sacrificing fast charge/discharge capability in the context of practical battery applications.

Returning to the experiments described in **Figure 6.6**, upon further lowering the z-position of the micropipette probe, the meniscus cell eventually breaks on the support surface, and the resulting CV is a superimposition of the $LiMn_2O_4$ particles and HOPG signals, as shown in **Figure 6.6c**. Again, encapsulating additional $LiMn_2O_4$ particles and/or wetting the support, further hinders the apparent Li^+ (de)intercalation kinetics, with no discernible anodic peak and a significantly shifted cathodic peak (from *ca.* 0.58 to 0.49 V) when comparing **Figure 6.6b** to **6.6c**. Thus, it is clear that while interparticle interactions largely dictate the charge-transfer barrier in $LiMn_2O_4$ ensembles [*e.g.*, compare S and M in **Figure 6.4a**], the nature of the particle-support contact (*i.e.*, *wet* vs *dry* contact) also play an important role [*e.g.*, compare M and MS in **Figure 6.4a**]. In addition, by comparing the CVs obtained from $LiMn_2O_4$/GC (**Figure 6.5a-ii** or **Figure 6.5b-ii**) and $LiMn_2O_4$/HOPG (**Figure 6.6c**), it seems that the nature of the support does not strongly influence *wet* contact resistance, as the morphology of these curves are very similar, especially the characteristic broad peak occurring at the same position (*ca.* 0.5 V) during the cathodic scan.

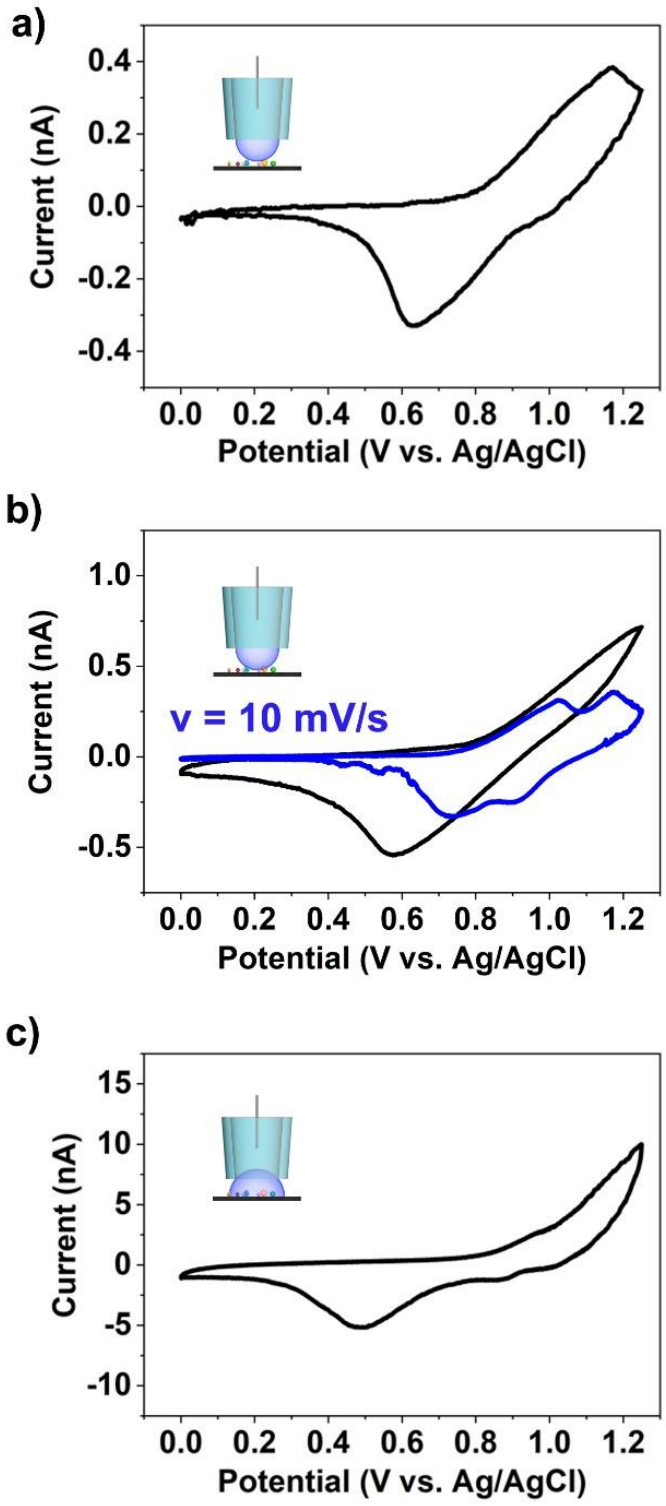

Figure 6.6 CV measurements at different status of **(a)** initial contact and **(b)** more particles involved contact and **(c)** touching substrate from $LiMn_2O_4$ particles supported on HOPG. The blue curve in **(b)** depicts a CV measurement at slow scan rate of 10 mV/s at this status. The

CV measurements (v = 1 V/s) were obtained with probes of diameter ca. 70 µm filled with 1 M LiCl unless specified. Corresponding SEM images of the scanning area is deduced by comparing the SEM images before and after experiment, as shown in Figure 6.20.

6.5 Conclusions

Restrained kinetic behavior leads to the discrepancy between the real performance and expected outcome of battery electrodes. To investigate the Li^+ (de)intercalation kinetics, previous research in this field mainly focuses on multicomponent battery electrodes, which shields the intrinsic properties of active particles. As an advanced characterization technique, SECCM makes stripping away the "matrix effects" possible, revealing that the Li^+ (de)intercalation kinetics in $LiMn_2O_4$ ensembles is largely dominated by interparticle interaction (relaxation) and also affected by particle-support contact resistance. From this prospective, an optimized battery electrode should possess fewer grain boundaries, particle-electrolyte and particle-current collector interfaces. All in all, this work presents new capabilities of SECCM in battery science as a powerful tool to study the kinetics evolution from single particle to cluster then to ensemble level, and also implies free-standing single crystal and/or monolith as ideal candidates for next generation of battery electrodes in the future.

6.6 Supporting Information

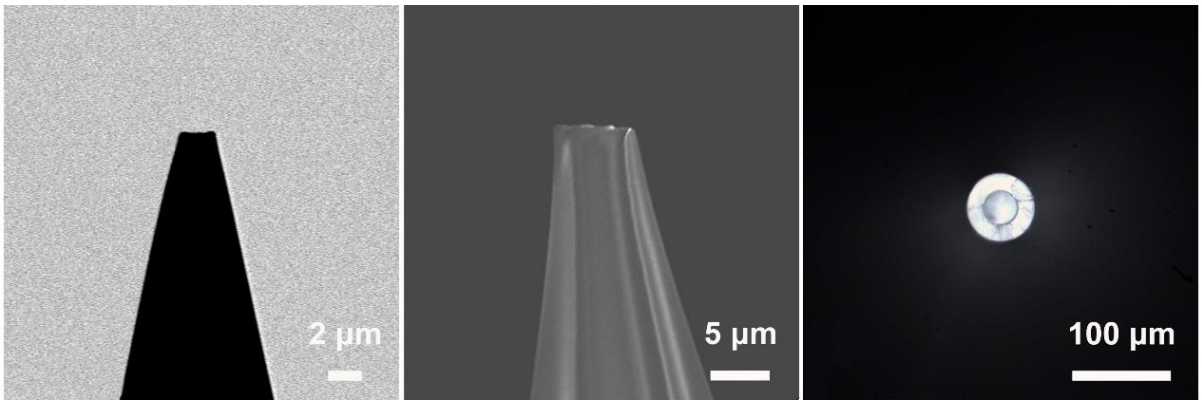

Figure 6.7 Micropipette with different sizes used in this work: **(a)** STEM image of a typical nanopipette with diameter of 2 µm, **(b)** SEM image of a nanopipette with diameter of 5 µm, **(c)** optical image of a nanopipette with diameter of 70 µm.

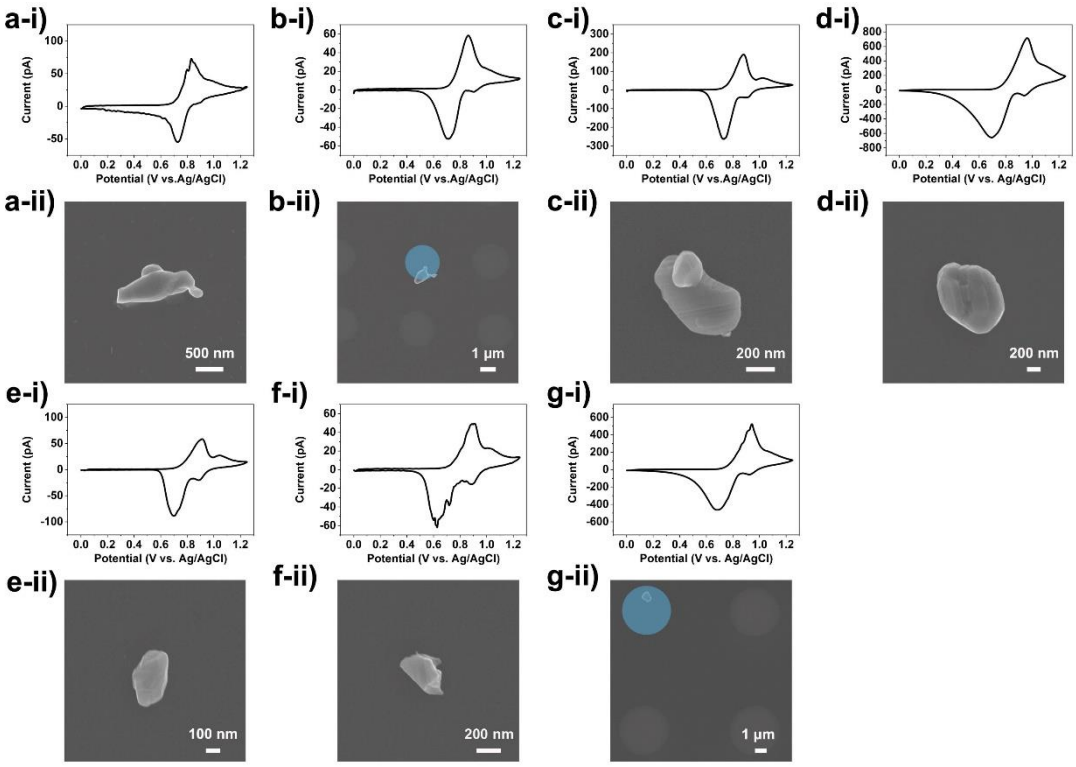

Figure 6.8 (i) CVs and **(ii)** corresponding SEM images from $LiMn_2O_4$ particles supported on glassy carbon at single particle with dry particle-support contact mode. **(a)** to **(f)** The CV measurements (v = 1 V/s) were obtained with probes of diameter ca. 2 µm filled with 1 M LiCl solution. **(g)** The CV measurements (v = 1 V/s) were obtained with probes of diameter ca. 5 µm filled with 1 M LiCl solution.

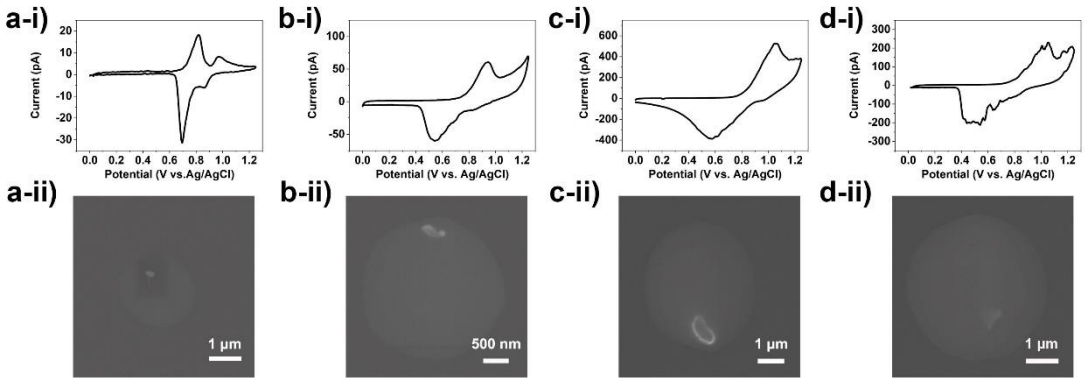

Figure 6.9 (i) CVs and **(ii)** corresponding SEM images from $LiMn_2O_4$ particles supported on glassy carbon at single particle with wet particle-support contact mode. **(a)** and **(b)** The CV measurements (v = 1 V/s) were obtained with probes of diameter ca. 2 µm filled with 1 M LiCl solution. **(c)** and **(d)** The CV measurements (v = 1 V/s) were obtained with probes of diameter ca. 5 µm filled with 1 M LiCl solution.

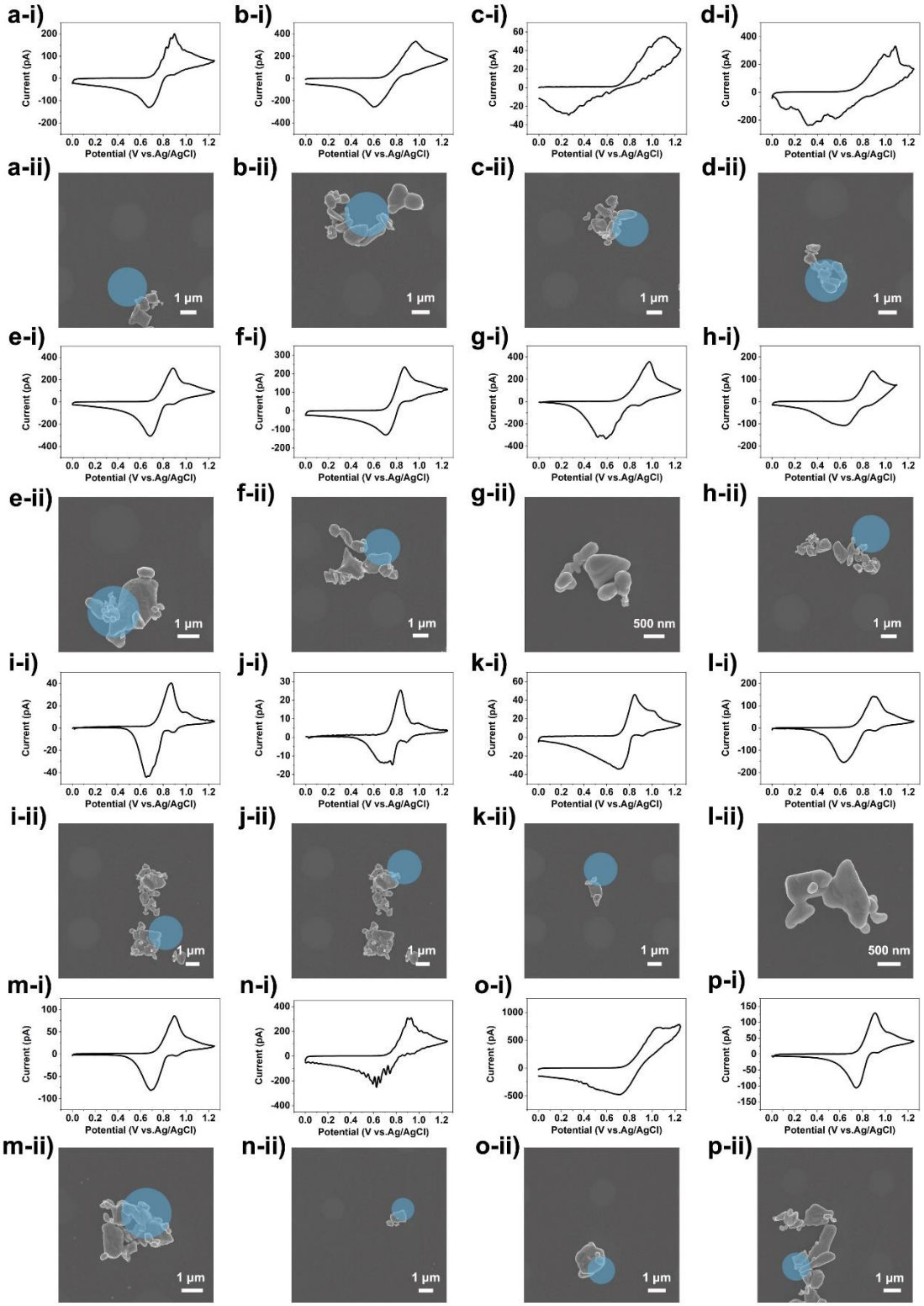

Figure 6.10 (i) CVs and **(ii)** corresponding SEM images from LiMn2O4 particles supported on glassy carbon at multiple particles with dry particle-support contact mode. **(a)** to **(p)** The CV measurements (v = 1 V/s) were obtained with probes of diameter ca. 2 µm filled with 1 M LiCl solution.

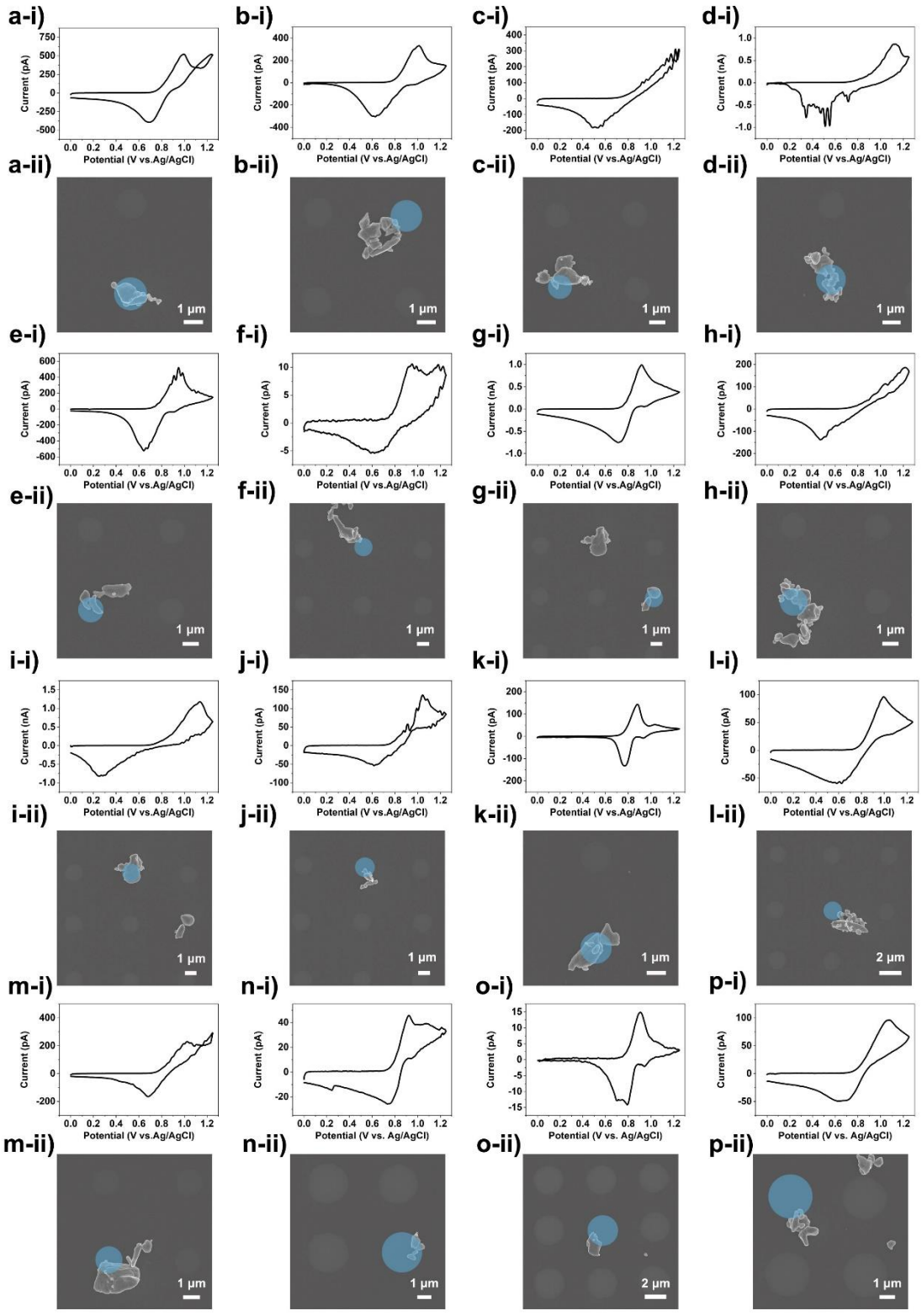

Figure 6.11 (i) CVs and **(ii)** corresponding SEM images from $LiMn_2O_4$ particles supported on glassy carbon at multiple particles with dry particle-support contact mode. **(a)** to **(p)** The CV measurements (v = 1 V/s) were obtained with probes of diameter ca. 2 µm filled with 1 M LiCl solution. Figure 6.11 is the continuation of Figure 6.10.

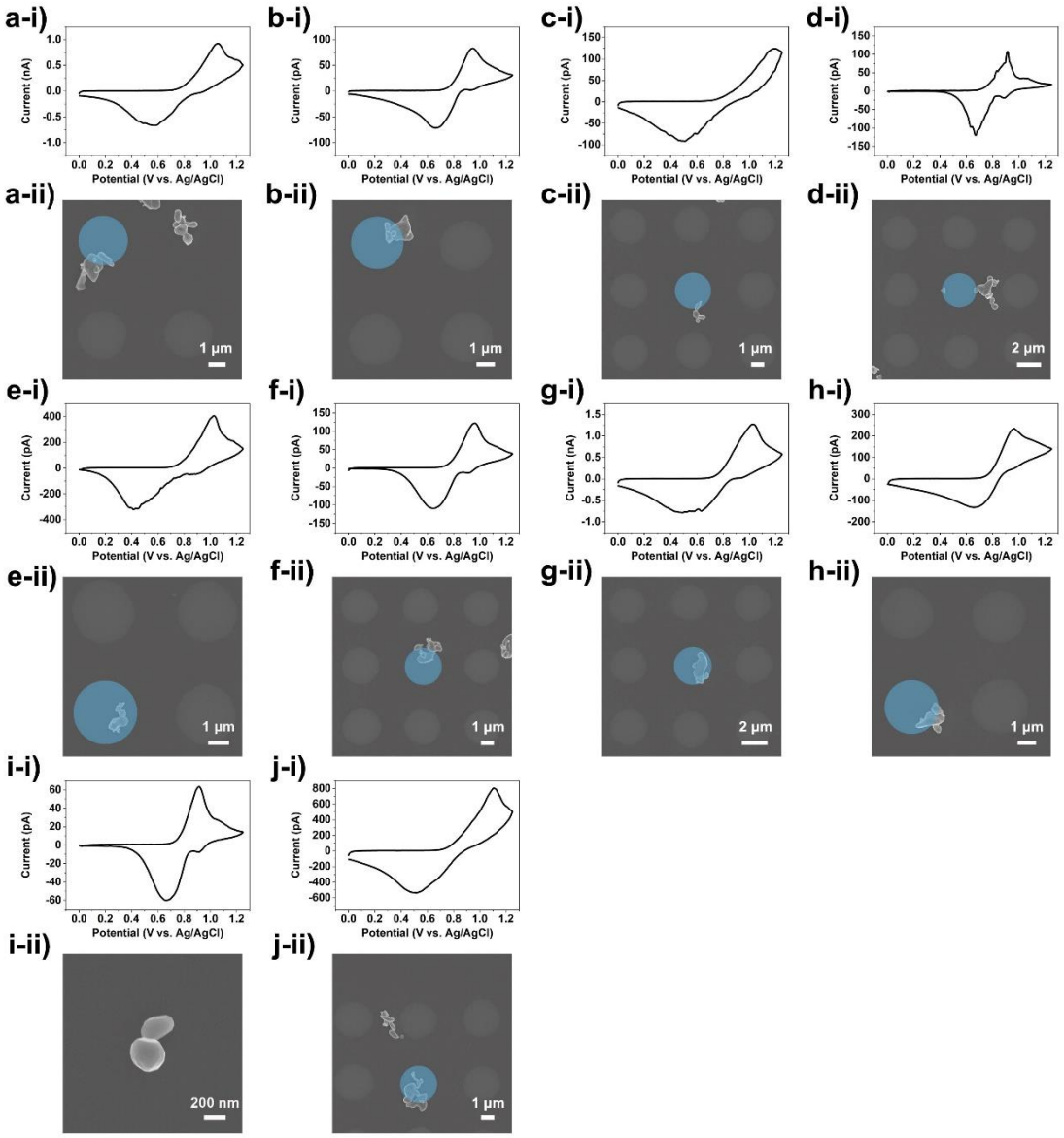

Figure 6.12 (i) CVs and **(ii)** corresponding SEM images from $LiMn_2O_4$ particles supported on glassy carbon at multiple particles with dry particle-support contact mode. **(a)** to **(j)** The CV measurements (v = 1 V/s) were obtained with probes of diameter ca. 2 µm filled with 1 M LiCl solution. Figure 6.12 is the continuation of Figure 6.10 and Figure 6.11.

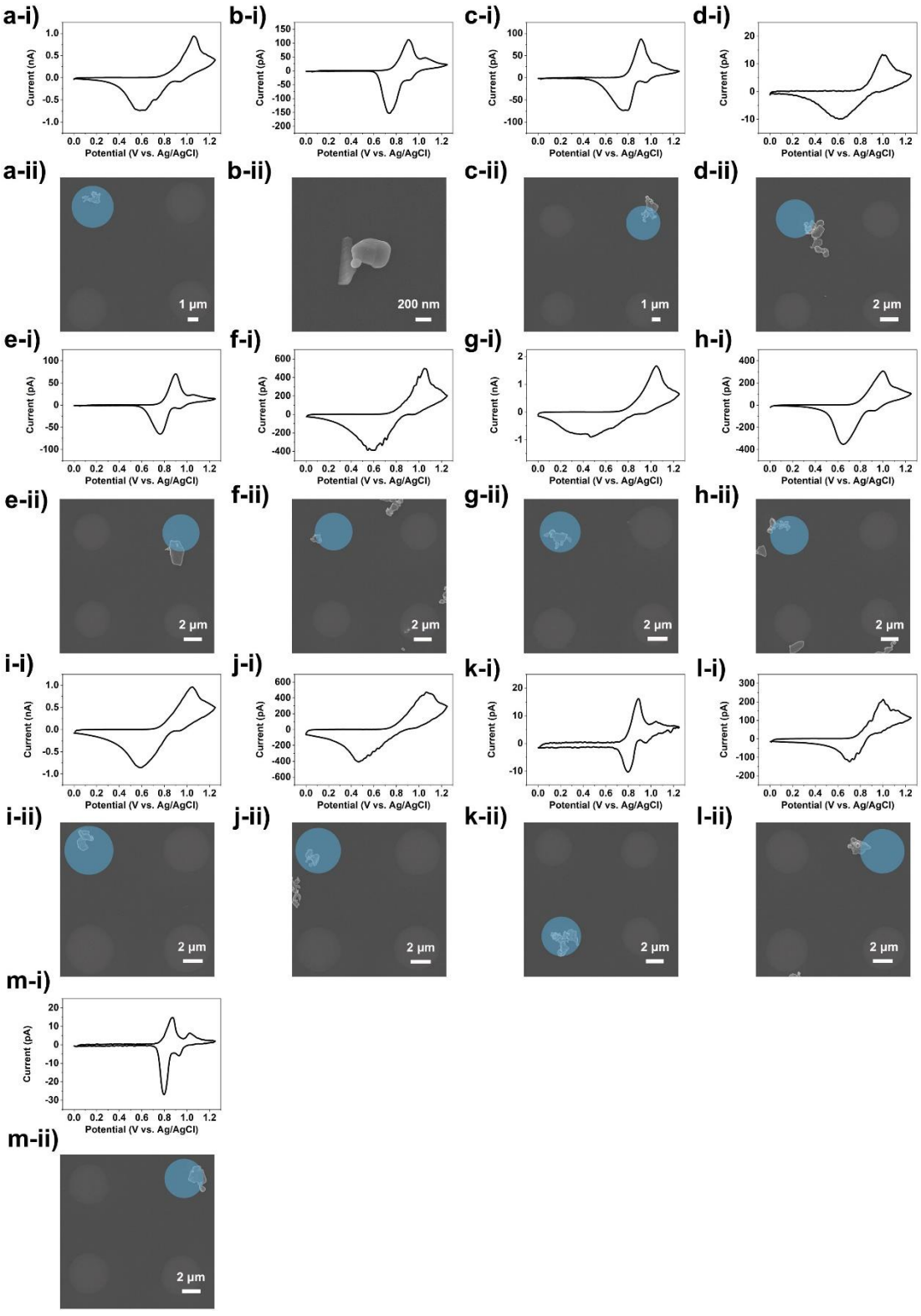

Figure 6.13 (i) CVs and **(ii)** corresponding SEM images from $LiMn_2O_4$ particles supported on glassy carbon at multiple particles with dry particle-support contact mode. **(a)** to **(m)** The CV measurements (v = 1 V/s) were obtained with probes of diameter ca. 5 µm filled with 1 M LiCl solution.

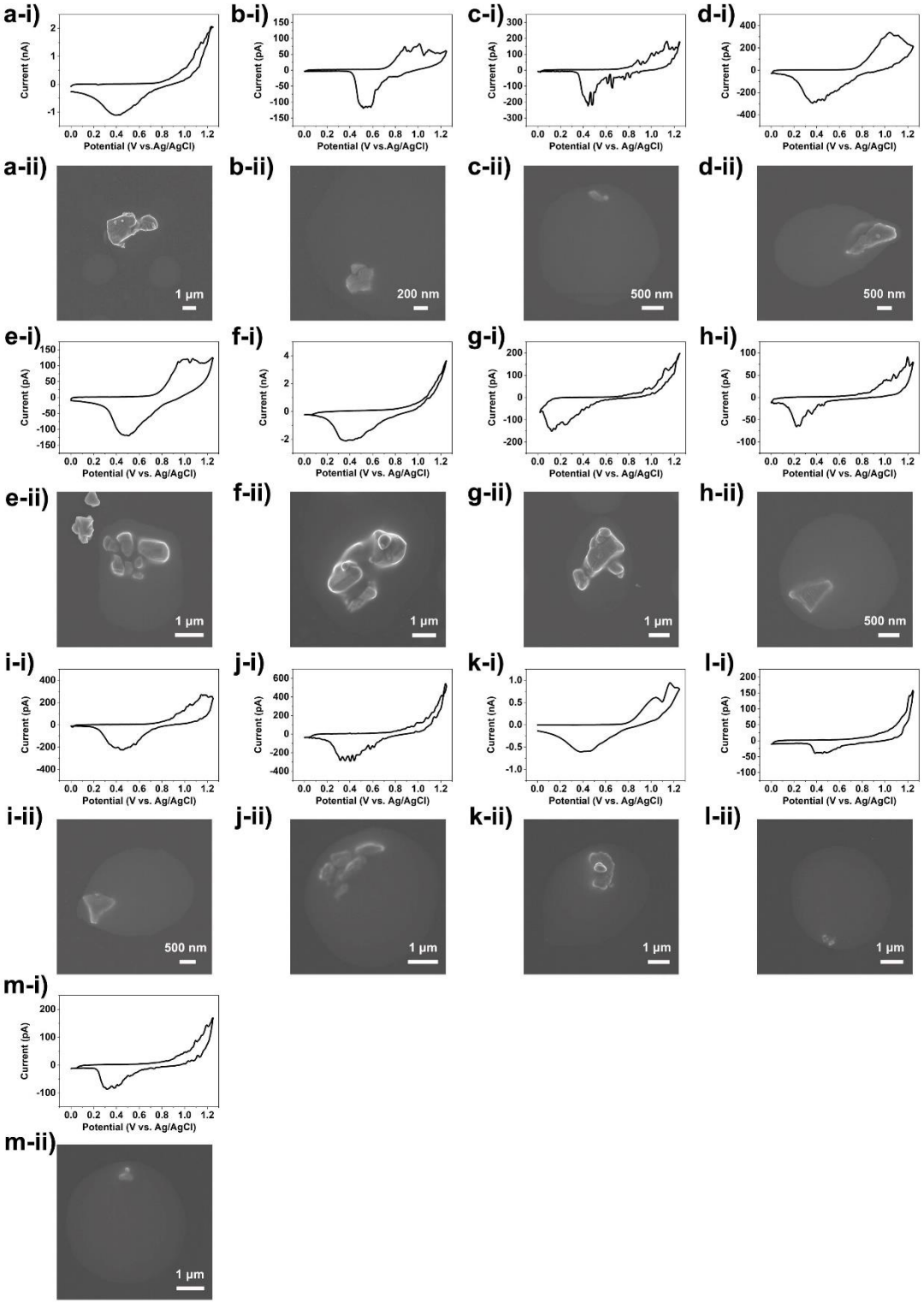

Figure 6.14 (i) CVs and **(ii)** corresponding SEM images from $LiMn_2O_4$ particles supported on glassy carbon at multiple particles with wet particle-support contact mode. **(a)** to **(i)** The CV measurements (v = 1 V/s) were obtained with probes of diameter ca. 2 µm filled with 1 M LiCl solution. **(j)** to **(m)** The CV measurements (v = 1 V/s) were obtained with probes of diameter *ca.* 5 µm filled with 1 M LiCl solution.

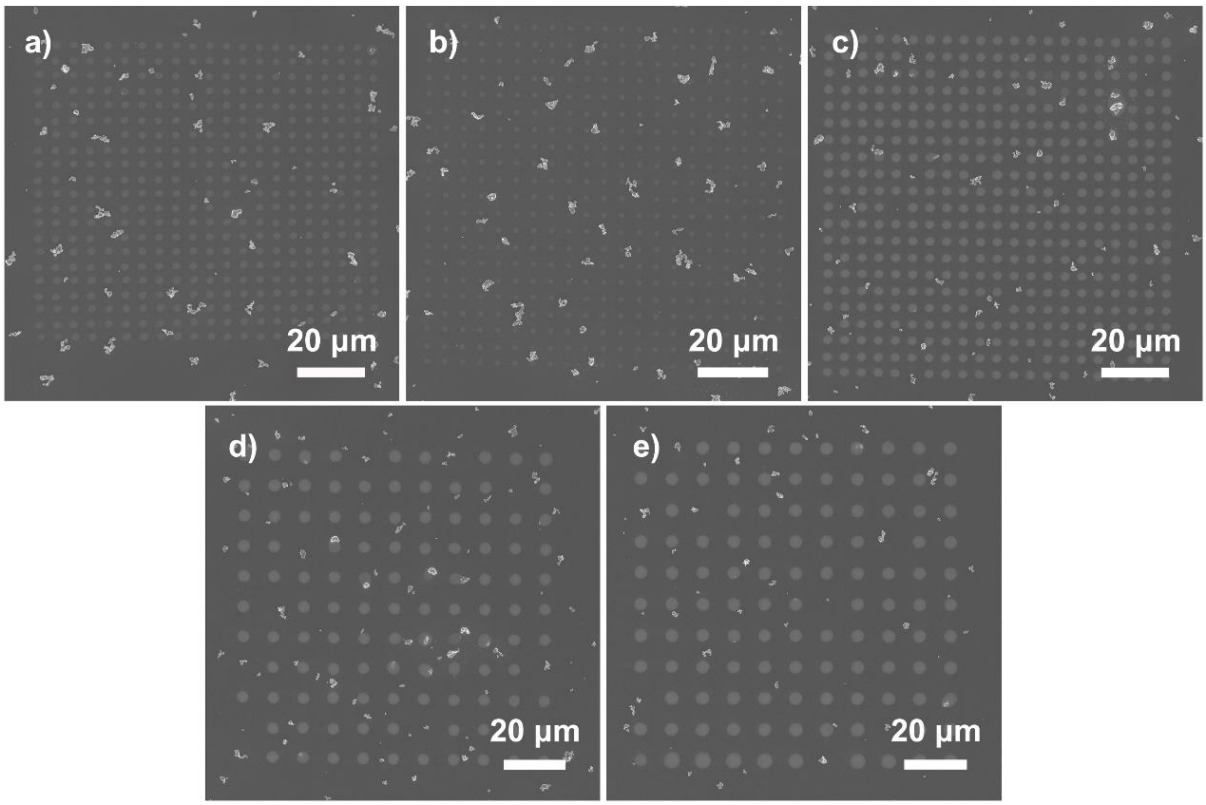

Figure 6.15 SEM images of the scanning areas of the cyclic voltammetry measurements of individual and aggregated $LiMn_2O_4$ particles supported on glassy carbon. **(a)**, **(b)** and **(c)** are performed with tips of diameter ca. 2 µm with hopping distance of 5 µm. **(d)** and **(e)** are performed with tips of diameter ca. 5 µm with hopping distance of 10 µm.

Table 6.1 Electrochemical characteristics of four different electrolyte-particle(s)-glassy carbon contact modes, derived from 5 different cyclic voltammetry scans (the corresponding SEM images shown in Figure 6.8). The particle sequence in this table is the same with Figure 6.9-15.

Tip size (µm)	Anodic Peak Voltage (V)	Anodic Peak Current (nA)	Cathodic Peak Voltage (V)	Cathodic Peak Current (nA)	Peak Separation (V)	Multiple or Single Particle(s)	Contact with Substrate or not
2	0.83	72	0.73	-55	0.1	S	N
2	0.86	58	0.71	-53	0.15	S	N
2	0.88	194	0.73	-263	0.15	S	N
2	0.96	722	0.7	-660	0.26	S	N

2	0.91	60	0.7	-90	0.21	S	N
2	0.9	50	0.63	-62	0.27	S	N
5	0.94	531	0.68	-468	0.26	S	N
2	0.81	18	0.7	-31	0.11	S	Y
2	0.94	62	0.54	-61	0.4	S	Y
5	1.03	531	0.58	-388	0.45	S	Y
5	1.05	233	0.49	-194	0.56	S	Y
2	0.89	187	0.68	-130	0.21	M	N
2	0.97	331	0.6	-256	0.37	M	N
2	1.1	55	0.25	-29	0.85	M	N
2	1.09	330	0.33	-237	0.76	M	N
2	0.89	300	0.68	-306	0.21	M	N
2	0.87	235	0.7	-129	0.17	M	N
2	0.97	354	0.55	-310	0.42	M	N
2	0.89	136	0.62	-108	0.27	M	N
2	0.87	40	0.65	-44	0.22	M	N
2	0.84	25	0.71	-14	0.13	M	N
2	0.85	46	0.71	-34	0.14	M	N
2	0.9	140	0.63	-154	0.27	M	N
2	0.9	85	0.7	-81	0.2	M	N
2	0.92	297	0.63	-243	0.29	M	N
2	1.05	729	0.71	-486	0.34	M	N
2	0.91	129	0.75	-106	0.16	M	N
2	1	520	0.7	-396	0.3	M	N
2	1	331	0.63	-303	0.37	M	N
2	1.25	311	0.52	-183	0.73	M	N
2	1.13	870	0.47	-660	0.66	M	N
2	0.95	517	0.64	-525	0.31	M	N

2	0.95	10.5	0.6	-5.4	0.35	M	N
2	0.92	1000	0.71	-754	0.21	M	N
2	1.22	188	0.47	-137	0.75	M	N
2	1.14	1180	0.25	-822	0.89	M	N
2	1.04	135	0.62	-54	0.42	M	N
2	0.88	145	0.7	-132	0.18	M	N
2	0.99	97	0.6	-58	0.39	M	N
2	1.02	230	0.68	-165	0.34	M	N
2	0.92	46	0.75	-26	0.17	M	N
2	0.9	15	0.8	-14	0.1	M	N
2	1.07	97	0.66	-49	0.41	M	N
2	1.05	933	0.54	-660	0.51	M	N
2	1.18	124	0.5	-93	0.68	M	N
2	0.94	84	0.66	-73	0.28	M	N
2	0.91	109	0.67	-120	0.24	M	N
2	1.03	413	0.42	-324	0.61	M	N
2	0.96	125	0.65	-110	0.31	M	N
2	1.03	1290	0.48	-789	0.55	M	N
2	0.96	238	0.67	-135	0.29	M	N
2	0.91	64	0.67	-60	0.24	M	N
2	1.1	810	0.51	-536	0.59	M	N
5	1.06	953	0.6	-741	0.46	M	N
5	0.91	115	0.74	-155	0.17	M	N
5	0.91	89	0.77	-74	0.14	M	N
5	1	13.3	0.61	-9.9	0.39	M	N
5	0.9	72	0.76	-66	0.14	M	N
5	1.05	502	0.6	-389	0.45	M	N
5	1.05	1692	0.47	-906	0.58	M	N

5	1	311	0.65	-355	0.35	M	N
5	1.05	974	0.59	-865	0.46	M	N
5	1.06	482	0.47	-412	0.59	M	N
5	0.89	16.5	0.8	-10.3	0.09	M	N
5	1	216	0.7	-127	0.3	M	N
5	0.87	15	0.8	-27	0.07	M	N
2	1.25	2050	0.4	-1107	0.85	M	Y
2	1.02	82	0.54	-114	0.48	M	Y
2	1.13	182	0.44	-220	0.69	M	Y
2	1.04	346	0.36	-293	0.68	M	Y
2	1.07	124	0.5	-120	0.57	M	Y
2	1.25	3650	0.37	-2125	0.88	M	Y
2	1.25	200	0.12	-152	1.13	M	Y
2	1.2	90	0.22	-65	0.98	M	Y
2	1.15	278	0.45	-230	0.7	M	Y
5	1.24	546	0.4	-292	0.84	M	Y
5	1.04	625	0.38	-611	0.66	M	Y
5	1.25	159	0.43	-38	0.82	M	Y
5	1.25	171	0.31	-88	0.94	M	Y

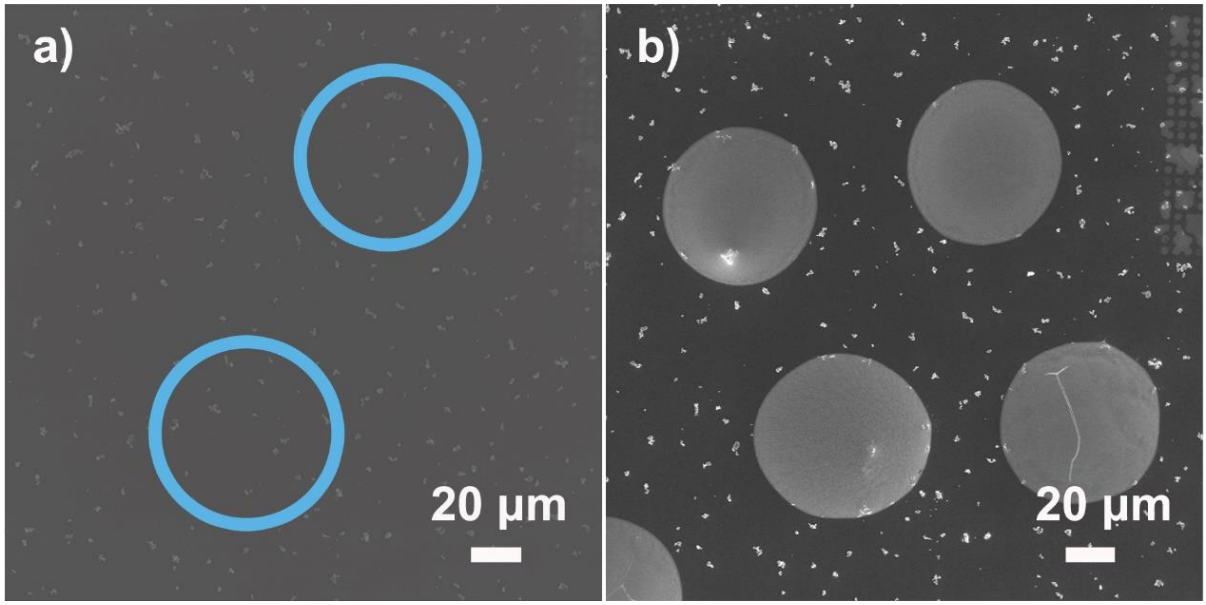

Figure 6.16 Cyclic voltammetric experiments performed on $LiMn_2O_4$ particles supported glassy carbon electrode with tips of diameter ca. 70 µm. Before **(a)** and after **(b)** experiment. The probing areas are indicated by blue circles in **(a)**.

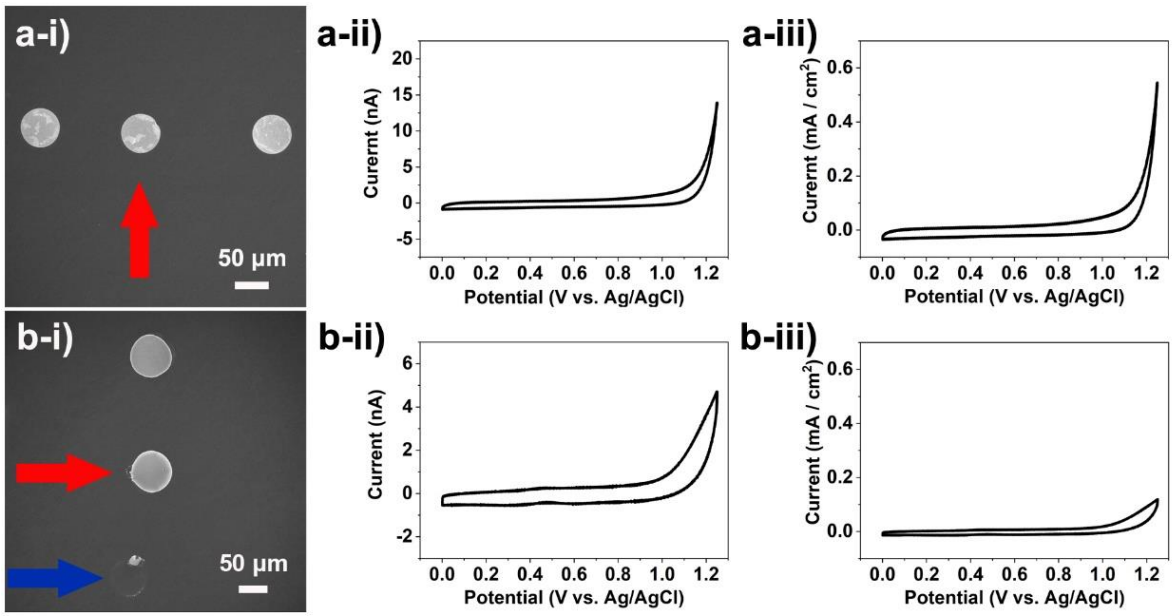

Figure 6.17 (i) SEM image of the footprints after experiment, **(ii)** CV curves and **(iii)** normalized CV curves of different kind of carbon substrates. Experiments were performed via probes with diameter of ca. 70 µm on **(a)** glassy carbon and **(b)** HOPG. The pixel under analysis are indicated by red arrow in both **(a)** and **(b)**. HOPG is highly hydrophobic, sometimes the meniscus would be lift up by the tip thus no obvious residue was left on the surface, as indicated by blue arrow in **(b)**. This property is highly important for the experiment design

('step-approach cyclic voltammetric measurements'), as explained in the main text. The CV measurements (v = 1 V/s) were obtained with probes of diameter ca. 70 µm filled with 1 M LiCl solution.

As discussed in the main text, the parasitic reactions should not interfere with the electrochemical reactions on $LiMn_2O_4$ particles. In order confirm this, experiment was firstly performed on two different kinds of bare carbon substrates (GC and highly oriented pyrolytic graphite, HOPG) via probes with diameter of *ca.* 70 µm (shown in **Figure 6.7c**). Electrochemistry comparisons of these two different substrates are shown in **Figure 6.17**. Relatively featureless CV curves were obtained on all of these supports (typical capacitance behavior on carbon-based material), with processes encountered at extreme anodic potentials attributable to carbon corrosion. It is obvious that the HOPG is much more inert compared with GC, and the side reaction current mainly resided at above 1.1 V in both cases. This means that the side reaction almost has no effect on the $LiMn_2O_4$ reaction on both substrates, as most of the Li^+ intercalation/deintercalation reaction can be finished before this voltage.

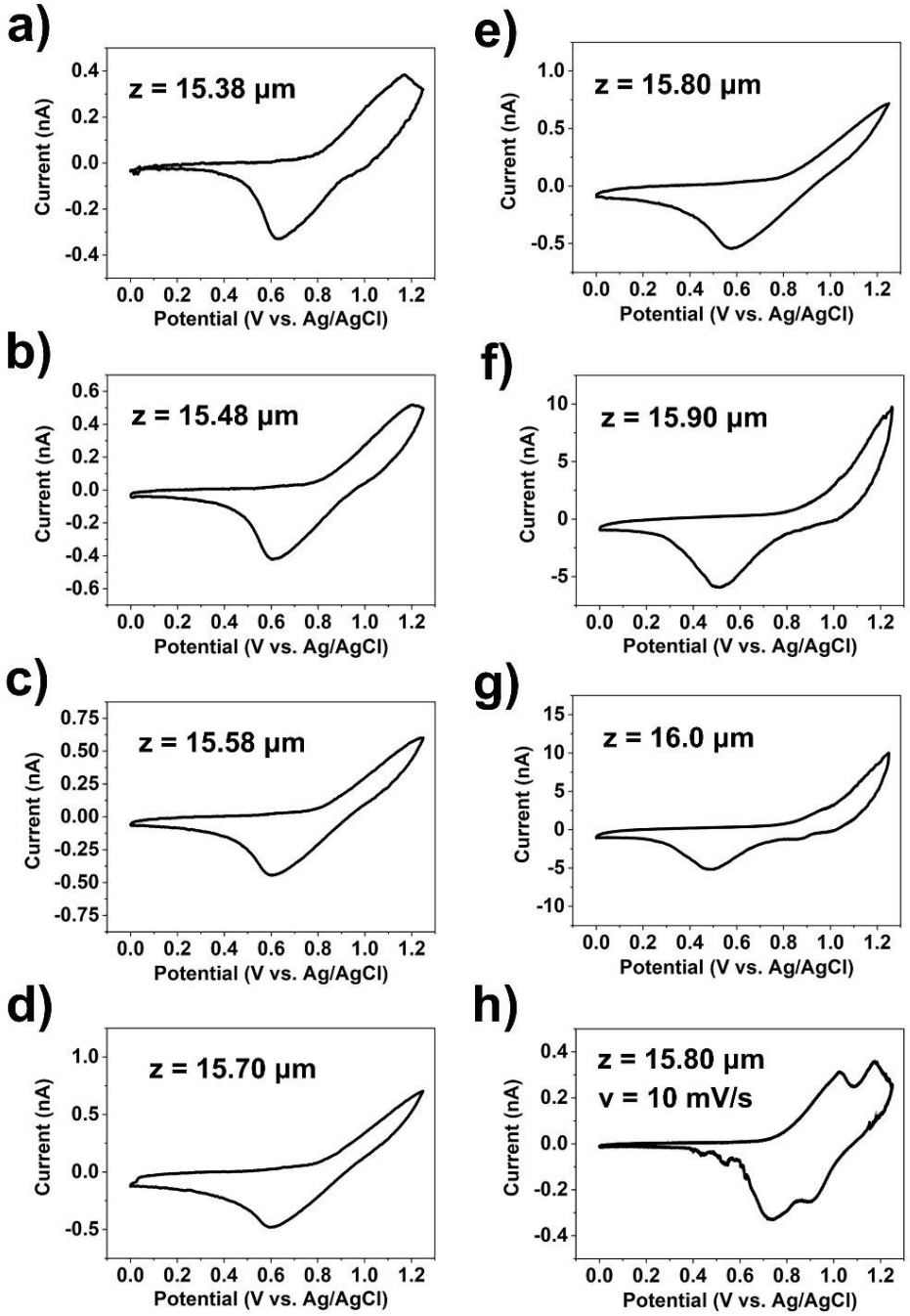

Figure 6.18 'Step approach and CV method' to study the electrochemistry of $LiMn_2O_4$ particles supported on HOPG. From **(a)** to **(g)** the height is 15.38, 15.48, 15.58, 15.70, 15.80, 15.90, and 16.0 µm, respectively, **(h)** was performed at same height with **(e)**, but the scan rate was decreased by 100 folds to 10 mV/s. **(a)**, **(e)**, (**g)** and **(h)** are reformatted in Figure 6.5 in the main text. In **(a)**, **(b)**, **(c)**, **(d)**, **(e)** and **(h)**, the meniscus was not contacted with HOPG, **(f)** and **(g)** was contacted with HOPG.

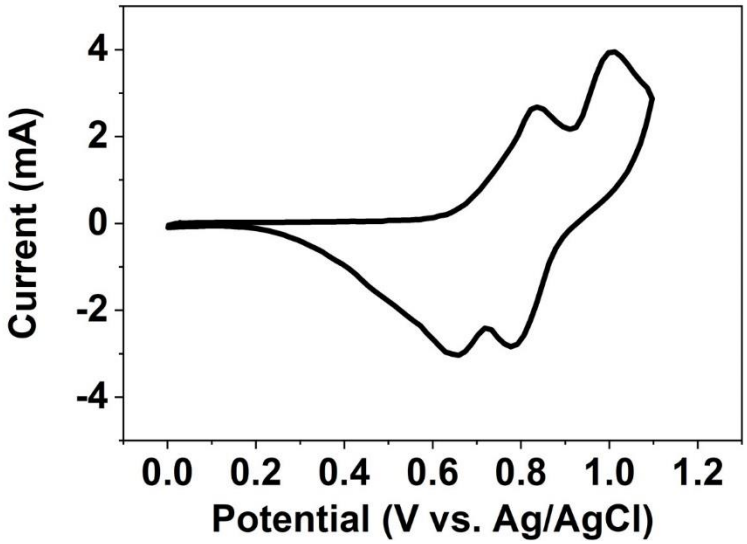

Figure 6.19 Macroscopic CVs obtained from a composite $LiMn_2O_4$ electrode, at scan rates of 2 mV/s. Two pairs of (de)intercalation peaks can be observed, which is very similar with the result from **Figure 6.6b** in the main text (or **Figure 6.18h** above).

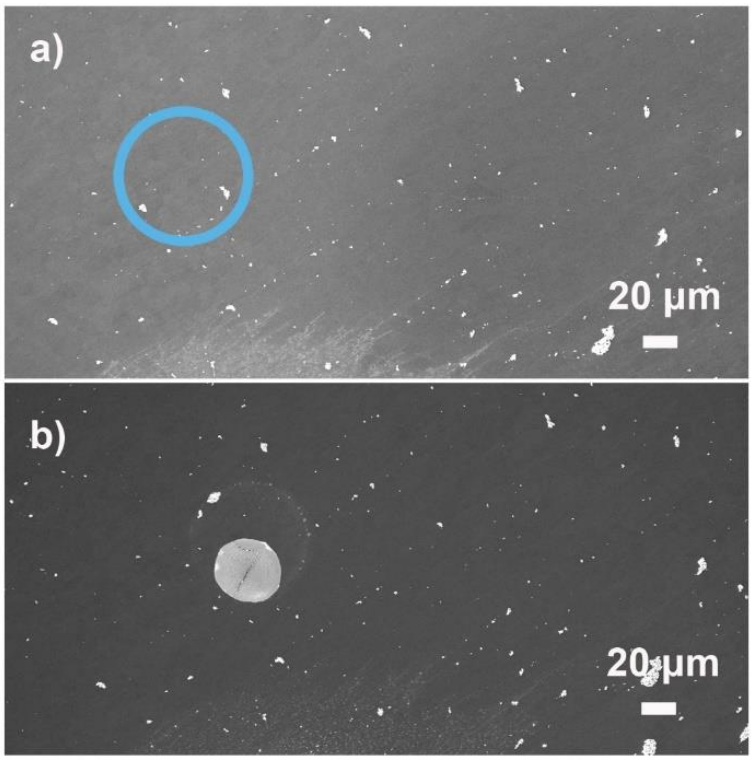

Figure 6.20 Cyclic voltammetric experiments performed on $LiMn_2O_4$ particles supported HOPG electrode with tips of diameter ca. 70 µm. Before **(a)** and after **(b)** experiment. The probing area is indicated by blue circle in **(a)**.

6.7 References

1. Lee, H. W.; Muralidharan, P.; Ruffo, R.; Mari, C. M.; Cui, Y.; Kim, D. K., Ultrathin Spinel $LiMn_2O_4$ Nanowires as High Power Cathode Materials for Li-Ion Batteries. *Nano Letters* **2010**, *10*, 3852-3856.

2. Lee, S.; Cho, Y.; Song, H.-K.; Lee, K. T.; Cho, J., Carbon-Coated Single-Crystal $LiMn_2O_4$ Nanoparticle Clusters as Cathode Material for High-Energy and High-Power Lithium-Ion Batteries. *Angewandte Chemie International Edition* **2012**, *51*, 8748-8752.

3. Hosono, E.; Kudo, T.; Honma, I.; Matsuda, H.; Zhou, H., Synthesis of Single Crystalline Spinel $LiMn_2O_4$ Nanowires for a Lithium Ion Battery with High Power Density. *Nano Letters* **2009**, *9*, 1045-1051.

4. Ding, Y. L.; Xie, J.; Cao, G. S.; Zhu, T. J.; Yu, H. M.; Zhao, X. B., Single-Crystalline $LiMn_2O_4$ Nanotubes Synthesized Via Template-Engaged Reaction as Cathodes for High-Power Lithium Ion Batteries. *Advanced Functional Materials* **2011**, *21*, 348-355.

5. Park, M.; Zhang, X.; Chung, M.; Less, G. B.; Sastry, A. M., A Review of Conduction Phenomena in Li-Ion Batteries. *Journal of Power Sources* **2010**, *195*, 7904-7929.

6. Heubner, C.; Langklotz, U.; Lämmel, C.; Schneider, M.; Michaelis, A., Electrochemical Single-Particle Measurements of Electrode Materials for Li-Ion Batteries: Possibilities, Insights and Implications for Future Development. *Electrochimica Acta* **2020**, *330*, 135160.

7. Xu, W.; Tian, Y.; Zou, G.; Hou, H.; Ji, X., Single Particles Electrochemistry for Batteries. *Journal of Electroanalytical Chemistry* **2020**, 113935.

8. Jiang, D.; Jiang, Y.; Li, Z.; Liu, T.; Wo, X.; Fang, Y.; Tao, N.; Wang, W.; Chen, H. Y., Optical Imaging of Phase Transition and Li-Ion Diffusion Kinetics of Single $LiCoO_2$ Nanoparticles During Electrochemical Cycling. *Journal of the American Chemical Society* **2017**, *139*, 186-192.

9. Lei, C.; Markoulidis, F.; Ashitaka, Z.; Lekakou, C., Reduction of Porous Carbon/Al Contact Resistance for an Electric Double-Layer Capacitor (EDLC). *Electrochimica Acta* **2013**, *92*, 183-187.

10. Ender, M.; Weber, A.; Ivers-Tiffée, E., A Novel Method for Measuring the Effective Conductivity and the Contact Resistance of Porous Electrodes for Lithium-Ion Batteries. *Electrochemistry Communications* **2013**, *34*, 130-133.

11. Deng, Z.; Huang, Z.; Shen, Y.; Huang, Y.; Ding, H.; Luscombe, A.; Johnson, M.; Harlow, J. E.; Gauthier, R.; Dahn, J. R., Ultrasonic Scanning to Observe Wetting and "Unwetting" in Li-Ion Pouch Cells. *Joule* **2020**, *4*, 2017-2029.

12. Louli, A. J., et al., Diagnosing and Correcting Anode-Free Cell Failure Via Electrolyte and Morphological Analysis. *Nature Energy* **2020**, *5*, 693-702.

13. Zhang, X.; Ju, Z.; Zhu, Y.; Takeuchi, K. J.; Takeuchi, E. S.; Marschilok, A. C.; Yu, G., Multiscale Understanding and Architecture Design of High Energy/Power Lithium-Ion Battery Electrodes. *Advanced Energy Materials*, **2020**, 2000808.

14. Tao, B.; Yule, L. C.; Daviddi, E.; Bentley, C. L.; Unwin, P. R., Correlative Electrochemical Microscopy of Li-Ion (De)Intercalation at a Series of Individual $LiMn_2O_4$ Particles. *Angewandte Chemie International Edition* **2019**, *58*, 4606-4611.

15. Uchida, I.; Fujiyoshi, H.; Waki, S., Microvoltammetric Studies on Single Particles of Battery Active Materials. *Journal of Power Sources* **1997**, *68*, 139-144.

16. Dokko, K.; Nishizawa, M.; Mohamedi, M.; Umeda, M.; Uchida, I.; Akimoto, J.; Takahashi, Y.; Gotoh, Y.; Mizuta, S., Electrochemical Studies of Li-Ion Extraction and Insertion of $LiMn_2O_4$ Single Crystal. *Electrochemical and Solid-State Letters* **2001**, *4*, A151.

17. Dokko, K.; Mohamedi, M.; Fujita, Y.; Itoh, T.; Nishizawa, M.; Umeda, M.; Uchida, I., Kinetic Characterization of Single Particles of $LiCoO_2$ by AC Impedance and Potential Step Methods. *Journal of The Electrochemical Society* **2001**, *148*, A422.

18. Dokko, K.; Mohamedi, M.; Umeda, M.; Uchida, I., Kinetic Study of Li-Ion Extraction and Insertion at $LiMn_2O_4$ Single Particle Electrodes Using Potential Step and Impedance Methods. *Journal of The Electrochemical Society* **2003**, *150*, A425.

19. Choi, M.; Siepser, N. P.; Jeong, S.; Wang, Y.; Jagdale, G.; Ye, X.; Baker, L. A., Probing Single-Particle Electrocatalytic Activity at Facet-Controlled Gold Nanocrystals. *Nano Letters* **2020**, *20*, 1233-1239.

20. Tarnev, T.; Aiyappa, H. B.; Botz, A.; Erichsen, T.; Ernst, A.; Andronescu, C.; Schuhmann, W., Scanning Electrochemical Cell Microscopy Investigation of Single ZIF-Derived Nanocomposite Particles as Electrocatalysts for Oxygen Evolution in Alkaline Media. *Angewandte Chemie International Edition* **2019**, *58*, 14265-14269.

21. Ebejer, N.; Güell, A. G.; Lai, S. C. S.; McKelvey, K.; Snowden, M. E.; Unwin, P. R., Scanning Electrochemical Cell Microscopy: A Versatile Technique for Nanoscale Electrochemistry and Functional Imaging. *Annual Review of Analytical Chemistry* **2013**, *6*, 329-351.

22. Bentley, C. L.; Andronescu, C.; Smialkowski, M.; Kang, M.; Tarnev, T.; Marler, B.; Unwin, P. R.; Apfel, U. P.; Schuhmann, W., Local Surface Structure and Composition Control the Hydrogen Evolution Reaction on Iron Nickel Sulfides. *Angewandte Chemie International Edition* **2018**, *57*, 4093-4097.

23. Bentley, C. L.; Kang, M.; Maddar, F. M.; Li, F.; Walker, M.; Zhang, J.; Unwin, P. R., Electrochemical Maps and Movies of the Hydrogen Evolution Reaction on Natural Crystals of Molybdenite (MoS_2): Basal Vs. Edge Plane Activity. *Chemical Science* **2017**, *8*, 6583-6593.

24. Bentley, C. L.; Kang, M.; Unwin, P. R., Nanoscale Structure Dynamics within Electrocatalytic Materials. *Journal of the American Chemical Society* **2017**, *139*, 16813-16821.

25. Bentley, C. L.; Perry, D.; Unwin, P. R., Stability and Placement of Ag/AgCl Quasi-Reference Counter Electrodes in Confined Electrochemical Cells. *Analytical Chemistry* **2018**, *90*, 7700-7707.

26. Luo, J. Y.; Xia, Y. Y., Aqueous Lithium-Ion Battery $LiTi_2(PO_4)_3/LiMn_2O_4$ with High Power and Energy Densities as Well as Superior Cycling Stability. *Advanced Functional Materials* **2007**, *17*, 3877-3884.

27. Lesel, B. K.; Cook, J. B.; Yan, Y.; Lin, T. C.; Tolbert, S. H., Using Nanoscale Domain Size to Control Charge Storage Kinetics in Pseudocapacitive Nanoporous $LiMn_2O_4$ Powders. *ACS Energy Letters* **2017**, *2*, 2293-2298.

28. Yi, Y.; Weinberg, G.; Prenzel, M.; Greiner, M.; Heumann, S.; Becker, S.; Schlögl, R., Electrochemical Corrosion of a Glassy Carbon Electrode. *Catalysis Today* **2017**, *295*, 32-40.

29. Elgrishi, N.; Rountree, K. J.; McCarthy, B. D.; Rountree, E. S.; Eisenhart, T. T.; Dempsey, J. L., A Practical Beginner's Guide to Cyclic Voltammetry. *Journal of Chemical Education* **2018**, *95*, 197-206.

30. Xia, Y.; Takeshige, H.; Noguchi, H.; Yoshio, M., Studies on an LiMnO Spinel System (Obtained by Melt-Impregnation) as a Cathode for 4 V Lithium Batteries Part 1. Synthesis and Electrochemical Behaviour of $Li_xMn_2O_4$. *Journal of Power Sources* **1995**, *56*, 61-67.

31. Wu, W.; Xiao, X.; Wang, M.; Huang, X., A Microstructural Resolved Model for the Stress Analysis of Lithium-Ion Batteries. *Journal of The Electrochemical Society* **2014**, *161*, A803-A813.

32. Engstrom, R. C.; Strasser, V. A., Characterization of Electrochemically Pretreated Glassy Carbon Electrodes. *Analytical Chemistry* **1984**, *56*, 136-141.

33. Oztekin, Y.; Yazicigil, Z., Preparation and Characterization of a 1,10-Phenanthroline-Modified Glassy Carbon Electrode. *Electrochimica Acta* **2009**, *54*, 7294-7298.

34. Kozbial, A.; Li, Z.; Sun, J.; Gong, X.; Zhou, F.; Wang, Y.; Xu, H.; Liu, H.; Li, L., Understanding the Intrinsic Water Wettability of Graphite. *Carbon* **2014**, *74*, 218-225.

35. Wei, Y.; Jia, C. Q., Intrinsic Wettability of Graphitic Carbon. *Carbon* **2015**, *87*, 10-17.

Chapter 7. Summary and Outlook

A sustainable society relies on electrochemical energy conversion and storage systems to produce clean energy and provide electricity power on demand, where new electrocatalysts and electrode nanomaterials are necessary. As subtle changes within a nanomaterial can greatly influence its electrochemical activity, it is important to develop robust and versatile techniques for electrochemical measurements/characterization at the nanoscale, such as SECCM, from which electrochemical processes can be better understood, and to allow the future rational design of optimal electrode materials and electrode architectures.

Chapter 3 described the utilization of SECCM for screening the hydrogen evolution reaction (HER) activities of hexagonal boron nitride (h-BN) nanosheets, which were supported on different metal substrates (Cu and Au). Although h-BN is a wide gap semiconductor, this property can be adjusted via strong interactions with metal substrates (changing the Fermi level), which tunes the electrocatalytic activity towards the HER. Through local voltammetry measurement and Tafel slope analysis, Au-supported h-BN was found to exhibit significantly enhanced HER charge-transfer kinetics (exchange current is *ca.* two orders of magnitude larger) compared to Cu-supported h-BN, making the former material a superior support from a catalytic sense. This work underlines that the metal substrate plays a significant role in modulating the electrocatalytic activity of 2D materials, such as h-BN. Work of this type opens up new possibilities for designing 2D electrocatalytic systems where the metal support could be used to tune the electronic properties of the electrode exposed to solution.

Chapter 4 demonstrated the use of SECCM as a tool for surface activity mapping. By investigating the hydrogen evolution reaction (HER) on pristine transition metal dichalcogenides (TMDs), *e.g.*, MoS_2 and WS_2, spatial variations in activities were observed across the surfaces both materials, attributed to different proportions of exposed edge plane (*e.g.*, steps, crevices, holes, cracks, *etc.*) and basal plane. Besides, aging these crystals in ambient conditions has detrimental effects on HER activity, due to the blockage of active sites by adventitious adsorbates and surface oxidation. Compared to conventional macroscopic electrochemical measurements, the advantages of scanning probe-based electrochemical mapping techniques (especially SECCM) is the ability to target specific surface features at the

nanoscale, which avoids variations due to macroscopic sample heterogeneity and further allows a direct cause-and-effect relationship to be built, leading to clear conclusions.

Chapter 5 of this thesis described the application of SECCM in detecting lithium-ion intercalation and deintercalation at single particle level, by correlating electrochemistry with scanning electron microscopy (SEM). As a proof of concept, a well-known cathode material, $LiMn_2O_4$, was selected as the example. Both cyclic voltammetry and galvanostatic charge-discharge measurements were investigated at a series of individual $LiMn_2O_4$ particles. Surprisingly, these nominally similar particles demonstrate their own unique electrochemical responses, attributed to differences in particle size, morphology, crystallinity, and other morphological factors visualized by co-location SEM afterwards. Besides, it was also demonstrated that single particles could be charge/discharged at unprecedented rates, and the solid-state diffusion inside of the particle is not the rate controlling step in Li-ion (de)intercalation process. This chapter highlighted how subtle changes in particle form can greatly influence electrochemical properties, which will allow the establishment of the structure-function relationships and further enable rational design in the field of energy storage materials.

Chapter 6 followed the work described in **Chapter 5**, going one step further to consider $LiMn_2O_4$ from the single particle to the agglomerate level, in order to mimic real battery electrodes, but without the interference from other non-electroactive components, such as binders and conducting agents. The scanning results were firstly classified into four groups according to the number of particles (*i.e.*, *single* vs *multiple*) and the nature of the electrolyte-particle(s)-GC contact (*i.e.*, *dry* vs *wet* contact), which helped to understand the controlling factors (such as contact resistance and ensemble effect) of Li^+ migration in charge-discharge process on cluster level (*ca.* 5-10 particles). After that, the electrolyte-particle(s)-substrate interfaces (presence *vs.* absence of substrate) are precisely controlled by manipulating the *z*-position of the probe (meniscus), deconvoluting ensemble effect from contact resistance effect. It has been proved that the ensemble effect dictating the Li^+ transfer kinetics within $LiMn_2O_4$ particles electrode (agglomerates level, *ca.* 100 particles), while the nature of the particle-support contact (i.e., *wet* vs *dry* contact) also plays an important role.

In summary, this thesis has shown a series of new applications of SECCM in materials science with cutting-edge imaging resolution and data acquisition speeds. In combination with complementary microscopy/spectroscopy techniques, SECCM offers unprecedented opportunity for determining structure−function relationships at the nanoscale. As the Nobel Prize in Chemistry 2019 was awarded for the development of lithium-ion batteries, this will encourage more scientific and technological attention on electrochemistry and advanced techniques for discovering and understanding new materials, including SECCM. For example, one interesting direction is to study the origins of dendritic electrodeposition such as (Li, Na and Zn) on corresponding metal anodes, as the non-planar deposition during battery charging is a fundamental barrier to achievement of full reversibility. With the high time and spatial resolution of the SECCM, individual nucleation, growth and evolution of dendrites during the deposition/stripping process could be resolved and analysed in detail. Another essential work of SECCM in future is to investigate the solid electrolyte interphases (SEI) formation process in tandem with cryogenic electron microscopy (cryo-EM). Correlating electrochemistry data from SECCM with the structure information from cryo-EM would enable spatially resolved SEI distribution on battery materials at different charge/discharge states to be visualized.